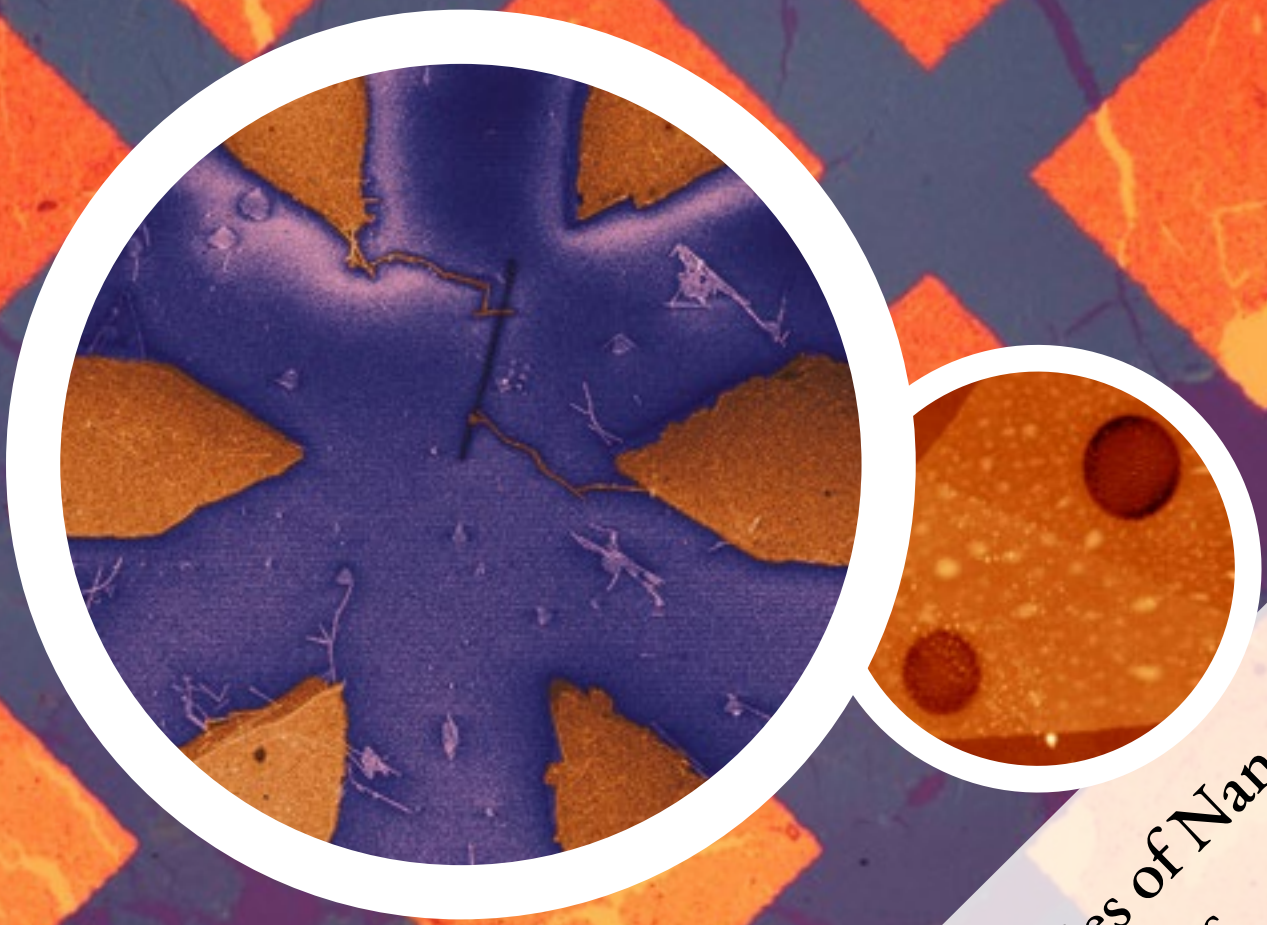

Electrical and Mechanical Properties of Nanomaterials: Characterization and New Techniques

Miriam Moreno Moreno

ELECTRICAL AND MECHANICAL PROPERTIES OF NANOMATERIALS: CHARACTERIZATION AND NEW TECHNIQUES

MIRIAM MORENO MORENO

Under the supervision of:
JULIO GÓMEZ HERRERO
CRISTINA GÓMEZ-NAVARRO GONZÁLEZ

PhD. in Physics
Condensed Matter Physics Department
Faculty of Sciences. Universidad Autónoma de Madrid

Madrid. March 2019

PROPIEDADES ELÉCTRICAS Y MECÁNICAS DE NANOMATERIALES: CARACTERIZACIÓN Y NUEVAS TÉCNICAS

MIRIAM MORENO MORENO

Bajo la dirección de:
JULIO GÓMEZ HERRERO
CRISTINA GÓMEZ-NAVARRO GONZÁLEZ

Doctorado en Ciencias Físicas
Departamento de Física de la Materia Condensada
Facultad de Ciencias. Universidad Autónoma de Madrid

Madrid. Marzo 2019

The research work that has led to this thesis was developed in the Nanoforces Group, Condensed Matter Physics Department, Faculty of Sciences. Universidad Autónoma de Madrid

Front cover. **Background**: optical micrograph of film of $[Cu_2I_2(TAA)]_n$ on $Si/SiO_2(300nm)$ with gold electrodes thermally evaporated on top. This sample is similar to that of figure 4.11(c). **Big circle**: coloured SEM image of the first stand-alone device fabricated by means of PANC. It corresponds to the specular view of nanocircuit shown in figure 5.13. **Small circle**: atomic force microscopy topography of drumheads of few-layer black phosphorus. This image is a rotated version of figure 3.5(c).

A mis padres.

A Juanma.

Shoot for your dreams.
Work hard, follow your heart,
and piece by piece,
it may just someday come together.

Erica Fuchs
Carnegie Mellon University, USA

Nada en el mundo sustituye a la constancia. El talento no la sustituye, pues nada es más corriente que los inteligentes frustrados. El genio tampoco, ya que resulta tópico el caso de los genios ignorados. Ni siquiera la educación sustituye a la constancia, pues el mundo está lleno de fracasados bien educados. Solamente la constancia y la decisión lo consiguen todo.

Baltasar Gracián
Escritor español del Siglo de Oro

RESUMEN

Desde la invención del transistor en 1947, el tamaño de los dispositivos electrónicos se ha ido reduciendo de forma continua hasta alcanzar hoy un tamaño difícilmente reducible a menos que se empleen nuevas técnicas. Esta miniaturización también se ha producido, entre otros, en dispositivos mecánicos y ópticos. La nanociencia y la nanotecnología han permitido esta reducción de tamaño. En este sentido, la aparición de nanomateriales y la caracterización de sus propiedades han sido cruciales. Los nanomateriales tienen al menos una dimensión en el rango nanométrico. Entre ellos, los materiales bidimensionales, con un grosor de pocas capas atómicas, han demostrado tener extraordinarias propiedades que se pueden modular de forma controlada y aplicar a diferentes funcionalidades, lo que hace de estos materiales unos candidatos prometedores en dispositivos variados.

Sin embargo, hay muchos hitos intermedios desde el descubrimiento de un nuevo material 2D hasta su aplicación: la obtención y procesado del mismo, la caracterización y control de sus propiedades así como la fabricación final del dispositivo. Para este fin, se deben desarrollar nuevas tecnologías que resuelvan tales desafíos. Esta tesis está motivada por estas cuestiones. Después de una introducción general a la tesis, se describen las principales técnicas experimentales utilizadas en este trabajo. Seguidamente se estudian experimentalmente las propiedades mecánicas y eléctricas de dos materiales 2D. El primero es un cristal inorgánico y el segundo un polímero metal-orgánico sintético. El estudio también se centra en los efectos ambientales en estas propiedades y, por otro lado, en el procesado de los materiales. A lo largo de tal investigación, nos fuimos encontrando con ciertos problemas que nos hicieron desarrollar una nueva técnica que los solucionara. Dicha técnica debía ser capaz de realizar contactos eléctricos en la escala nanométrica, o incluso menor, de manera limpia, inocua y versátil. Conseguimos desarrollar dicha técnica, que se describe en la última parte de la tesis. Ahí, se demuestra además que, esta nueva metodología proporciona nanocircuitos complejos incluso en dispositivos independientes. Finalmente, se muestran características adicionales y muy ventajosas de dicha técnica, como su resistencia a las variaciones de temperatura y presión, la estabilidad y baja resistencia de los contactos eléctricos que se obtienen con ella y su potencial aplicación en el ámbito de la electrónica molecular, un campo prometedor (y casi único) en la futura miniaturización de circuitos.

ABSTRACT

Since the invention of the transistor in 1947, the size of electronic devices has been continously reduced reaching nowadays a size no longer reducible unless new techniques are employed. This miniaturization also occured in mechanical and optical devices, among others. Nanoscience and nanotechnology has enabled this devices' size evolution. In this regard, the emergence of nanomaterials and the characterization of their properties have been crucial. Nanomaterials have at least one dimension in the nanometer range. Among them, two-dimensional materials, with a thickness of few atomic layers, have shown remarkable, useful and tuneable properties which make these materials promising candidates for diverse devices.

However, some challenges arise along the path from the discovery of a new 2D material until its application: the 2D material obtention and processability, the characterization and tunability of its properties and the final device fabrication. To this end, new technologies that solve those challenges must be developed. This PhD finds its motivation in such issues. After a general introduction to the thesis, a description of the main experimental techniques used along this work is given. Next, the mechanical and electrical properties of two 2D materials have been experimentally studied. The first one is an inorganic crystal and the second one is a synthetic metal-organic polymer. The study also focuses on the environmental effects on these properties and the procesability of the materials. Throughout the research, we encountered certain problems that led our efforts towards the development of a new technique that would solve them. This technique should be able to create electrical contacts in the nanometer, or even smaller, scale in a clean, innocous and versatile manner. We were able to develop such technique, which is described in the last chapter of this manuscript. Moreover, this new procedure is proved to provide complex nanocircuitry even for stand-alone devices. Finally, additional desirable features of this methodology are shown, such as the endurance to temperature and preassure variations, the stability and low resistance of the so-obtained electrical contacts and its potential application in the molecular electronics realm, a promising (and almost unique) field in the future circuit miniaturization.

AGRADECIMIENTOS

Éste no ha sido ni el viaje más largo ni el más agradable que he emprendido, pero quizá uno de los más apasionantes. Ha estado lleno de dedicación, trabajo, frustración, emoción, tensión, risas, lágrimas, algún castigo y recompensa. Todo esto ha sido reflejado en mis notas de laboratorio escritas en 15 cuadernos por varios bolígrafos bic durante los últimos cuatro años y medio. Sin duda el destino de este viaje ha sido un hito en mi vida. Pero lo importante en un viaje no es el destino, sino el viaje en sí mismo y la compañía. Que estas líneas sirvan para expresar mi gratitud a todos aquellos que de alguna forma me han acompañado durante este camino.

Gracias a mis directores Julio y Cristina, que confiaron en mí por segunda vez para realizar la tesis doctoral (¡esta vez sí!) en su laboratorio, uno de los más importantes y punteros de AFM en España. A Julio por su constante seguimiento y preocupación de nuestra investigación, su ilusión por la ciencia, su insaciable sed de conocimiento, sus ganas de hacer experimentos y sus infinitas ideas. A Cristina por su supervisión más práctica, crítica y realista de nuestra investigación y publicaciones. También por su implicación más que directa en muchos experimentos, y en correcciones a contrarreloj. Creo que ambos directores se han complementado en varios aspectos.

Gracias a los compañeros del laboratorio y colaboradores altamente involucrados en esta tesis. A Pablo, por todo lo que me ha enseñado no sólo durante la tesis sino en la etapa de Nanotec. Por sus lecciones de AFM, de instrumentación, por su ayuda en multitud de problemas experimentales, disponible en cualquier momento y eficiente como muy pocos. Gracias por los desarrollos experimentales que me han permitido realizar muchas medidas de esta tesis. Por supuesto gracias por toda su dedicación en parte del trabajo aquí presentado. A Willy por su clases particulares de nanoindentaciones, *stamping* y por resolver dudas en la primera etapa de la tesis. Gracias a Javier Troyano por dejar que le hiciéramos *perrerías* a sus pequeños y recién sintetizados films, por enseñarme su síntesis y resolver dudas. Gracias a Félix por su aportación variada a esta tesis: por los nanomateriales aportados, por sus ideas, por sus respuestas y explicaciones a mis muchas preguntas y por completar parte de la investigación de esta tesis con medidas más allá de nuestras fronteras. A Consuelo por su cercanía, eficiencia y preocupación por todo lo que pudiéramos necesitar para llevar a cabo los últimos experimentos de esta tesis (nanohilos, nanorods, nanopartículas y recubrimientos con moléculas). También por contestar pacientemente a todas mis preguntas y mails. A Pilar muchas gracias por sus cristales, sus medidas, sus palabras de ánimo, su amabilidad y su flexibilidad a la hora de compartir la *Probe Station*. Gracias a Salomé igualmente. Quiero agradecer el tiempo e ideas dedicadas por Andrés Castellanos en el trabajo de la primera parte de esta tesis. No dudó en colaborar con nosotros por segunda vez, gracias. Gracias también a Óscar del Castillo, Christian A. Nijhuis y L. Yuan por su granito de arena.

Me gustaría agradecer a otras muchas personas que, a pesar de no estar tan implicadas en esta tesis, su contribución ha sido indispensable para la realización de la misma. Me

gustaría empezar por Nacho. Gracias por todo el desarrollo instrumental y software que has llevado a cabo, sin el cual muchas medidas y análisis de esta tesis habrían sido imposibles. Gracias por contestar mis numerosas preguntas, por escucharme y aconsejarme. Gracias especialmente por todo lo que me has enseñado tanto profesional como personalmente, no sólo durante esta etapa, sino desde hace unos cuantos años. Eres una de las personas más inteligentes y seguras de sí mismo que conozco. Gracias a José por nuestras conversaciones, por tus consejos, por las piezas hechas de forma tan profesional. Muchas gracias a ambos por las comidas caseras (a veces casi festines) que hemos compartido durante este tiempo. ¡Hay que intentar mantenerlo! Gracias a Santiago por estar siempre disponible para casi cualquier cosa: una pieza, una reparación urgente, una instalación, guantes, vasos *pyrex*, y mil cosas más que te he pedido así como algunas charletas. A José Luis por los trabajos electrónicos que te hemos encargado, las reparaciones, pedidos de componentes, plaquitas de PCB soldadas... y también alguna que otra conversación. ¡Gracias a todos los involucrados en la reposición del nitrógeno líquido! Gracias al personal del SEGAINVEX que alguna vez me ha ayudado, especialmente a Patricio y Mariano. Creo que se debe reconocer mucho más el trabajo de los técnicos, el cual es fundamental para el desarrollo de la investigación y en general no está suficientemente valorado. Desgraciadamente creo que pasa lo mismo con la ciencia en este país.

¡Merche! ¡Guapi! Muchas gracias por todo tu apoyo y ayuda en temas variados a lo largo ya de muuuuchos años. También por nuestras comidas+confidencias en el Plaza Mayor, que me gustaría mantener. Mucha suerte en tu futuro personal y profesional ;) Conseguirás todo lo que te propongas gracias a tu perseverancia. A Adriana, una de las personas más sabias, sensatas y prudentes que conozco, quiero agradecerte tu saber escuchar y tus consejos siempre útiles. Mucha suerte en la nueva andadura profesional. ¡Nos vemos! Gracias al resto de compis de Nanotec no mencionados aún: Alejandro, Jaime, Edu, Luis y María, por nuestras quedadas, partidas de juegos de mesa y partidos de pádel. Gracias igualmente a los clientes de Nanotec que traté durante esos años.

Al resto de mis compis del laboratorio les agradezco el hacer mucho más llevaderas las jornadas intensas de medidas, su ayuda durante las mismas así como los ratos más festivos en salidas, comidas de Navidad o verano y demás celebraciones. De la parte de AFM 2ª planta, gracias a Yolanda (la más sonriente y que menos tacos dice del labo, siempre dispuesta a ayudar), a Diego Aldave (exfoliador, usuario de superláser con Nuria y ahora señor de los nanohilos), a Aitor (murciano empeñado en que engordemos con los dulces traídos de sus viajes), a los exfoliadores Raúl y Eva Durán (uno de tus *flakes*, Eva, ha dado resultados importantes en esta tesis). Gracias a David Martínez y Fran por compartir tiempo de medidas y ocio en mi primera estancia en el laboratorio. De la parte de STM, gracias a Chema e Iván por su opinión sobre mi investigación y presentaciones. A Antonio por su ayuda en cualquier tema, por su amabilidad y empatía, tanto en nuestros primeros años en el labo como en los cuatro últimos. A Mariano, principalmente, por hacerme reír y preocuparse de cómo me iban las cosas. ¡Mucho ánimo, crack! A Alba, el compartir en paralelo la primera etapa de la tesis, con mismo contrato y papeleo. A Bruno, Ana, Héctor, Eva, Diego Expósito y a Hao gracias por vuestra ayuda, colaboración y risas. También gracias a Miguel Moreno y a Nicoleta con los que compartí mis primeros años en el labo. De la parte Bio, quiero "desagradecer" a Pedro sus vaciles :D :D y agradecerle sus ideas y experiencia aportadas a algunos de nuestros experimentos, también sus sugerencias

y preguntas en presentaciones. Gracias a Álvaro, Aída, Marina, Natalia, Manu (sonrisa perpetua), Alicia (calibrando fuerza lateral) y Paco (competiciones con Miguel Ángel por ver quién abandonaba antes el sótano y así perdía). Menciono de nuevo a Merche como parte de este equipo Bio en los primeros años de investigación de ambas, así como a Carolina y David Olea. ¡Suerte a todos incluidos los nuevos fichajes! ¡¡Gracias por todas las veces que me habéis esperado a que terminara de comer, siempre la última!! Quiero agradecer también a Macarena, casi única aliada en el mantenimiento de la limpieza y orden del laboratorio (misión imposible), gracias también por cuidar mis plantas y charlar sobre nuestros achaques y demás. Cuando entregue este ejemplar me acordaré de ti porque será tu cumple.

Nuestros colaboradores químicos también han sido importantes en esta andadura. Gracias por vuestra ayuda y, muchas veces, compañía y charla. Gracias a Miguel Ángel (material, medidas en AFM, etc.), Carmen (por tu simpatía e implicación en medidas con nanohilos), David, Carlos, Javier Conesa, Verónica, Íñigo, Jesús A. M., Jesús L. y Pablo. Gracias también a los ya mencionados, Javier Troyano, Félix, Consuelo, Pilar y Salomé. Recuerdos especiales aquí a mis viejos compis químicos: Lorena, Rodrigo, Isadora, Vicente, Cristina, Almudena, Álex, Elías, Gonzalo y Pablísimo.

Gracias al marivolloso equipo de administración de nuestro departamento: Elsa, Luisa, Ángeles y ahora también Ana Isabel, facilitando toda la burocracia e incluso haciendo algún favorcillo de última hora.

Muchas gracias a otros compañeros del departamento. A Edu Lee por su ayuda en el uso de la *Wire Bonder* y sus consejos en algunos de nuestros experimentos y artículos. Gracias a Natalia Lera por comer a mi misma velocidad y sobre todo por dejarme compartir con ella momentos de estrés de la tesis, especialmente en las semanas previas a su depósito. Gracias a otros compañeros de la familia y congresos: Arturo Baró, Jaime Colchero, Eilsa Palacios, Elena López, Elena Pinilla, Carmen Munuera, Eider, Miriam Jaafar, Agustina, Álex Valbuena, Fernando Moreno, Maru, Alejandro Martín y Carlos Salgado. Muchas gracias a Carlos Romero por nuestras conversaciones sobre el mundo dentro y fuera de la ciencia.

Gracias a los científicos con los que colaboré en mi primera etapa de investigación en física: José Manuel Calleja, Herko van der Meulen, Snezana Lazić, Dipankar Sarkar, Arvind Raman, Ron Reifenberger, Fernando Flores, F. J. García Vidal, Per Sundqvist, J. Scott Bunch, Gabino Rubio, Nicolás Agraït, Andrés Castellanos y Danny Porath. Y también a todos los *ATVSianos* con los que compartí mis años de investigación en reconocimiento biométrico en la EPS de la UAM, con mención especial a Sara, Rubén, Ester y Julián.

Fuera del ámbito científico muchas gracias ante todo a mis padres, a los que les debo lo que soy. Habéis sido, sois y seréis unos pilares fundamentales y referentes para mí. Me habéis apoyado y guiado durante toda mi vida intentando que fuera feliz en todo momento. Gracias también por vuestro apoyo en las semanas previas a la entrega de la tesis. Muchas gracias a esa persona que conocí ahora hace dos años y que se ha convertido de la forma más natural en alguien esencial en mi vida. Gracias por haber asistido a esos cortos italianos y a las siguientes citas. Gracias por tu paciencia, comprensión y apoyo en

todos los momentos que he flaqueado durante la tesis. Tú, como doctor, sabías mejor que nadie lo que estaba pasando. Gracias por nuestros viajes, tus comiditas y nuestras *tontás*, *abuelete*! :D. ¡Gracias Juanma! Os quiero mucho a los tres. Gracias a mi abuela materna por *no olvidarse de mí* y por su fuerza vital, y a mi abuela paterna que falleció durante el transcurso de esta tesis. A mis tíos, tías y primos, especialmente a mi tío David, y primos Víctor y Gabriel. Gracias a Tomasa, Ana y Miguel, siempre pendientes de cómo me iba (y una que yo me sé deseosa de asistir a mi defensa de tesis).

Gracias a todos mis amigos. Empiezo por Sara, Sandra y Amelia, cuya valiosa amistad ha ido madurando a lo largo de estos años. Son muchas las experiencias y viajes compartidos. Gracias por vuestra comprensión, alegría y apoyo. Sin vosotras me habría costado mucho más avanzar en mi camino. Perdonad si la tesis me han tenido apartada de vosotras estos últimos meses. Gracias a mis amigas del cole: Susana, Almu, Raquel y María que, muchas veces, me han inspirado y dado ejemplo. Gracias a mis amigas de física Ana y Bea por su apoyo e interés. Gracias a Lupe e Isa por sus ánimos constantes y nuestras quedadas con *Saru*. También a mis amigos de teleco (Sandra, Patri, Ana, Diego, Pablo, Eva, Sergio, Ricardo, Moni, Héctor, Miguel, Davor, David Castro, Cristina y Noe). Muchas gracias especialmente a Paco por su gran ayuda con la realización de la portada de esta tesis, soportando mis pijoterías hasta bien tarde, y al día siguiente, y al otro... Eres uno de los chicos más amables y atentos que conozco. Gracias a Jorge por hacerme un hueco siempre que viene a España. Gracias a mis amigos más allá del charco: a Arturo y a Richard por no olvidarse de mí. Arturo, gracias por la viñeta de la ciencia experimental que me enviaste (diciendo que era yo la que aparecía en ella :D), ¡aparece al principio de esta tesis!

Finalmente gracias a todo aquél que habiendo leído estos agradecimientos, no haya encontrado su nombre en ellos. Era inevitable que alguien se me olvidara. Ya sólo el que lea esta *parrafada* se merece mi gratitud.

CONTENTS

LIST OF FIGURES

LIST OF TABLES

ACRONYMS

AFM Atomic Force Microscopy (or Microscope)

AM-AFM Amplitude Modulation Atomic Force Microscopy

BP Black Phosphorus

BDT Benzene Dithiol

C-AFM Conductance Atomic Force Microscopy

CC Compliance Current

CNT Carbon Nanotube

COF Covalent Organic Framework

CP Coordination Polymer

CPD Contact Potential Difference

CTAB Cetyl Trimethyl Ammonium Bromide (Hexadecyltrimethylammonium bromide)

DAM-AFM Drive Amplitude Modulation Atomic Force Microscopy

DNA Deoxyribonucleic Acid

DSC Differential Scanning Calorimetry

DUT Device Under Test

EBL Electron Beam Lithography

ECM Electrochemical Metallization

FET Field-Effect Transistor

FIB Focused Ion Beam

FLG Few-layer Graphene

FM-AFM Frequency Modulation Atomic Force Microscopy

FN Fowler-Nordheim (Tunneling)

FTIR Fourier-Transform Infrared (Spectroscopy)

GB Grain Boundary

HOPG Highly Oriented Pyrolytic Graphite

HV High Vacuum

ITO Indium Tin Oxide

IV Current *vs.* Voltage curve

IV_g Current *vs.* Gate Voltage curve

JM Jumping Mode

KPM Kelvin Probe Microscopy

LRS Low Resistance State

HRS High Resistance State

MBE Molecular Beam Epitaxy

MCBJ Mechanical Controllable Break Junction

MEMS Micro-Electro-Mechanical Systems

MOF Metal-Organic Framework

MWCNT Multi-Walled Carbon Nanotube

NW Nanowire

PANC Probe-Assisted Nanowire Circuitry

PCB Printed Circuit Board

PDMS Poly(dimethylsiloxane)

PMMA Poly(methyl methacrylate)

PSD Power Spectral Density

OBD Optical Beam Deflection

RH Relative Humidity

RIE Reactive Ion Etching

RMS Root Mean Square

RRAM Resistive Random Access Memory

RS Resistive Switching

RT Room Temperature

RTS Random Telegraph Signal

SCLC Space Charge Limited Current

SEM Scanning Electron Microscope

SMD Shadow Mask Deposition

SMU Source-Measure Unit

SNOM Scanning Near-field Optical Microscopy (or Microscope)

SPL Scanning Probe Lithography

STM Scanning Tunneling Microscopy (or Microscope)

SWCNT Single-Walled Carbon Nanotube

TAA Thioacetamide

TGA Thermal Gravimetric Analysis

TEM Transmission Electron Microscopy (or Microscope)

XPS X-ray Photoelectron Spectroscopy

XR X-Ray

XRPD X-ray Powder Diffraction

UHV Ultra High Vacuum

UV Ultraviolet

VIS Visible

1 INTRODUCTION

If you google *We are living in the age of* the search engine automatically suggests these possible endings in this order: *science*, *technology*, *globalization*, *money success fame glamour* and finally *information* (see figure 1.1). This simple fact reveals the importance of science and technology nowadays. It is not a coincidence that both appear not only at beginning, but also one followed by the other: they are intrinsically linked to each other. Thanks to technological developments, science is able to progress, and vice versa: there would not be any further instrumentation development without advances in science. This mutual momentum between science and technology is clearly evidenced in the development of their *nano* counterparts: *nano*science and *nano*technology. Indeed, it was the invention of the Scanning Tunneling Microscope in 1981 [1–3] what trigered, to a great extent, the development of both fields.

Nanotechnology comprises the synthesis, design and manipulation of matter with at least one dimension sized from 1 to 100 nm for its further application. It is based on the recognition that particles smaller than 100 nm confer the nanostructures built from them new properties and behaviors [4]. This happens because every property of a macroscopic material has a characteristic length associated with it (e.g. average distance between defects, electron mean free path, magnetic domain size, etc.). When at least one dimension of a material becomes comparable to one or more of these characteristic lengths (many of which are in the nm range), the fundamental physics and chemistry change. Here is where nanoscience arises. **Nanoscience** is the study of materials and structures on the scale of nanometers (the so-called nanomaterials) [5].

We have introduced the nanomaterials and their **size-dependent properties**. Not only new fascinating physical properties arise when the size is reduced, but also novel chemical

Figure 1.1: Proposed endings for the Google search *We are living in the age of...*

properties blossom. The latter ones are highly related with the fact that the percentage of surface atoms in the nanomaterials is very high compared with bulk objetcs, hence reactivities of nanomaterials are larger than those of bulk materials. The **chemical properties** thus include enhanced reactivity, high catalytic activity, porosity, self-assembly, reversible interactions (error-checking) and selectivity [6]. On the other hand, among the **physical properties**, it is worth mentioning the enhanced mechanical properties (high strength, crack resistance), ballistic or quasiballistic electronic transport, surface plasmon resonance in metal nanoparticles, superparamagnetism in magnetic nanoparticles and lower melting point or phase transition temperature just to name a few [7].

Many of these properties can be tuned and exploited in many diverse **applications** such as high density data storage, faster, flexible, and extremely miniaturized electronics, optical devices, highly sensitive sensors, stronger and lighter materials, catalysis, water purification, gas storage, gas detection, energy generation, energy storage, separation processes, in-vivo imaging, diagnostics, drug delivery and many more.

Regarding the nanomaterials, in the eighties, with the discovery of *fullerenes* (spherical structures made of carbon atoms) [8], was time for zero-dimensional materials. In the nineties, with the finding of *carbon nanotubes* (cilindrical structures of carbon atoms) [9], there was a growing interest for one-dimensional materials. Nowadays there is a trend towards **two-dimensional (or 2D) materials** research. A 2D material has only one dimension restricted to the nanometer range. This tendency started in 2004 with the isolation of the first single atomically thin layer of carbon atoms with a honeycomb lattice, known as *graphene* [10]. Since then numerous 2D materials have been researched [11, 12]. 2D materials, that almost include all the elements of the periodic table, can be classified into the following groups according to their composition [11–15]:

- *X-enes*: atomically thin materials of a single element (X): graphene (carbon atoms) [10], silicene (silicon atoms) [16], germanene (germanium atoms) [17], phosphorene (phosphorus atoms) [18] and antimonene (antimonium atoms) [19, 20].
- *Carbide or nitride-based X-enes*: carbon or nitrogen saturated forms of X-enes such as hexagonal boron nitride (h-BN) [21] and silicon carbide (SiC) [22].
- *Transition Metal Dichalcogenides (TDMs)*: with the form MX_2, being M a transition metal (from the 4th, 5th, or 6th group of the periodic table) and X a chalcogen (such as S, Te or Se). MoS_2, WS_2, TiS_2, TaS_2, $MoSe_2$ and WSe_2 belong to this group [23–25].
- *Semimetal Chalcogenides (SMCs)*: of the form MX, where M is a semimetal (Ga or In) and X a chalcogen (S or Se). Examples: GaS, GaSe, InS and InSe. Despite their name, they are semiconductors [26, 27].
- *MX-enes*: transition metal carbides, nitrides of carbonitrides with the form $M_{n+1}X_n$ where M is an early transition metal, X is C and/or N, and n = 1, 2 or 3. Some MX-enes are: Ti_2C, Ti_3C_2, V_2C and Ti_3CN [28, 29].
- *Layered metal oxides* such as Ga_2O_3, NiO, ZnO, TiO_2, V_2O_5 and MnO_2 [30].
- *Layered Double Hydroxides (LDHs)*: a class of ionic lamellar compounds made up of positively charged brucite-like layers with an interlayer region containing charge compensating anions and solvation molecules. Examples: Mg_3Al-NO_3, Zn_2Al-NO_3, Ca_2Al-Cl and $LiAl_2$-NO_3 [31].

- *Synthetic organic 2D polymers*: covalent organic frameworks (COFs), metal organic frameworks (MOFs), and other coordination polymers [32].

But... how can we jump from 2D materials to real world applications based on them? There is much work in between that comprises the measurement, understanding and tuning (if necessary) of their properties and subsequent steps. Here the technology emerges again with the available techniques for those purposes. On one hand there are **techniques to characterize the 2D materials**. Some of the most important ones are [4, 5]: the aforementioned Scanning Tunneling Microscope (STM), the Atomic Force Microscope (AFM), the Scanning Near-field Optical Microscope (SNOM), the Scanning Electron Microsocope (SEM), the Transmission Electron Microscopy (TEM), probe stations, tweezers for grabbing molecules, X-ray diffraction, Infrared, Raman or X-Ray photoelectron spectroscopy (XPS), magnetic resonance and techniques based on fluorescence. On the other hand, there are **technologies to synthesize 2D materials** [33]: Chemical Vapor Deposition (CVD), Molecular Beam Epitaxy (MBE), mechanical exfoliation, stamping transfer, chemical/-solvent exfoliation, chemical synthesis, etc. The fabrication of nanostructures containing the 2D materials are often needed to study such nanomaterials. The **techniques used to fabricate nanostructures** are [4, 5]: optical litography, Electron Beam Lithography (EBL or e-beam), MBE, Focused Ion Beam milling (FIB mill), Scanning Probe Lithography (SPL), stamping transfer, Shadow Mask Deposition (SMD) combined with sputtering or thermal evaporation and techniques to achieve **nanoscale junctions** (break junctions, electromigration, STM and Conductive-AFM) [34].

1.1 MOTIVATION

This thesis is motivated by some of the open problems existing in nanoscience and nanotechnology. From having a 2D material in the laboratory until its final application there are several obstacles that hinders its use in real life. In the first stages of this process the main challenges are: (i) achieve new 2D materials, (ii) properly characterize them to obtain and tune their most appealing properties and finally (iii) develop new techniques to perform this characterization (without damaging the nanomaterial) and possibly to use them for the final application.

1.2 OBJECTIVES

Accordingly, the major goal of this thesis is to solve, to some extent, mentioned problems. Specifically, it pursues the following objectives:

O1 To synthesize new 2D materials in a cost-effective manner

O2 To measure electronic and mechanical properties of new or already existing 2D materials

O3 To develop new techniques to characterize them (specifically the electronic properties)

1.3 CONTRIBUTIONS

The realization of the work presented here, focused on the achievement of these objectives, has generated these contributions:

C1 Synthesis of a new metal-organic few nanometer thick film. Its synthesis is cost-effective and is based on unexpensive reactives. The main contribution of this PhD concerning this film is its electronic and mechanical characterization, where we found outstanding properties. This kind of 2D material belongs to the last group of two dimensional materials described above.

C2 Study of the mechanical properties of few-layer black phosphorus in ambient controlled conditions. One atomic layer of black phosphorus corresponds to the previously introduced phosphorene.

C3 Development of a new methodoly in order to fabricate electrical contacts in nano-objects with high resolution, versatility, low cost and innocuousness for the nano-object under test. This method enables the fabrication of nanocircuits and constitutes an alternative/complementary technique to already mentionted techniques used to create nanostructures or molecular junctions such as EBL, break juntion or Conductive-AFM (which were introduced above).

1.4 STRUCTURE OF THE DOCUMENT

This document is structured as follows:

- Chapter 1 (present chapter) gives a brief introduction to the nanoscience, nanotechnology, nanomaterials, their properties, their applications, 2D materials and experimental techniques used in nanoscience. It also presents the motivation, objectives and contributions of this thesis.
- Chapter 2 describes the main experimental characterization techniques used in this work, namely, the Atomic Force Microscope and the Probe Station. The different working modes that are used in this thesis are overviewed.
- Chapter 3 reports on the mechanical properties of few-layer Black Phosphorus nanosheets. These properties are measured by means of indetantions curves performed with the AFM. The measurements are conducted in high vacuum and in air ambient atmosphere. We characterize the time evolution of the mechanical properties with the exposure to ambient conditions and propose some mechanisms responsible for the results obtained.
- Chapter 4 introduces a new coordination polymer which can be easily process to form few-nm thick films. These films are characterized to obtain their mechanical and electrical properties which turn out to be very appealing for applications. Special attention is paid to its electrical properties, that include high conductivity and resistive switching. The mechanisms behind both phenoma are unraveled.
- Chapter 5 presents a new approach for the fabrication of nanocircuits. We have named this technique PANC, which stands for Probe Assisted Nanowire Circuitry. It

is based on the adsorption of gold nanowires and its further nanomanipulation with the AFM. Its main steps as well as its advantages are described. Some nanocircuits fabricated via this technique are presented as well as representative measurements performed on them. Finally, some future perspectives of this methodology are given.

- Chapter 6 presents the conclusions of this thesis and describes the future research lines.

1.5 THREE MINUTE THESIS

I would like to finish this introductory chapter by adding a short introduction to this thesis that I presented in the framework of the Three Minute Thesis competition in Universidad Autónoma de Madrid in 2017. This is an activity contemplated within the Doctoral Program of mentioned university. This competition is annually held in over 200 universities worldwide. It is open to PhD students to present their research in just 180 seconds with the aid of a single slide. The participants should engage the audience that has no background in the research area.

To capture the attention of the (non-expert) audience, I focused my presentation in one of the main potential applications of my research which is the miniaturized electronics (see figure 1.2). I overviewed the evolution of transistor size, that follows the well-known Moore's law. This law states that the number of transistors that can be installed on an

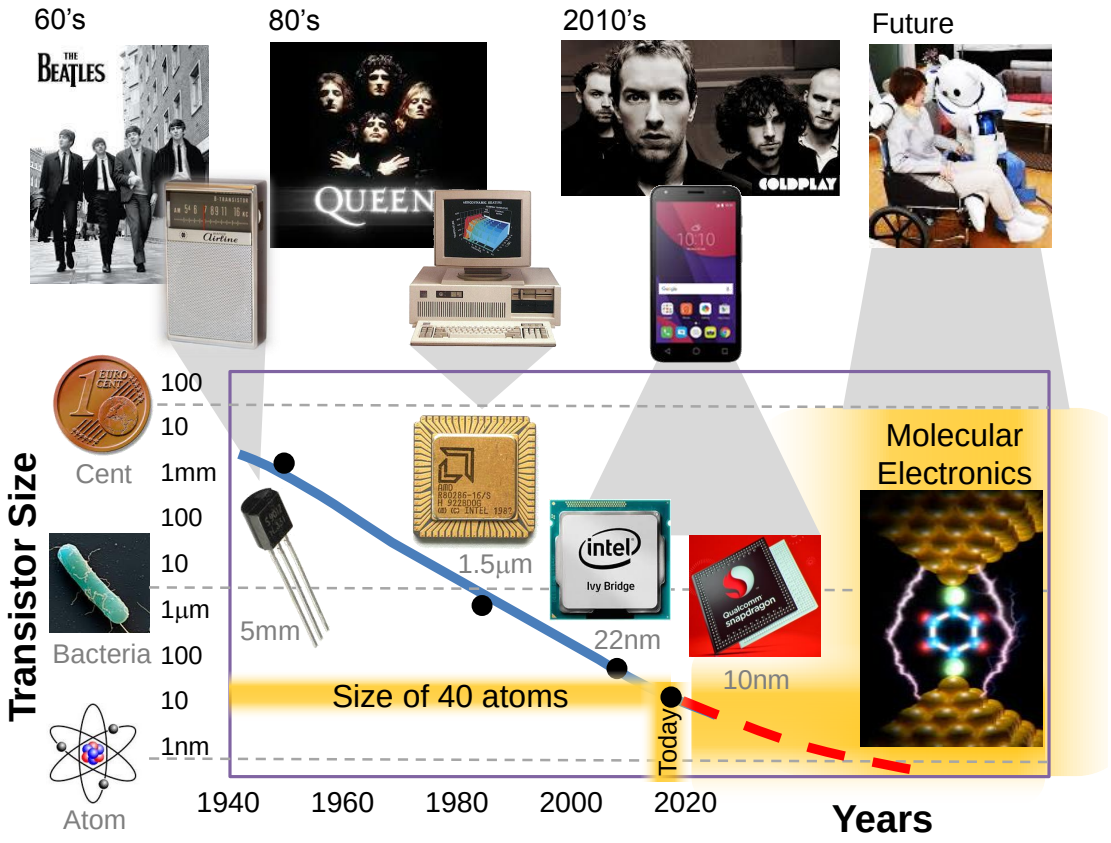

Figure 1.2: My three minute thesis competition slide. Slide that I used in the competition to support my exposition.

integrated circuit doubles every two years [35]. I performed, in parallel, a comparison between the evolution of the characteristic length of the transistor with the size of known objects (in the Y axis of figure 1.2). Furthermore, I presented typical electronic devices that employed those transistors at each decade (a pocket radio, a personal computer and a smart phone), including some representative music groups in order to make a framework of reference. Then, my speech introduced the problem of the further size reduction of the transistor, that is currently reaching a limit if no new technology is used. This new technology corresponds to the **molecular electronics**. At that particular moment is when I revealed my thesis's targets: (i) the development of new ways to construct smaller and more efficient transistors, (ii) the measurement of properties of materials that are candidates to be part of these transistors and finally (iii) the development of new technologies for the study of those materials. I also enumerated then some of the main problems we face when accomplishing such tasks. Finally, I stated the expected impact of my thesis, which is the use of its results (i) by other researchers to progress in the same research line and (ii) in the fabrication of devices that increase our life quality (as for example being part of robots).

2

EXPERIMENTAL TECHNIQUES

This chapter describes the two main experimental tools used along this thesis, which are: the Atomic Force Microscope (AFM) and the Probe Station. First, the fundamentals of AFM are presented including its main parts and the particular AFMs I used. Second, the AFM modes used in this work are described. Third, the principle features of a Probe Station are given. After that I describe the two types of Probe Stations employed in this thesis. Finally, the operation modes of this tool are reported.

2.1 ATOMIC FORCE MICROSCOPY

2.1.1 *Introduction*

The Atomic Force Microscope belongs to the **Scanning Probe Microscope (SPMs)** family. This family comprises some of the instruments used for studying the properties of materials from the atomic (10^{-10} m) to the micro (10^{-6} m) level. All the microscopes belonging to SPM essentially work by positioning a sharp tip (probe of a few nm at its apex) in contact, a few angstroms or one or several nm above the sample to be measured [36]. The tip scans the surface of the sample line by line to obtain the image. The key feature of a SPM is the ability to maintain the tip-sample distance constant while the tip is rastering accross the substrate (in the XY plane) in a highly controlled manner. To accomplish this with a few picometers (10^{-12} m) precision, a signal (that should be very sensitive to the tip-sample distance) must be acquired. That signal comes from the tip-surface interaction that can have different physical origins. The different tip-sample interaction yields the different kind of SPMs, the most well-known are: (i) the **Scanning Tunneling Microscope (STM)** where the interaction is the tunnel current between the tip and a conductor or semiconductor sample, (ii) the **Atomic Force Microscope (AFM)** where the interaction is the set of forces that exist between tip and sample at that scale and finally (iii) the **Scanning Optical Near-field Microscope (SNOM)** where the interaction corresponds to the evanescent waves of light. All mentioned interactions decay very quickly with the tip-sample distance. It is just this strong dependency between interacion and distance what gives the SPMs the extremely high sensitivity to the topographic features of the sample and the origin of their high resolution [37]. The use of (i) a Z closed control loop that keeps constant the tip-sample interaction and so the tip-sample distance and (ii) a high resolution XY scanner that perform the raster scan, allow the acquisition of high resolution three-dimensional images with SPMs. Figure 2.1 shows the scheme of a generic SPM. In order to probe the different local properties of the sample in an SPM, a proper transducter is required to transform the changes in the tip-sample interaction into a magnitude that is processable by the feedback system.

As it was mentioned in chapter 1, the STM was developed in the early 80's by Gerd Binnig and Heinrich Rohrer [1–3]. In 1986 both scientist were awarded with the Physics Nobel Prize for their development of the STM (award shared with Ernst Ruska for his

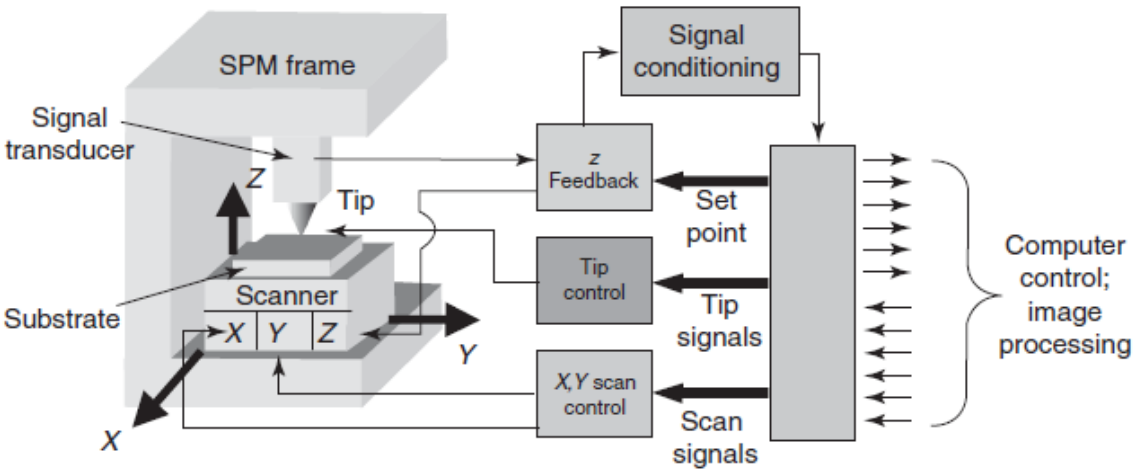

Figure 2.1: Schematic of a generalized SPM. Source: [36].

design of the first electron microscope). In the same year, Gerd Binnig, together with Calvin Quate and Christoph Gerber, developed the AFM [38].

As the STM is based on the measurement and control of the tunnel current, it is restricted to conductor or semiconductor samples. On the contrary, the AFM can be applied to insulator samples too. This ability of the AFM combined with its versatility to operate under different kind of environments (air, liquid, vacuum, controlled atmospheres, etc.) make the AFM the **most flexible** and **widespread** microscope among the SPMs. As evidence of it, AFM is used not only for fundamental research but also for technological applications. Moreover, the AFM is able not only to take 3D images with high magnification, but also is capable of manipulating nanostructures [39], performing lithography [40] and spectroscopy [41], measuring the electrical [42, 43], mechanical [44], magnetic [45], piezoelectric [46] and friction [47] properties, among others.

Nanoforces group, where I carried out my doctoral thesis, is pioneer in the development of the AFM technique in Spain. In fact, some professors of the previous research group (Laboratorio de Nuevas Microscopías), founded a company devoted to the manufacuring, development and sale of SPMs, the software used to control them and to process the acquired data, and also auxiliary technology. This company was Nanotec Electrónica. After working some years in the Laboratorio de Nuevas Microscopías, I had the chance to work in Nanotec Electrónica for two years and a half as a technician, in the testing and R&D department.

Part of the work of previous thesis accomplished in the Nanoforces group [37, 48–53] performed improvements in the AFM technique, and they describe it in detail. In this dissertation I described the basic concepts and the working modes employed in the experiments.

An AFM, as it was explained before, is a SPM in which the tip-sample interaction used to acquire the images is the force existing between them. In this case the tip is located at the end of a **microcantilever**, and the interaction yields a **deflection** of it (or, depending on the mode, a change of its amplitude and/or resonance frequency if it is oscillating). This deflection can be detected by different ways being the optical beam deflection (OBD) the predominant one (and the one used here). OBD consists on using of a focused laser beam that hits the end of the cantilever (just above the tip). The beam is reflected there reaching

a photodiode detector. A change in the deflection of the cantilever (due to the tip-sample interaction) leads to a shift in the vertical and horizontal coordinates of the spot laser on the detector [37]. The latter transforms this spot shift into a pair of voltages: one accounts for the vertical deflection (**normal force**) and the other for the torsional deflection (**lateral force**). In most AFM modes the lateral force is almost constant (compared to the normal force) and is the normal force the most considered one.

The **tip is approached** to the sample surface firstly by a coarse positioning systems (DC motors, stepper motors, piezoelectric motors, etc.) until it is several microns far from the sample. Afterwards, a piezoelectric system brings the tip closer to the sample, until the tip-sample interaction reaches the value at which the sample can be imaged. Then the feedback system maintain the tip-sample distance constant by keeping constant the value of a magnitude that is related to the tip-sample interaction (e.g. the normal force, the oscillation amplitude, the resonance frequency, etc.). By doing that while the sample is scanned, a Z(X, Y) surface of it is obtained. That **scan** is performed by a piezoelectric scanner which can move either the tip over the sample, or the sample under the tip in a raster pattern. The AFMs I used along my thesis have the second setup (the tip is fixed and the sample moves).

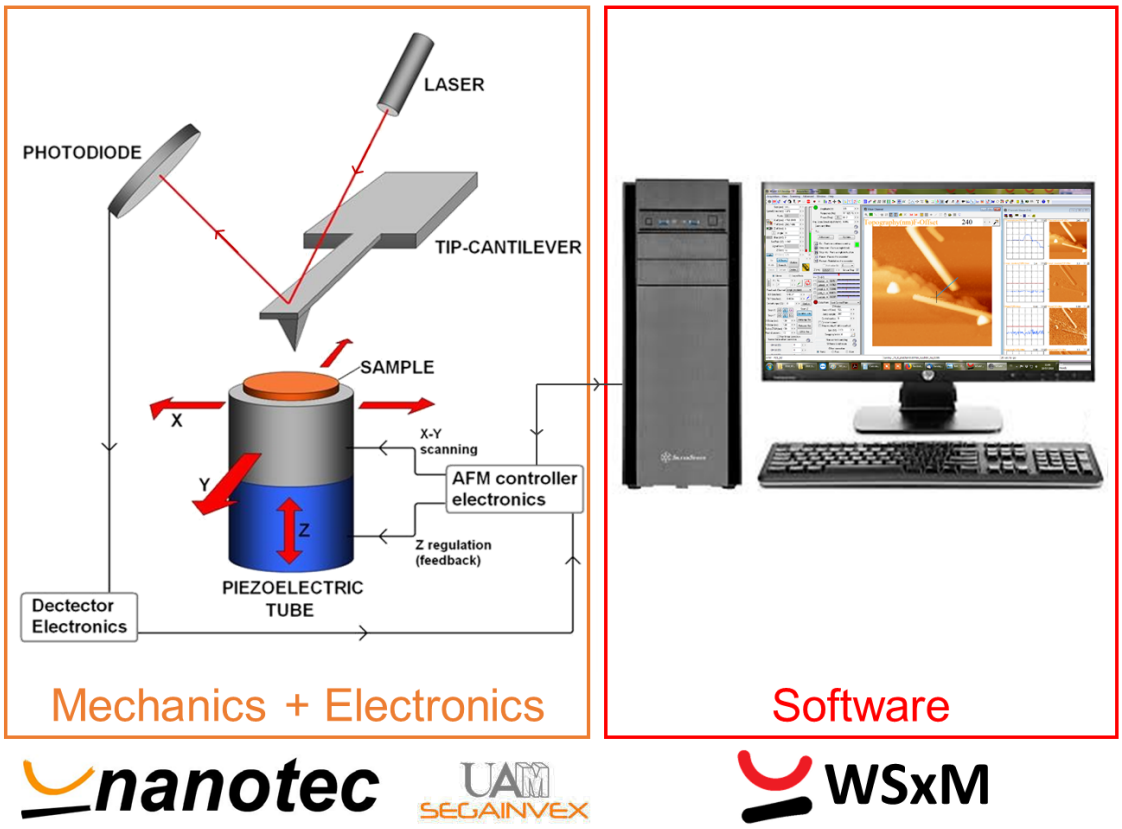

Figure 2.2: Schematic of an AFM. Nanotec Electrónica and/or UAM-Segainvex developed the mechanics and electronics of the AFMs used along this thesis. The software package used with them (WSxM) [54, 55] was developed at and Nanotec Electrónica. Left schematic was extracted from: [56].

The **main parts of an AFM** are: (i) **the mechanics**, that includes: the coarse Z positioning system, the piezo scanner, the sample holder, and the so-called AFM head (that contains the laser, cantilever holder, cantilever with the tip and the photodiode detector), (ii) **the electronics**, comprising the photodiode detector electronics, the high voltage unit, the signal conditioning unit and the controller, and finally (iii) **the software**. A diagram showing a generic AFM with the mentioned parts is depicted in figure 2.2. Furthermore, an AFM is usually coupled to an optical microscope to place the tip in the area of interest of the sample.

2.1.2 *AFMs used along this PhD*

The electronics and mechanics of all the AFMs used along this thesis, were designed and fabricated by Nanotec Electrónica and UAM-SEGAINVEX. Prof. Julio Gómez Herrero (full proffesor at U.A.M., Nanoforces group leader and former co-founder of Nanotec Electrónica) and Dr. Pablo Ares (former Nanotec Electrónica application scientist and PhD by U.A.M. at Nanoforces group) were intensively involved in the mechanics and electronics of them. The software I used to control de AFMs and process the acquired data is the WSxM [54, 55]. It was created and developed in Nanotec Electrónica. It is a free software worlwide used. Currently, Ignacio Horcas Calvo (former director of software and technical project manager in Nanotec Electrónica, and current software and electrical engineer in the Condensed Matter Physics Department at U.A.M.), is in charge of the mantainance of this software among other tasks.

Three AFMs were used to perform most experiments of this thesis. Two of them can operate in air and in a controlled atmosphere (such as argon, nitrogen, etc.). The other one can also work at a controlled pressure from high vacuum (~10^{-6} mbar) to 3 bar. I used the two first at air and at argon atmosphere and the second one in high vacuum and in air.

Figure 2.3 shows the electronic control unit (2.3(a)) and the software (software cover shown) (2.3(b)) that were used whith each AFM employed in this thesis. Figure 2.4 displays two pictures of the mechanics of each AFM used in this thesis.

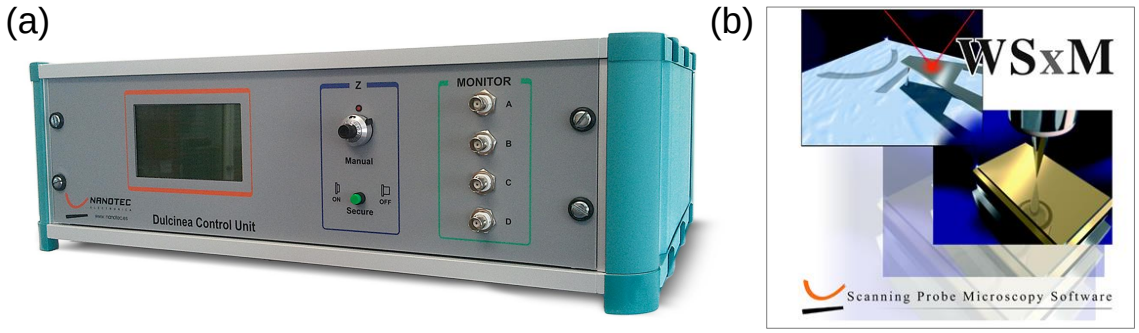

Figure 2.3: Electronic control unit and software used with the AFMs employed in this thesis. (a) Electronic control unit. (b) Software cover.

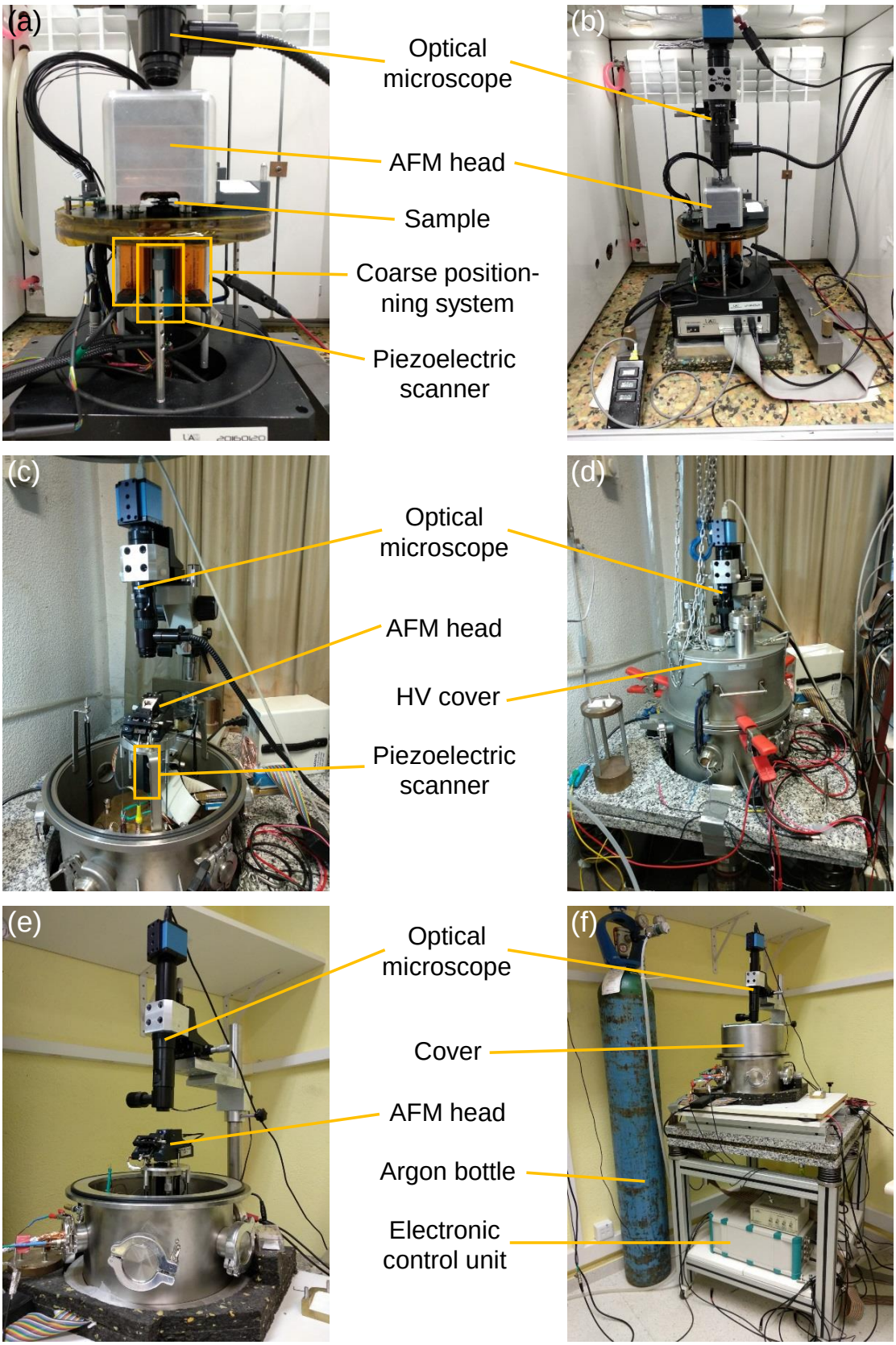

Figure 2.4: Mechanics of each AFM used in this thesis. Some of their main parts are highlighted. (a) and (b) correspond to the first AFM used, that can operate in air and in controlled atmosphere. (c) and (d) depict the second AFM used, that works in ambient conditions or at a controlled presure ($\sim 10^{-6}$ mbar - 3 bar). (e) and (f) displayed the last AFM employed, it can operate at air or in a controlled atmosphere such as argon environment.

2.1.3 *AFM standard operation modes*

In a AFM there are different **forces** that cause the cantilever deflection. They can divided into: (i) **long range attractive or repulsive forces** (electrostatic and magnetic forces), (ii) **medium range forces** (van der Waals forces, attractive as well) and (iii) the **short range forces** (chemical, Pauli eletronic repulsion, capillary, adhesion, deformation, friction, meniscus, etc. forces). Depending on the tip-sample distance at which the AFM image is acquired, we will have a mix of some of the previous forces. However, one of them usually prevails over the others. Therefore, by keeping constant a magnitude related to that predominant interaction, the AFM image is acquired. But this is just an approximation due to the fact that several interaction actually contribute to the formation of the image [37]. The main AFM operation modes are classified according to the kind of interaction whose magnitude is kept constant. But when acquiring a topographic image, the repulsive and attractive forces (mainly electronic repulsion and van der Waals forces respectively) define the **common measuring modes**:

- *Contact mode (CM)*. This is the first mode developed and the simplest one. The tip is in mechanical contact with the sample while the scanner traces the sample under the tip. The magnitude which is kept constant is the vertical deflection of the cantilever (proportional to the normal force). The forces that cause this deflection are the Pauli repulsion (which is repulsive and the prevailing one) and others such as capillary and adhesion forces (both attractive but much more lower). Although this mode presents some advantages (is not affected by the artifacts of other modes when measuring heights, and it can achieve *lattice* or *pseudo-atomic* resolution) it has a major drawback: the dragging or friction forces caused by the lateral displacement of the tip can substantially modify the sample (specially when the nanoobjects adsorbed on the sample surface are weakly attached).

- *Dynamic modes*. The common feature of these modes is the oscillation of the cantilever close to its resonance frequency. The tip-sample interacion forces cause a shift of its resonance frequency (due to conservative forces) and a reduction of its amplitude (due to non-conservative forces). One or several magnitudes related to the dynamics of the cantilever (e.g. amplitude, frequency, phase or dissipation) are kept constant during the scanning. By using these modes one can choose to measure in the hard intermittent contact regime (governed by the repulsive forces, tapping the surface) or in the soft non-contact regime (attractive regime). This second option is less invasive, since the tip is almost never in contact with the sample. In any of both regimes the tip-sample friction force is negligible, thus, the dynamic modes are much less invasive than the contact mode. Aditionally they allow measuring lower forces than contact mode. There exist several dynamic modes, the most used ones are: the **Amplitude Modulation AFM** (AM-AFM) [57] and the **Frequency Modulation AFM** (FM-AFM) [58]. AM-AFM is used in this thesis to acquire images in ambient conditions. Another dynamic mode, called **Drive Amplitude Modulation AFM** (DAM-AFM) [59] is also used here, specifically to take images at high vacuum. They will be addresed in some detail below. Ricardo García and Rubén Pérez [57], as well as Franz Giessibl [60] published superb reviews of AFM dynamic modes.

- *Jumping mode (JM)*. In this mode the magnitude that is maintained constant is the normal force, as in the contact mode. However, in the Jumping Mode [61] the lateral

displacement of the tip is performed far from the sample. At each point the tip approaches the sample until a fixed value of the normal force is reached, then the tip withdraws, moves to the next point at repeats the same process. Hence, as the lateral displacement is performed out of contact, the friction forces vanish. JM is a clear intermitent contact mode. It allows controlling the forces down to pN. As in liquid environment the adhesion forces are very low, this mode is highly efficient in that environment.

In what follows, only the AFM modes used along this thesis will be described in some detail.

2.1.4 *Amplitude Modulation AFM (AM-AFM)*

Each AFM dynamic mode is characterized by keeping constant a certain (or a few) magnitude(s) of the dynamics of the cantilever within the feedback loop to image the sample. In AM-AFM mode, the amplitude of the cantilever is maintained constant. In a first approximation, the amplitude decreases linearly with the tip-sample distance, thus, keeping the amplitude constant means having a constant tip-sample distance. Therefore, the output of the feedback loop is the change of the Z vertical position the scanner piezo must undergo to mantain the amplitude constant. In other words, the output of the loop is the topography.

In order to acquire the amplitude (and the phase) of the oscillating motion of the cantilever, a Lock-in amplifier is used.

If we consider the cantilever as a point-mass spring, **in the absence of tip-sample interaction but under the influence of damping**, it is derived that (see appendix A.1): (i) damping causes a change in the resonance frequency of the cantilever and (ii) this change modifies the phase shift. Hence, phase imaging in the AM-AFM mode is a way to map the tip-sample inelastic interactions [62], such as adhesion, viscoelasticity, Young's modulus, etc. [63, 64].

If we now **discard the damping but introduce a tip-sample force** (F_{ts}), assuming a parabolic tip-sample interaction potential, we will have that (see appendix A.1): (i) the resonance frequency is modified by the gradient of the interaction force and (ii) this implies a whole shift of the resonance curve and a shift in the phase curve.

For small force gradient, the amplitude change is given by [65]:

$$\Delta A = \frac{2A_0 Q}{3\sqrt{3}k}\frac{dF_{ts}}{dz} \tag{2.1}$$

where z is the vertical position of the tip at each moment, k is the spring constant of the cantilever, A_0 is the amplitude at the resonance frequency of the free cantilever and Q is the quality factor of the cantilever. Therefore the amplitude change is proportional to Q and very sensitive to the variations of the tip-sample distance. This allows the use of the amplitude as the feedback magnitude to image the samples in the AM-AFM mode. In summary: a change in the tip-sample distance yields a variation in the force gradient, this implies a shift of the resonance frequency which changes the amplitude.

It is important to stress that there are **two causes for the decrease in the amplitude**: (i) the change of the amplitude itself due to non-conservative interactions (dissipation by the change of the Q factor with tip-sample distance [66]) and (ii) the change of the resonance

frequency due to conservative interactions (the mentioned variation of the effective force constant caused by the tip-sample force gradient).

Another interesting aspect to mention here is that **real interactions** such as van der Waals, electrostatic or repulsive interactions, are not described by a quadratic potential, and the oscillation amplitude are not small. Hence, the above approximation cannot generally be applied to the understanding of realistic dynamic AFM [67].

AM-AFM mode is the most used imaging mode along this thesis, indeed it was always employed except in high vacuum environment.

2.1.5 *Amplitude Modulation + Phase Lock Loop AFM (AM+PLL-AFM)*

This is a variation of the standard AM-AFM mode, in which there is an extra parallel feedback loop to maintain the cantilever phase constant. This loop is called Phase Lock Loop (PLL) [68]. As explained in appendix A.1, when the cantilever is at its resonance frequency, the phase shift takes the value $\pi/2$, ergo, by keeping the phase shift equal to $\pi/2$, the cantilever will oscillate at its resonance frequency.

In AM-AFM the amplitude drop is originated by a mix of conservative and dissipation interactions. On the contrary, in AM+PLL-AFM the amplitude drop is caused exclusively by dissipaction forces (the cantilever is allways at resonance). Another advantage of the use of PLL is that, as the cantilever is always oscillating at its resonance frequency, it is very sensitive to amplitude changes caused by topography variation. For more details about this mode see appendix A.1.

2.1.6 *Drive Amplitude Modulation AFM (DAM-AFM)*

In the case of DAM-AFM dynamic mode, the magnitude that is kept constant to acquire the topography of the sample is the amplitude of the driving force, which is related to dissipation (for detailed information see appendix A.3).

The use of AM-AFM cannot be extended to high vacuum environments. In such cases, the Q factor is highly increased (~1-2 orders of magnitude with respect to air environment). For those high Q factors, the dynamics of the cantilevers is dominated by transients, which is reflected in large response times against parameter variations. This makes the slope detection method used in AM-AFM not suitable for vacuum applications [57]. This problems is overcome by FM-AFM and by DAM-AFM.

FM-AFM is the most extended mode for vacuum environment, however the transition from noncontact to contact regime causes a instability in the feedback loop [69]. This drawback is overcome, to some extend, by DAM-AFM thanks to the fact that the dissipation generally increases monotonically as the tip approaches the sample [70].

DAM-AFM mode was used in this PhD to measure in high vacuum conditions (part of the chapter 3).

2.1.7 *Conductive AFM (C-AFM)*

As it was emphasized before, not only does the AFM acquire topographic images of the surface of the sample, but it is also able to measure a variety of properties of it or of the nanoobjects adsorbed on it. A special case, which will be treated in this thesis, is

the measurement of electrical properties. There are basically **two ways** to probe such properties of a nanoobject with an AFM: (i) using a metal-coated tip as an active and movable electrode or (ii) use it as a probe to detect the electrostatic force between the tip and the sample when there is a voltage difference between them. The first method is called **Conductive AFM (C-AFM)** whereas the second one is known as **Electrostatic Force Microscopy (EFM)**.

The simplest way to carry out electrical transport measurements on a material is to place it between two electrodes, apply a voltage ramp between them while the current flowing through them is registered simultaneously. This basic experiment yields a **Current *versus* Voltage curve** (IV characteristic, IV curve or simply IV). Although the execution of this experiment seems quite easy, it becomes highly difficult when the material under study is a nanoobject. This is due to its small dimensions and the difficult realization of good electrical contacts between the nanoobject and the required electrodes. The above introduced C-AFM uses a conductive tip that acts as a mobile electrode to locally measure the current when a bias voltage is applied between the tip and the sample (V_{ts}) while the tip is in contact with the sample. The other required electrode is already present in the sample and can be made by several ways (thermal evaporation using stencil masks, EBL, sputtering, etc.).

Possible C-AFM setups are shown in figure 2.5. Panel 2.5(a) shows the **vertical geometry**, in which a conductive substrate is required. Assuming a 1D or a long 2D nanoobject, this configuration allows measuring the transversal (or out-of-plane) current of the it. Panel 2.5(b), on the contrary, shows a configuration able to measure the longitudinal (or in-plane) current of the nanoobject. This is the **horizontal geometry** in which the nanoobject must be partially covered by (or placed on) the other electrode and adsorbed on an insulating substrate. Whithin the C-AFM technique, the tip features a nanoscale positional control, nano-Newton force control and pico-Ampere current sensitivity [71].

There are several variations of C-AFM: (i) measure in **contact mode** while V_{ts} is applied [72, 73], (ii) measure in **jumping mode** at the same time that V_{ts} is fixed between the tip and the sample [74] and (iii) under contact or jumping mode, **acquire a IV curve at each pixel of the image**. These methods are based on contact or jumping mode, so, they cannot be used for all kind of nanoobjetcts. Furthermore, the conductive tip, as it is in contact with the sample, becomes contaminated and/or peeled off, giving an increased tip-sample resistance.

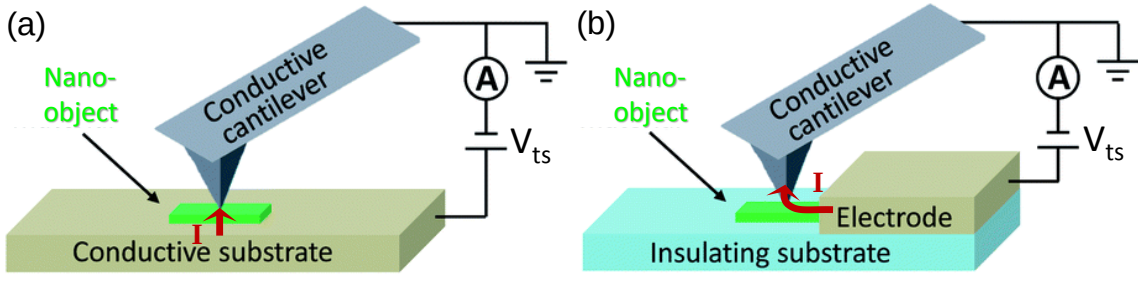

Figure 2.5: Conductive AFM configurations. Red arrow depicts the path followed by the current in each scheme. (a) Vertical geometry, used to acquire the transversal current through the nanoobject under study. (b) Horizontal geometry, employed to measure the in-plane current. Adapted from [71].

In order to solve mentioned issues, Nanoforces group conceived a new C-AFM methodology: **image the sample in a dynamic mode and perform IVs in selected points**. Firstly, we should measure the topography of the sample by means of a dynamic mode, second zoom in on the area of interest, third select a point where to obtain the current, fourth bring the tip into stable contact with the sample at that point and then perform an IV curve. In addition to get rid of lateral forces of CM and JM (at the edges of a nanoobject) this technique allows the measurement of IVs at preselected points of a nanoobject yielding an electrical characterization as function of its length. In figure 2.6(a) the setup of this type of characterization is depicted (extracted from [75]). In particular, an IV curve is performed at three points of a 1D nanoobject (at distances L_1, L_2 and L_3 from the gold electrode). From each IV, the resistance of the nanoobject is obtained (R_1, R_2 and R_3) for each distance. This enables us to plot of the resistance *vs.* the length of the nanoobject (R(L)). Figure 2.6 shows the procedure to obtain a R(L) of a SWCNT (adapted from [75] and [76]).

The first advanced AFM measurements I carried out in Nanoforces group were the electrical characterization of carbon nanotubes and graphene nanoribbons using this last type of C-AFM, some years before the beginning of this PhD [75, 76]. In the framework of this thesis, I used C-AFM in chapter 5 to accomplish R(L) plot of a few-layer graphene flake.

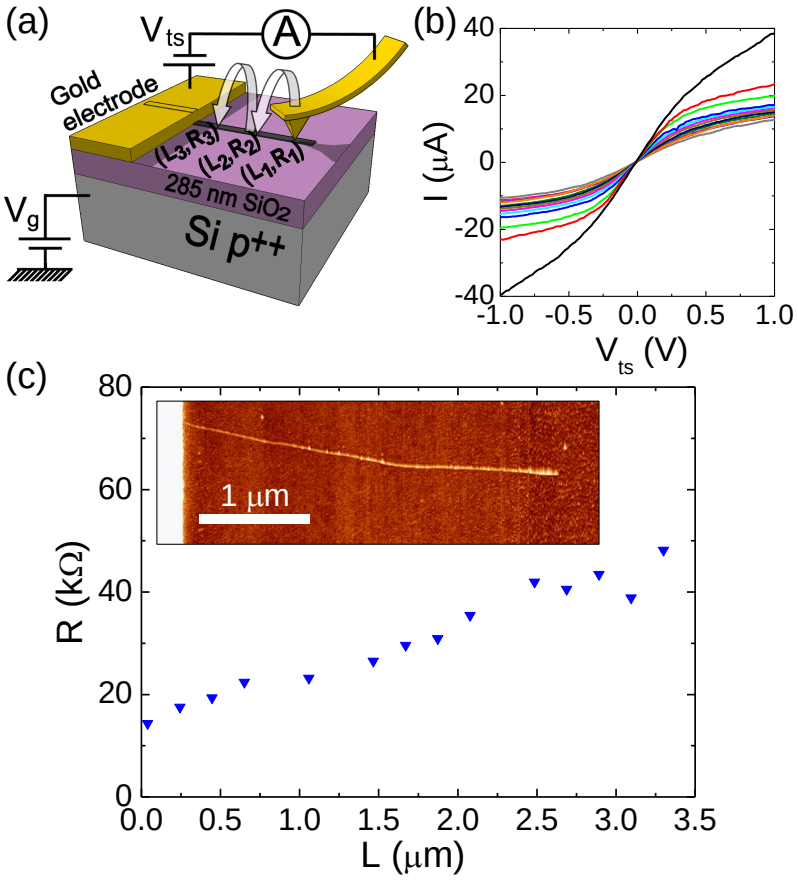

Figure 2.6: Conductive AFM to perform a R(L) on a 1D nanoobject. (a) C-AFM setup used to acquire a R(L) on a SWCNT. (b) IV curves acquired at different points of the nanotube. (c) R(L) obtained from the inverses of the slopes (at 0 V) of IVs in (b), the nanotube measured is shown in the top AFM topography of (c). Adapted from [75] and [76].

2.1.8 *Kelvin Probe Microscopy (KPM)*

The electrostatic interaction has a long range and it is usually stronger than other long range interactions (e.g. van der Waals or magnetic interactions). It is produced by the presence of an electrostatic potential between the tip and the sample (which can be caused by charges, dipoles, polarization induced in the substrate, a voltage applied to a metal, etc.).

As it was introduced in section 2.1.7, EFM probes the electrostatic force between the tip and the sample when there is a electrostatic potential between them (U) [77]. U induces an electric field that gives rise to the interaction energy (W) and the subsequent electrostatic force (F). If we assume the absence of nett charges, we have:

$$W = \frac{1}{2} C U^2 \implies F(z) = -\frac{\partial W(z)}{\partial z} = -\frac{1}{2}\frac{\partial C(z)}{\partial z} U^2 \tag{2.2}$$

where C is the capacitance of the system that depends on the tip-sample distance, on the geometry and on the dielectric properties of the tip-sample system. This wide depency of the capacitance hinders the interpretation of the EFM data. Moreover, due to the long range character of this interaction, not only the tip apex, but also the tip cone and the cantilever, contribute to the electrostatic force acquired by EFM. These problems were addressed by plenty of researchers [42, 78–82]. By measuring the force gradient ($\partial F(z)/\partial z$ in this case) instead of the force, the cantilever and the tip cone contributions are removed [42, 67].

Although the electrostatic interaction is usually stronger than others, it is not always easy to extract it from the rest of the forces exerted on the probe. There are two main approaches to isolate the electrostatic force:

- Perform the scanning of the sample with the tip placed at a higher distance from the sample while a constant voltage is applied between them. If the tip is withdrawn more than 10 nm and there are no magnetic forces, the electrostatic force will dominate over the rest. This approach is mainly carried out through the **lift mode** or **retrace mode**, in which the tip performs a second scan of a line repeating the topographic profile but at a higher distance from the sample, with a voltage applied to it and with the feedback loop open [83]. This results in a pair of images: the topography and the map of the electrostatic interactions. The latter one could be the phase or the frequency shift of the oscillation of the tip in the second scan.

- Apply an alternate voltage between the tip and the sample whose frequency is different from the one used to acquire the topography (a dynamic mode is usually employed in EFM). By means of Lock-in techniques, the electrostatic contribution can be isolated. An obvious advantage over the previous method is the higher acquisition speed of this approach, since in this case a second scan is not required.

Kelvin Probe Microsocopy is a technique that belongs to the second approach [43, 80, 84]. KPM measures the Contact Potential Difference (CPD, V_{CPD}) between the sample and the tip. The CPD is due to the difference of the work functions of the tip and the

sample (Φ_{tip} and Φ_{sample} respectively) when they are electrically connected. CPD is defined as [85]:

$$V_{CPD} = -\frac{\Phi_{tip} - \Phi_{sample}}{e} \tag{2.3}$$

where e is the electron charge. If it is assumed that the work function of the tip does not change during the measurement, then the differences in the measured values of V_{CPD} can be directly related to the work function of the sample. Indeed, if the work function of the tip is calibrated, the absolute value of the work function of the sample can be obtained.

The electrostatic potential (U) that appears in the expression of the electrostatic force (equation 2.2), includes the voltage difference applied externally between the tip and the sample, and the V_{CPD}. In the case of KPM the voltage applied to the sample has a direct and a alternate component with angular frequency (ω): $V_{ext} = V_{DC} + V_{AC}\sin(\omega t)$ therefore, the electrostatic force takes the form:

$$F(z) = -\frac{1}{2}\frac{\partial C(z)}{\partial z}(V_{DC} + V_{AC}\sin(\omega t) - V_{CPD})^2 \tag{2.4}$$

The resulting electrostatic force has a DC, a ω and a 2ω components:

$$F(z) = F_{DC} + F_{\omega}\sin(\omega t) + F_{2\omega}\sin(2\omega t) \tag{2.5}$$

where:

$$F_{DC} = -\frac{1}{2}\frac{\partial C(z)}{\partial z}\left[(V_{DC} - V_{CPD})^2 + \frac{1}{2}V_{AC}^2\right] \tag{2.6}$$

$$F_{\omega} = -\frac{1}{2}\frac{\partial C(z)}{\partial z}(V_{DC} - V_{CPD})V_{AC} \tag{2.7}$$

$$F_{2\omega} = \frac{1}{4}\frac{\partial C(z)}{\partial z}V_{AC}^2 \tag{2.8}$$

According to expressions 2.6 and 2.7, when the DC component of the external voltage applied between the tip and the sample V_{DC} is equal to the contact potential difference V_{CPD}, F_{ω} is cancelled and F_{DC} is minimized. KPM is, therefore, based on an extra feedback loop that applies the proper V_{DC} to nullify the F_{ω} term. The output of this feedback provides the CPD map and the sample work funtion image if Φ_{tip} is known.

There are two major KPM approaches: the **Amplitude Modulation** scheme (AM-KPM) and the **Frequency Modulation** one **(FM-KPM)** [86]. The first one is the one described before, where the amplitude of the ω component is detected and cancelled (or minimized). The FM-KPM detects the frequency shift of the ω component of the motion of the cantilever, which is propotional to the ω component of the electrostatic force gradient.

$$\omega_{eff} \approx \omega - \Delta\omega = \omega\left(1 - \frac{1}{2k}\frac{dF}{dz}\right) \tag{2.9}$$

where F is the "perturbating" force that, in this case, corresponds to F_ω given by expression 2.7.

In addition, the **selection of** ω in both modes is different: in AM-KPM the first resonance frequency of the cantilever is used to mechanically excite it, to follow the topography, and the second resonance frequency is used for the electric bias voltage. This enhaces the sensivity due to Q factor amplification at that resonance. In FM-KPM the bias voltage oscillates at low frequency (1-10 kHz, very far from the mechanical cantilever resonance) to minimize cross-talk with topography.

FM-KPM has an outstanding advantage, which was already mentioned: thanks to the use of the force gradient (instead of the force itself), the contribution to the electrostatic signal coming from the cantilever and from the tip cone are minimized for a certain range of tip-sample distances. Therefore the tip apex contribution is dominant enhacing the resolution of the KPM data [42, 67].

Along this PhD, KPM was used in chapter 4 to acquire the contact potential difference, or surface potential, of metal-organic ultrathin films. The FM-KPM approach was employed with $\omega \approx 10$ kHz while imaging the sample with the AM+PLL dynamic method.

2.1.9 *Force vs. Distance curves*

A very common measurement in AFM is the acquisition of the so-called Force *vs.* Distance curves (**FZ**) [87]. The acquisition of such curves consists of registering the normal force (through the vertical deflection of the cantilever) as the piezoscanner monotonously moves the sample up and down in the Z direction (perpendicular to surface). From the data of these curves a lot of information can be extrated: adhesion, stiffness, elasticity, hydrophobicity and mechanical properties of nanoobjects, just to name a few [87, 88].

Fig 2.7 displays a **FZ curve acquired during a complete load/unload cycle** on a highly-ordered pyrolytic graphite (HOPG) substrate in ambient conditions. It comprises an **approach** (green) and a **retract** (red) **cycles**. At the beggining the tip is at point A, some nanometers far from the sample, thus the cantilever does not experienced any deflection. The sample starts approaching the sample maintaining the zero deflecion. This is the case of the B flat part of the green plot. As the sample gets closer to the tip, the cantilever is not longer stiff enough to mantain its zero deflection: the attractive force between the sample and the tip has a gradient higher than the elastic constant of the cantilever, the systems becomes unstable and the tip "jumps into contact" getting in touch with the sample. That is the vertical C section (**snap in**) of the green plot. After that, the piezo scanner keeps pushing the sample against the tip moving both together. If the sample is hard enough not to be deformed with the applied force, the cantilever deflection (in Z, in nanometers) should be the same as the piezo's displacement. That stage corresponds to the D linear part of the green graph. At point E the approach cycle has finished and the piezo scanners starts moving down (retract cycle). Again, as the scanner moves backward, tip and the sample move together until point F. In this retract cycle, the tip does not detach from the sample at the same Z nor force as in the approach cycle: there is an extra force needed to separate them. That force is the adhesion between the tip and the sample. The adhesion force in air (enviroment at which the curve was acquired) is high due to the always present layer of water on the sample, that creates a water meniscus between the tip and the sample. Indeed, the same curve acquired with the same kind of cantilever performed in liquid enviroment would have almost no hysteresis. At point F, the tip gains

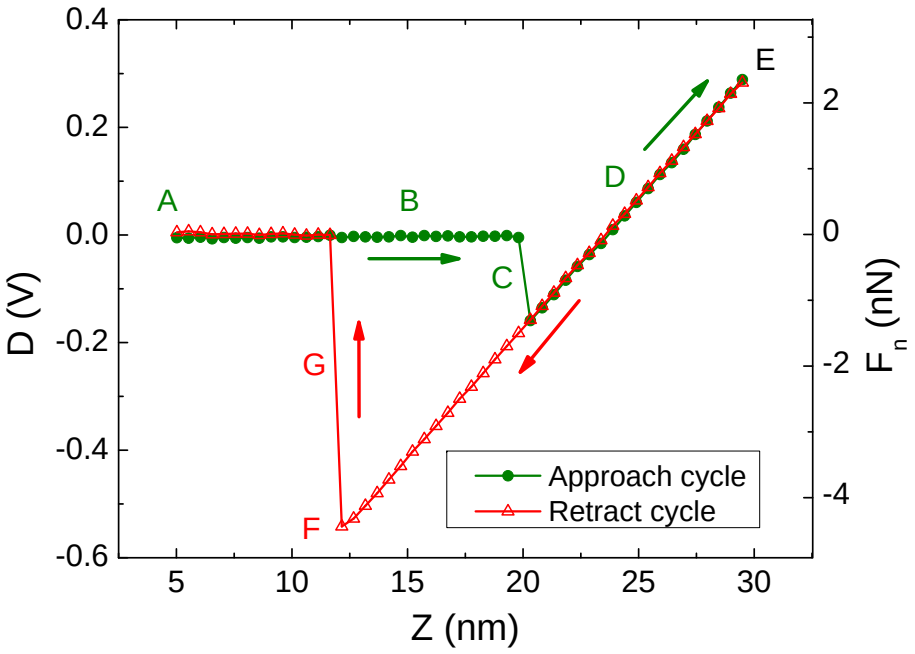

Figure 2.7: Deflection and force *vs.* distance curves. DZ and FZ curves acquired at air on a HOPG substrate. The most important points and parts of the curve are marked. See main text for details.

enough elastic energy to detach from the sample and comes back to the initial deflection point. This abrupt change in the deflection of the cantilevers corresponds to the G vertical part (**snap off**) of the red plot.

Assuming a substrate hard enough not to be deformed, the applied force (F_n, normal force) can only deflect the cantilever and therefore the deflection (D) detected by the photodiode sensor (in volts) accounts exclusively for that deflection. As the cantilever follows the Hooke's law, we will have, that $F_n = k_c \Delta Z$, where k_c is the spring constant of the cantilever and ΔZ is the change of the Z position of the cantilever. This linear relationship between the normal force and the Z displacement of the piezo in hard surfaces allows us to obtain the sensitivity (S) of the photodiode sensor in nm/V (the output of the photodiode is the deflection D, in volts). The sensitivity, thus, is merely the inverse of the linear part of a FZ curve (strictly speaking of a deflection curve "DZ" yet) performed on a very hard surface (see figure 2.7). Hence, S, together with the cantilever spring constant, provides the conversion from the volts of D given by the photodiode to nanoNewtons of the F_n:

$$F_n(nN) = k_c \left(\frac{nN}{nm}\right) S \left(\frac{nm}{V}\right) D(V) \tag{2.10}$$

The shape of an FZ depends on the environment at which it was performed, as we have seen, but also on: the Z excursion, the value of the spring constant of the cantilever used and the elastic constant of the nanoobject or substrate where it was acquired. Besides, FZ curves are affected by the piezo's non-linearities.

2.1.10 *Indentation Curves*

When the sample under study is deformed by the applied forces, the comparation of the FZ curves acquired on it and the ones acquired on a hard substrate gives information about the deformation and the mechanical properties of the sample. This method has been followed to mechanically characterized biological materials [89], nanosized protein cages (such as viruses) [90, 91] and 2D materials [44, 92], just to name a few.

Let's assume we have a nanosheet on a cylindrical hole, and we pushed the resultant drumhead at its center: it will become deformed. This is prortrayed in figure 2.8(a) that shows the cross-sectional view of the system. In that case, as in any in which a nanoobject is deformed, part of the total displacement of the piezo (Z) is used to deflect the cantilever (deflection, d) and another part to deform the nanoobject (deformation called indentation, δ) (see figure 2.8(a) and (b)). Therefore:

$$Z = d + \delta \tag{2.11}$$

The curves from which the mechanical properties, such as the elastic constant or the Young's modulus, can be extracted are the indentations curves. They plot the normal force *vs.* the deformation of the nanoobject: $F(\delta)$ or $F\delta$. Once we have performed a FZ on the nanoobject (figure 2.8(a) and (d) green line where the nanoobject is the drumhead) and another one on the hard substrate (figure 2.8(c) and (d) blue line) for the same force range, we have two sets of data for Z. As the deformation of the hard substrate is zero ($\delta = 0$), we have:

$$\left.\begin{array}{l} Z_{nanoobject} = d + \delta \\ Z_{hard-subs} = d \end{array}\right\} \Longrightarrow Z_{nanoobject}\rfloor_{F_0} - Z_{hard-subs}\rfloor_{F_0} = \delta\rfloor_{F_0} \tag{2.12}$$

where $Z_{hard-subs}$ is the piezo displacement of the FZ on the hard substrate and $Z_{nanoobject}$ the same magnitude on the nanoobject. Hence, according to equation 2.12, δ is obtained by subtracting, for each value of the force, the Z (piezo displacement) of the FZ on the hard surface from the Z of the FZ on the nanoobject (see figure 2.8(d)). Then, the indentation curve is simply the force of the FZ on the nanoobject *vs.* δ computed that way (figure 2.8(e)).

In chapter 3 I will present indentation curves performed on few-layer black phosphorus nano-drums to extract mechanical properties of that 2D material.

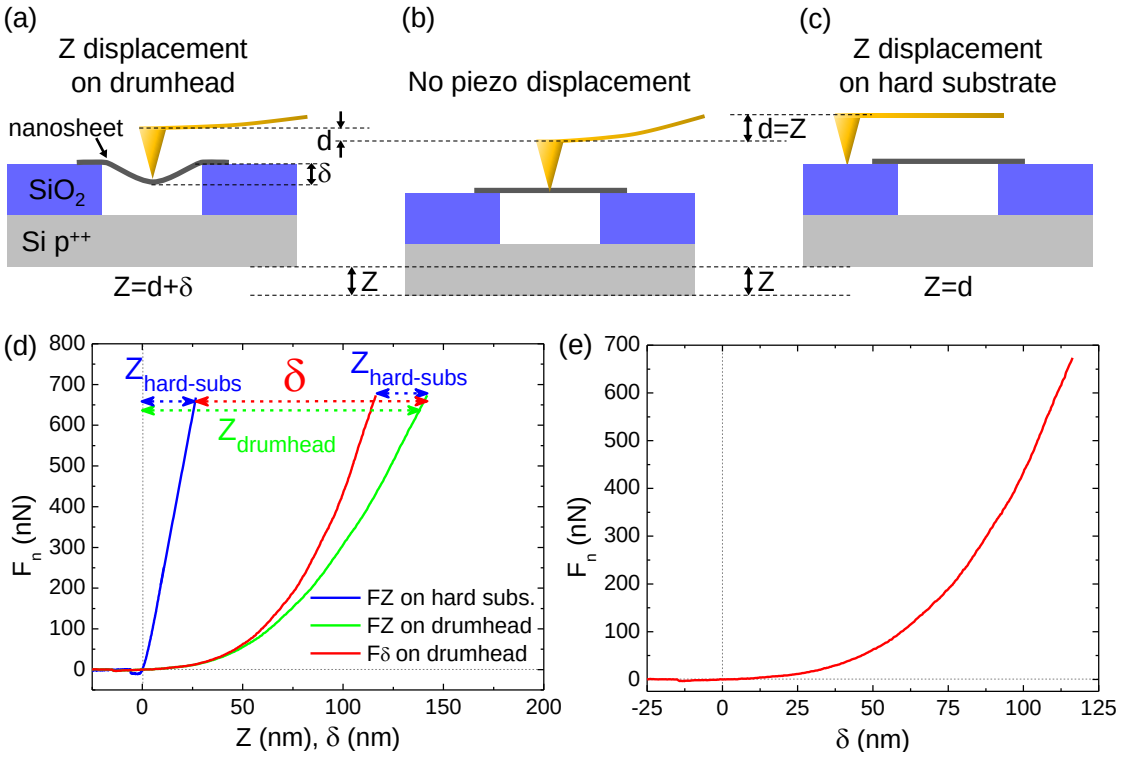

Figure 2.8: Nanoindentation experiment chart and obtaining of an indentation curve. (a) Cross-sectional view of a drumhead pushed by the AFM tip through a Z vertical piezo displacement. (b) Same view as (a) but without piezo displacement. (c) Same view as (a) but the tip is on the hard substrate of the sample. (a), (b) and (c) includes relevant distances and their relationships. (d) FZ on the hard substrate (blue line), FZ on the drumhead (green line) and Fδ (indetation curve) on the drumhead (red line). Vertical displacement of piezo when pushing the drumhead, when pushing the hard substrate and the deformation of the nanosheet (δ) are highlighted with dashed arrows. (e) Indentation curve on the drumhead extracted from (d). Red lines in (d) and (e) plot the same data.

2.1.11 *Generalized Curves vs. Distance*

The ability to register a magnitude while the piezo scanner is moving up and/or down is much more general than what we have seen so far, where solely the normal force is acquired. WSxM allows recording different signals while the vertical position of the sample is changed. Some of the most relevant are:

- When working **in dynamic mode**: the **amplitude** (A) and the **phase** (ϕ) of the oscillating motion of the tip, together with the FZ (see figure 2.9(a)). In these plots three regimes are visible: (ii) noninteractive regime (region with $Z \lesssim 0$ nm where the amplitude and the phase are constant), (ii) control regime (for 0 nm $\lesssim Z \lesssim 22$ nm where the amplitude approximately has a linear dependence with Z allowing AM-AFM mode) and (iii) contact regime (for $Z \gtrsim 22$ nm where the amplitude and phase are constant again).

- When measuring **with a C-AFM setup**: the **current** (I) that flows through the tip coming from the sample, along with the FZ (see figure 2.9(b)). The green lines plot

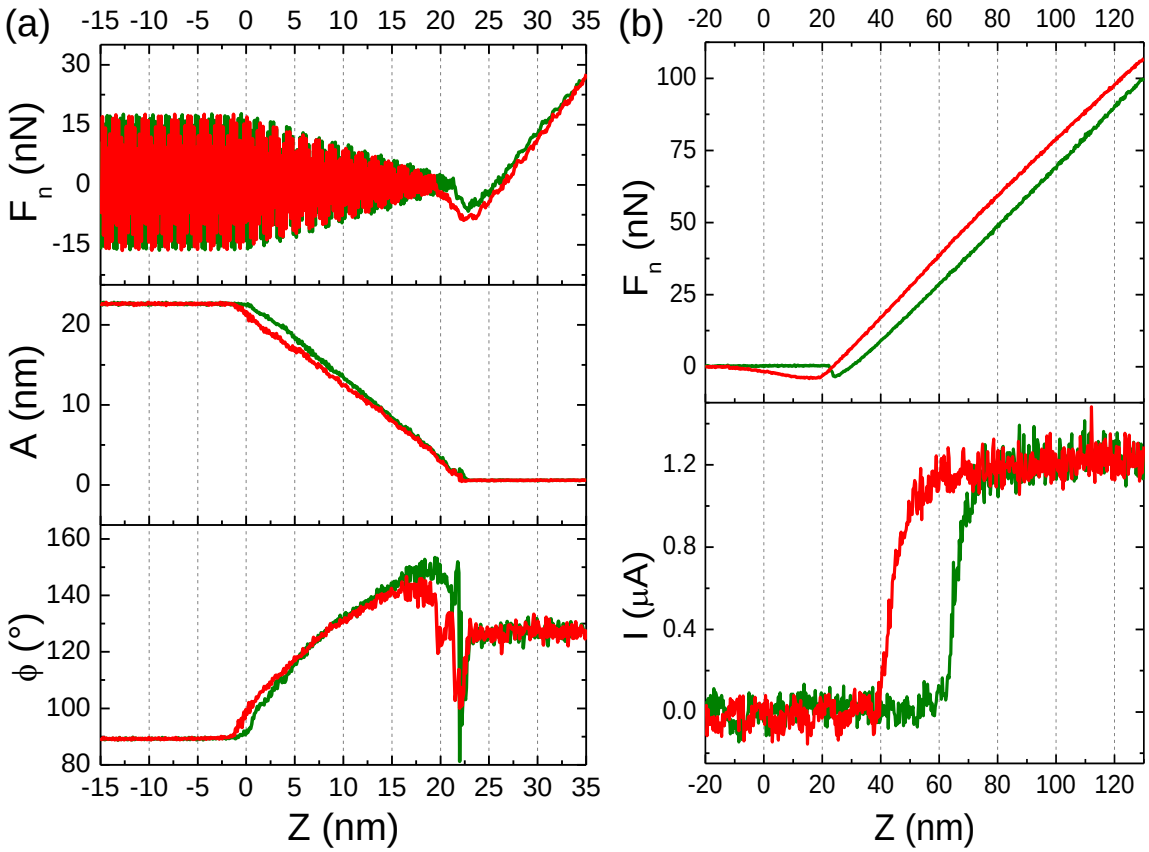

Figure 2.9: Multiple signals *vs.* distance curves. Green lines correspond to the approach cycle and red ones to the retract cycle. (a) Normal force, amplitude and phase *vs.* piezo displacement plots from AM-AFM mode working conditions. The curves were performed with a 3 N/m (nominal) silicon cantilever on a SiO_2 substrate. (b) Normal force and current *vs.* Z graphs working with the horizontal C-AFM set up. The plots were acquired on a gold microelectrode with a 56 N/m (nominal) doped diamond tip and a bias voltage between the tip and the sample of few mV. There was a protective resistor of few kΩ connected in series.

the signals when the tip approaches the sample and the red ones the same signals when it withdraws. As the tip approaches the sample, unless a force higher than 50 nN is applied ($Z > 80$ nm), there will be no current. This is due to contamination and the need for a good mechanical contact for the current to flow. For higher forces the current remains the same. In the retract cycle the current is kept constant until a force of about 25 nm ($Z \approx 60$ nm) is reached. At lower forces it vanishes. The hysteresis in the current *vs.* Z plot is due to adhesion between the tip material and the sample. There is a considerable hysteresis in the linear part of the FZ which can be explained in terms of change of the tip apex during the flow of current at the maximum Z.

The amplitude and phase signals *vs.* Z are acquired with certain frequency to check the dynamic mode work point along the AM-AFM measurements of this thesis. On the other hand, the current *vs.* Z plots (also known as IZ curves) are performed in chapter 5, in the way explained above and in a modified version, to check the electrical resistance of the tip and of different electrical contacts performed along the measurements.

2.1.12 *Scanning Probe Lithography and Nanomanipulation*

So far we have seen different ways to image a sample and how to perform single point measurements with AFM. But fortunately SPM allows more than that. One of the main advantages of it over other types of microscopies is the possibility to "write" patterns or manipulate features at the nanoscale. The former is known as **Lithography** while the latter is called **Nanomanipulation**. Both are usually considered together because both of them manipulate matter at the nanoscale obtaining a similar result: a nano-pattern on the sample surface. Furthermore, both use the same kind of software tools.

To better understand the Scanning Probe Lithography and Nanomanipulation, one can picture them as drawing on the sample surface with the tip. The sample would be the paper and tip would act as a pen. The different actions performed and the material manipulated would correspond to the drawing actions and the ink, respectively.

In the context of **Scanning Probe Lithography (SPL)**, there are three main methodologies to pattern materials with nanoscale resolution. Each of them is based on a different kind of action executed on the sample surface: (i) modification, (ii) deposition or (iii) removal of matter [93]. Nanomanipulation of matter can be also considered here as a fourth type of SPL, however I consider it apart in the next paragraphs. Another possible classification of the SPLs depends on the physical or chemical nature of the process followed or on the dominant tip-sample interaction used to carry out the nanopatterning (electrical, thermal, mechanical or diffusive process). A possible taxonomy of SPLs

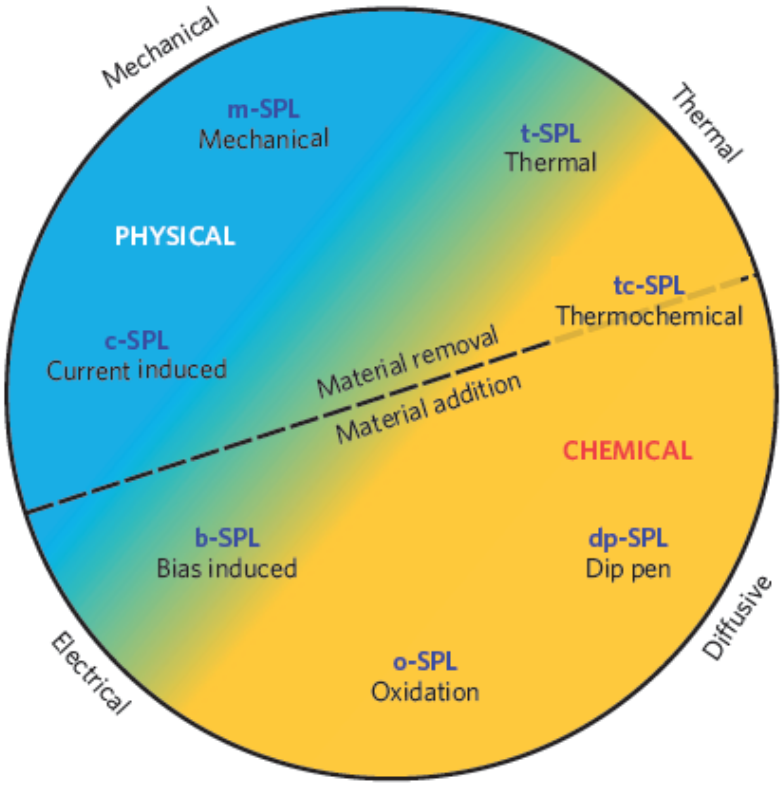

Figure 2.10: Scanning Probe Lithographies taxonomy. Chart showing the classification of SPLs according to the removal or addition of material and to the tip-surface interaction employed for patterning. Source: [40].

is depicted in figure 2.10 extracted from [40]. The majority of SPLs rely on the use of an AFM. The most important lithography techniques developed so far are the local oxidation [94–96], nanoindentation and nanoscratching [97] and dip-pen lithography [98]. Other methodologies correspond to thermal and thermochemical lithographies [99, 100], magnetic field tip-induced nanolithography [101], local resistive switching [102] or nanografting [103].

Nanomanipulation goes back to the early eighties with the first STM manipulations, which include: atomic and molecular manipulation [104–106] and the positioning of single atoms [107]. After these works, SPM nanomanipulation considerably spread among researchers. They started to use also the AFM to manipulate matter: nanoparticles [39, 108], nanoclusters [109], carbon nanotubes [110, 111], nanorods [112] and eventually even atoms in ultra high vacuum (UHV) conditions [113–115]. More recently metallic nanowires have been manipulated by means of AFM [116] and even applying highly automated methods [117]. These manipulations are based on different procedures. In STM the manipulations are achieved through the modification of the interactions in the tunnel junction of the microscope by changing the tip voltage or the tunnel current. The AFM manipulations are performed by different methods. The most relevant procedures are: (i) soft controlled nanoindentations to grab or deposit an atom with the AFM tip [113], (ii) lateral atom interchanges (between atoms of the sample surface by scanning the line that connect them while reducing the tip-sample distance [114]), (iii) vertical atom interchanges (between atoms of the sample surface and atoms of the tip approaching the sample to the tip until an instability causes the interchange [115]) and (iv) lateral displacements of the tip in contact with the surface pushing or sweeping a nanowire [116].

This wide spectrum of nanomanipulation and lithography techniques offers the possibility to design on-demand experiments and create almost *à la carte* nanostructures enabling the development of nanodevices and driving us closer to nanoengineering.

In this thesis, AFM nanomanipulation is used in chapter 5 to accurately move and connect gold nanowires. The target of that manipulation is to create gold nanowires paths that act as nanolectrodes. They electrically contact nanoobjects thus allowing the fabrication of nanocirtuits. This manipulation will be explained in more detail in chapter 5. Figure 2.11 depicts the manipulation of a gold nanowire from its initial position (encircled by a dashed yellow line in the first image) until it is connected to another gold nanowire (encircled by a dashed cyan line in the first image). The spontaneous welding of two gold

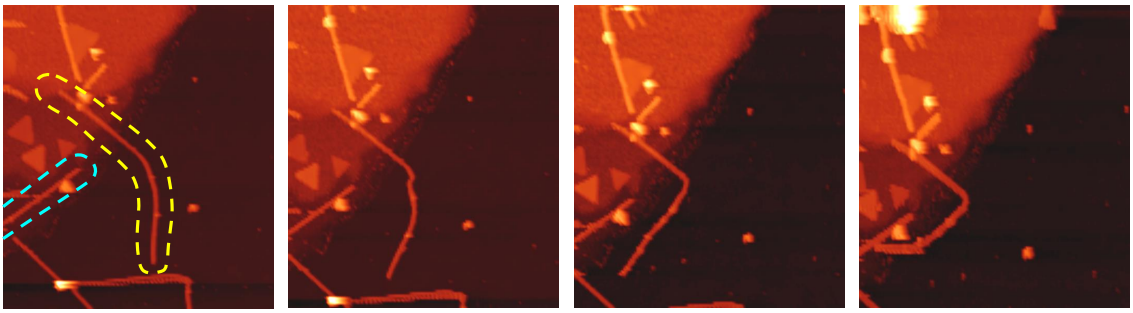

Figure 2.11: Manipulation of a gold nanowire. Sequence of a few AFM topographic images showing the evolution of the position of a nanowire from its initial position (encircled by a dashed yellow line in the first image) until its connection with another nanowire (encircled by a dashed cyan line in the first image). AFM images' size: $10 \times 10\ \mu m^2$.

nanowires by simple approach at ambient conditions is due to the so-called cold welding of metal nanowires and it is related to the high surface energy of these nanowires [118].

2.2 PROBE STATION

2.2.1 *Introduction*

Probe stations are systems used for **testing circuits and devices** on silicon wafers, open microchips or other substrates. They are used in research, product development and failure analysis applications [119]. In research, probe stations are used to test and electrically characterize micro- and nano-devices. This is done by acquiring signals from the internal nodes of the devices under test [120]. They are useful in a variety of fields including semiconductors, Micro-Electro-Mechanical Systems (MEMS), superconductivity, electronics, ferroelectrics, material science, physics and optics [121].

A probe station consists of the following **basic parts**: (i) a **sample holder** where the device under test (DUT) is placed, (ii) a certain number of **probes** that will electrically contact some nodes of the device, (iii) **probe holders mounted on a positionning system** to place each probe's tip in the right node of the device, (iv) an **optical microscope** mounted above the sample holder to see the probes and the sample with a suitable magnification, (v) a **damping system** to avoid the influence of external vibrations in the measurements, (vi) the **electronics** to test the device once all the probes electrically contact the sample in their correct location and (vii) the **software** to control the measurements and acquire the data. Figure 2.12 shows a commercial probe station together with some of its main parts.

The **electronic equipment** of a probe station usually comprises a source-measure unit (SMU), which applies a stimulus (a current or a voltage) and measures its corresponding

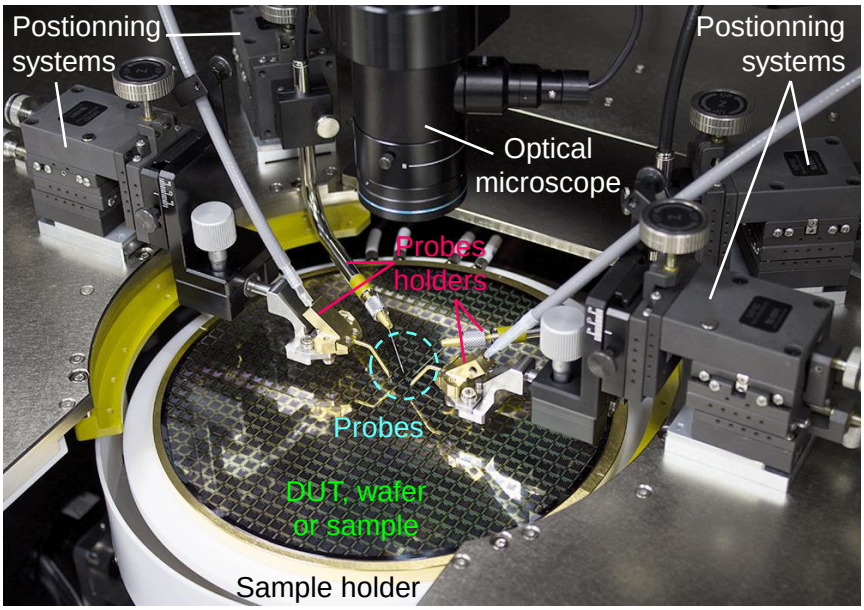

Figure 2.12: Example of probe station with its main parts. The damping system, the electronics, software and cooling/heating systems are not shown. Source: [122].

(voltage or current) response. One can choose the measurement mode (source current/measure voltage or vice versa).

Additionally, **probe stations can include** cooling and/or heating systems, an ambient-controlled chamber, a vacuum system, electric/magnetic fields, light sources, etc. [121]. Moreover, with the proper electronic design, probe stations can operate at high frequency (~70 GHz) allowing radio frequency applications [123, 124].

To carry out electrical testing or characterization with a probe station we must follow some steps. First we should place the sample on the holder with a suitable tape or glue. When a backgate voltage is applied to the sample holder, the sample must be glued with conductive glue on its back to the holder. Second, each probe should be place at the right point of the sample until a good electrical contact is reached. Then, by means of the software that controls the electronics, we perform the desired electrical measurements. Optionally, and provided that the system allows it, we could reach a certain temperature in the sample and/or a pressure of a certain atmosphere.

2.2.2 *Circuit Configurations*

There are different **circuit configurations** to carry out electrical characterizations. They are used in a probe station or in a another setup to measure electronic properties (criostat, AFM, etc.). The main circuit configurations are the two-electrode and the four-electrode setups. In both, a global or local backgate voltage can be applied to the back of the sample providing an external electric field, resulting in three- and five-terminal schemes, respectively. The **two-electrode scheme (or 2-wire sensing)** is suitable to measure DUTs with high electrical resistance (at least one order of magnitude higher than the resistance of the leads plus the sum of all the contact resistances between the probes and the nodes of the device). When these resistances are comparable or higher than the resistance of the DUT, the two-electrode configuration is not longer valid. In that case the **four-electrode setup (4-wire sensing or Kelvin sensing)** is needed because it allows the electrical measurements without contact and leads' resistances [125, 126]. Other methods to measure low resistances are the Kelvin's double bridge, the potentiometer method and the Ducter ohmmeter [127].

Figure 2.13 depicts the **two main circuit configurations** used for electrically characterized devices:

- The **2-wire sensing setup** (figure 2.13(a)) comprises a unique loop with a voltage source and an ammeter. By measuring the current that flows through the loop (I) for a certain voltage (V), the total resistance (R) of the circuit is obtained through the Ohm's law ($V = I \cdot R$). R includes not only the resistance of the DUT ($R_{subject}$) but also the contact resistances (R_{c1} and R_{c2}) and the resistances of the wires (R_{w1} and R_{w2}). Therefore the resistance delivered by this method is: $R = R_{subject} + R_{c1} + R_{c2} + R_{w1} + R_{w2}$, causing this method only suitable for the cases where $R_{subject} >> R_{c1} + R_{c2} + R_{w1} + R_{w2}$.

- The **4-wire sensing configuration** (figure 2.13(b)) includes two loops. The outer one has a pair of current-carrying electrodes, whereas the inner loop has pair of voltage-sensing electrodes. A current source in the outer loop forces a current (I) to flow through the sample causing a voltage drop between the arms of the inner loop. This voltage drop is measured by the voltmeter located in that loop. As the

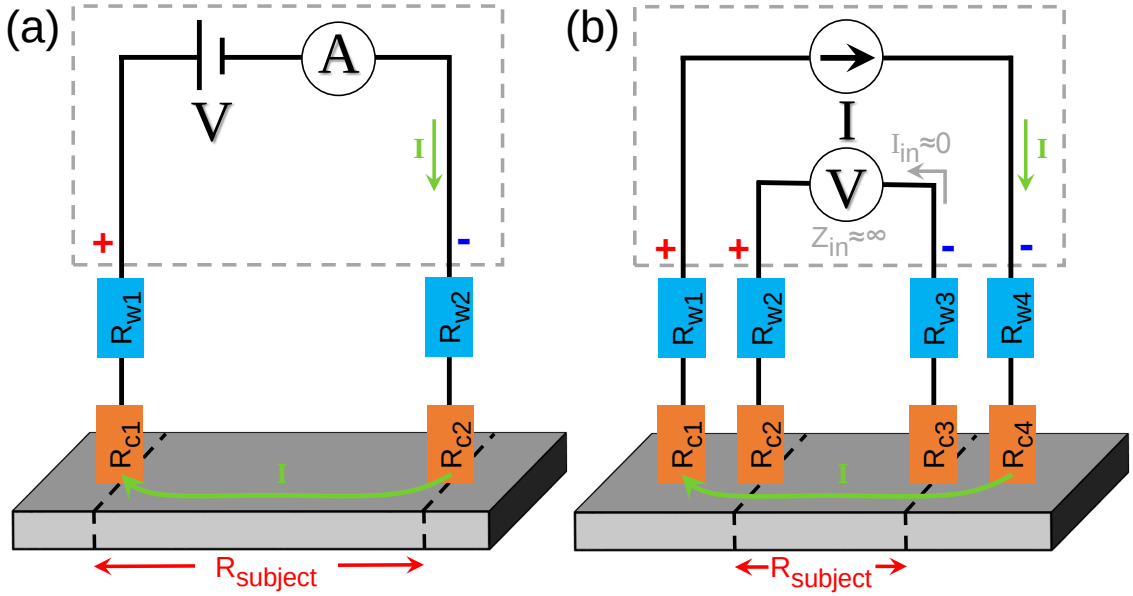

Figure 2.13: 2-wire and 4-wire sensing setups to perform electrical measurements. The sample is depicted with a grey parallelepiped emulating a 2D nanomaterial, the resistance that can be measured of it is the portion marked with the red arrows ($R_{subject}$). The dashed grey squares are the limits of the electronic unit in each configuration. The symbols "+" and "-" indicate the polarity of electronic unit connections to be considered when connecting the wires, extremely important in the 4-wire configuration. The R_{c1}, R_{c2}, R_{c3} and R_{c4} are the contact resistances while the resistances of the wires are R_{w1}, R_{w2}, R_{w3} and R_{w4}. (a) 2-wire sensing configuration. (b) 4-wire sensing scheme, where Z_{in} and I_{in} are the input impedance and the input current of the voltmeter, respectively.

voltmeter has a very high input impedance (Z_{in}), the current in those two inner arms (I_{in}) is negligible. Therefore, the drop voltage in contact resistances R_{c2} and R_{c3} and in the resistances of the leads R_{w2} and R_{w3} are almost zero. Consequently, the voltage registered by the voltmeter (V) is the voltage drop in the sample between the two inner electrodes ($R_{subject}$), without being influenced by the resistances of the wires or the contacts, thus: $R_{subject} = V/I$. In summary, the separation of current and voltage electrodes eliminates the impedance contribution of the wiring and the contact resistances.

2.2.3 *Standard electrical measurements using a probe station*

The 2-wire sensing topology together with a backgate voltage has a **Field Effect Transistor (FET) configuration**, thus, the voltage applied between the 2 wires (or probes) is usually called V_{ds} (drain-source), V_s (source) or simply V, while the backgate voltage is V_g (gate).

Some of the most **common electrical measurements** that are performed on a device using a probe station (or another setup) are detailed in appendix B.

A significant issue when performing those measurements is the **variation of the independent variables**. For example the excitation voltage can have different **waveforms**. Furthermore, they can have abrupt changes or they can change smoothly. Another key parameter, in some experiments, is the waveforms' **speed** or frequency. As I will present

in chapter 4, the speed of the excitation voltage (in V/s) can cause different responses of the samples studied. Further information regarding waveforms, their frequency can be found in appendix B together with the case of having two excitation magnitudes.

Sample temperature is another magnitude usually changed during experiments. Its control is more complicated due to the thermal inertia of the parts to be heated or cooled.

2.2.4 *Probe Stations used along this PhD*

In this thesis **I used three probe stations**. The **first one**, installed by Dr. Cristina Gómez Navarro, had two manual micromanipulators, a sample holder that acts as a backgate voltage, and an optical microscope. It operates only in air ambient conditions. The electronic part includes two SMUs, a high precision multimeter, and a variable-gain low noise current amplifier. It was controled by a Labview-based software. I carried out the first electronic measurements of chapter 4 in this probe station. However, at that time, Dr. Pablo Ares García and Dr. Julio Gómez Herrero were developing a new improved probe station located inside a vacuum chamber. This was the **second one** and the one I used the most along my thesis. Furthermore, I tested its developments during my experiments. I describe it below. For less-demanding experiments, I employed a **third probe station**, described at the end of this chapter. It is similar to the first one but it has superior software and positionning system and new simpler electronics.

2.2.4.1 *Variable temperature ambient-controlled motorized Probe Station*

This probe station was designed and assembled by Dr. Pablo Ares García and Dr. Julio Gómez Herrero in the Nanoforces group in collaboration UAM-SEGAINVEX and the technicians from the department of Condensed Matter Physics. Its mechanical part is fully described in Dr. Ares' thesis [37].

The **main features of the mechanical part** of this probe station are:

- **A chamber that allows different working environments**: high vacuum, air ambient conditions or controlled gas atmosphere. Its base pressure is 10^{-6} hPa.
- **Two motorized probe holders**. Each of them is coupled to a X, Y, Z motorized compact stage to position the probes with nanometer resolution.
- **A cooling/heating system** to change the sample temperature from 80 to 400 K.

The **electric equipment** comprises: (i) two Keithley 2400 source meters (one applies the excitation V_{ds} voltage and measures the generated current between both probes, and the other generates the V_g and measure the leaking current that flows accross the sample and the backgate electrode), (ii) a high precision Keithley 2000 multimeter and (iii) a variable-gain low noise FEMTO DLPCA-200 current amplifier. The use of the two latter is an alternative to the V_{ds} SMU to measure the current between drain and source electrodes (in that case the V_{ds} SMU is used only as a source).

Figure 2.14 depicts the **electrical circuit** formed by the two probes and the gate voltage electrode. 4-wire sensing experiments are also possible using both probes and other pair of electrodes existing in the sample, such as microelectrodes connected to pads of a printed circuit board (PCB) or to macroscopic wires. The Keithley 2400 itself allows these measurements by using two extra connectors.

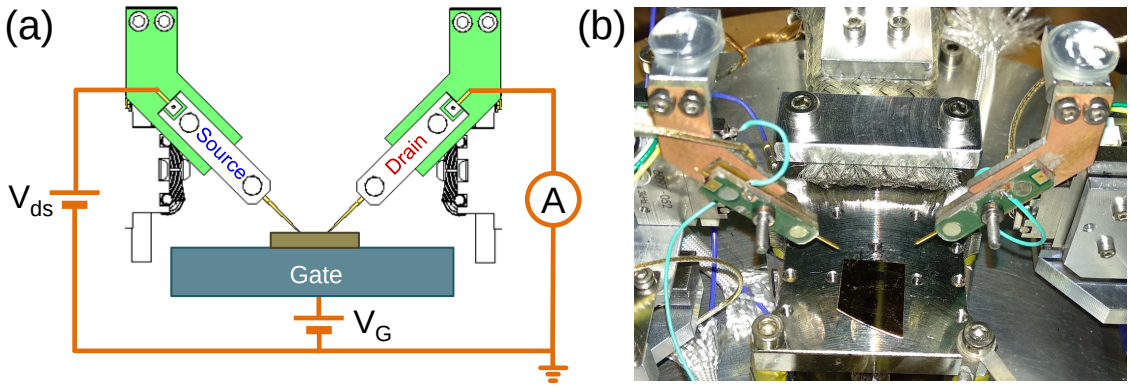

Figure 2.14: Electrical circuit in the variable temperature ambient-controlled motorized probe station. (a) Representation of the circuit. It has a 2-wire sensing configuration (figure 2.13(a)) with a V_g terminal, (FET scheme). The ammeter can be implemented by a current amplifier+voltmeter or with a unique SMU (that also applies V_{ds}). Extracted and adapted from [37]. (b) Picture of the sample holder with a sample and both probes over it.

The main parts of the probe station are summarized in the photograph 2.15(a). Panel (b) of the same figure shows the interface of the Matlab-based **application software**, developed by the technician Ignacio Horcas Calvo and Dr. Julio Gómez Herrero. It controls the motion of the probe holders and the electrical measurements.

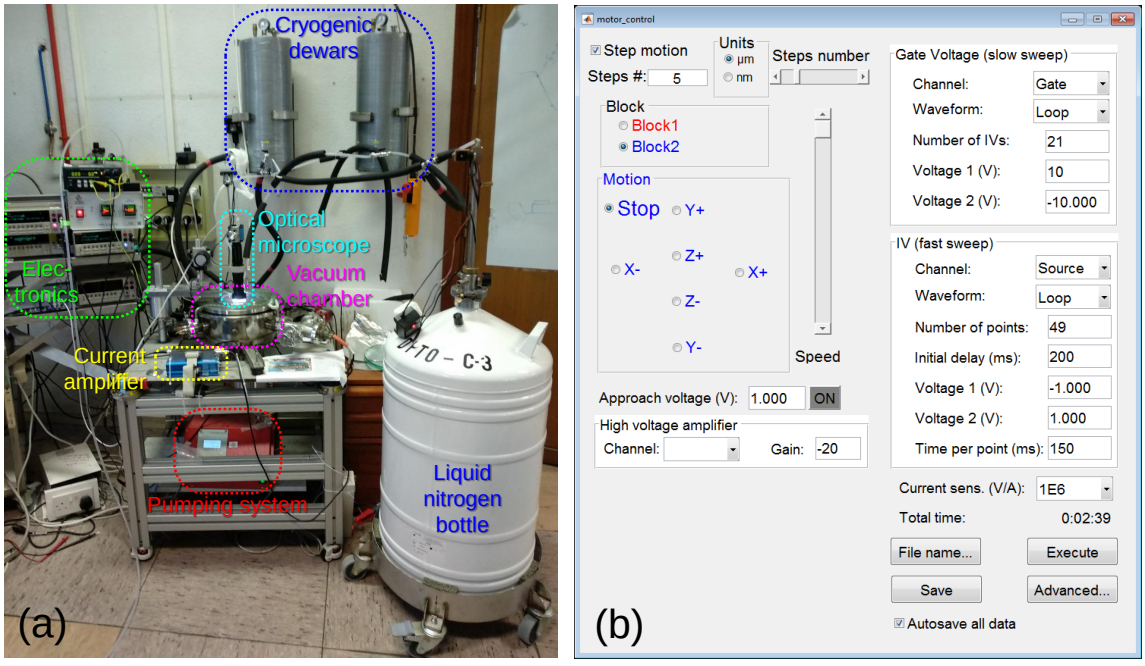

Figure 2.15: Main parts and software of the variable temperature ambient-controlled motorized probe station. (a) Main parts of the probe station. Inspired by [37]. (b) Interface of the application software that controls the movement of the probes and the electrical measurements.

The **probes** I used within this probe station were:

- **Commercial straight tungsten probes** with a length of 1.25" and an apex radius of 7 μm (nominal). We bought them in Cascade Microtech Inc.
- **Home-made gold probes** with a length of ~1" and an apex radius of very few microns.

Figure 2.16 shows optical microscope images of a commercial probe and a home-made probe.

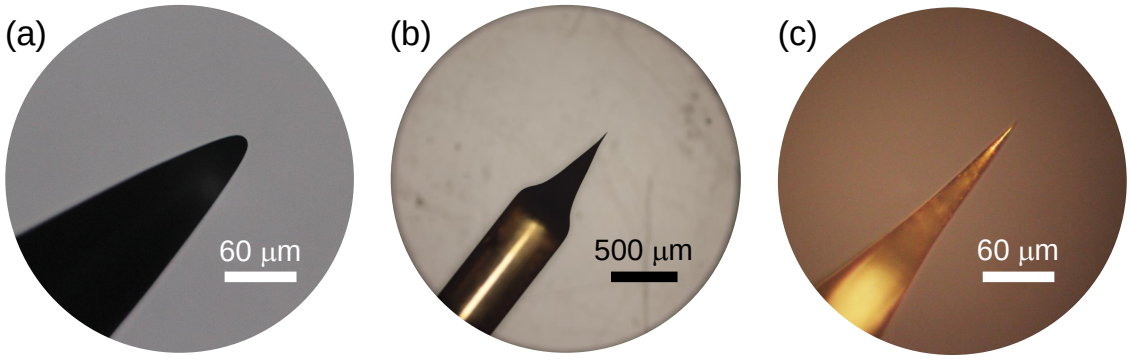

Figure 2.16: Probes used in the variable temperature ambient-controlled motorized probe station. (a) Commercial tungsten probe. (b) Home-made gold probe. (c) Zoom in on the probe's apex of (b).

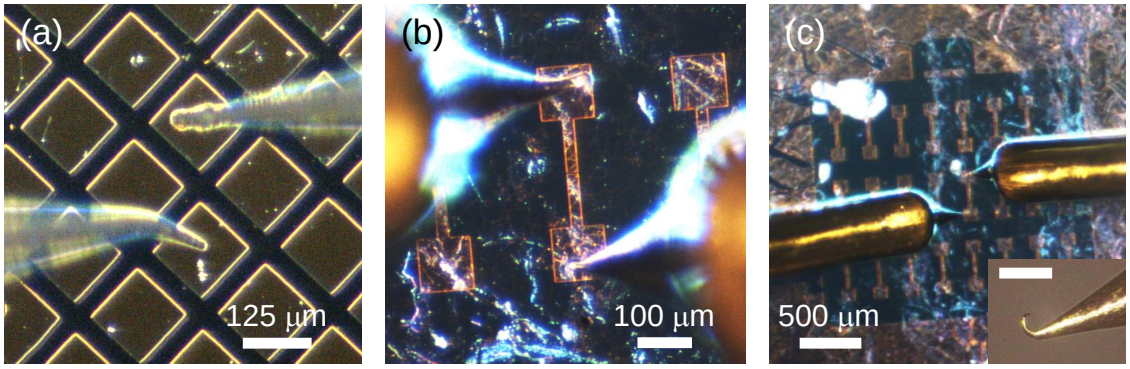

Figure 2.17: Probes contacting microelectrodes inside the variable temperature ambient-controlled motorized probe station. (a) Commercial tungsten probes on 125 μm × 125 μm microelectrodes. (b) Home-made gold probes on T-shape electrodes with a narrow gap between them. (c) Zoom out of (b) showing the thicker part of the probes. The inset in (c) shows the apex of one of these gold probes after its use, the scale bar length is 60 μm. All microelectrodes are made of Cr+Au.

I started using the tungsten probes to contact samples with silver paint or graphite paint electrodes. Then I used them to contact microelectrodes obtained by thermal evaporation of a thin layer of chromium (or titanium) followed by a thicker layer of gold (Cr+Au, Ti+Au). Unfortunately, these probes' tips scrachted that kind of microelectrodes due to the toughness of tungsten and its small apex radius. Therefore we began to fabricate our own probes. They should be made of a softer material that does not get oxidized

nor dirty and provides good electrical contacts. We chose gold, which meets all those requirements. I made these probes by electrochemical sharpening of a ⌀0.5 mm gold wire following the procedure described in [128] (which is similar to other procedures used to fabricate STM or multi-purpose sharp tips [129, 130]). The mechanics and electronics that perform that sharpening was carried out again by technicians of the department. When a gold probe approaches a microelectrode, instead of sratching it, the probe bends a little at the very end. Figure 2.17 shows a pair of commercial tungsten probes and other pair of home-made gold probes. They are inside the probe station making mechanical and electric contact with Cr+Au microelectrodes of two samples. As it can be readily seen, the left tungsten probe in (a) is also bent, but not at the end, probably this was caused by accident when manipulating the probe (and not by the final approach). The inset in (c) is micrograph of a gold probe apex after its use, showing a hook shape produced when it touches the microelectrode.

2.2.4.2 *Air ambient atmosphere manual Probe Station*

For fast electrical checkings and simple measurements a much **simpler probe station** is more suitable. For that reason, Dr. Julio Gómez Herrero, in collaboration with technicians from the department, built another probe station.

This system can only work at ambient atmosphere. It has two probe holders and an extra one not so used. Each of them consists of a stage with three micrometer screws (one per direction) that enable the manual motion of the probes over the sample. The sample holder can be moved manually as well (without micromanipulators). A metal plate can be placed on it to apply a backgate voltage. An extra sample holder allows heating the sample by means of a halogen lamp at its bottom (although not much heating is recommend in ambient atmosphere). Above the sample holder an optical microscope is coupled. The electronics of the probe station consist of a home-made unit with two voltage sources (one for V_{ds} and the other for V_g), a voltmeter and a separate variable gain current amplifier. Thus, 2-wire sensing measurements are possible but not the 4-wire ones. The same application software of the previous section is used (figure 2.15(b)), having the piezomotors movement dialog disabled. Figure 2.18 shows all the elements that form the system.

The easy accesibility to the different parts and the simplicity of this system makes it quite **versatile**. In fact, by changing some accesories, it can be used for very different applications. For instance, we have used it to perform micro-weldings by means of thin metal wires and conductive epoxy, and to transfer 2D materials to substrates (stamping) [131].

Due to the geometry of the probe holders, the **probes** that can be used within this system must bent near its end (see figure 2.18(c)). I used:

- **Commercial tungsten probes bent 45°at the end** (figure 2.18(c)). They have exactly the same features as the tungsten probes of the previous section except their bent shape at the end.
- The same **home-made gold probes** of previous section. They can be easily bent by hand.
- **Commercial tungsten probes with a thinner tungsten wire attached at the end** (figure 2.19). Their length is 2.2". The apex radius is 0.35 µm (nominal). They

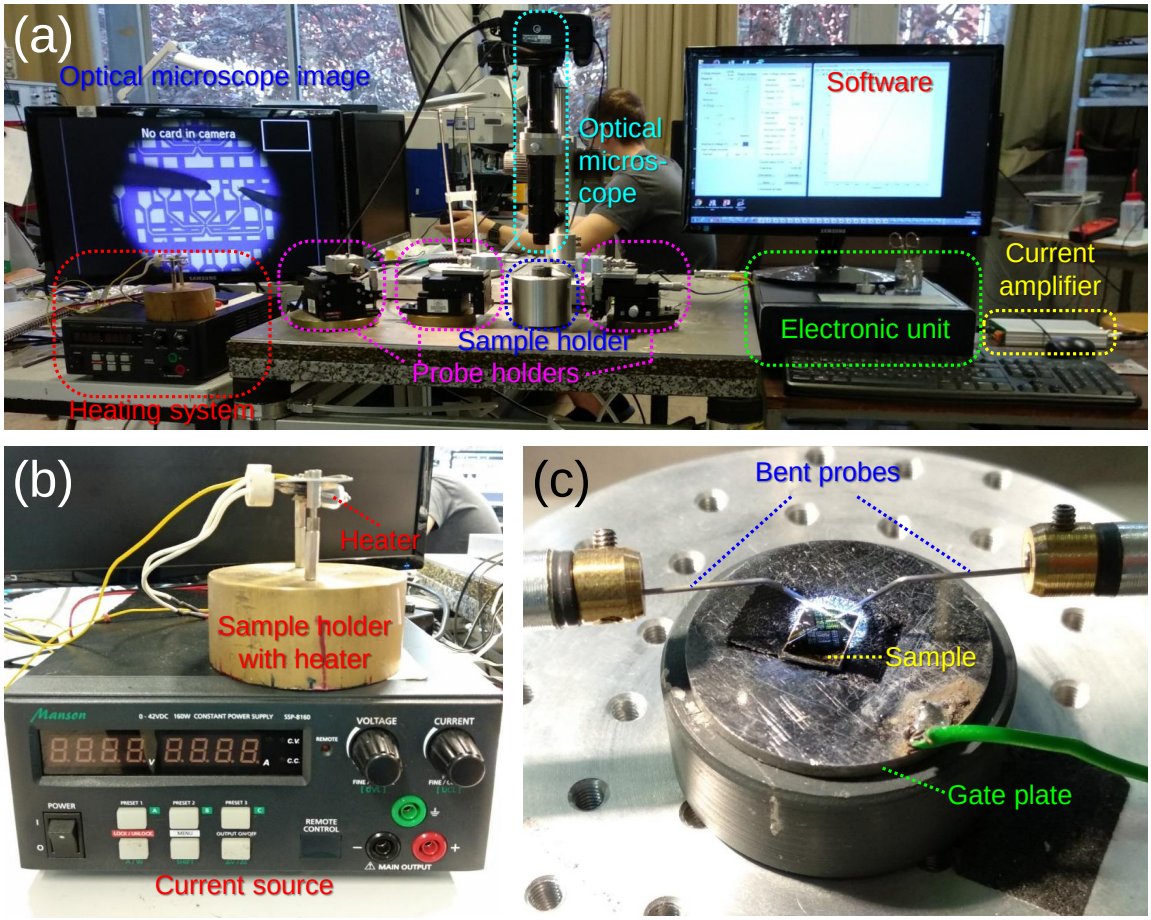

Figure 2.18: Air ambient atmosphere manual Probe Station. (a) The complete system with all its elements highlighted. (b) Heating system. (c) The "heart" of the probe station: the two probes on the sample, which lies on the gate voltage plate.

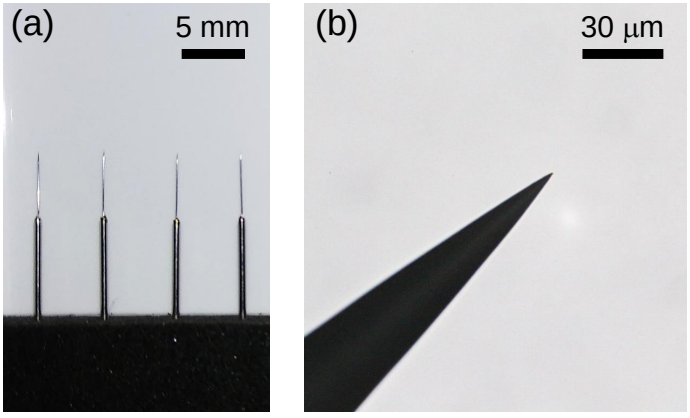

Figure 2.19: Tungsten probes ended with a thinner wire. (a) Photograph of some of them. (b) Optical micrograph of the apex of one.

are straight but the wire can be manually bent. American Probe & Technologies Inc. manufacturates them. They allow electrical contact without scratching the microelectrodes due to the low rigidity of the thin wire. Eventually, we have also used them in the variable temperature ambient-controlled motorized probe station.

3

ENVIRONMENTAL EFFECTS IN MECHANICAL PROPERTIES OF FEW-LAYER BLACK PHOSPHORUS

3.1 INTRODUCTION TO BLACK PHOSPHORUS AND MOTIVATION OF THE CHAPTER

3.1.1 *Black Phosphorus*

Black phosphorus is the **most stable allotrope of phosphorus** [132, 133]. It was obtained for the first time by Bridgman in 1914 [134] by heating white phosphorus (another allotrope) under high preassure. Furthermore, Bridgman was awarded the Nobel Prize in 1946 for his research in high preassure physics. The early research on black phosphorus (BP) studies its **bulk form** (see figure 3.1(a)), including structure, transport, optical, phonon and superconducting properties, and more recently, application in battery electrodes [133]. However these studies did not receive much attention. Only since the beginning of 2014, BP has been investigated from the perspective of a thin film material. In fact, the number of indexed research papers including "Black Phosphorus" in its title rose from 142 in 2013 to 922 in 2014 due to the interest in its layered form, reaching more than 14500 papers in 2018.

3.1.1.1 *Structure*

Black phosphorus can have an orthorhombic, simple cubic or rhombohedral crystalline structure [135]. The one under normal conditions of temperature and pressure, is the **orthorhombic crystal structure** with phosphorus atoms covantly bonded to three neighboring atoms in the same layer. This bonding in BP is due to **sp^3 hybridization** of 3s and 3p orbitals of phosphorus atoms. Each phosphorus atom has five valence electrons ($3s^2$ $3p^3$): three of them are shared with the three neighboring atoms (each electron in a sp^3 hydrid orbital forming a covalent σ bond with a neighbour's electron), and the other two electrons form a lone pair in the fourth sp^3 orbital (which is oriented out-of-plane as shown in figure 3.1(c)) [136, 137]. This leads to layers with a **puckered honeycomb-structure** [138] that is depicted in figure 3.1(b) and (d). As a result of this puckered structure, a single layer of the honeycomb network contains two atomic layers and two kind of P-P bonds: the shorter connects nearest P atoms in the same plane, and the longer one connects top and bottom atoms as it is shown in figure 3.1(e) [139]. Single BP layers are stacked together by weak van der Waals forces. This fact allows mechanical [140] and liquid phase [141] exfoliation of bulk BP into thin flakes, as if it were graphite. Furthermore, single layers of BP, called *phosphorene*, have been isolated via mechanical exfoliation [18]. 2D BP films have been grown by chemical vapor deposition approach too [142]. The **interlayer distance is 0.555 nm**, and therefore the thicknesses of few-layer phosphorene flakes are: 0.555 nm (monolayer, ~0.85 nm in AFM [18]), 1.110 nm (bilayer, ~1.2-1.6 nm in AFM [140, 141, 143]), 1.665 nm (trilayer), 2.222 nm (4 layers), etc. The AFM higher thicknesses are common to other 2D material flakes, and are reported to be caused by a layer of adsorbates between the substrate and the 2D material [140, 144]. Few-layer BP has a ABAB... stacking sequence.

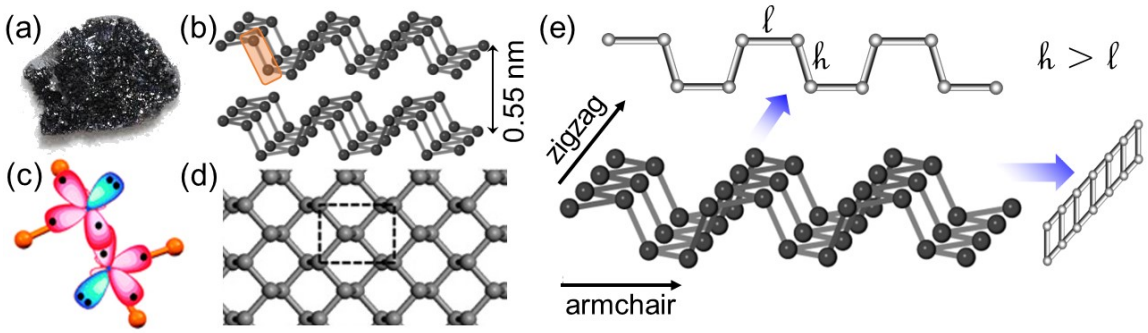

Figure 3.1: Black Phosphorus structure. (a) Bulk BP. The sides of the image are of the order of few millimeters. (b) Layered structure of BP, only two layers are shown. (c) sp^3 hybridization of the two phosphorus atoms inside the orange rectangle in (b), showing the σ bond between them and the lone pair of each (in blue orbitals). (d) Top view of a layer of BP, which has a hexagonal structure. The unit cell is highlighted. (e) A single layer of BP showing its two non-equivalent in-plane directions and the lateral projection of each. Sources: (a): [145], (b) and (e): [146], (c): [137] and (d): [147].

One of the exciting features of BP is its **in-plane anisotropy**, that can be exploited to design new devices and applications. XY plane has two non-equivalent directions: the **armchair** and the **zigzag** (see figure 3.1(e)). The effective mass of carriers along the zigzag direction is one order of magnitude larger than that along the armchair direction [133]. This leads to a strong in-plane anisotropy in its electrical, optical, mechanical and phonon properties. A representative example of the in-plane anisotropy is the fact that the prominent electrical and thermal conducting directions are orthogonal to one another [148].

3.1.1.2 *Properties*

Since 2014 thounsands of theoretical and experimental **research works** on BP in its single-layer, few-layer or thin film forms have arisen. They cover topics such as: (i) band structure [149], (ii) structural varieties (nanotubes and nanoribbons, bilayer and heterobilayer [150]), (iii) characterization methods [140], (iv) stability and passivation methods [151], (v) novel physics properties [148] and (vi) promising applications in several fields (electronic, photonics, thermoelectrics, gas sensing devices etc.). The **most remarkable features of few-layer BP** are [146]: (i) natural p-type semiconductor with a narrow direct bandgap (from 0.3 eV to 1.5 eV) that bridges the gap between graphene (zero gap semiconductor) and TMDCs (~1-2 eV, wide gap semiconductors) which is depicted in figure 3.2, (ii) relative high carrier mobility, (iii) ambipolar field-effect, (iv) good on-off ratio, (v) broad and fast photodetection and (vi) in-plane anisotropy. In addition, its electrical and optical properties can be tuned with the numbers of layers [152], the strain [136] and by alloying with arsenic (b-AsxP1-x) [153]. Figure 3.2 compares the BP bandgap with those of several 2D semiconductor materials.

3.1.1.3 *State of the Art of Mechanical Properties*

BP **mechanical properties** have been researched as well. Most of the first works were **theoretical** [154–161]. They study the mechanical behaviour of single- [155–158, 160, 161], few- [155] , multi-layer [159] and bulk BP [154]. Hao *et al.* [158] deals with nanoribbons

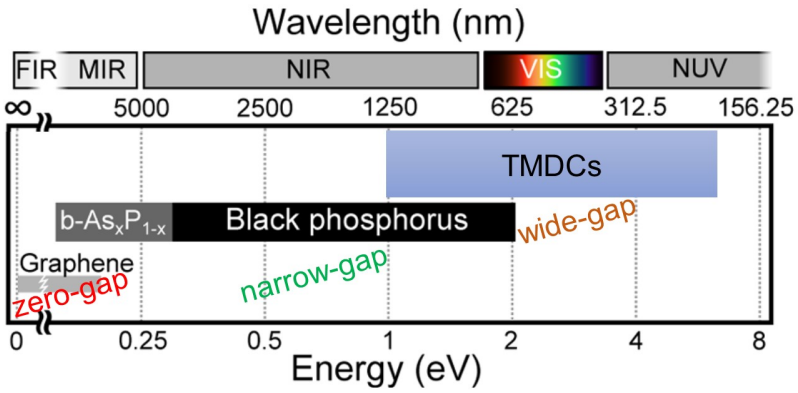

Figure 3.2: Band gaps values for different 2D semiconductor materials. The BP horizontal bar spanning a range of band gap values indicates that the band gap can be tuned over that range by changing the number of layers, straining, or alloying. Adapted from [146].

and oxides whereas Wang *et al.* [159] with nanomechanical resonators. All these works mechanically characterize the BP by calculating its *elastic constants*, its *strain-stress curve*, its *maximum strain*, its *Young's* (or elastic) *modulus*, its *Poisson's ratio* and other **mechanical parameters**. Moreover, all those works address the *influence of the in-plane anisotropy* in these parameters. The initial theoretical works were eventually followed by fewer **experimental** researchs performed in few-layer BP nanosheets [162, 163] and nanoribbons [164]. The *elastic modulus*, the *strain* and the *breaking strength* were experimentally obtained in them. A more recent paper studies the fracture mechanism of phosphorene under indentation [165]. I will introduce below all mechanical parameters afore mentioned.

An interesting field of research connected with the mechanical behaviour of BP, is the use of **strain engineering**: the modification of the electrical, optical and mechanical properties of a material by subjecting it to a mechanical deformation. Strain engineering is particularly suitable for 2D materials since they can withstand large deformations (up to 20%) opposite to 3D semiconductors that break at moderate deformations (<1.5%) [140, 166, 167]. Regarding 2D BP, strain engineering is even more appealing due to its intrinsic in-plane anisotropy. Several theoretical approaches have address the strain engineering in BP to modify the electrical, optical and mechanical properties of a single [136, 161, 168] and few-layer BP [169].

3.1.1.4 *Environmental Instability*

A significant issue in BP is its **environmental instability**. BP is unstable in ambient conditions in its single- and few-layer form [170]. As I explained before, within the sp^3 hybridization, each phosphorus atom has a lone pair of electrons. This generates an out-of-plane dipole moment that makes BP highly hidrophilic as it can interact with the dipole moment of water [140, 170, 171]. Indeed, Density Functional Theory simulations indicate that water molecules make BP crystal lattice shrinks by 25% [140]. Castellanos-Gómez *et al.* [140] and Island *et al.* [170] experimentally showed that after the fabrication of few-layer BP flakes, droplets appear on the BP surface flakes, that keep growing and coalescence (shown in figure 3.3(a)). However they dissapear after storing the flakes in vacuum for a few hours. A long exposure (~a week) deteriorates the flakes, causing an overall reduction in thickness and etching away the thinner parts of the flakes. Furthermore, they

saw that thinner flakes adsorb water faster than the thicker ones. All these phenomena suggest a thickness-dependent wetability that results in a layer-by-layer thinning of the flakes, being more dramatic for the thinner ones. Additionally, the presence of oxygen leads to the degradation of the material due to the formation of oxidized species [151]. This was experimentaly evidenced by Favron *et al.* who reported a thickness-dependent photoassisted oxidation reaction with oxygen dissolved in adsorbed water [172].

Several techniques have been used to **reduce this degradation**. These includes the use of: oxidized aluminum as a passivation layer (figure 3.3(b) and (c)) [151], poly(methyl methacrylate) (PMMA) coating [173] and graphene and hexagonal boron nitride encapsulation [174]. Nevertheless, the aging of BP flakes at ambient conditions is slow enough to allow fabrication of field-effect transistors with strong ambipolar behavior. Besides, this hygroscopic character could be a strength of BP in, for instance, biological applications or humidity sensors [175, 176].

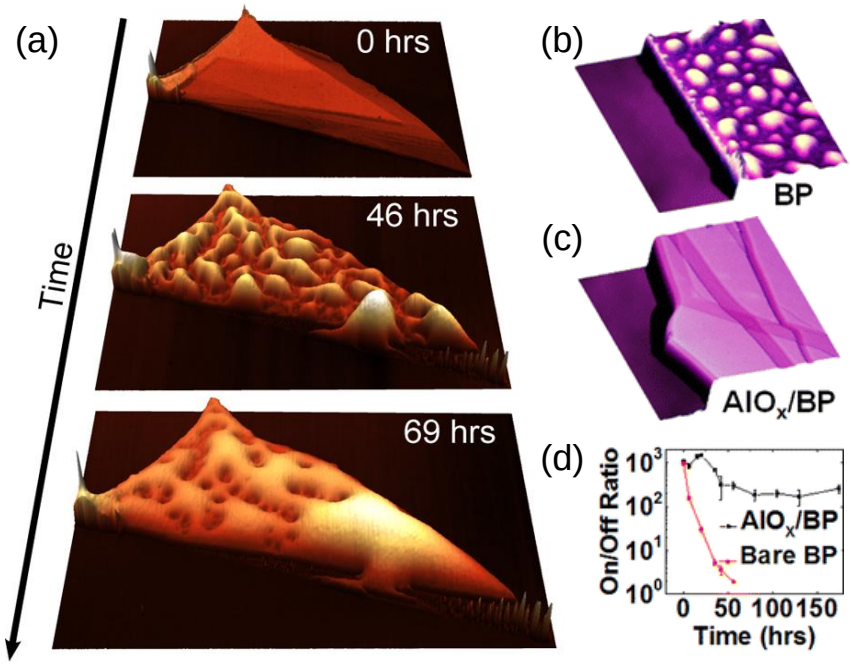

Figure 3.3: Environmental instability of few-layer BP sheets and encapsulation. (a) Selected AFM topographies of a BP flake scanned in air at several times after the exfoliation. Extracted from [170]. (b) AFM topographic images and on-off ratio of BP thin FETs without and with AlOx overlayer protection *vs.* ambient exposure time. Source: [151].

3.1.2 *Motivation of this chapter*

Although there are some studies that have already addressed the environmental effects in the electronic properties of BP, as it is depicted in figure 3.3(d) and reported by [170, 175–178], little is still known about its **effect on the mechanical properties**. Furthermore, there is a lack of experimental data of mechanical properites of BP in vacuum. The scarce experimental works are all performed in ambient conditions, without monitoring the influence of the time of exposure to atmosphere on the mechanical properties. This is where the motivation of this chapter lies. Here I present the mechanical properties of

few-layer BP nanosheets measured at high vacuum conditions as well as the evolution of them once the nanosheets are exposed to ambient conditions.

The essence of the work presented in this chapter is published in reference [179]: **Miriam Moreno-Moreno**, Guillermo López-Polín, Andrés Castellanos-Gómez, Cristina Gómez-Navarro, and Julio Gómez-Herrero, **"Environmental effects in mechanical properties of few-layer black phosphorus."** In: 2D Materials 3.3 (2016), p. 031007. The work has been performed in collaboration with Andrés Castellanos-Gómez, who has a long experience and knowledge about 2D materials, and specifically BP. He proposed the research and prepared the samples. Guillermo López-Polín, an experienced researcher in measuring graphene's mechanical properties by nanoindentations, taught me how to perform the nanoindentations, to analize the data and helped me in the first measurements.

3.2 SAMPLE PREPARATION, CHARACTERIZATION AND STORAGE

3.2.1 *Sample preparation*

For this study BP drumheads (as the ones shown in figure 2.8(a-c)) were prepared as follows. First, BP flakes were obtained by **mechanical exfoliation** of bulk black phosphorus (from Smart Elements GmbH) on Poly(dimethylsiloxane) (PDMS) stamp. Then, the flakes were deterministically placed over substrates of oxidized Si (300 nm of thermal SiO_2) with predefined wells of different shapes created by projection optical lithography and reactive ion etching (RIE) on the SiO_2. Figure 3.4 shows a SEM image of the pattern of the holes. The diameter of the circular wells are between 0.5 and 3 microns and the depth is 300 nm, like the SiO_2 thickness. These substrates were fabricated by the research group of Francesc Pérez-Murano at the Instituto de Microelectrónica de Barcelona IMB-CNM (CSIC).

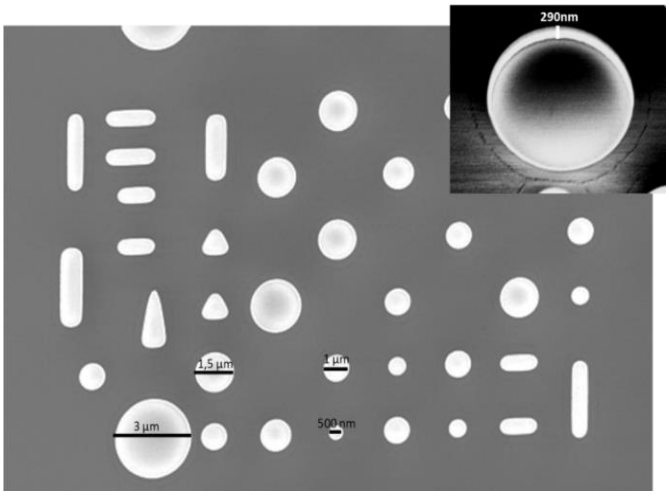

Figure 3.4: SEM image of the Si/SiO_2 substrate with wells. The longest scale-bar is 3 microns long. In the top right panel a zoom of one hole is included to appreciate the verticality of the walls.

The **deterministic all-dry transfer** of BP flakes with the PDMS stamp was performed as described in references [131, 180]. There are two main advantages of using this preparation method with respect to standard microexfoliation [181] for this experiment: the first one is its higher yield covering circular wells, and the second one is that 2D material layers stamped over the holes present a very uniform and low pre-tension.

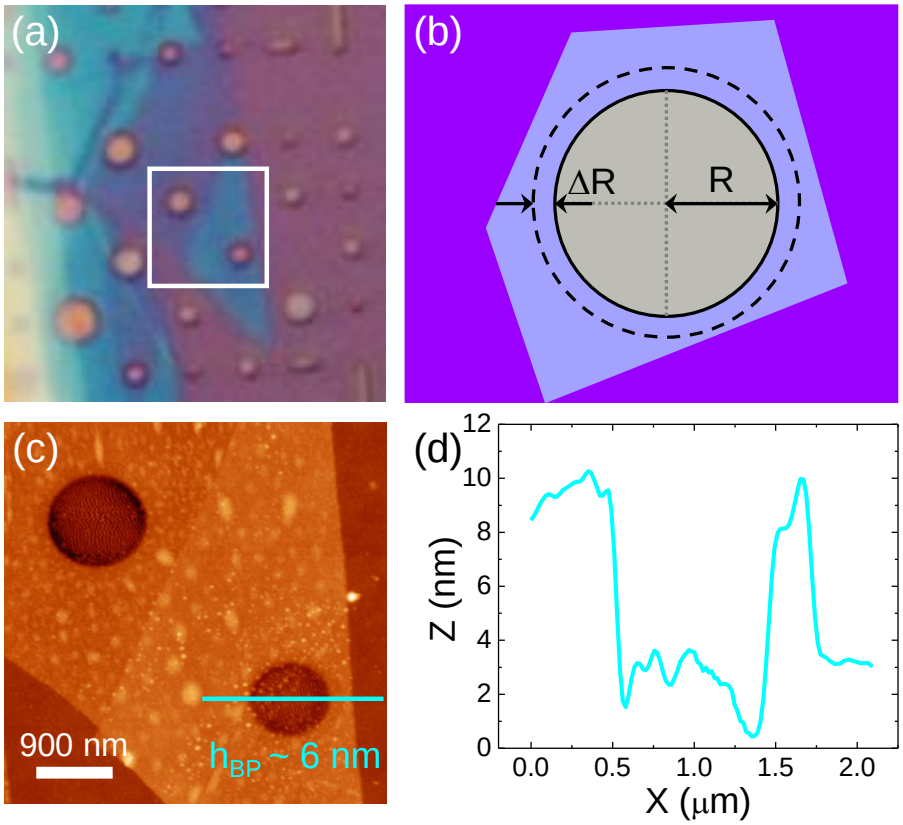

Figure 3.5: Few-layer BP drumheads topology. (a) Optical micrograph of a sample with BP flakes covering some substrate's holes. (b) Sketch of a hole covered by a BP flake highlighting the outer ring considered for the estimation of the ring minimum width to avoid the sliding of the flake. (c) AFM topographic image of the area inside of the square in (a). (d) Topographic profile along the cyan line in (c).

3.2.2 *Sample preliminar characterization and storage*

After preparing a sample, we visualize the BP flakes using an **optical microscope** (see figure 3.5(a)). The thickness of the SiO_2 on the Si is crucial to estimate the thickness of the BP by optical microscopy [182, 183].

The inspection under the optical microscope provides a fast way to check the flakes and select the best ones for our experiments: the ones with few BP layers that fully cover one or several substrate's holes. They must cover not only the hole but also the area around it (see figure 3.5(b)). This is needed to ensure a high enough clamping to the substrate **avoiding the sliding of the flake** when performing the indentantion experiments (indentation curves explained in section 2.1.10).

During the nanoindentations, the highest deformation takes place at the area of the flake in contact with the AFM tip, while the edges of the nanodrum have very low stress, lower than the 2% [183]. We can estimate an upper bound to the sliding of the BP flakes considering the work by Cui *et al.* [184]. They reported that the friction force of BP flakes (on SiO_2) with a n-type Si AFM tip (with a radius of 8 nm and surely around 1 nm thick oxide layer) increases as the number of BP layers decreases and it tends to the bulk value for more than 10 layers. So the worst scenario for us would be have a thick flake, for which they report a measured force friction of around 8 nN. Assuming a tip-flake contact

area of about $2\pi R_{tip}^2$ (half sphere area[1]), we obtain a friction force per unit area of ~0.02 nN/nm^2. In our experiments we have never loads higher than 2000 nN. We assume that the clamping is caused by the outer ring of BP flake around the hole, with an area of $2\pi R\Delta R$, being R and ΔR the radius of the hole and the width of the ring respectively (see figure 3.5(b)). Therefore the drumheads must fulfill: $2\ \pi R \cdot \Delta R \cdot 0.02\ nN/nm^2 >> 2000$ nN. That condition is achieved if the width of the outer ring is $\Delta R >> 40$ nm (for a well with a diameter of 750 nm), which is always fulfilled by far in our drumheads even for other holes' radii.

After this initial characterization, the samples were **stored in a chamber at HV conditions** until the beginning of their mechanical characterization. This was done to avoid the degradation process of BP flakes in ambient conditions. During sample preparation and the initial characterization in ambient conditions, BP samples were not exposed to atmospheric conditions for more than 2 hours (below this time no substantial degradation is appreciated [170]).

3.3 MECHANICAL PROPERTIES OF 2D MATERIALS

I introduce here the main mechanical magnitudes of two-dimensional materials. In the next sections of this chapter I will present our experimental results of some of them for few-layer black phosphorus nanosheets, while in chapter 4 I will do the same for the metal-organic ultrathin film studied in that part.

3.3.1 *Stress-Strain Curves*

The main mechanical properties of a material can be obtained from its stress-strain curve. The **stress** (σ) is simply the force applied per unit area ($\sigma = F/A$), while the **strain** (ϵ) is the deformation (compression or streching) of a material due to stress and corresponds to the change of a dimension divided by the original value of that dimension ($\epsilon = \Delta L/L$).

$$\sigma = \frac{F}{A}; \qquad \epsilon = \frac{\Delta L}{L} \tag{3.1}$$

The stress-strain curve simply plots σ *vs.* ϵ. Figure 3.6 shows a typical stress-strain curve of a **ductile material**. These curves are obtained performing a tension test in the material: apply a stress and measure the caused strain [185, 186]. This approach is feasible for macroscopic materials, but not for 2D materials. This is due to the lack of a reliable technology that provides a good clamping of the nanosheets. For that reason the mechanical properties of 2D materials are usually measured by other techniques. One of the most popular is the **nanoindentation**. It is conducted by an AFM and it consists in indenting an AFM probe on a free-standing nanosheet anchored at the edges to the substrate while the force and the deformation of the nanosheet are measured, as it was explained in section 2.1.10. This technique is the one used in this thesis to mechanically characterize nanosheets. It cannot induce high global deformations in the sheets because the stress of the sheets is mainly concentrated under the tip [183].

1 That assumption is not valid, Hertz Model should be taken into account, but the order of magnitude of the result would be the same.

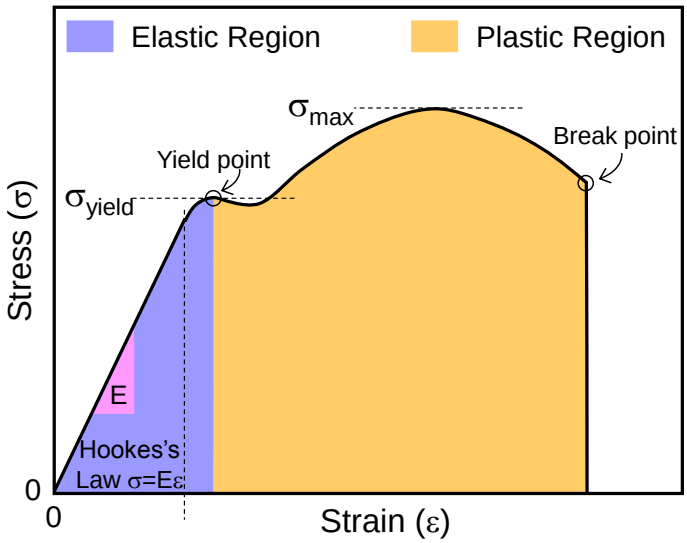

Figure 3.6: Stress-strain curve of a ductile material. Its most important parts and values are highlighted. Adapted from: [183, 187].

3.3.2 *Young's Modulus*

The Young's modulus, also known as **tensile modulus** or **elastic modulus (E)**, is the slope of the stress-strain curve in the linear region, where the *Hooke's law* takes place (see figure 3.6). In other words, E tells us the amount of stress needed to create a certain strain in a material while it has a linear response [185, 188].

$$\text{Hooke's law} : \sigma = E \cdot \epsilon \implies \text{Young's modulus} \equiv E = \frac{\sigma}{\epsilon} \tag{3.2}$$

In 3D materials E has pressure units (Pa=N/m^2), however in 2D materials, the magnitude that can be measured is the **two-dimensional E: E_{2D}**. This magnitude is proportional to the force we should apply to stretch or compress a sheet of a certain width (W) as it is shown in figure 3.7(b). Consequently, E_{2D} has N/m units. To compare E_{3D} (or E) with E_{2D} we should divide E_{2D} by the thickness of the sheet (t), by doing that we obtain the equivalent E_{3D} (see figure 3.7).

3.3.3 *Breaking and Yield Strength*

Breaking stress, or **breaking strength** ($\sigma_{max} = \sigma^{3D}_{max}$), is the maximum stress that a material can withstand before breaking. It corresponds to the maximum stress point of the stress-strain curve (see figure 3.6). The maximum stress for a clamped, linear elastic, circular membrane under a spherical indenter as a function of applied load has been derived on the basis of a continuum model [44, 189] as:

$$\sigma^{2D}_{max} = \sqrt{\frac{F_{fr} E_{2D}}{4\pi R_{tip}}} (N/m) \tag{3.3}$$

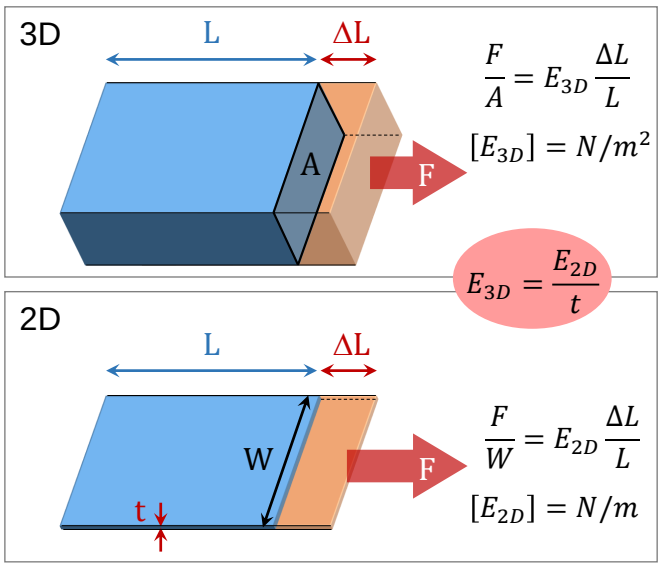

Figure 3.7: Relationship between Young's modulus of 3D and 2D materials. Adapted from: [183]

where F_{fr} is the force at which the material breaks (**fracture force**), and R_{tip} the spherical indenter (AFM tip apex) radius. To obtain the 3D equivalent magnitude, we should divide σ^{2D}_{max} by the thickness of the sheet (t), as in the case of Young's modulus:

$$\sigma^{3D}_{max} = \frac{\sigma^{2D}_{max}}{t} = \sqrt{\frac{F_{fr}E_{2D}}{4\pi R_{tip}t^2}} = \sqrt{\frac{F_{fr}E_{3D}}{4\pi R_{tip}t}}(Pa) \tag{3.4}$$

Yield strength ($\sigma_{yield} = \sigma^{3D}_{yield}$) is defined in engineering as the amount of stress (Yield point) that a material can undergo before moving from elastic (reversible) deformation into plastic (irreversible) deformation [190]. In other words, is the maximum stress that can be applied before the material begins to change its shape permanently (plastically). The yield strength and the yield point are marked in the stress-strain curve of figure 3.6.

For **brittle materials**, the yield strength and the breaking stress coincide because this kind of materials cannot undergo plastic deformations, they break before (their stress-strain curve only contains the elastic region, breaking at the Yield point). Theoretical works have reported brittle response for BP from its fracture behaviour [191, 192].

3.3.4 *Poisson's Ratio*

The Poisson's ratio (ν) quantifies the compression caused in a material in the axis perpendicular to the one in which it undergoes a stretching (see figure 3.8), or the opposite (the stretching caused in the perpendicular direction to the one where is being compressed), therefore:

$$\nu = -\frac{(Y_2 - Y_1)/Y_1}{(X_2 - X_1)/X_1} = -\frac{\epsilon_{trans}}{\epsilon_{long}} \tag{3.5}$$

The Poisson's ratio only applies **within the elastic region** of the stress-strain curve. It is usually a positive magnitude being 0.3 in most metals [188]. On the contrary, for BP it

is predicted to be negative in the out-of-plane direction under uniaxial deformation in the direction parallel to the pucker [157]. This occurs only in that direction and it is due to its puckered structure: when stretching BP along the puckers' direction, the grooves would get closer, increasing their heigth.

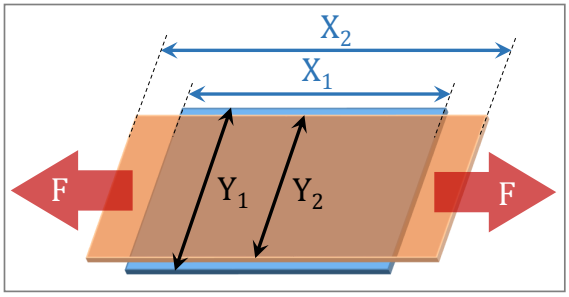

Figure 3.8: Poisson's ratio meaning. Adapted from [183].

3.3.5 *Bending Rigidity*

The bending rigidity (κ) accounts for the resistance offered by a structure while undergoing bending. It is defined as the force couple required to bend a non-rigid structure in one unit of curvature (1 radian). Therefore for macroscopic materials its units are N·m^2 while for two-dimensional materials are N·m, which are energy units, because it is the force couple per length unit.

The **bending rigidity of a sheet** is defined by the classic equation:

$$\kappa = \frac{E_{3D} t^3}{12(1-\nu^2)} \tag{3.6}$$

where E_{3D} is the Young's modulus, t the thickness of the sheet, and ν the Poisson's ratio [193]. As κ increases with the cube of the thickness of the sheet, it will become more relevant for the thicker flakes and negligible for single layer flakes. For monolayer sheets, the thickness is not well defined, thus the above expression may not be fulfilled

3.4 EXTRACTION OF MECHANICAL PROPERTIES FROM INDENTATION CURVES

We have already learnt how to acquire indentations curves with an AFM (section 2.1.9 and 2.1.10) and the main mechanical magnitudes of a 2D material (section 3.3). In this section we analyze how to obtain mechanical properties from the indentation curves.

Due to the geometry of our experiments (indentations at the center of BP circular membranes), the obtained E_{3D} will be the average of the elastic modulus in both in-plane directions (zigzag and armchair). This applies to the stress as well (and in particular to σ_{max}).

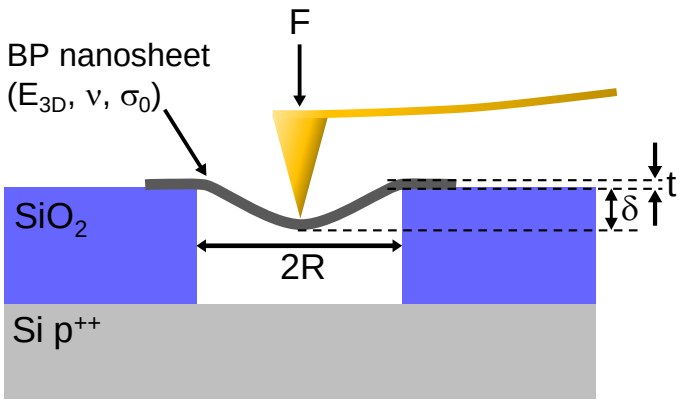

Figure 3.9: Drumhead geometry. The magnitudes present in equation 3.7 are highlighted.

3.4.1 *Young's Modulus and Pre-stress*

For a circular, drum-like structure, like our drumheads (see figure 3.9), the **force (F) *vs.* sheet's deformation (δ) relationship** follows this expression [92, 194–196]:

$$F = \left[\frac{4\pi E_{3D}}{3(1-\nu^2)} \cdot \left(\frac{t^3}{R^2}\right)\right] \cdot \delta + \pi\sigma_0 \cdot \delta + \left(\frac{q^3 E_{3D} t}{R^2}\right) \cdot \delta^3 \tag{3.7}$$

where E_{3D} is the conventional (3D) elastic modulus, t the thickness of the nanosheet, R the drumhead's radius, ν the Poisson's ratio, σ_0 the two-dimensional pre-stress of the sheet produced during the sample preparation, and $q = 1/(1.05 - 0.15\nu - 0.16\nu^2)$. We use 0.45 for ν, as the average of the Poisson's ratio in the [100] and in the [010] direction, taken from [155]. The first two terms of F in equation 3.7 (terms in δ) prevail over the third one for low indentations. The first one accounts for the **bending rigidity** (in fact it is proportional to κ, see equation 3.6), being negligibe for very thin flakes as it increases with the cube of the thickness. The second terms is associated with the effect of the small pre-stress (**pre-tension**) acumulated in the membrane during the fabrication method. It varies randomly among drumheads (although the deterministic transfer of flakes favors a uniform σ_0). Finally, the term in δ^3 prevails at large indentations and it is governed by the intrinsic **elastic modulus** of the sheets.

The thickness and deflection dependences reflected in Equation 3.7 provides two complementary methods for determining E_{3D}. The first one is valid for **large indentations**, where the third term dominates, whereas the second method is valid in the **low indentation regime**, where the linear terms prevail.

3.4.1.1 *Large indentations Method*

In this first method the experimental data of each indentation curve are fitted to a polynomial with terms in δ and δ^3 and the **elastic modulus** is extracted from the cubic coefficient. It requires large indentations but the value of E_{3D} can be obtained with data of exclusively one drumhead. This method automatically separates the linear coefficients from the elastic modulus, however it is not easy to apply to thick flakes where the large indentation regime is difficult to achieve (their high bending ridigity makes the first linear term prevails until large indentations). Therefore, by using this method, the elastic modulus is directly obtained from each indentation curve, however, the bending rigidity

and pre-tension are not separately accessible since both contribute to the linear coefficient. This method actually provides $\mathbf{E_{2D}}$, we then simple divide by the thickness of the flake to compute E_{3D}.

In the fitting procedure it is **critical to fix the zero force level** and the **zero displacement point**: inaccuracy of 2-5 nm in this point leads to a 10 % error in the final calculated E_{2D}. Considering the previous experience of the group analyzing indentation curves [197], the protocol followed to determine that point was: the zero force level is given by the horizontal line (zero cantilever deflection, $\mathbf{F = 0}$), an initial zero displacement point (δ = **0**) is the value of X axis where that horizontal line cuts the curve. A zoom in this region shows a purely experimental noise. To avoid it as much as possible, we find the (0,0) point by fitting the data to a third order polynomial. To this end we take about 20 experimental points to the left and about 70 to right of the initial zero. Figure 3.10 portrays the method followed to fix the zero force level.

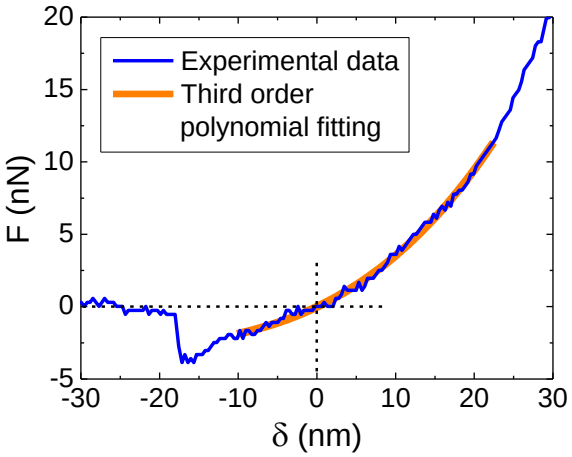

Figure 3.10: Method followed to determine the zero force level and zero displacement point.

The **fitting errors** of equation 3.7 for the measurements in vacuum were under 20%, however, the fitting error increases with time of exposure to atmospheric conditions, as we will see in section 3.7.2. The increase of the error can be caused by the layer of adsorbed water that hinders the determination of the zero indentation point of the membrane. For these cases we used a **complete third order polynomial** to fit the indentation curves, which gives lower fitting error as it can be expected. The elastic modulus was then obtained merely from the third order term, as I explain below. This type of analysis had been previously used in graphene membranes very effectively [197].

If μ is the error we have in δ when fixing the zero displacement point, and we insert it in equation 3.7, we have [183]:

$$F = \left[\frac{4\pi E_{3D}}{3(1-\nu^2)} \cdot \left(\frac{t^3}{R^2}\right)\right] \cdot (\delta - \mu) + \pi\sigma_0 \cdot (\delta - \mu) + \left(\frac{q^3 E_{3D} t}{R^2}\right) \cdot (\delta - \mu)^3 \tag{3.8}$$

that results in:

$$F = -\frac{4\pi E_{3D}\mu}{3(1-\nu^2)}\cdot\left(\frac{t^3}{R^2}\right) - \pi\sigma_0\mu - \frac{q^3 E_{3D} t\mu^3}{R^2} + \\ + \left[\frac{4\pi E_{3D}}{3(1-\nu^2)}\cdot\left(\frac{t^3}{R^2}\right) + \pi\sigma_0 + \frac{3q^3 E_{3D} t\mu^2}{R^2}\right]\cdot\delta - \\ - \frac{3q^3 E_{3D} t\mu}{R^2}\cdot\delta^2 + \frac{q^3 E_{3D} t}{R^2}\cdot\delta^3 \tag{3.9}$$

we finally obtain a term in δ^3 which is the same of the one in equation 3.7: $q^3 E_{3D} t/R^2$. Therefore, by fitting the indentation curves to a **complete third-order polynomial**, and extracting the Young's modulus from the cubic coefficient, we avoid the errors caused by the fixing of zero displacement point. The values of the elastic modulus of this chapter were computed by (i) fitting the curves to equation 3.7 when the indentation curves are obtained at HV and (ii) fitting to a complete third degree polymonial (equation 3.9) at air conditions, due to its better reliability and reproducibility.

An example of experimental curves and their fittings are plotted in figure 3.11(a, b, d, e). (a) and (d) depicts two experimental deflection curves acquired on the same drumhead in HV and in air, respectively, while (b) and (e) portrays the experimental indentation curves obtained from those deflection curves, together with its polynomial fittings (to a polynomial with exclusively therms in δ and δ^3, and to a complete third order polynomial). It is plain to see that at HV both kind of fittings almost coincide whereas at air the full third order polynomial fitting reproduces much better the experimental data.

The polynomial fittings were performed by means of a **Matlab script** previously used in the group, developed by Dr. Julio Gómez Herrero and Dr. Guillermo López-Polín. I improved this script by: (i) including a correction for the FZ curves that were not completely flat before the jump-to-contact point, (ii) including a more general q factor variable, (iii) plotting the computed E_{2D} *vs.* load and (iv) saving several statistical parameters as well as graphs. The graph mentioned in (iii) allows us to check the reliability of the computed E_{2D} *vs.* the maximum load. That graph plots, the E_{2D} obtained from the experimental indentation curve but considering only the points below the force showed in X axis (F_{max}). In other words, this plot shows the evolution of the value of E_{2D} when considering more and more points of the indentation curve. It should have a flat part for the highest forces, indicating that the tip has indented enough to be in the large indentation regime, yielding a steady E_{2D}. This is depicted in figure 3.11(c, f).

Although with this method the bending rigidity and pre-tension are not separately accessible (both contribute to the linear coefficient), there is a way to **estimate the pre-tension of the thinner flakes**. These flakes have a very low thickness yielding a very low bending rigidity according to equation 3.6. Hence, the linear coeficient in δ in equation 3.7 will have a much higher contribution coming from the pre-tension than that coming from the bending rigidity (which will be negligible), allowing us to extract the pre-tension from the linear coefficient. Alike, when having an error μ in the zero displacement point, $\pi\sigma_0$ will be much higher than the two other contributions to the linear coefficient in equation 3.9 (the bending rigidity is very low, and $\mu^2 << R^2$). Figure 3.12 depicts the contribution of the bending rigidity term ($\{4\pi E_{3D}/[3(1-\nu^2)]\}\cdot(t^3/R^2)$) and the contribution of the pre-tension term ($\pi\sigma_0$) to the linear coefficient as a function of the thickness of the nanosheet. The values used are: E_{3D} = 41 GPa, ν = 0.45, R = 500 nm and σ_0 = 0.1 N/m (the two

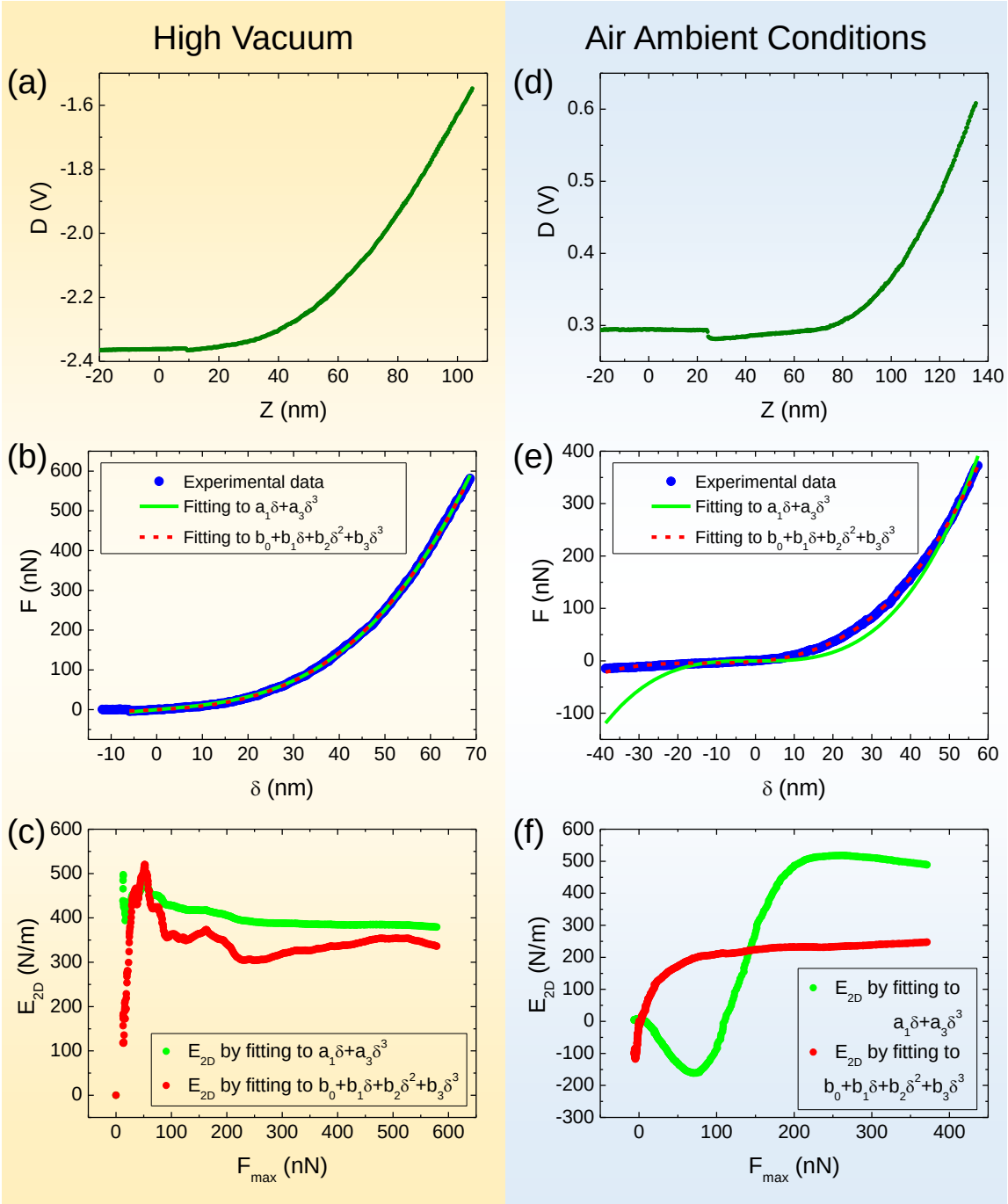

Figure 3.11: Deflection, indentation and E_{2D} *vs.* F_{max} curves of a BP drumhead. (a) Experimental deflection curve of a drumhead at HV. (b) Indentation curve derived from (a) fitted to two kind of polynomials. (c) E_{2D} *vs.* F_{max} yielded from both fittings in (b): every point of each curve corresponds to the E_{2D} obtained from a certain fitting of $F(\delta)$ considering up to a maximum force (F_{max}). (d, e, f) depicts the same kind of data as (a, b, c) respectively, obtained in the same drumhead after 125 hours of exposure to air. All data correspond to a BP drumhead with a radius of 485 nm and a flake of thickness 7.5 nm.

first reported for BP [155, 162]). As it can be readily seen, the pre-tension term prevails for very low thickness (< 3 nm) and becomes equal to the bending rigidity term for a thickness close to 7 nm.

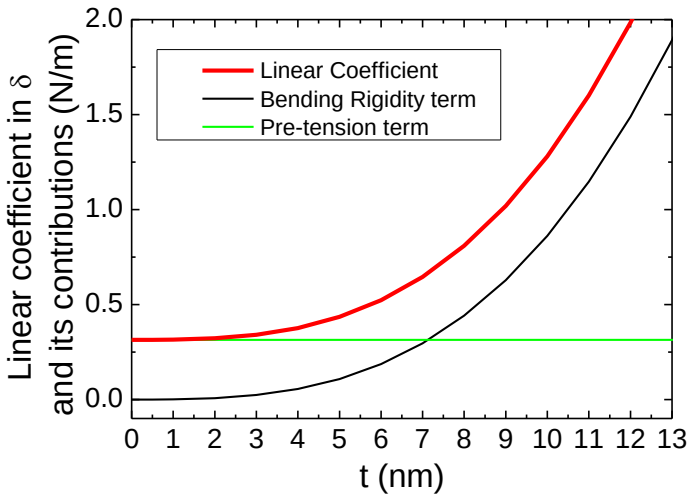

Figure 3.12: Theoretical contributions to the linear coefficient in δ *vs.* the nanosheet thickness. The curves were computed with these values: E_{3D} = 41 GPa, ν = 0.45, R = 500 nm and σ_0 = 0.1 N/m.

3.4.1.2 *Low indentations Method*

The second method consists in measuring a set of flakes with different thicknesses and/or radii in the low indentation regime, where the term in δ^3 in equation 3.7 is negligible. Therefore the $\partial F/\partial\delta$ (the spring constant of each flake, k_{flake}) scales with t^3/R^2 [92]. Consequently, the elastic modulus is inferred by linear fitting of k_{flake} versus t^3/R^2 for several drumheads, according to this expression:

$$k_{flake} = \left.\frac{\partial F}{\partial \delta}\right|_{\delta\approx 0} = \frac{4\pi E_{3D}}{3(1-\nu^2)} \cdot \left(\frac{t^3}{R^2}\right) + \pi\sigma_0 \tag{3.10}$$

This second method is valid while the pre-tensions of all the drumheads are similar and/or negligible compared to the bending rigity. Under that assumption, a linear fit would provide information about the **Young's modulus** (from the slope) and **the average pre-tension** of them (from the intercept).

3.4.2 *Breaking Strength*

Towards obtaining the breaking strength (σ_{max}) of a 2D material, some drumheads need to be indented until rupture. When the fracture occurs while performing an indentation, the FZ curve shows a sudden fall (breaking point, depicted in figure 3.13). The fracture force (F_{fr}) is the maximum force of the FZ, just before the fall. In order to estimate the breaking strength, we then make use of equation 3.4.

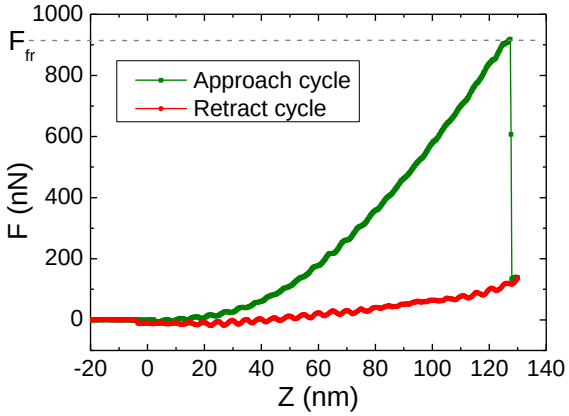

Figure 3.13: FZ curve on a drumhead that breaks. The plot was acquired on a BP drumhead of radius 600 nm and the BP flake was 11 nm thick. The rupture takes places at a fracture force of around 900 nN and a piezo displacement of nearly 130 nm.

3.4.3 *AFM cantilevers to conduct nanoindentations*

The cantilevers to be used to conduct the nanoindentation experiments must meet several requirements. Namely, they should: (i) be made of a hard material, (ii) have a smooth and well defined contact geometry, (iii) have a suitable spring constant and (iv) an appropiate tip radius. We used HSC60 commercial cantilevers from Team Nanotec-NanoScience Instruments [198]. Their tips have hemispherical geometry and low wear coating of tungsten carbide with nominal final tip radius of 60 nm. The cantilever spring constants vary between 25 and 35 N/m. Further information regarding the choice of cantilevers and their spring constant calibration is given in appendix C.

3.5 MEASURING MECHANICAL PROPERTIES OF BP IN TWO ENVIRONMENTS

We initially measured each sample in **high vacuum** using the HV-AFM of figure 2.4(c-d): We took the sample from the HV chamber where it was stored, place it in the HV-AFM and start pumping immediately. Then, we measured the topography and thickness of preselected flakes using DAM-AFM mode (see figure 3.5(c)). We **discarded** the drumheads that do not cover any hole with a wide enough outer ring and the ones that presented wrinkles.

In each drumhead we conducted 10 indentation curves to check their reproducibility and to obtain an averaged value for their elastic modulus. Only the approach cycle of each indentation curve was considered for the fitting. All curves presented here were obtained at the same loading/unloading rate of 100 nm/s. We checked that results are independent of the variation of this parameter within our experimental range.

Subsequent to a complete **characterization of their mechanical properties in HV conditions**, a set of measurements in each membrane was performed while they were **exposed to environment** to assess the influence of ambient conditions on few-layer BP mechanical properties. Figure 3.14 summarizes the whole experimental procedure. One of the main differences between HV and ambient conditions is the water partial preassure, which is reduced in ~8 orders of magnitude in HV. We should remind that water is the most responsible agent for BP environmental instability (see section 3.1.1).

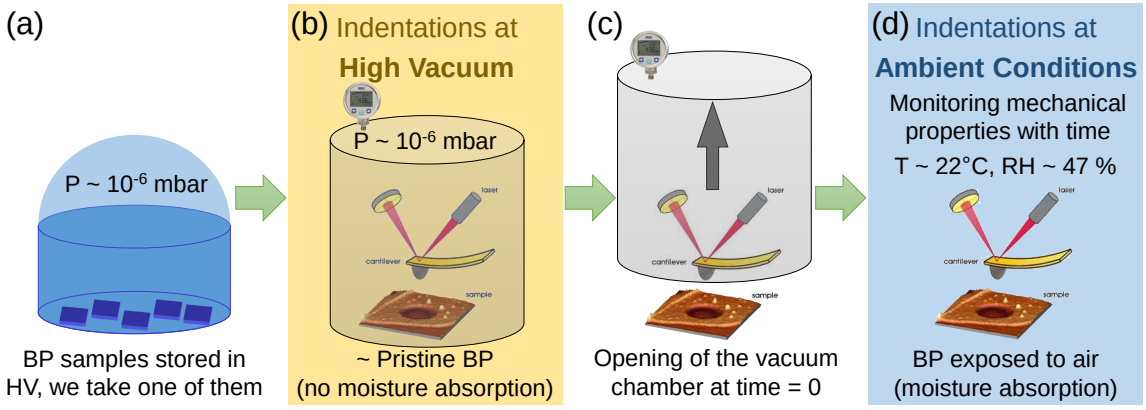

Figure 3.14: Sequence of experiments conducted in black phosphorus drumheads. (a) BP samples are stored in HV to avoid moisture absorption. We take one, place it inside the HV-AFM and close the system. (b) Indentantions at HV are performed to obtain the mechanical properties of almost pristine BP. (c) Then we open the HV-AFM chamber, that time is considered 0. (d) We finally monitor the mechanical properties of BP as function of the exposure time.

3.6 MECHANICAL PROPERTIES OBTAINED IN HIGH VACUUM

3.6.1 *Young's Modulus and Pre-tension*

Figures 3.15 and 3.16 show the results yielded from nanoindentations conducted at HV conditions. Figure 3.15 portrays up to 5 representative **indentation curves** acquired on flakes with thicknesses ranging from 4.5 up to 29 nm. Figure 3.16(a) displays a histogram of the values obtained for the **elastic modulus** of 39 different flakes (with thickness ranges between 4 and 29 nm) as obtained employing the first method aforementioned (**large indentations method**). The average value for E_{3D} is **41 ± 15 GPa**, without any appreciable tendency with flake thickness. The pre-stress obtained from the linear term are in the range of **0.05 up to 0.3 N/m** (obtained exclusively from the 5 thinnest flakes, with t = 4 - 4.5 nm, in which the bending rigidity is much lower than the pre-stress).

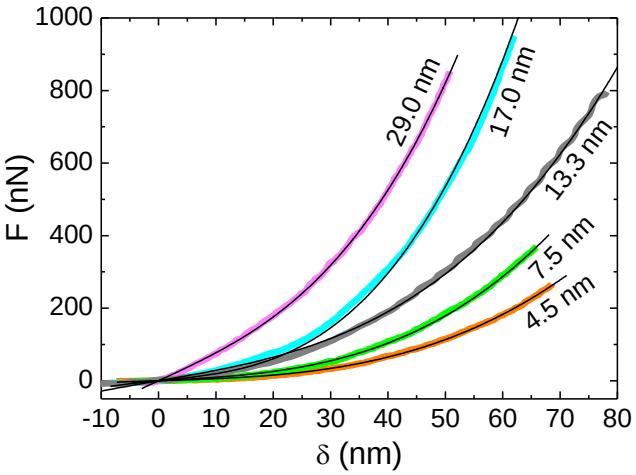

Figure 3.15: Indentation curves acquired on BP drumheads at HV. Experimental F(δ) curves (colored lines) performed on five BP drumheads with different thickness (4.5, 7.5, 13.3, 17 and 29 nm) and their fittings to equation 3.7 (thin black lines).

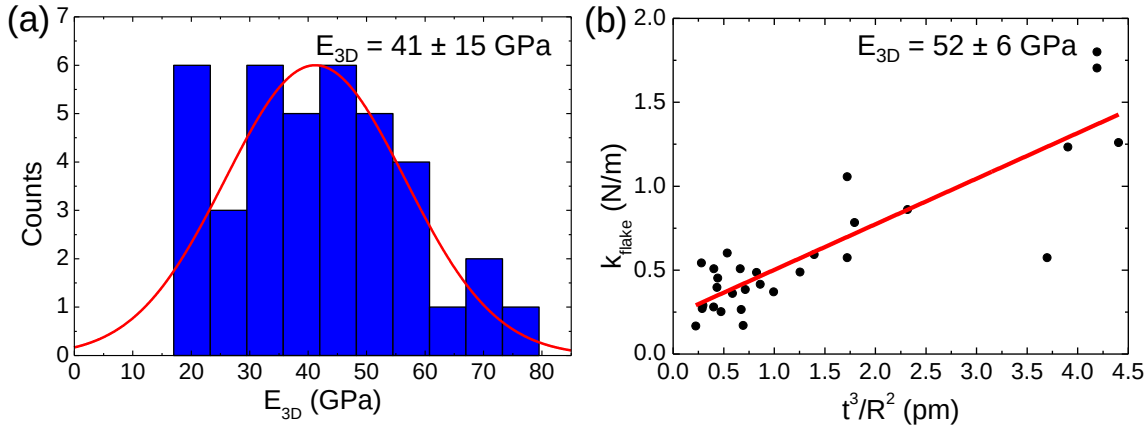

Figure 3.16: E_{3D} of BP drumheads at high vacuum. (a) Histogram of the E_{3D} values obtained from the fit of F(δ) to equation 3.7 in 39 BP drumheads, following the first method described. The fitting of the data of the histogram to a normal distribution yields E_{3D} = 41 ± 15 GPa. (b) Elastic constant versus t^3/R^2 measured for 29 BP drumheads, and their linear fit to the expression 3.10 (red solid line). This method yields E_{3D} = 52 ± 6 GPa.

To check the **validity of the pre-stress value**, we can plot the theoretical dependence of the total linear coefficient with the flake thickness together with the the bending ridigity contribution and the pre-tension contribution (see equation 3.7). We plot it considering a standard drumhead radius of 500 nm, a pre-stress of 0.1 N/m (which belongs to the obtained range 0.05 - 0.3 N/m), the measured E_{3D} = 41 GPa and ν = 0.45 (from reference [155]). The resulting graph is the one that was shown before in figure 3.12, that was ploted for exactly those values. From it we conclude that: the pre-tension term prevails over the bending rigidity's one for thickness below 3 nm, being higher for thicknesses up to 7 nm. Therefore the values yielded for σ_0 are slightly overestimated since only nanosheets with thickness between 4 and 4.5 nm were considered (we lacked thinner flakes). Anyway, a precise determination of the pretension is not very relevant for our goals.

Figure 3.16(b) depicts a set of experimental data points obtained in the **low indentation regime**, and it plots k_{flake} versus t^3/R^2, following the second method described above. The obtained elastic modulus value is **52 ± 6 GPa**, within the error of the elastic modulus obtained in figure 3.16(a), and an average pre-tension of **0.07 ± 0.02 N/m** (also in agreement with the pre-tensions derived from the first method).

In order to analyze the **influence of random pre-tensions** in the flakes (which would lead to different intercepts in the linear fit of figure 3.16(b)), we have numerically simulated F(δ) curves with random pre-tensions in the low indentation regime (see figure 3.17). Here we observe that the dispersion of the simulated data is similar to that of our experiments. This suggests that the variation of pre-tension among nanosheets is the main source of noise in the experimental data.

Summarizing, both methodologies yield similar results of the elastic modulus of few layered BP, being **46 ± 10 GPa** the weighted average of both values (taking into account the number of drumheads analyzed with each method).

The measured value of E_{3D} is in good agreement with previous measurements by Tao *et al.* [162] in atmospheric conditions of thick (> 14 nm) flakes, but in clear disagreement with a more recent publication by Wang *et al.* [163]. Our elastic modulus for BP is also in agreement with theoretical predictions [154–156, 160, 165]. A comparison of the values

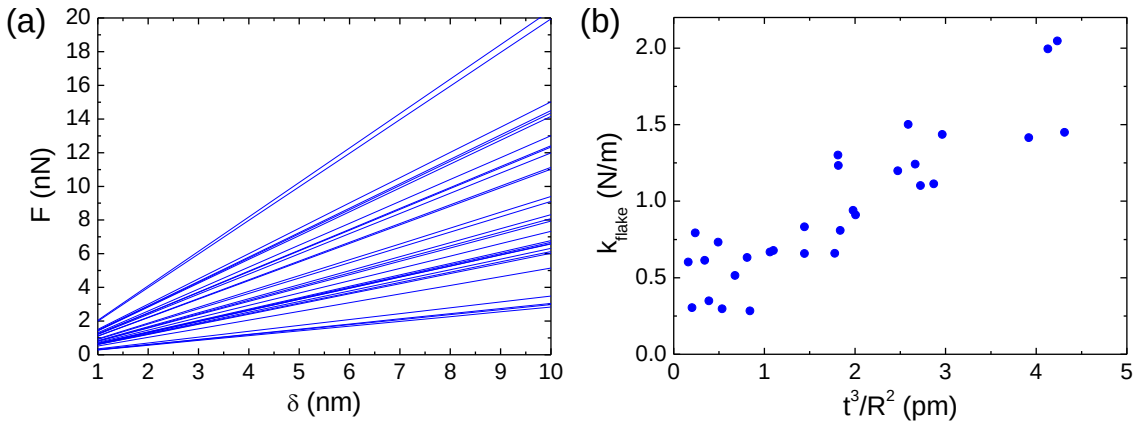

Figure 3.17: Influence of random pre-tensions in k_{flake} *vs.* t^3/R^2. (a) Simulated force *vs.* indentation plots in the low indentation regime for flakes with growing thickness. The lines are spanned by random pre-tensions. (b) Plot of the stiffness of the flakes, calculated as the slopes of the lines in figure (a), *vs.* t^3/R^2. For constant pre-tension this plot should be a perfect straight line. The noise reflects the contribution of the random pre-tensions, which is similar to our experimental noise.

of the Young's modulus for BP found in this thesis and the ones from aforementioned publications is shown at the end of this section together with the values of the breaking strength (see subsection 3.6.3).

3.6.2 *Breaking Strength*

After performing indentations on some drumheads until their rupture, we were able to compute their breaking strength by measuring their rupture force and assuming the expression 3.4 for σ^{3D}_{max}. Figure 3.18(a) depicts a chart of the breaking strength versus thickness for 14 BP drumheads measured in high vacuum. The plot does not show any

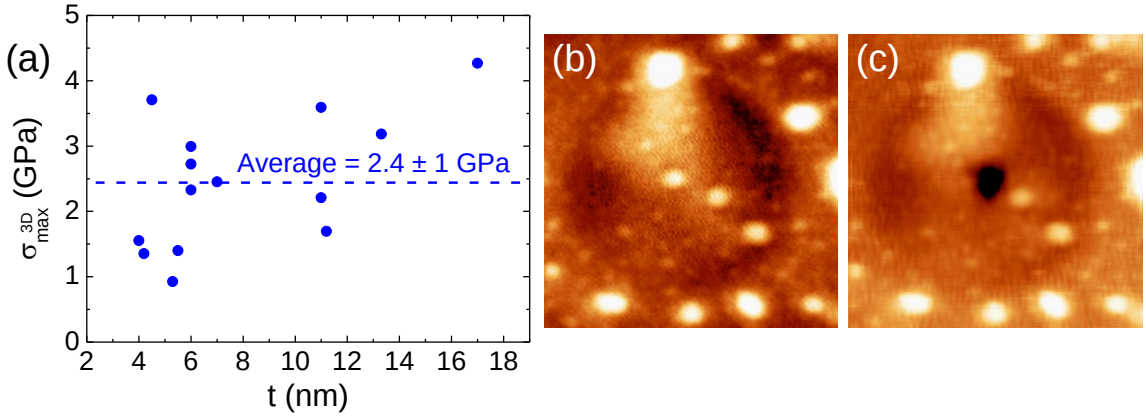

Figure 3.18: Breaking strength and crack in BP drumheads at HV. (a) Breaking strength of 14 BP drumheads *vs.* the BP thickness measured at high vacuum (having an average σ_0^{max} = 2.4 ± 1 GPa). (b) AFM image of a BP drumhead in HV before its breaking. (c) AFM image of the same BP drumhead as in (b) after its rupture, also in HV. The size of the AFM images is 1.5 × 1.5 μm^2.

clear correlation between these two magnitudes. The average breaking strength is 2.4 ± 1 GPa. This value compares quite well with previous measurements in atmospheric conditions [162].

Figures 3.18(b) and (c) displays a BP membrane before and after breaking. As it can be readily seen, the crack is confined around the tip-sample contact point in contrast with pristine graphene [199], in which tears span more than microns.

Recently, Liu and coworkers [165], through an atomic scale simulation, studied the fracture mechanism of freestanding phosphorene under indentation. Their data reveal that the crack grows firstly along the armchair direction and then along the zigzag direction (see figure 3.19(b)). Moreover, they predict the fracture of the freestanding BP monolayer to be firstly brittle-like and then ductile-like. During the indentation process they found two instantaneous drops in the force (see figure 3.19(a), transitions A→B, C→D). After the two cracks, the fracture behavior is ductile-like, with sawtooth shaped steps of F(d) curve (curve on the right side of point D in figure 3.19(a)). They also show that the stress

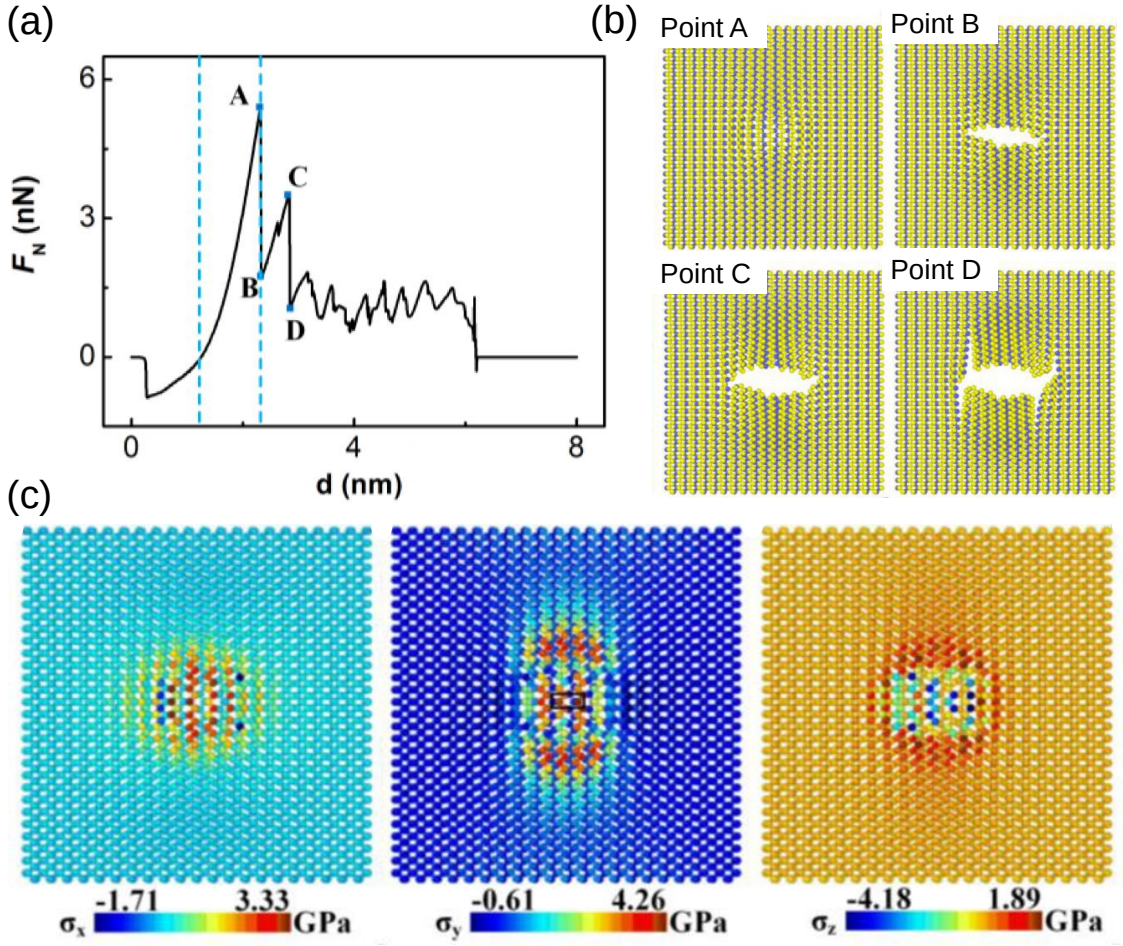

Figure 3.19: Simulation results of the fracture mechanism of freestanding phosphorene under indentation. (a) Force-displacement curve for the indentation process. (b) Top view of the freestanding BP monolayer during the indentation process, each image correspond to a point of the curve in (a). (c) Distribution of σ_x, σ_y and σ_z in the freestanding phosphorene before the generation of the first crack (point A in (a)). Source: [165].

distribution has the maximum normal stress component at elastic stage in zigzag direction (see figure 3.19(c) middle).

The indentations we performed until rupture, were conducted until an indentation between points B and C of figure 3.19(a), as in the case of figure 3.13. We must remind that the breaking strength we measured is the averaged one in X and Y directions, just below the tip. Likewise, the experimental Young's modulus we obtained is the averaged modulus in both in-plane directions.

3.6.3 *Comparison of E_{3D} and σ_{3D}^{max} with reported values and other materials*

Table 3.1 shows the values reported up to now for the elastic modulus and breaking strength for two-dimensional BP. There are two main kind of approaches: theoretical (second and third column) and experimental (fourth column). The average value of both directions (armchair and zigzag) is shown when the source gives separately the values for each direction. The third column presents the values for an oxidized BP monolayer with a 50% ratio of oxygen/phosphorus content. The values of last column are obtained experimentally in air, except the ones derived from this thesis (highlighted with bold font, reference [179]) which were measured in HV.

Approach:	Theo. Pristine BP	Theo. BP+O	Exp. BP at air or HV
E_{3D}(GPa):	44, 52, 74, 98, 105 [18],[160],[156],[158],[155]	69[158]	43, 90-276*, **46** [162], [163], [179]
σ_{max}^{3D}(GPa):	2.4, 3.8, 10, 13 [160],[18],[158],[155]	6.4[158]	3.5, 25, **2.4** [162], [163], [179]

Table 3.1: Reported values of elastic modulus and breaking strength of 2D BP. Sources are shown in brackets. (*) the Young's modulus from source [163] was thickness-dependent. Values in bold font are derived from this thesis.

This table reveals that our results are in agreement with those from the theoretical approaches by Liu *et al.* [18] and by Yang *et al.* [160] as well as with those from the experimental work by Tao *et al.* [162]. However our results are in clear disagreement with those from the publication by Wang *et al.* [163]. The lower values we obtained compared to those from most of theoretical works, can be explained in terms of deviations of ideal conditions in our experiments. For instance, in the flakes there could be defects, not visible wrinkles or cracks as well as stacking faults, that reduce the value of mechanical parameters.

Finally, comparing with **other materials**, black phosphorus has a much lower elastic modulus than, for example, graphene, steel and MoS_2, and lower yield strength than that of graphene and MoS_2 (see table 3.2). Remarkably, BP owns a breaking strength higher than that of steel, and similar to that of PDMS. This fact together with its lower E_{3D}, its electrical properties and anisotropy makes black phosphorus a suitable substitute of conventional narrow gap semiconductors in devices requiring thin, flexible, and quasitransparent material.

Material:	Graphene[44]	MoS_2[200]	Steel[190]	BP[179]	PDMS[201]
E_{3D}(GPa):	1000	270	200	46	~0.6
σ^{3D}_{max}(GPa):	130	23	0.5	2.4	2.2

Table 3.2: Comparison of mechanical properties of several materials.

3.7 EVOLUTION OF MECHANICAL PROPERTIES IN AMBIENT ATMOSPHERE

Subsequent to mechanical characterization in HV conditions, measurements in ambient atmosphere were performed. Once the samples were exposed to ambient conditions, measurements separated by intervals of few hours were carried out in each membrane. The relative humidity (RH) was ~47% and the room temperature (RT) ~22°C. This scheme allows monitoring the evolution of E_{3D} with the exposure time to ambient conditions.

3.7.1 *Evolution of BP topography in ambient atmosphere*

As previously reported [170], our **AFM topographic images** of BP drumheads showed significant **changes as a function of time** of ambient exposure. Figure 3.20 displays AFM images showing the evolution of the topography of a representative BP flake with exposure time. As a consequence of water absorption, there is a random population of protrusions increasingly covering the surface. It should be noticed the difference between bubbles, that were present immediately after sample preparation, and protrusions originated by moisture.

The water adsorption that takes place during the exposure to atmospheric conditions seems to be somehow **dependent on the flake thickness**. This is shown in figure 3.21, where the flake shows different topographic features depending on its thickness. Before exposure, the thickness of the flake was around 6 nm in the area covered by blobs while the flat part of the flake was 4.5 nm thick. Therefore, during exposure to air, the measure of the real thickness of BP flakes by AFM becomes infeasible.

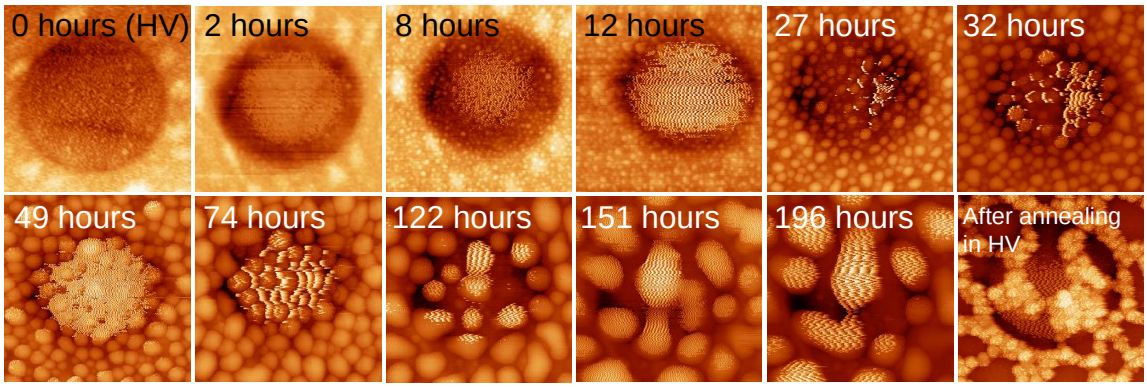

Figure 3.20: Evolution of a BP drumhead topography under ambient conditions. Set of AFM images of a 7.5 nm thick BP drumhead under the exposure to ambient conditions (from 0 h of exposure, i.e. HV conditions, up to 196 h of exposure followed by annealing at HV). The size of the images is 1.5 × 1.5 μm^2.

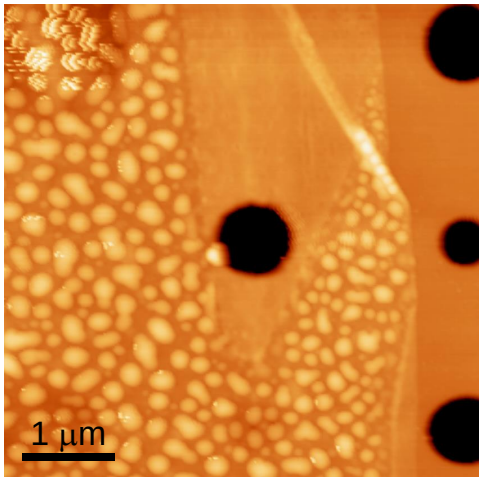

Figure 3.21: AFM topography of a flake after being exposed 120 h to atmosphere. Previous to the exposure, the flake had a thickness of 6 nm in the area covered by blobs while the rest had a thickness of 4.5 nm. The drumhead was spontaneously broken during the exposure to air.

3.7.2 *Analysis of the indentation curves acquired at air*

For the **analysis of the nanoindentation curves** acquired under atmospheric exposure, the **large indentations' fitting method** described above was used. Specifically, the indentation curves were fitted to a **complete third order polynomial in** δ (equation 3.9), that yielded much lower fittings errors than those of a fitting to a polynomial with only terms in δ and δ^3. Furthermore, the fitting error increased with time of exposure to atmospheric conditions (see figure 3.22). This figure also shows the decrease of the error once the sample is cleaned in vacuum through annealing (data inside a black circumference). This suggests that the protusions of adsorbed water causes the error increase, hampering the determination of the zero indentation point of the membrane. For that reason we used a complete third order polynomial fitting, which is not affected by the error when fixing the zero displacement point, as we saw in section 3.4.1.1.

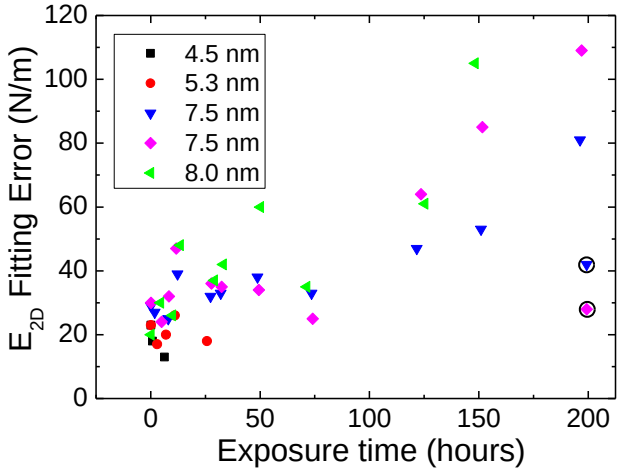

Figure 3.22: Error of the fitting of the indentation curves to a full third polynomial *vs.* the time of exposure. The data plotted at 0 h were acquired in HV (before exposure), and the ones inside a black circumference after the entire exposure and final annealing in HV.

3.7.3 *Evolution of the Elastic Modulus in Ambient Atmosphere*

The results of the evolution of the **elastic modulus** with the time of exposure to atmosphere are summarized in figure 3.23. Panel (a) shows several indentation curves acquired at increasing exposure time on a 5.3 nm thick flake. It is plain to see that the elastic modu-

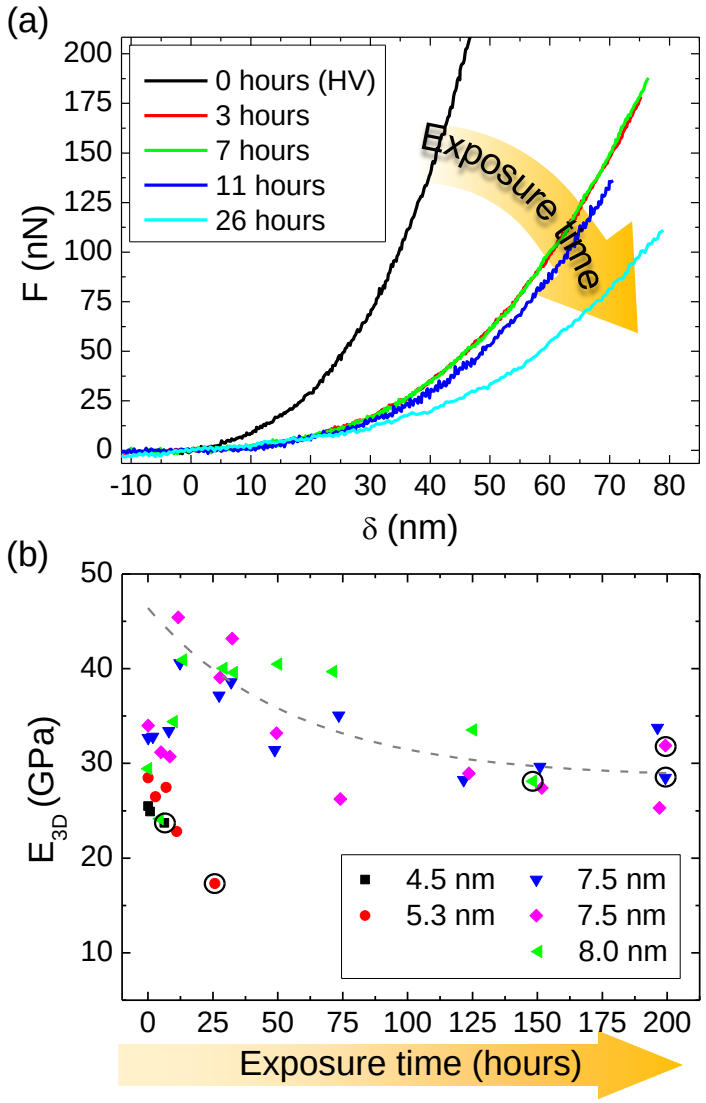

Figure 3.23: Evolution of the mechanical properties of BP drumheads under ambient conditions. (a) F(δ) curves for a 5.3 nm thick BP drumhead in HV after 3, 7, 11 and 26 h of exposure. In the last indentation (after 26 h) the drumhead broke. (b) E_{3D} *vs.* the time of exposure to atmosphere and after heating in HV. Data points sharing color and shape correspond to the same BP drumhead, whose thickness is indicated in the legend. The data points plotted inside a black circumference correspond to the last set of indentations on each drumhead, after that the drumhead broke. The data at 0 h are acquired in HV, and the two last data, at almost 200 h (and inside a black circumference), are acquired on two drumheads after the whole exposure (~200 h) and the subsequent heating in HV. The dashed line is the fitting of data from flakes thicker than 7 nm to a model proposed in section 3.7.5.

lus highly decreases with time in this case. The **elastic modulus** *vs.* time of exposure to atmosphere are depicted in figure 3.23(b) for that drumhead (red dots) and four more, whose thicknesses are in the legend. The evolution of the E_{3D} for the 4.5 nm thick flake (black squares) also shows a high decrease with exposure, and broke soon. Therefore, **flakes with thickness below 6 nm show a clear tendency of decreasing elastic modulus** when exposed to air, reaching a decrease of a factor of almost two at 24 h of exposure to ambient. However, **BP flakes with thickness above 7 nm show a minor reduction of its elastic modulus**. This is evidenced in the rest of the data shown in figure 3.23(b). This kind of response **suggests the growth of a passivation layer**. Passivation is the creation of a thin inert layer on a surface of a material. It spontaneously occurs in some materials, like many metals, when they come into contact with an external agent [202]. An example is the formation of alumina (Al_2O_3) on aluminum surface in air. Moreover, black phosphorus has been reported to form oxidized species in the presence of oxygen [151], which can lead to passivation of its surface. For all this we have considered a simple passivation process (see section 3.7.5). According to this model, an exponential decay fitting of these three sets of data (blue, pink and green symbols) is depicted by a dashed line.

We do not have the evolution of the **breaking strength** with the exposure time (that would mean breaking many drumheads, being no longer available for future experiments). The 4.5 nm thick flake spontaneously broke after the first 10 h of exposure, which is already indicative of a reduction of its breaking strength. Furthermore, all the flakes studied under ambient conditions, broke at forces well below forces that were previously supported. We were able to acquire the fracture force of two 7.5 nm thick flakes once they were exposed ~200 hours to air and subsequently annealed in high vacuum at 230°C during 15 h. The breaking strength obtained from those measurements yielded a σ^{3D}_{max} (200 h exposed BP) ~1.6 GPa, that is $0.66 \cdot \sigma^{3D}_{max}$(pristine BP).

In brief: the **main conclusions** derived from our latter experiments are three: (i) the elastic modulus of flakes thicker than 7 nm is slightly reduced (inspite of the substantial changes of the BP topography in air), (ii) BP flakes thinner than 6 nm, experience a significant decrease of their E_{3D} upon exposure to ambient conditions, and (iii) for both thickness ranges the rupture forces seem to decrease with the ambient degradation.

3.7.4 *Flakes' Thickness in Ambient Atmosphere*

The elastic modulus of the flakes upon degradation yields the magnitude $E_{2D} = E_{3D} \cdot t$. For the results plotted in figure 3.23(b), the value of thickness, t, used to derive E_{3D} is the height of the flake measured by AFM under high vacuum conditions. Upon exposure to atmosphere this magnitude becomes experimentally inaccessible for some time, i.e. the topography of the flakes reflects a growing height due to water absorption on the flakes that does not correspond to their actual thickness. Hence, the decrease of elastic modulus observed in our measurements might be ascribed to two different physical origins: (i) an inherent decrease of the E_{3D} of the material and/or (ii) a decrease of the thickness of the membrane. In order to investigate these effects the samples were annealed in high vacuum at 230°C during 15 h. Following previous works, under these conditions a removal of adsorbed water occurs. This allows measuring the real thickness of the flakes. According to our AFM images before and after annealing (see figure 3.24) the change in thickness is negligible, suggesting that a decrease of the intrinsic elastic constants is taking place

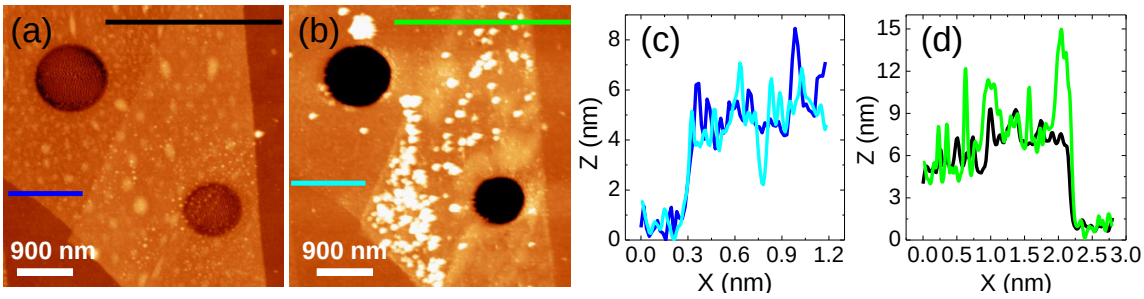

Figure 3.24: Topographic changes in BP flakes after nearly 200 h of exposure to ambient conditions and annealing in HV. (a) Topography AFM image (the same one as figure 3.5(c)) of a BP flake in HV, before the exposure to atmosphere. (b) Topography AFM image of the same flake, acquired in HV at RT but once the sample has been in contact to air for almost 200 h, and subquently heated in HV. There are some left-over residues. Both membranes appear broken due to indentations experiments performed until rupture in HV before exposure to air. (c) Topographic profiles along the blue and cyan lines in (a) and (b). (d) Topographic profiles along the black and green lines in (a) and (b).

during exposure to atmospheric conditions. This agrees with the reduction of the breaking strength measured after annealing.

3.7.5 *Passivation Model*

This decrease in E_{3D} could be attributed to the passivation of the outer layers of the BP flakes leading to phosphorus oxide layers [151] with a lower elastic modulus than that of pristine BP. Therefore, we consider a simple passivation model. It is based in the following **assumptions** (see figure 3.25(a)):

1. The total thickness of every BP flake during the entire exposure time is constant and equal to the initial thickness of the BP flake measured in high vacuum before the passivation process starts (t_{BP}^{ini}):

$$t_{BP}^{ini} = t_{pass}(\tau) + t_{BP}(\tau) = constant \tag{3.11}$$

   where τ is the exposure time, t_{pass} the thickness of the outer passivated BP and t_{BP} the thickness of the underlying pristine BP flake. This assumption is supported by the experimental preservation of flakes' height shown in figure 3.24.

2. The growth of the passivation layer takes place at a speed that exponentially decays with time, i.e., the passivation process experiences saturation, having a maximum passivation depth, t_{pass}^{max}. This is suggested by the data of thicker flakes at advanced exposure in figure 3.23(b). This leads to the following relations:

$$t_{pass}(\tau) = t_{pass}^{max} \cdot [1 - exp(-\tau/\tau_c)] \tag{3.12}$$

$$t_{BP}(\tau) = t_{BP}^{ini} - t_{pass}(\tau) \tag{3.13}$$

where τ_c is a passivation characteristic time.

3. The elastic moduli of the pristine and passivated BP are constant with time and equal to E_{3D}^{BP} and E_{3D}^{pass} respectively, being $E_{3D}^{pass} = \alpha \cdot E_{3D}^{BP}$, $\alpha < 1$. According to [158] a value of α = 0.66 is expected for phosphorene, considering the average of the elastic modulus of both in-plane directions at two stages: when the oxidation ratio is 0% and 100%.

4. The E_{2D} of a layered material is the sum of the E_{2D} of each layer ($E_{2D} = E_{2D}^{BP} + E_{2D}^{pass}$) (negligible inter-layer interactions).

Considering assumptions above and that the magnitude that is obtained from our measurements is $E_{2D} = E_{3D} \cdot t = E_{3D}^{BP} \cdot t_{BP}(\tau) + E_{3D}^{pass} \cdot t_{pass}(\tau)$, the **elastic modulus measured during the exposure time** is:

$$E_{3D}^{measured}(\tau) = \frac{E_{3D}^{BP}}{t_{BP}^{ini}} \left\{ t_{BP}^{ini} - t_{pass} \left(1 - \alpha\right) \left[1 - exp(-\tau/\tau_c)\right] \right\} \tag{3.14}$$

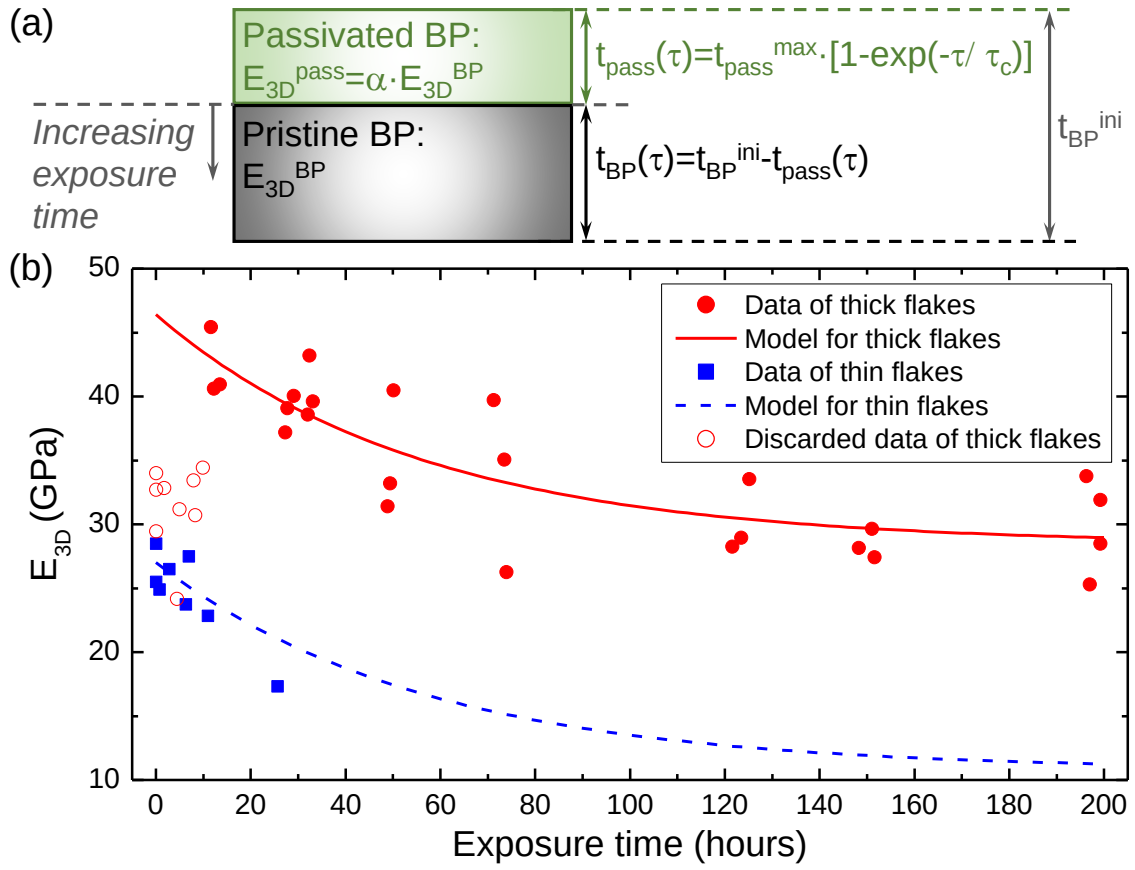

Figure 3.25: Passivation model proposed for few-layer BP flakes. (a) Diagram of the passivation model proposed herein. (b) Temporal evolution of the elastic modulus of few-layer BP flakes under exposure to ambient conditions. The symbols correspond to experimental data (red solid and empty dots for drumheads thicker than 7 nm, and blue solid squares for drumheads thinner than 6 nm). Red line corresponds to the fit of the red solid dots to the proposed model and the dashed blue line depicts the model for the thinner flakes.

The **initial increase in the elastic modulus** of the thicker flakes in figure 3.23(b) is in agreement with the evolution of E_{3D} of phosphorene under oxidation process according to Hao *et al.* [158]. In this reference an increase of E_{3D} in the armchair direction until an oxidation ratio of 25% is ascribed to small relaxations of phosphorene that occur due to chemisorbed oxygen atoms. This increase is not observed in our data of the thinner flakes, probably because it took place in the short exposure prior to the measurements in high vacuum. We will discuss it in the next section.

Figure 3.25(b) shows the evolution of the elastic modulus of exposed drumheads with the exposure time. There are **two sets of data**. One corresponds to the flakes thicker than 7 nm of figure 3.23(b), whose average thickness is 7.6 nm, plotted with red empty and solid dots. The second set comprises the data of the flakes thinner than 6 nm of figure 3.23(b), with an average thickness of 4.9 nm, plotted with blue solid dots. In order to fit the data to the suggested model, firstly, only the data of the thick drumheads are considered, since they present a longer evolution. The data acquired in the first 10 hours (empty triangles) are discarded to avoid the aforementioned increase of E_{3D} at low oxidation rates. Hence, the solid triangles are fitted to the exponential decay expression of $E_{3D}^{measured}(\tau)$ given above. The following values are fixed: $t_{BP}^{ini} = 7.6$ nm (average thickness of thick flakes) and $\alpha = 0.66$ (reported by [158]). This fitting, depicted with a red line in figure 3.25(b), yields an **elastic modulus for pristine BP of $E_{3D}^{BP} = 46 \pm 5$ GPa**, a **maximum passivation depth of $t_{pass}^{max} = 9 \pm 5$ nm** and a **passivation characteristic time of $\tau_c = 60 \pm 20$ hours**. The value for elastic modulus of pristine BP coincides with the one measured in vacuum environment in section 3.6.1. For the thinner flakes, we use the obtained values for t_{pass}^{max} and τ_c while we use $t_{BP}^{ini} = 4.9$ nm (average thickness of thin flakes), $E_{3D}^{BP} = 27$ GPa (provided by the intercept of the linear fit of the first seven data) and $\alpha = 0.66$ again. In this case the blue dashed line in figure 3.25(b) is obtained.

The proposed model and the characteristic values obtained from it, result in some **important consequences**. Firstly, all the flakes considered in this section, after a long enough exposure, would be completely oxided, considering that their thicknesses are lower than the maximum passivation depth. Secondly, and more important, every few-layer BP nanosheet thicker than 9 nm would undergo a passivation process until the passivated layer reaches that thickness, similarly to the natural passivation of some other materials such as stainless steel, aluminum, cooper, etc. However, this expected behaviour could deviate from some other actual tendencies due to the dispersion of our data. In fact, this model would not apply for very thick BP flakes (around 100 nm or more), in which water ends covering the BP surface causing a layer-by-layer etching as was reported in [170] and confirmed by us through some optical images of flakes thicker than 100 nm. Moreover, the presented model does not consider the likely circumstance of having passivation on the underside of the flake, nor simultaneously passivation and etching processes. This later situation was not reflected by our experimental results in few-layer BP flakes.

3.7.6 *Oxidation Hypothesis*

According to our model, the maximum of the elastic modulus should occur at 0 h of exposure. However, the experimental results for flakes thicker than 7 nm show an **increase of E_{3D} for low exposure times**. This behavior was theoretically predicted for phosphorene oxide by Hao *et al.* [158] as we had already anticipated.

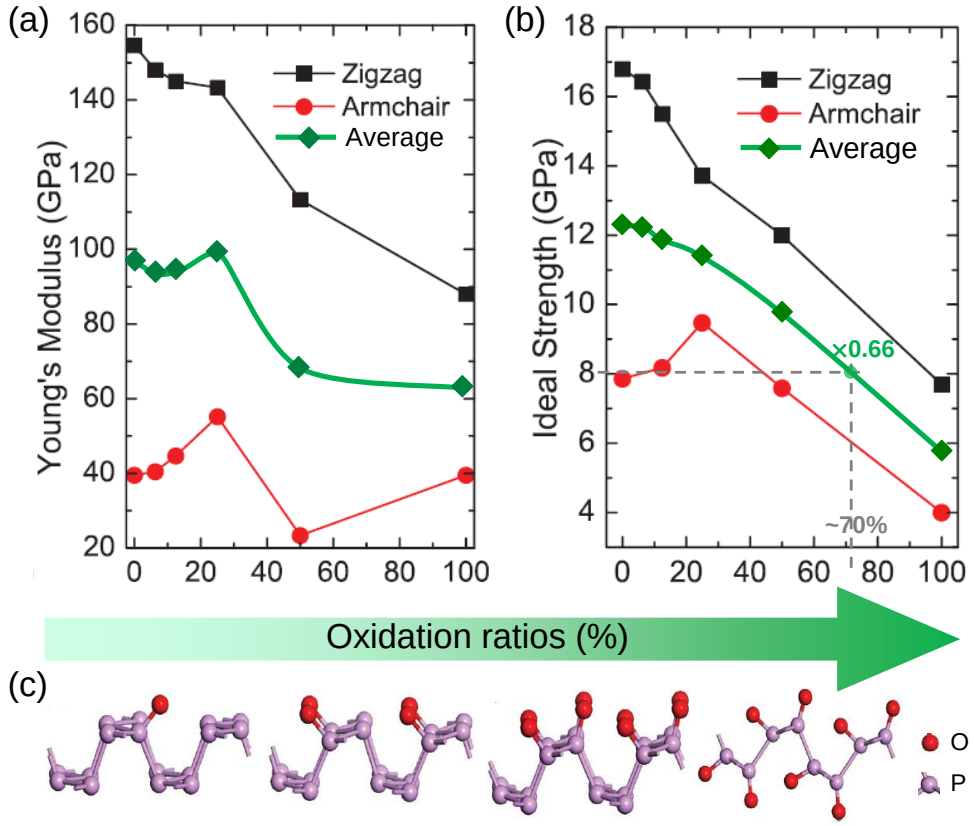

Figure 3.26: Influence of oxidation in the mechanical properties and structure of phosphorene. (a) Elastic modulus of phosphorene with increasing oxidation ratios. (b) Breaking strength of phosphorene under different oxidadtion ratios. (c) Phosphorene oxide structure with various oxidation ratios: 6.25%, 25%, 50% and 100%. Adapted from [158]. Green curves in (a) and (b) were computed to compare with our experimental data.

It is known by experimental works that the moisture and oxygen in air, lead to the formation of oxidized phosphours species [172]. In [158] the Young's modulus of phosphorene is computed for the two in-plane directions as the phosphorene oxidizes. That is depicted in figure 3.26(a). Panel (c) of the same figure depicts one BP layer with an increasing number of oxygen atoms bonded to phosphorus atoms. The oxidation ratio, that appears in the X axis, is simply the number of bonded oxygen atoms divided by the number of phosphorus atoms. We average the results of both in-plane directions, obtaining the green curve, that can be compared with our experimental results. We carry out this comparison assuming that, as the exposure time increases, the number of bonded oxygen atoms increases too (maybe not linearly but both increase).

Comparing our results with the ones by Hao *et al.*, we see that the **thick flakes** have approximately the same behavior as the theoretical prediction:

- For **low times** there is a **small increase of** E_{3D}, this is explained in [158] in terms of small relaxations of phosphorene due to chemisorbed oxygen atoms.
- For **higher times the** E_{3D} **decreases and finally saturates**, this is attributed to the fact that the oxygen atoms affect the strength of phosphorus-phosphorus bonds, and they can substantially change the structure of the phosphorene [158].

The **thinner flakes**, on the contrary, do not follow the theoretical prediction. Indeed, the experimental elastic modulus we measure for thinner nanosheets decreases during the whole exposure. Furthermore, Hao *et al*. predict, for oxidation ratios below 10% a very sligth decrease of E_{3D}, which is not reflected by the experimental data of thick flakes. The reason behind both discrepancies could be connected with the content of **oxygen at the beginning of the experiments**. When the samples are kept in vacuum they have been exposed to ambient conditions for less than 2 hours. After that time some oxygen atoms could have been bonded to the BP flakes, so the **starting point** in our experimental plots of E_{3D} *vs.* time of exposure corresponds to a **non-zero oxidation ratio** (see figure 3.27):

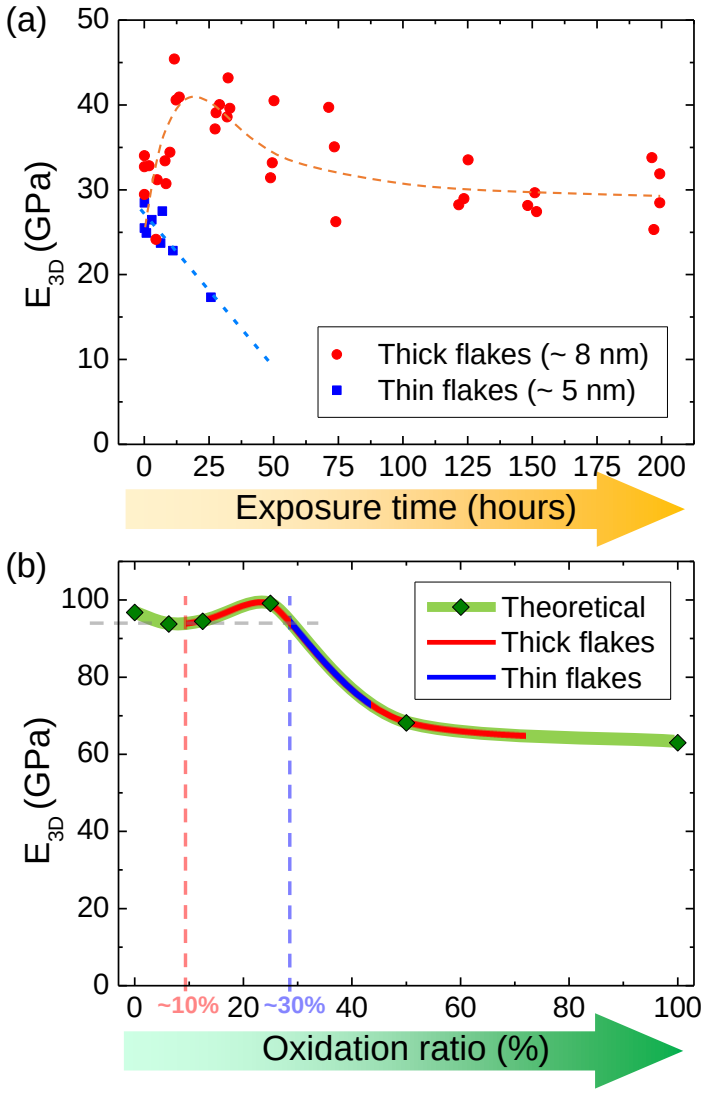

Figure 3.27: Comparison experimental and theoretical Young's modulus evolution. (a) Experimental E_{3D} *vs.* exposure time highlighting the two kind of thicknesses measured. Dashed lines are simply guides to the eye. (b) Theoretical evolution of E_{3D} *vs.* oxygen content (green curve). Red and blue lines marked the tendencies followed by the experimental data for flakes of both thicknesses, from whose beginning the oxygen content can be estimated. The absolute values of the elastic modulus are not taken into account.

- For the case of **thick flakes** the begining of our experimental plot should be **around 10%**. This is based on the fact that from a 10% oxidation ratio E_{3D} slight increases, then decreases and finally saturates.
- For the **thin flakes** the initial oxidation ratio seems to be higher, **around 30%** (from that value we found the decrease of the elastic modulus). For longer exposure times our thinner flakes unfortunately broke.

The latter hypothesis concerning the oxygen content at 0 hours makes sense: the thinner flakes exposed to ambient conditions for the same interval of time, will have proportionally higher content of oxygen than the thicker ones.

For the **breaking strength** the theoretical results from [158] reveal a dramatic **decrease** with the oxidation ratio (see figure 3.26(b)). As stated before, we measured the values of σ_{max} in HV (pristine BP) and after 200 hours of exposure to air, for 7.5 nm thick flakes. Their breaking strength has a **a reduction factor of 0.66** after the whole exposure to ambient conditions (from 2.4 GPa to 1.6 GPa). This reduction corresponds to an **oxidation ratio of 70%** according to figure 3.26(c). Remarkably, the reduction factor of the **elastic modulus** with an oxygen content of 70% is predicted to be around 0.66 as well, which is exactly the reduction of the experimental Young's modulus we obtained for very high exposure times (from 46 GPa measured in HV to around 30 GPa measured for long exposures).

3.8 CONCLUSIONS

In this chapter we have reported on the mechanical properties of few-layer black phosphorus in two environments: high vacuum and air ambient conditions. Indentation experiments performed at high vacuum yield elastic modulus of 46 ± 10 GPa and breaking strength of 2.4 ± 1 GPa. The elastic modulus barely decreases in atmospheric conditions for thick flakes, however, we found a clear decreasing tendency for the thinnest flakes measured in our experiments. These results are compatible with previous works where the variation in the mechanical properties is ascribed to the oxidation of black phosphorus in air. They suggest a ~70% oxygen content in our thick flakes after 200 hours of exposure, based on the reduction of the elastic modulus and breaking strength in those BP sheets.

4

A NEW METAL-ORGANIC ULTRATHIN FILM WITH OUTSTANDING PROPERTIES

4.1 INTRODUCTION TO COORDINATION POLYMERS AND MOTIVATION OF THE CHAPTER

4.1.1 *Coordination Polymers*

Coordination polymers (CPs) [203], also named metal-organic polymers, consist of **metal centers** linked by **organic ligands** via **coordination bonds**. A coordination (or coordinate) bond is the donation of a lone electron pair of the ligand to the metal cation and the electrostatic attraction between that cation positively charged and the negatively polarized or charged donor atom of the ligand [204]. The CPs can extend in one, two or three dimensions (see figure 4.1). Although the existence of coordination bonds is essential in the formation of the CPs, other kind of non-covalent interactions (**supramolecular interactions** such as hydrogen bonding, $\pi - \pi$ interactions, van der Waals forces, electrostatic forces, etc.) can also be present being decisive in the nature of the CPs [204].

The first use of the term "coordination polymer" may be traced to J. C. Bailar in 1964 [206]. However, the crucial momentum of CPs took place in the 90's with the works by Kitagawa [207] and Yaghi [208] with the raise of the so-called MOF (metal-organic frameworks). MOFs are a subclass of CPs that contain porous in their structure. From then, MOFs started to be considered as an emerging class of materials with promising properties. In recent decades, the study of these compounds has stablished as a consolidated scientific discipline that continues to grow today.

The **structure and properties** of CPs are governed by their building blocks (their metal centers and organic ligands) and by the interactions among them. By a molecular recognition and **self-assembly** process, the building blocks are joined together in a selective manner (see figure 4.1). Thus, by understanding these interactions, and selecting the proper building blocks, one can **rationally predict, design and synthesize** new CPs with fascinating structures and functionalities. Therefore, coordination polymers offer the possibility of creating *à la carte* compounds based on modular chemistry. Much work in this field has shown coordination polymers as promising candidates in several applications,

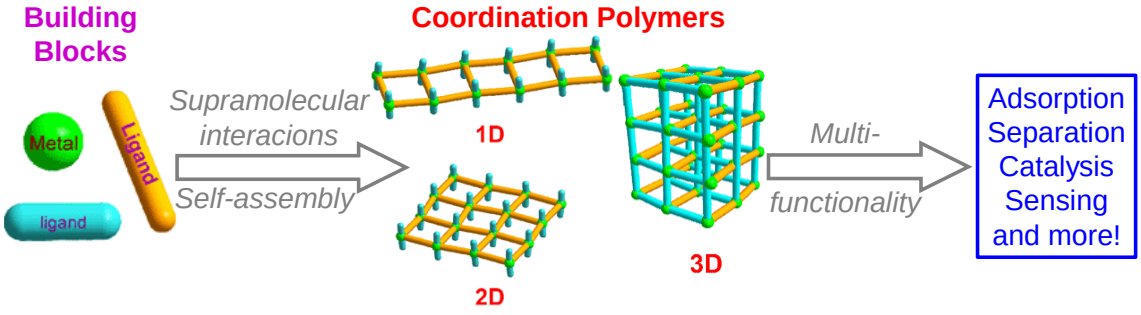

Figure 4.1: Formation and common properties of coordination polymers. Adapted from: [205].

including adsorption, separation, catalysis, magnetism, sensing and hostguest chemistry [209, 210].

Among coordination polymers, very few exhibit **electronic transport**. However, in the last decade, some conductive CPs have been found in our closest scientific environment [211, 212]. Even so, their conductivity is well below than that of other 2D inorganic crystals, such as graphene, MoS_2 or indium tin oxide. But CPs present the remarkable benefit that their electrical properties can be tuned by chemically altering the linker or the metal ion [213]. Furthermore, experimental results and theoretical calculations provide indications that CPs might be suitable as semiconductors in future electronics [214]. In addition to their chemical versatility, CPs allow a larger variety of structures than inorganic crystals with different dimensionalities and properties.

Regarding the **mechanical robustness** of 2D coordination polymers, although nanoindentation is becoming a more common tool to characterize single CPs thin films, very few have been characterized in depth [215, 216]. The higher expected flexibility of CPs compared to inorganic functional materials could be an unexpected advantage. With increasing attention for flexible and wearable devices, elasticity is a highly desired property [213].

The main **current challenges** in this field rely in combining **processability** and the desired electrical, optical and mechanical **properties** in a single material to integrate them in future devices. To date, most of the research involving these multifunctional materials has been focused on bulk material, however processability down to lower dimensional forms is still little developed [217, 218]. Some seminal works have already demonstrated 1D metal-organic polymers [211, 212] as well as **CP-nanosheets** obtained by either *top-down* methods [216, 219–221] or *bottom-up* approaches [222–227]. Almost none of these 2D CPs have shown high electrical conductivity. In addition, very few works, if existing at all, have achieved 2D CPs that gather simple synthesis, high processability, and exceptional physical properties.

Previous results of our collaborators have shown that the combination of **copper metal centers with sulfur-containing ligands** as building blocks are able to produce multifunctional materials showing electrical conductivity together with optical emission [228]. Some of these compounds have been investigated in films showing conductivities as high as 1580 S/cm for film thickness of about 200 nm [229]. Nevertheless, future developments depend on the ability to obtain even thinner but robust films to integrate them in flexible electronics devices [213].

4.1.2 *Motivation of this chapter*

The aim of this chapter is to **characterize a new rationally designed coordination polymer** that is expected to be mechanically robust and with promising electrical and optical **properties**. This prediction is based on the nature of its building blocks: copper metal centers and sulfur-containing ligands. Additionally, this compound has a remarkable **processability**: it can be processed in different ways producing 3D crystals and 2D ultrathin films with variable thickness. Superior processability, and remarkable physical properties have been barely joined together in the 2D form of a unique metal-organic polymer. We, therefore, conduct a complete characterization of this compound concerning its structure, different topologies, electrical, optical and mechanical properties, paying special attention to its 2D ultrathin layered form.

The core of this chapter is based on reference [230]: **Miriam Moreno-Moreno**, Javier Troyano, Pablo Ares, Oscar Castillo, Christian A Nijhuis, Li Yuan, Pilar Amo-Ochoa, Salomé Delgado, Julio Gómez-Herrero, Félix Zamora, and Cristina Gómez-Navarro. **"One-Pot Preparation of Mechanically Robust, Transparent, Highly Conductive, and Memristive Metal-Organic Ultrathin Film."** In: ACS nano 12.10 (2018), pp. 10171-10177. This work was performed in collaboration with many people. Javier Troyano synthesized the compound supervised by Félix Zamora and Salomé Delgado. Eventually J. Troyano taught me to perform such synthesis and the processing to obtain 2D ultrathin films of the compound. Christian A. Nijhuis and Li Yuan carried out XPS studies and the out-plane electrical characterization. Pilar Amo-Ochoa synthesized the 3D crystals and performed an initial electrical characterization of them. Óscar del Castillo conducted the crytallographic studies. Pablo Ares performed some potential maps of the films. Cristina Gómez-Navarro conducted some electrical and mechanical measurements and coordinated the whole work with Félix Zamora. Both and Julio Gómez-Herrero conceived the work and designed most experiments. I was the one that performed the majority of the electrical and morphological characterization of the films. In addition, I conducted the synthesis and adsorption on different substrates of most of the films. Moreover, after attending a workshop on Memristive Phenomena, I was able to design complementary electrical experiments.

4.2 INTRODUCTION TO $[Cu_2I_2(TAA)]_n$ COORDINATION POLYMER

4.2.1 *Building Blocks and Structure*

The building blocks that constitute our coordination polymer are simple, industrially available and highly inexpensive: **Copper(I) Iodide** (CuI) and **thioacetamide** (TAA). CuI provides the metal center (Cu^+) and the TAA the organic ligand. Iodine acts as an inorganic ligand. As reported previously by our collaborators [231], the reaction between CuI and TAA yields to a variety of structures that can be tailored by fine-tuning the ratio between the initial building blocks and the reaction speed modulated by the concentration of the reactants and the solvent. Thus, the slow diffusion of an acetonitrile solution of CuI and thioacetamide (2:1) into diethyl ether gives rise to the formation of single-crystals (see figure 4.2).

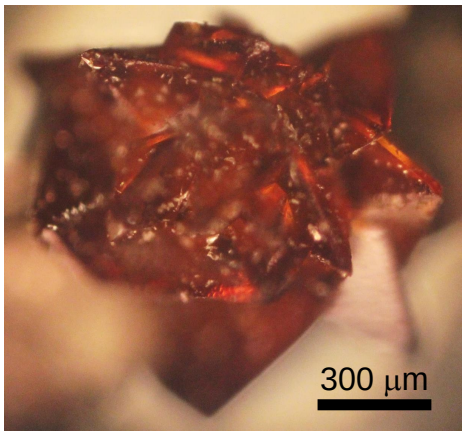

Figure 4.2: $[Cu_2I_2(TAA)]_n$ crystal.

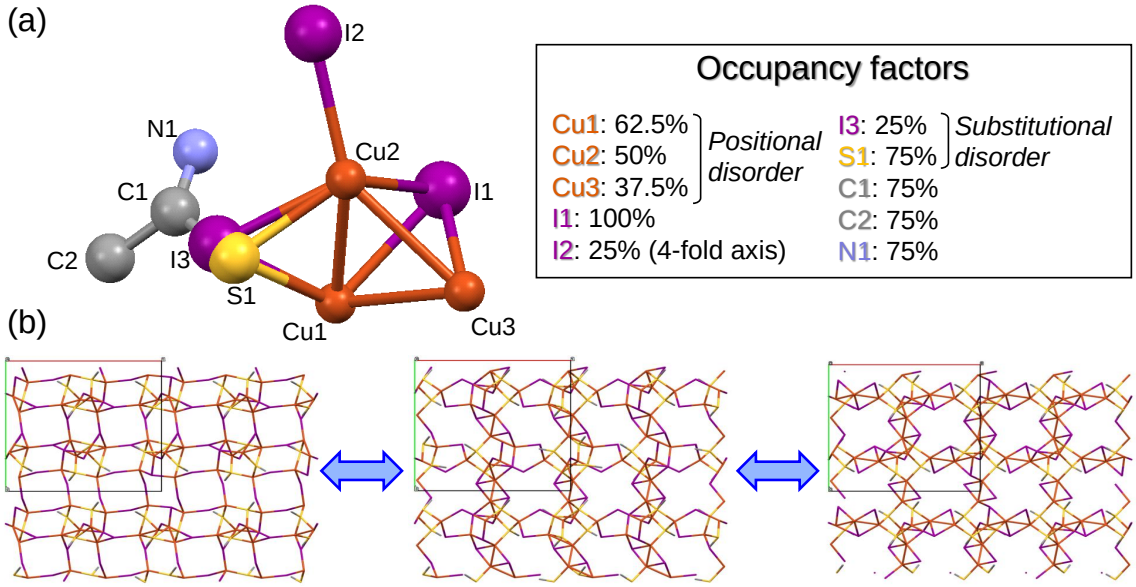

Figure 4.3: Structure of $[Cu_2I_2(TAA)]_n$ compound. (a) View of its asymmetric unit with the occupancy factors. The disorder of the thioacetamide ligand was omitted for sake of clarity. (b) Some plausible ordered models contributing to the highly disordered final crystal architecture obtained from single crystal X-ray diffraction. The colour code used for elements is the same one used in (a).

X-ray diffraction indicates that the crystals correspond to a coordination polymer of formula $[\mathbf{Cu_2I_2(TAA)}]_n$ that presents a notable degree of **structural disorder** (figure 4.3(a)) involving the copper(I) atoms, which are distributed among three positions (*positional disorder*) but also a position in the coordination sphere of the metal center which is shared by an iodide atom (I3) and the TAA ligand (*substitutional disorder*). This degree of disorder makes it difficult to provide a straightforward description of the crystalline structure based on the coexistence of a limited number of ordered arrangements. In fact, the amount of possible ordered models contributing to the mixture is large. In order to represent some of them, figure 4.3(b) provides just three possible structures, which are chemically and structurally compatible with a suitable crystallographic solution. In any case, all the structural models consist of a **three-dimensional crystal structure** build up by means of iodide bridged by tetrahedral copper(I) metal centers with coordination spheres formed by four or three iodides and one sulfur atom from the thioacetamide ligand. The coordination bond distances (Cu-I: 2.51-2.68 Å and Cu-S: 2.31-2.41 Å) are in agreement with the values typically found in the The Cambridge Structural Database [232]. This type of disorder of soft metal centers has been reported for several ionic conductors such as α-AgI, Ag_3SI, and $RbAg_4I_5$ compounds, among others, in which the silver atoms are disordered over many available positions [233–238]. Interestingly, our good quality crystals showed much lower electrical conductivity than that of more amorphous crystals (as we will see in section 4.4.1.2). The unusual X-ray structure found for $[Cu_2I_2(TAA)]_n$ as well as these electrical features prompted us to explore the nanoprocessability of this new material.

4.2.2 *Film Preparation*

To this end, we carried out a direct reaction at the **water-air interface** upon addition of 50 µL of an acetonitrile solution of the two simple building blocks, CuI and TAA, in 2:1 ratio (figure 4.4(a)). Immediately after that, we observed a transparent film on the water surface. We used Langmuir-Schäfer technique (*fishing*) to deposit the film on a variety of substrates such as Si/SiO_2, fused quartz, or glass (figure 4.4(b) and (c)). Inspection under an optical microscope of deposited films on substrates of Si with thermally grown SiO_2 of thickness 300 nm (figure 4.4(b)) shows the formation of **thin films with coverage higher than 85% through mm^2** scale areas. UV-VIS spectroscopy of ~20 nm thick films prepared on quartz substrates (figure 4.4(c)) revealed that their **transparency was > 80%** for the whole visible window (figure 4.5(a)). X-ray analysis of the as-formed $[Cu_2I_2(TAA)]_n$ films deposited on SiO_2 agrees with that determined for the material prepared as a single crystal, therefore confirming its structure (figure 4.5(b)). Although the coordination bond sustained 3D architecture, the synthetic approach determines the crystal growth to be limited to the water-air interphase affording this compound in the form of ultrathin sheets. Spectroscopic and analytical data confirm that the films show a similar structure and composition to that found in the $[Cu_2I_2(TAA)]_n$ single crystals (see appendix D). The **thermal stability** of the films agrees with that observed in the bulk confirming no thermal degradation below ~170 °C in an inert atmosphere (see appendix D).

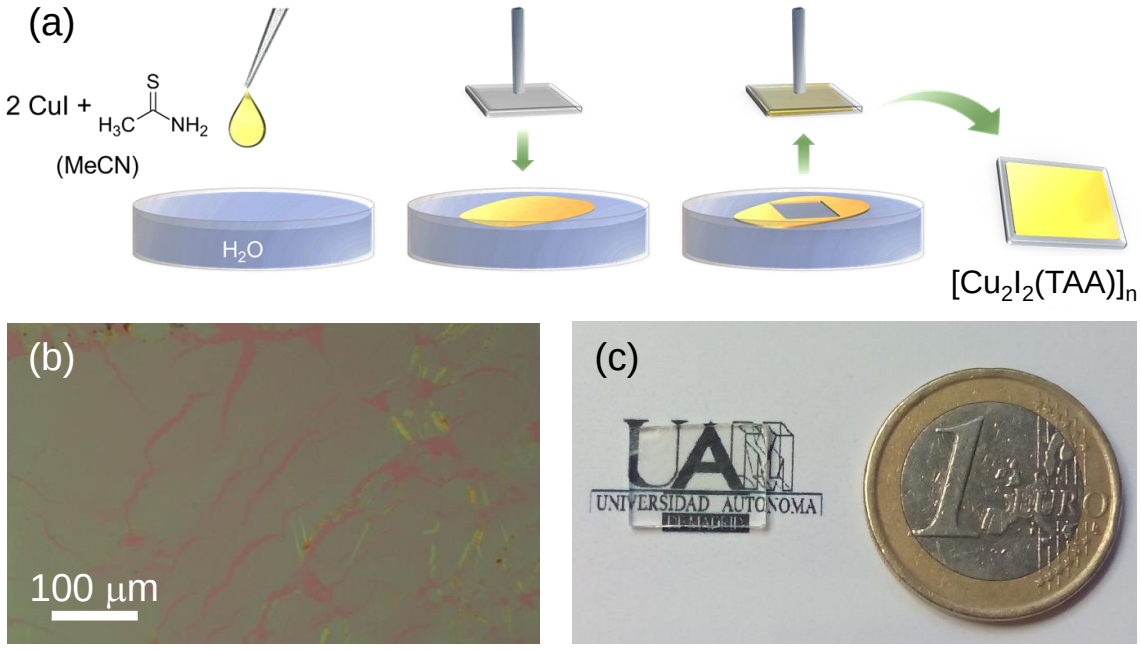

Figure 4.4: Preparation of $[Cu_2I_2(TAA)]_n$ films on substrates. (a) Scheme of the film preparation at the water-air interface and the Langmuir-Schäfer technique used to collect it on surfaces. (b) Optical image of a representative sample deposited on a SiO_2 substrate. (c) Photograph of a film collected on fused quartz with 1 € coin as size reference. The transparency of the film is evident.

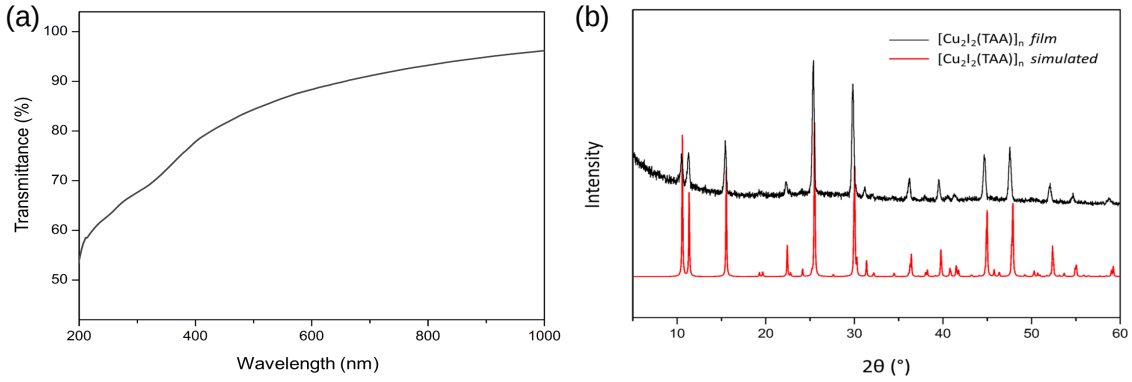

Figure 4.5: Transmittance and XR diffraction of $[Cu_2I_2(TAA)]_n$ films. (a) Transmittance of the film shown in figure 4.4(c) in UV-VIS spectrum. (b) Grazing Incidence XR diffraction (incidence angle, $\alpha = 0.5°$) of a film collected on SiO_2 (black) and its comparison with that calculated from the single crystal X-ray diffraction data (red).

4.2.3 *First observations that triggered our research*

In the first films we obtained, we made a quick measurement of their electrical resistance using graphite paint as electrodes, glass as substrate, and a simple multimeter, as it is shown in figure 4.6. We surprisingly obtained a vey low value of the resistance: 600 KΩ, that, taking into account the geometry of the film, corresponds to a first conductivity estimation of ~0.5 S/cm. This conductivity and the high transparency of the film (80% in VIS region) constitute essential properties for some technological applications, for instance in touchscreens. To put in context, ITO (indium tin oxide, a compound whose films are widely used in screens and touchscreens) has a conductivity of 10^3 S/cm and a transparency of 90% in the VIS spectrum [239]. In spite of the remarkable properties of ITO, due to the lack of Indium, its production difficulties and its low flexibility, other

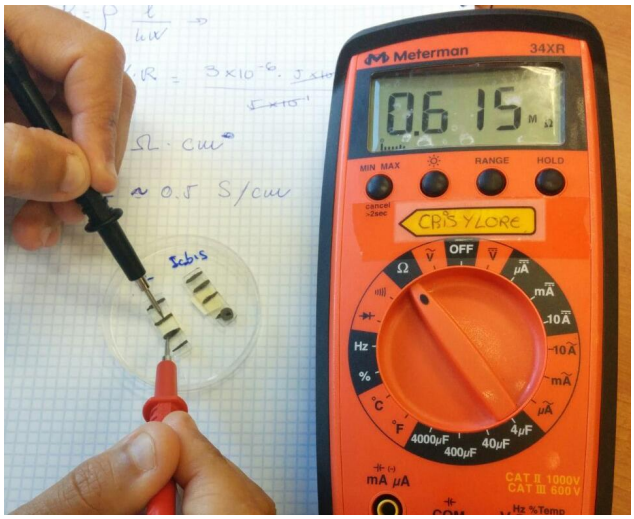

Figure 4.6: Macroscopic measurement of resistance of a $[Cu_2I_2(TAA)]_n$ film. A rough estimation of the corresponding conductivity is written in the notebook. As a historical note the hands in the image correspond to Dr. Pilar Amo.

materials are being researched to replace it such as organic polymers like PEDOT:PSS [240, 241].

4.3 FILM MORPHOLOGICAL CHARACTERIZATION

Atomic force microscopy images, as the one shown in figure 4.7(b) from the rectangle of figure 4.7(a), confirm that these films mostly present thicknesses ranging from 4 to 10 nm. We also found few regions with films of thickness up to 60 nm; the film thickness can be adjusted just by optical inspection of the layers created at the air-liquid interphase during the transfer process to the substrate. Histograms of topographic heights measured in areas of ~100 μm^2 of the films, as that depicted in figure 4.7(c), showed RMS roughness as low as that of the substrate (~1 nm) and similar to that of ITO films [242], indicating extremely smooth surfaces. The roughness of films could be important not only from a morphological point of view, but also from an electrical perspective: it could be related to electrical conductivity, as it has been reported for ITO films [242], the lower the roughness, the higher the conductivity.

The combination of the presented AFM images and **scanning electron microscopy** (SEM) images (see figure 4.8) allows discarding a nanoplatelet structure as reported previously in similar metal-organic films [229].

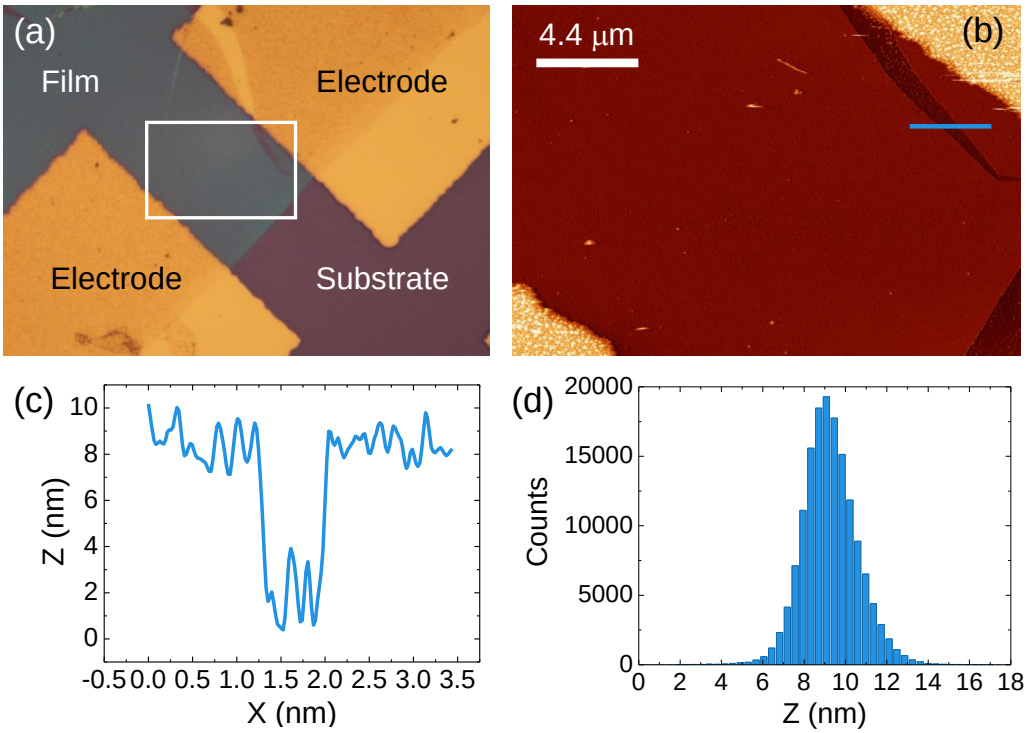

Figure 4.7: AFM topography and roughness analysis of $[Cu_2I_2(TAA)]_n$ films. (a) Optical image of a film contacted by two gold electrodes. (b) AFM topographic image of the area inside the white rectangle in (a). (c) Profile of the blue horizontal line in (b) along the film and a crack in it. From this profile a film thickness of 8 nm is obtained. (d) Histogram of topographic heights of a 10 × 10 μm^2 area in the film shown in (b). The origin of the horizontal scale is arbitrary. From the histogram, RMS roughness of 1.2 nm is derived.

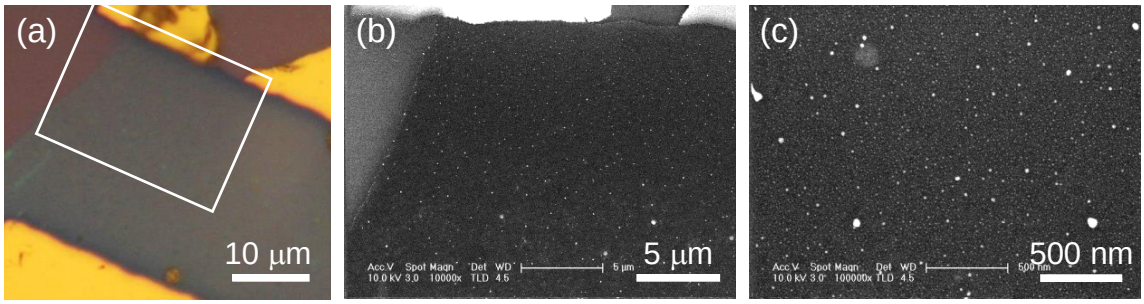

Figure 4.8: SEM images of $[Cu_2I_2(TAA)]_n$ films on substrates. (a) Optical image of an 8 nm thick film with gold electrodes on top. (b) and (c) SEM images with different magnifications of the film inside white rectangle in panel (a). While SEM images, as well as AFM, show some granular structure they allow discarding a nano-platelet structure as reported previously in similar metal-organic films.

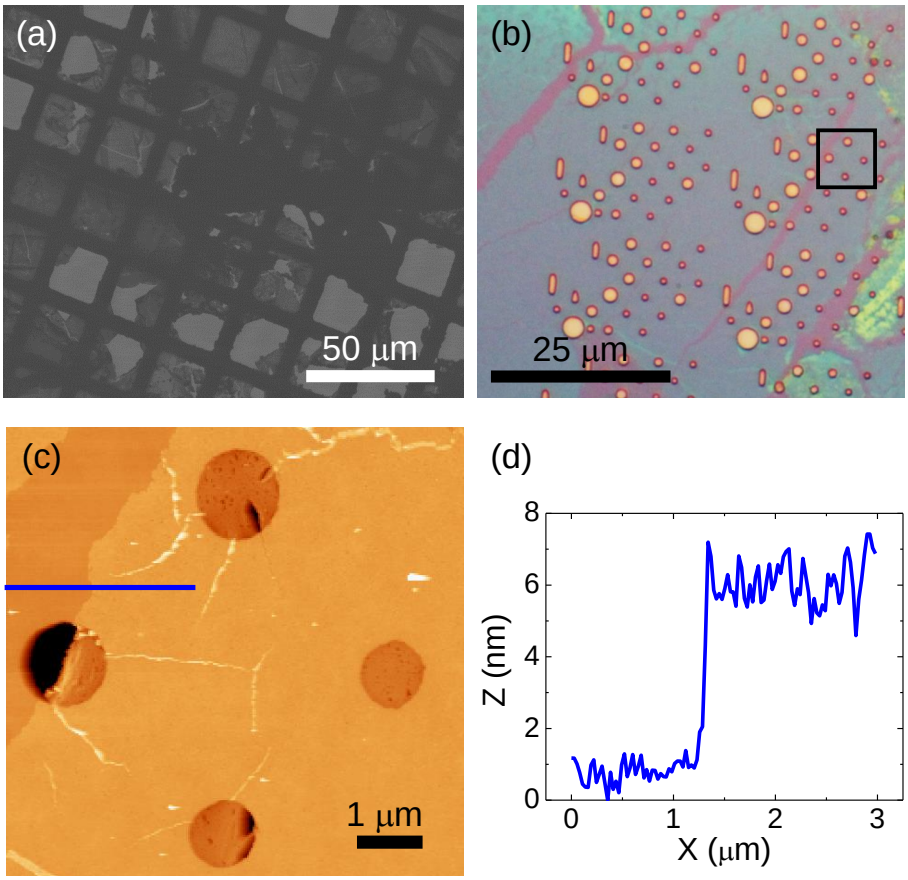

Figure 4.9: Free-standing $[Cu_2I_2(TAA)]_n$ films. (a) TEM image of a film on a regular copper TEM grid. Dark areas correspond to unsupported films. (b) Representative optical micrograph of films suspended over circular wells. (c) AFM image of area inside the square in (b) which shows a 6 nm-thick film suspended over several wells. Here we observe that even those regions presenting cracks remain suspended. (d) Height profile along the blue line in (c).

We also employed the Langmuir-Schäfer technique to deposit the films on regular copper **Transmission Electron Microscopy (TEM) grids** (figure 4.9(a)) and on SiO_2 substrates (figure 4.9(b) and (c)) with **predefined circular wells** with diameters ranging from 0.5 to 3 μm (the same kind of substrates used in chapter 3). Surprisingly, we found that during the Langmuir-Schäfer process, the films were suspended over these holes of SiO_2 substrates not collapsing to the substrate. An AFM image of these microdrums is shown in 4.9(c). The obtaining of these free-standing films is partially indicative of mechanical robustness. Indeed, most 2D materials studied so far tend to collapse or break during transfer to this type of substrate due to capillary forces in wet processes [243]. Surprisingly, graphene oxide, with a much higher elastic modulus than that of these films, tends to collapse. This suggests that the collapse must be related with and additional property, such as the *hidrophobicity* of the material.

Further analysis of compound $[Cu_2I_2(TAA)]_n$, regarding XPS, FTIR spectra and thermal stability can be found in appendix D. In the next sections of this chapter the **electrical** and the **mechanical** properties of films of this coordination polymer will be analyzed in detail.

4.4 ELECTRICAL PROPERTIES OF $[Cu_2I_2(TAA)]_n$ COORDINATION POLYMER: CONDUCTIVITY AND RESISTIVE SWITCHING

4.4.1 *First Measurements of the Electrical Conductivity*

4.4.1.1 *Electrical Conductivity of Films*

After the first coarse measurement of the electrical resistance of the films (figure 4.6), we were willing to measure the conductivity of the films with higher precision. To perform this electrical characterization, we deposited the $[Cu_2I_2(TAA)]_n$ films on highly doped Si substrates (which serves as the gate electrode) with thermally grown SiO_2 of thickness 300 nm. Then, we placed micro- or nano-electrodes at both sides of films. The resulting devices have the geometry schematized in figure 4.10.

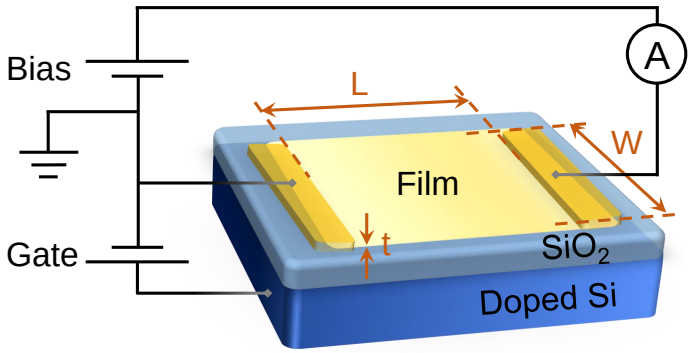

Figure 4.10: Scheme of the setup used to electrically characterize the films.

Once we know the thickness of the film (t), its length (L) between electrodes, its width (W) and its resistance (R), we can compute its electrical conductivity (σ) as:

$$\sigma = \frac{L}{R \cdot S} = \frac{L}{R \cdot W \cdot t} \tag{4.1}$$

assuming constant thickness and width between the electrodes. S is the cross-sectional area of the film.

We electrically contacted the films with **different kind of electrodes** to asses the effect of different metals on the electrical response of the films. We used these electrodes: graphite flakes [244], silver paint, graphite paint, thermally evaporated gold, thermally evaporated silver and the combination of silver in one electrode and gold in the other. Figure 4.11 shows devices with different kind of electrodes. Moreover, the dimensions of the films varied among them: L = 3-400 μm, W= 15-750 μm, t = 4-170 nm.

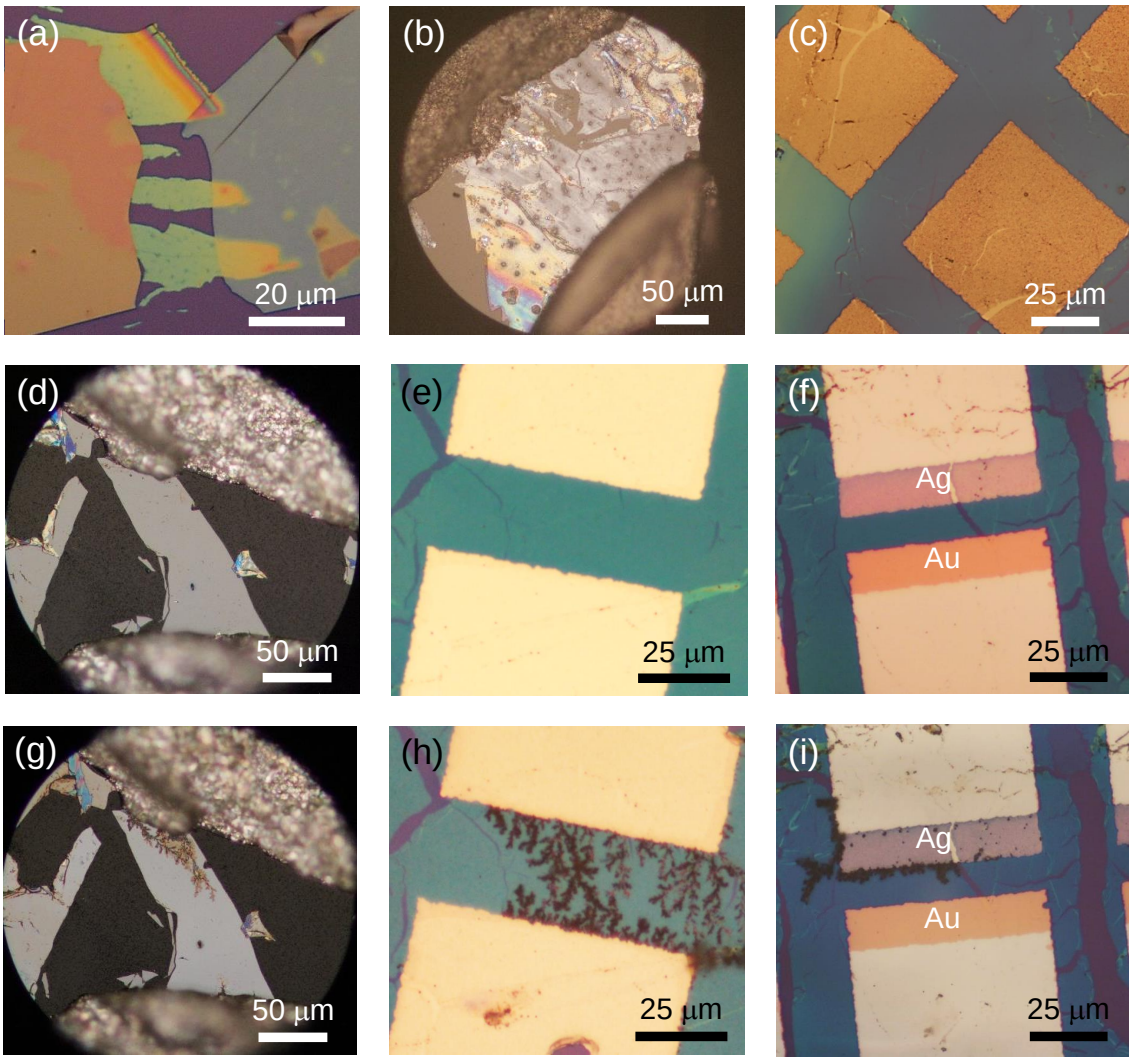

Figure 4.11: Optical micrographs of $[Cu_2I_2(TAA)]_n$ films electrically contacted by different electrodes. (a) 3 ribbons of film contacted by 2 graphite flakes. (b) Film between graphite paint electrodes. (c) Film covered by square gold electrodes. (d) Flake contacted by silver paint. (e) Same as (c) but with silver electrodes. (f) Film covered by electrodes that have a rectangular area with solely silver (marked with 'Ag') and another one with only gold (marked with 'Au'). (g-i) Same devices as (d-f) after performing IVs on them, dendritic paths have emerged. Devices (a-c) look the same after the electrical measurements. Thicknesses of the films/flakes: (a) ~47 nm, (b) ~40 nm, (d) ~25 nm, and ~10 nm for (c), (e) and (f). All the substrates are Si/SiO_2(300 nm) except the ones of (b), (d) and (g) which are glass.

We conducted the first electrical measurements in the manual probe station assembled by Dr. Cristina Gómez Navarro, and then in the variable temperature ambient-controlled motorized probe ptation presented in section 2.2.4.1 (designed and assembled by Dr. Ares and professor Julio Gómez). The probes we used to electricallly contact the electrodes were the commercial straight tungsten probes and the home-made gold probes described in 2.2.4.1. The former to contact silver or graphite paint and the latter to contact the thermally evaporated electrodes. For measuring the electrical resistance (R), we carried out several current (I) *vs.* bias voltage (V_{sd}, V_{sd} or V) curves, from which R is simply V_{sd}/I at a certain voltage. The excitation voltage had triangular waveform: it started at zero, increased until a maximum voltage, then it decreased to the inverse voltage (running through zero) and finally came back to zero finishing a cycle. Having R and by measuring the dimensions of the flake and the distance between electrodes (using the AFM and the optical microscope), we can compute the conductivity with equation 4.1.

The first IV curves we acquired in several films were very different among them. They differed not only in shape but also in the order of magnitude of the current. This leads to a huge **dispersion in the conductivity** (from $\mathbf{10^{-4}}$ **up to 50 S/cm**, and extraordinarily higher than **100 S/cm** using **silver** electrodes). To make it worse, the curves were **not even reproducible** in the same film: they change with time, and forward and backward curve of a IV cycle did not match. We attributed all this to artifacts in the setups and to possible cracks in the films. After perfoming a large number of IV curves in many films, we found out that:

- In the devices in which at least one electrode is made of **silver**, some **paths with dendritic fashion** appeared when performing the IV characteristics. They were visible with the optical microscope, as figure 4.11(g-i) shows. Once a path had connected boths electrodes, the conductivity increased several orders of magnitude leading to linear IVs, as figure 4.12 depicts.
- When flowing **high current densities** through a film, it **eventually degrades** yielding lower conductivity. Therefore we reduced the excitation bias voltage. This is illustrated in figure 4.13(a).
- There were mainly **two kind of IV characteristics**: some films yielded **linear** IVs while others presented **hysteresis** giving loops. The loops have varied widths and shapes, but all loops were pinched at the origin. Figure 4.13 summarizes the casuistry of acquired IVs.

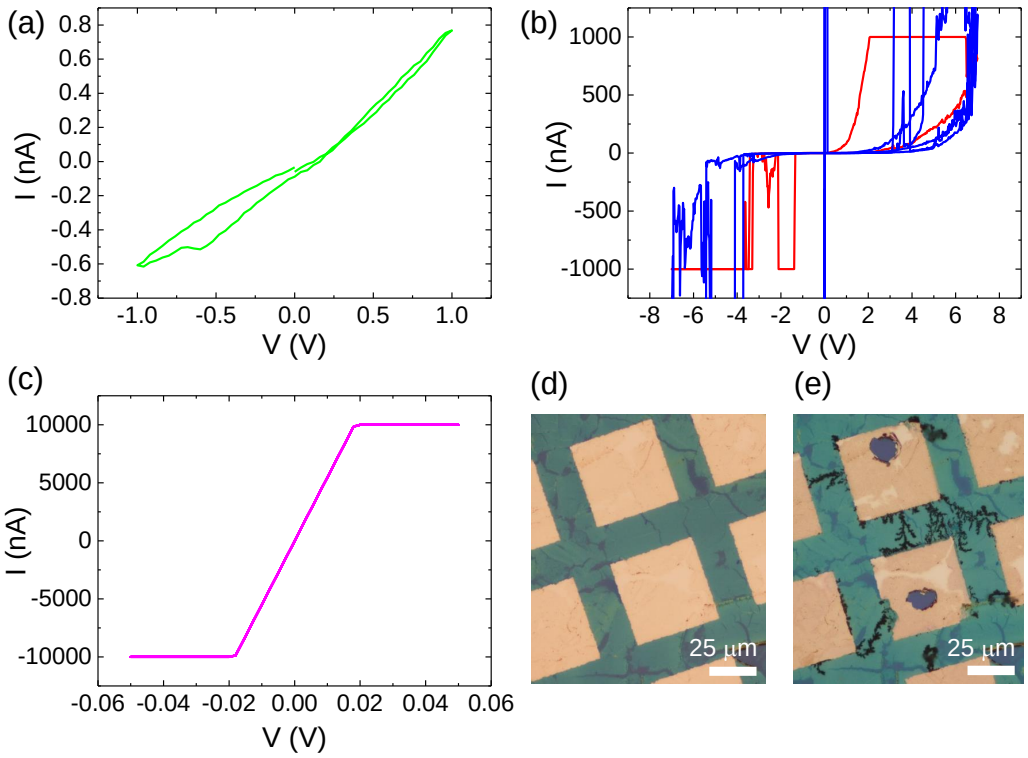

Figure 4.12: IV curves and images of a $[Cu_2I_2(TAA)]_n$ film contacted by silver electrodes. (a) First IV. (b) Second (red) and third (blue) IVs conducted in the same device, at higher voltages. (c) Fourth IV at much lower bias voltage and with a higher compliance current to appreciate the slope of the IV. There is a substantial increase of the conductivity: from $2.3{\cdot}10^{-4}$ S/cm in (a) to 157 S/cm in (c). This increase takes place in the blue IV of (b), in which it suddenly becomes linear with a steep slope (silver paths have connected electrodes). (d-e) Optical micrographs of the device before (d) and after (e) conducting the IVs, revealing the growth of dendrites. Film's thickness ~15 nm.

4.4.1.2 *Electrical Conductivity of Bulk Crystals*

The electrical conductivity of crystals was measured by contacting them with graphite paint, like the crystal shown in figure 4.2, or with the home-made gold probes described in 2.2.4.1, like the crystal depicted in the insets of figure 4.14(a). Electrical characterization of obtained crystals showed that good quality crystals (selected by optical inspection of their morphology) presented conductivity values of 10^{-5} - 10^{-3} S/cm, but crystals with irregular morphology presented values up to 10 S/cm. To corroborate this suggested relation between crystallinity and electrical conductivity, we tested good quality crystals (as indicated by X ray diffraction) and annealed them with the aim of amorphizating the structure, measuring electrical conductivity on the same crystal before and after annealing. The results are gathered in figure 4.14. Panel (a) shows the **amorphization of a crystal after annealing** with the change in the micrographs and X ray difraction patterns of the same crystal before and after heating up to 70°C. Panel (b) of the same figure evinces the increase of conductivity through annealing. It displays IV curves acquired on the crystal at two sweep rates (0.1 V/s on the left and 0.7 V/s on the right) before (blue lines) and after (red lines) heating the crystal. The plots also reveal certain hysteresis in the IV curves.

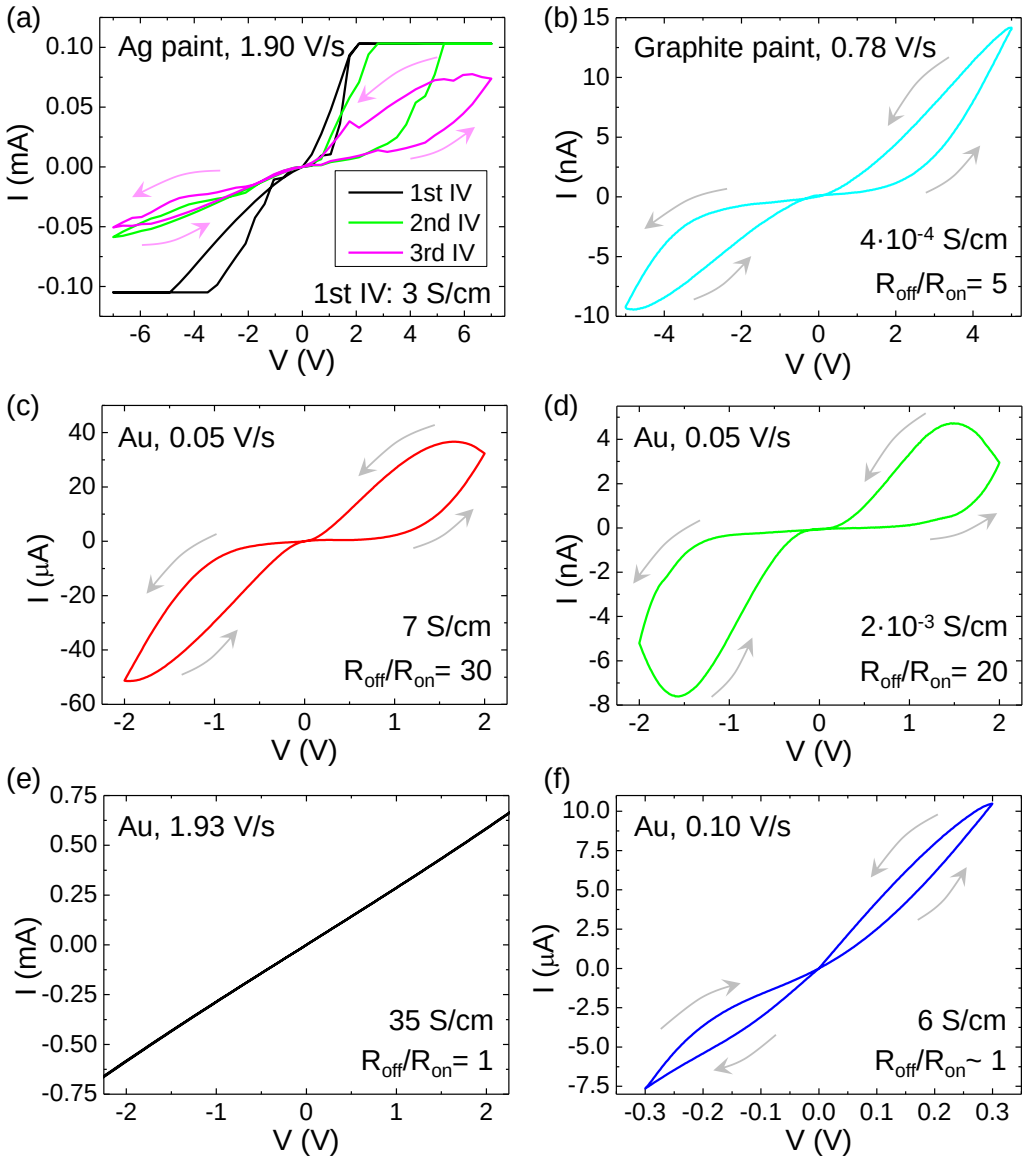

Figure 4.13: IV curves casuistry of $[Cu_2I_2(TAA)]_n$ films. The material of the electrodes and the voltage sweep rate is indicated at the top left of each panel whereas the electrical conductivity and the figure of merit R_{off}/R_{on} is shown at the bottom right. The voltage at which this ratio was computed was: (b) -1.8 V, (c) 0.50 V, (d) -0.63 V, (e-f) at any voltage. Panel (a) shows IVs where the conductivity decreased in the second and third IVs. A compliance current of 0.1 mA was imposed. The device of (d) works at much less power (nA instead of μA for the same bias voltage). (e) Shows a linear IV with high conductivity. The films' thicknesses are 150 nm for (a) and tens of nanometers for the rest. The lateral sizes of the devices were L×W: (a, b) ~100×300 μm^2, (c, d) ~25×58 μm^2 and (e, f) ~3×15 μm^2.

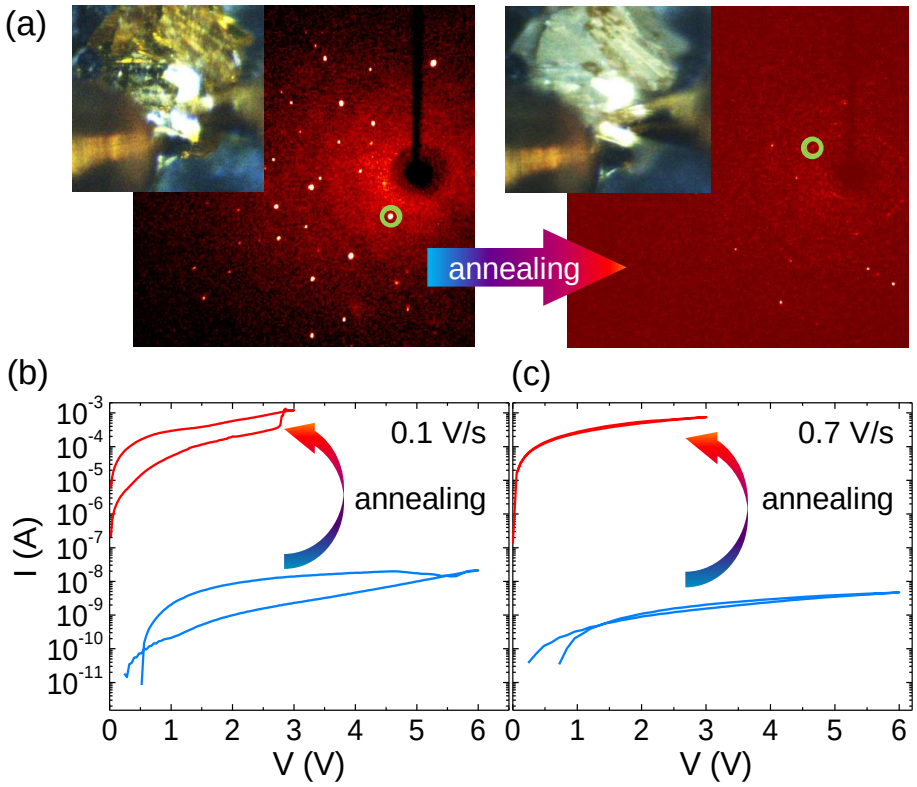

Figure 4.14: Measurements on $[Cu_2I_2(TAA)]_n$ bulk crystals. (a) Intense and well defined diffraction spots are observed for a single crystal that has been kept under room conditions (left), but significantly less intense diffraction spots are found in the same crystal upon heating up to 70°C (right), indicative of a loss of crystallinity. The (420) diffraction peak, in the centered tetragonal system I, has been encircled in both images for comparative purposes. In both cases the same exposure time was employed. The insets show optical images of the $[Cu_2I_2(TAA)]_n$ crystal before and after annealing from RT to 70°C. (b) and (c) show IV curves on the crystal in a semi-log plot before (blue) and after (red) annealing for two sweep rates. The crystals showed an increase in conductivity of 5 orders of magnitude upon annealing and showed similar memristive character as the films.

4.4.2 *Introduction to Resistive Switching*

When I showed my supervisors the IV characteristics with the pinched loops, Julio exclaimed: "¡Eso es un memristor!" ("That is a memristor!!") and I asked him: "¿¿Mem... qué?? ("Mem... what??"). What at the beginning were artifacts for me, it turned out to have its own name and be a well-known phenomenon. I did not discover anything new at all :(but, fortunately, we had found by serendipity metal-organic films that seemed memristors.

A ***memristor*** is the fourth passive element (apart from the resistor, R, capacitor, C, and inductor, L) in the relationships among the voltage (v), current (i), charge (q) and magnetic flux (ϕ) [245]. It was predicted by Leon O. Chua in 1971 from simmetry arguments [246]. Figure 4.15 shows the relationships among mentioned magnitudes including the *memristor*, and its characteristic property: *memristance* (M).

Until today it is a purely hypothetic element which is not represented by a simple device. After the publication titled "The missing memristor found" in Nature by Dimitri

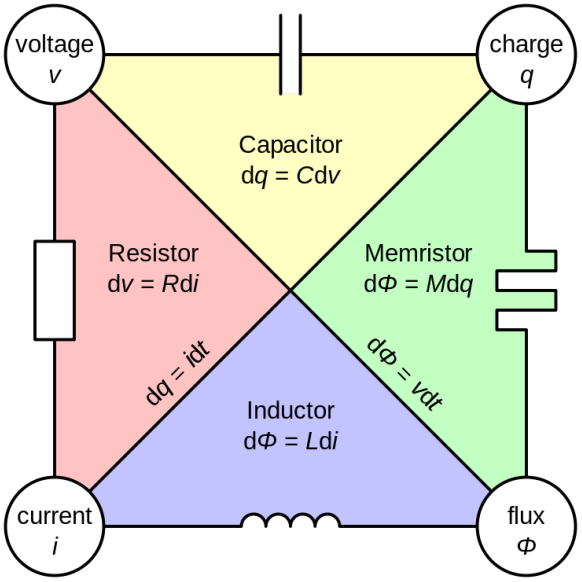

Figure 4.15: Conceptual symmetries of resistor, capacitor, inductor, and memristor. The relationships of each characteristic property (R, C, L and M) with v, i, q and ϕ are shown. Source [247].

B. Strukov, the controversy about the existence or absence of the ideal memristor arose [248]. What does exist are the so-called ***memristive systems***, which are a more general memristor, defined by Chua as well in 1976 [249]. A memristive system is a device in which the resistance state is memorized until the next stimulus strong enough to change that state [245]. It is a two-terminal device defined by a complex state-dependent Ohm's law:

$$V(t) = R(\mathbf{x}, I, t) \cdot I(t) \tag{4.2}$$

where t is time and x is a state variable vector (temperature, magnetization, chemical composition, crystallographic phase, the length of a conducting filament, charge, magnetic flux, etc.) with this state equation:

$$\frac{\partial \mathbf{x}}{\partial t} = f(\mathbf{x}, I, t) \tag{4.3}$$

A memristor is simply a special case of a memristive system, in which x is only the flowed charge ($\mathbf{x} = q \implies V = R(q) \cdot I$). The consequences of the definition of a memristive system are:

- The value of the resistance at any time will depend on the entire past history of the device (which inspired the names **MEM**ory+**R**es**ISTOR** and **MEM**ory+**R**es**ISTIVE**). This memory in the resistance is reflected in this expression:

$$\mathbf{x}(t) = \int_{-\infty}^{t} f(\mathbf{x}, I, \tau) d\tau \tag{4.4}$$

- The **IV curves**:
  - present **hysteresis loops** when exciting with a periodic stimulus (usually the voltage).
  - are **pinched** at the origin.
  - have loops whose **size depends on the speed** of the periodic stimulus.
  - have **two regimes**: the Low Resistance State (LRS) and the High Resistance State (HRS). They are also called ON and OFF state respectively.

The features of the IV characteristics of a memristive device are displayed in figure 4.16.

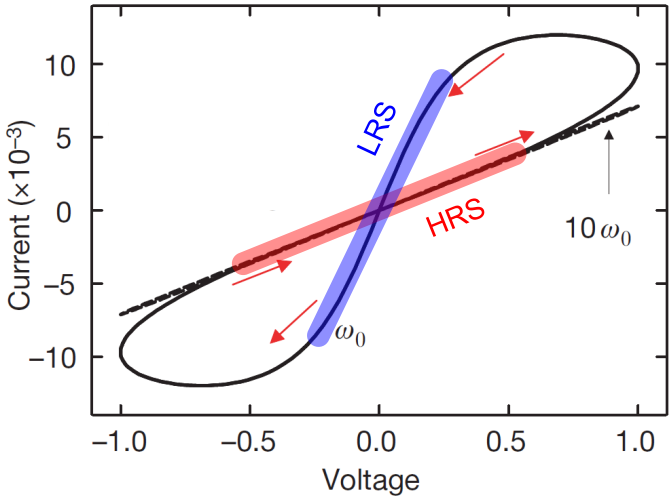

Figure 4.16: IV characteristics of a memristor. Solid line corresponds to an IV acquired with ω_0 sweep rate, and the dashed line to another one acquired with a tenfold increase in sweep frequency (its loops are so closed that are hardly visible). The other features of a menristor's IV are shown: hysteresis loops pinched at the origin and both resistance sates (HRS and LRS). Adapted from [250].

There was not previous knowledge nor experience with memristive systems in my research group. That prompted me to attend a Spring School titled "Memristive Phenomena - From Fundamental Physics to Neuromorphic Computing". It took place in the Forschungzentrum Jülich in Aachen (Germany) only some months after the first measurements. That prestigious research center has organized a Spring School every year since 1970 covering a hot topic in Physics in each edition. In fact, research in memristive systems, memristors or resistive switching (another common name used to refer to mentioned phenomena) has been increasing since 2010 reaching a maximum in 2017, one year later than my attendance to the Spring School. This time evolution is depicted in figure 4.17.

Engineering is the research area where this topic has been mainly investigated, followed by Physics, Materials Science and Computer Science. This increasing and wide interest is partly due to the fact that memristive systems can act as **memories**. Indeed, the existence of both resistance regimes and the ability of retaining the internal resistance state enable the **store of information** in memristive systems, giving rise to the so-called *Resistive Random Access Memories* (RRAMs) [252]. They could also be used to develop

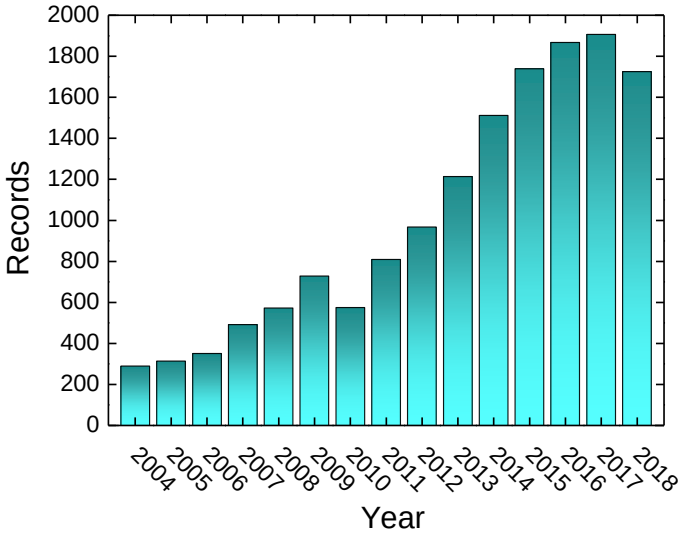

Figure 4.17: Time evolution of research publications on memristive systems. Source: Web of Science searching for publications with the topic "memristive system" OR "memristor" OR "resistive switching" [251].

alternative **computer logic** architectures [253]. For all this, each memristive device formed by 'electrode+insulator+electrode' is usually called **cell** (from memory cell concept).

There are mainly **two type of resistive switching** in memristive devices: unipolar and bipolar switching. To explain them, we should first introduce the write and read operations in a memristive device. We assign the logic '0' state to the HRS and the logic '1' to the LRS. A **write operation** changes a memristive cell from the HRS to the LRS ('0'→'1'), this is called SET operation and it takes place at a excitation voltage called V_{SET}. The opposite write operation ('1'→'0') is called RESET operation and occurs at V_{RESET}, that is usually lower in absolute value than V_{SET}. **Read operation** consists in measuring the current at voltage V_{READ} ($|V_{READ}| < |V_{RESET}| < |V_{SET}|$), detecting if the cell is in the LRS or in the HRS.

Bipolar resistive switching needs the use of both voltage polarities to perform the two write operations: the SET operation occurs at one polarity and the RESET requires the opposite polarity. On the contrary, all the operations can be carried out at one voltage polarity in the **unipolar resistive switching**. Often, a compliance current (CC) is used in both modes to limit the current in the SET operation. This is done in order to avoid irreversible cell breakdown yielded by very high density currents. Figure 4.18 shows the IV characteristic of both types of resistive switching.

The **kinetics** of the resistance switching process in a memristive system is directly linked to the sweep rate of the (triangular) excitation voltage signal during IV measurement. As the sweep frequency increases: (i) the hysteresis loop area decreases [250, 254], (ii) the loops tend to collapse in the LRS and (iii) $|V_{SET}|$ and $|V_{RESET}|$ increase (the resistive cell has less time to switch and need a higher voltage). This is portrayed in figure 4.19.

Among the **performance parameters** in memristive devices, one of the most important ones is the $\mathbf{R_{off}/R_{on}}$ **ratio**. It is just the quotient of the resistance of the OFF state (or HRS) divided by the resistance of ON state (or LRS). This parameter obviously depends on the sweep rate of the excitation voltage. It could also be affected by the temperature [255]. Other performance parameters are the values of both resistances themselves, the

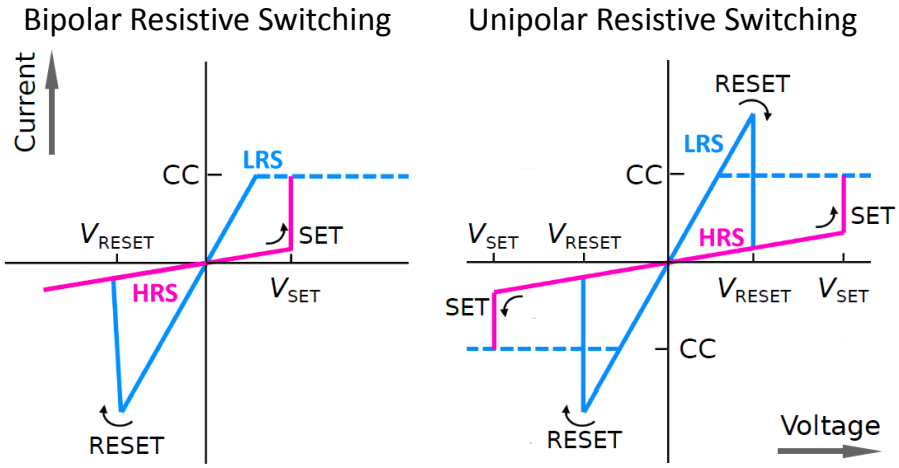

Figure 4.18: Bipolar and unipolar switching modes. IV characteristics of the two most common operation modes of memristive elements: bipolar and unipolar RS. Source: chapter C1 from [245].

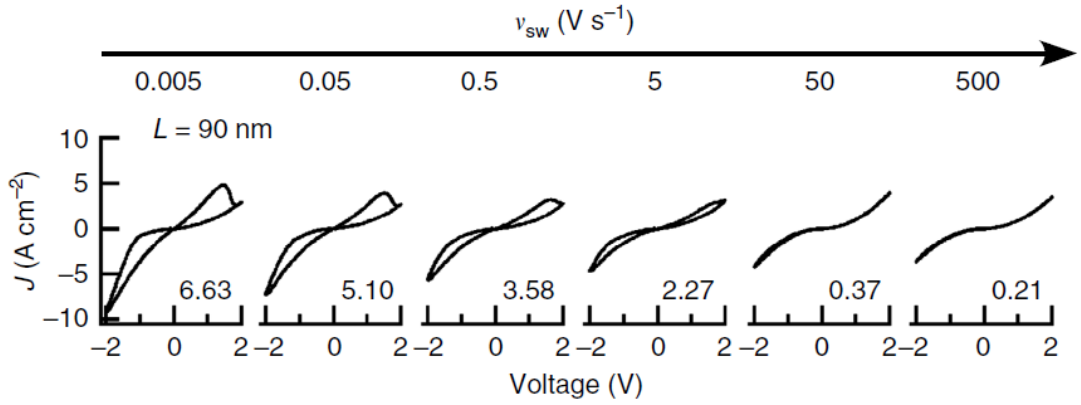

Figure 4.19: Effect of the sweep rate of the excitation signal on the IVs of a memristive device. Variable hysteretic IV loops of a Pt/GaO_x/ITO device, measured with various voltage-sweep rates (v_{sw}) in the range of 0.005–500 V/s. Y axis plots the current density J (not the current). The numbers in each graph denote the hysteretic area (VA/cm^2) of the loop. Source: [254].

value of V_{SET} and V_{RESET}, the number of write/read operations the memristive cell can withstand (endurance), and many more [245].

There are two types of memristive cells according to their geometry. The most common one is the **stack switching cell**, in wich the electrodes and the insulator are arranged in stacked layers. The **planar switching cell**, on the contrary, has the electrodes and the insulator in the same plane. Figure 4.20 displays both kind of structures.

The physical principles of memristive phenomena can be manifold. A coarse-grained classification of the **memristive mechanisms** includes (i) magnetic effects, (ii) electrostatic effects and (iii) different classes of effects based on atomic configuration. Memristive phenomena has been investigated since the 1960's. Some types of underlying mechanisms are reasonably well understood while others are not [252]. Figure 4.21 shows a possible memristive mechanisms classification.

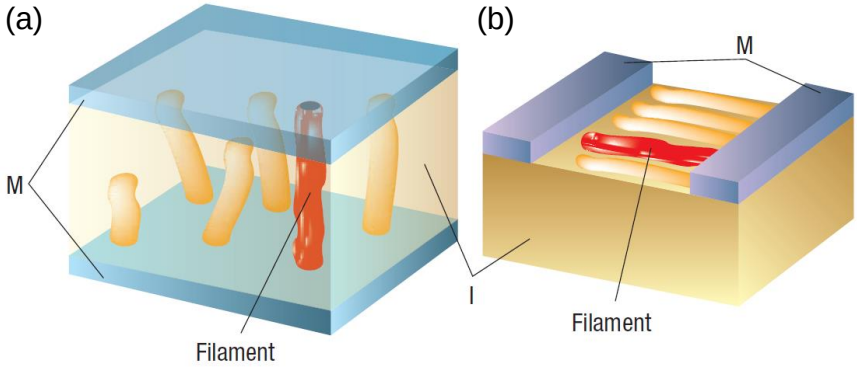

Figure 4.20: Switching cell geometries. (a) Vertical stack configuration. (b) Lateral, planar configuration. M stands for metal and I for insulator. In the depicted cells there are conductive filaments, being the red tubes, the ones conecting both electrodes. Extracted from: [256].

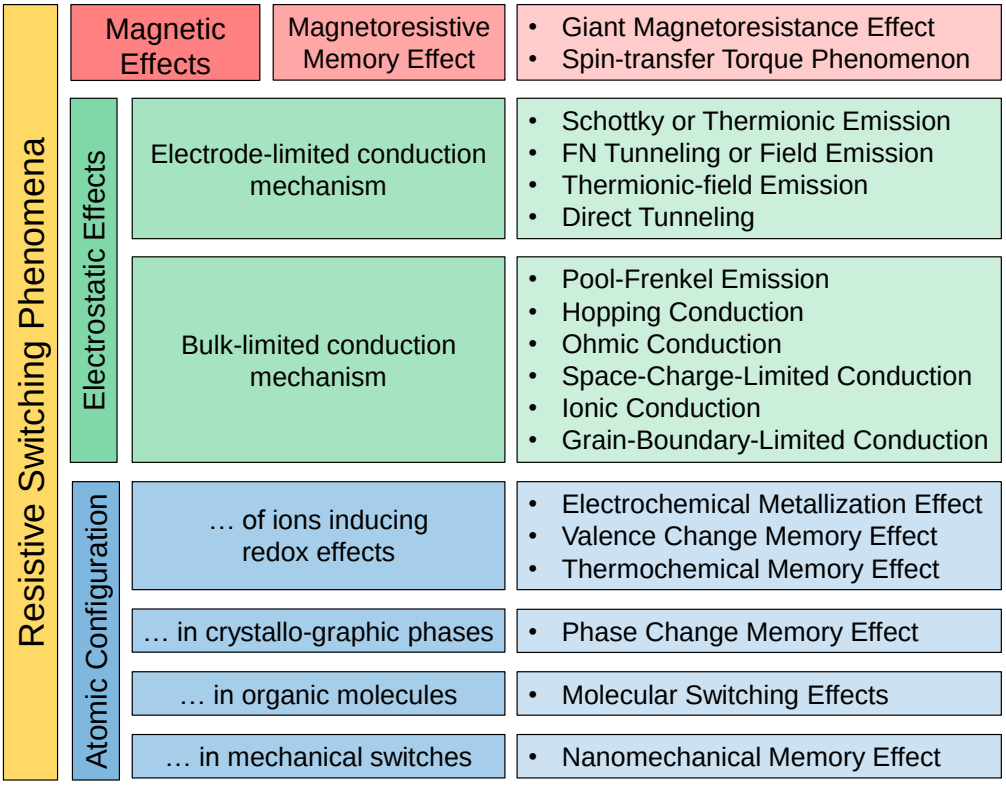

Figure 4.21: Classification of resistive switching effects. Adapted from: [257] and [258].

Some proposed mechanisms for memristive response include growth of conducting filaments in dielectric materials, phase transitions, field-induced motion of ions leading to reduction-oxidation (red-ox) processes, configuration change of individual molecules and switching in the polarization of a ferroelectric material, among others [245, 252, 256].

According to the **type of conducting path** in the material between electrodes, we can categorize the resistive switching (RS) mechanisms in: (i) the ones with **filamentary** conducting path, in which the RS originates from the creation and rupture of conductive filaments in an insulating matrix (figure 4.22(a)) and (ii) the ones that have an **interface-**

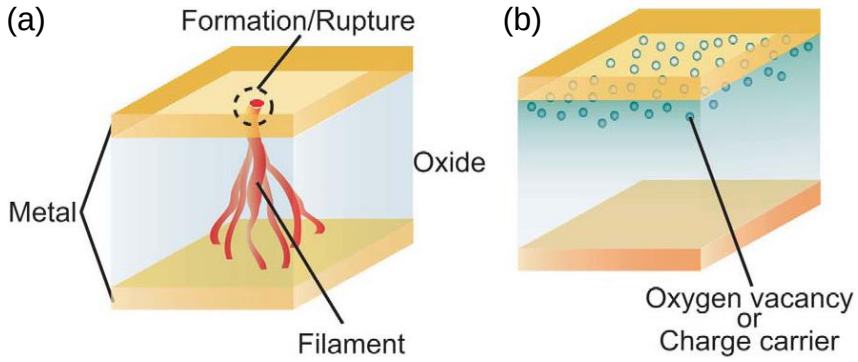

Figure 4.22: Types of conducting path in memristive cells. (a) Filamentary conducting path. (b) Interface-type conducting path. Source: [259].

type path, in which the RS takes place at the interface between the metal electrode and the insulator (figure 4.22(b)) [259].

The **electrodes**, depending on the metal they are made of and on the mechanisms that can take place in the material between electrodes, can play an **active role** in the resistance switching. A well-known example is the **Electrochemical Metallization** effect (ECM). In ECM the resistive switching is performed by an electrochemical metal deposition and subsequent disolution. It takes place in cells made of (i) an electrochemically active metal (silver, copper or nickel) that acts as anode (oxidation on it), (ii) an inert counter metal (platinum, iridium, tungsten or gold) that acts as a cathode (reduction on it) and (iii) a film of a solid (typically amorphous selenides, sulfites and oxides) that acts as electrolyte, conductor of the active metal ions. The whole ECM SET process is illustrated in figure 4.23(a). It leads to the growth of filaments made of the active metal in a dentritic fashion from the inert electrode (see figure 4.23(b)).

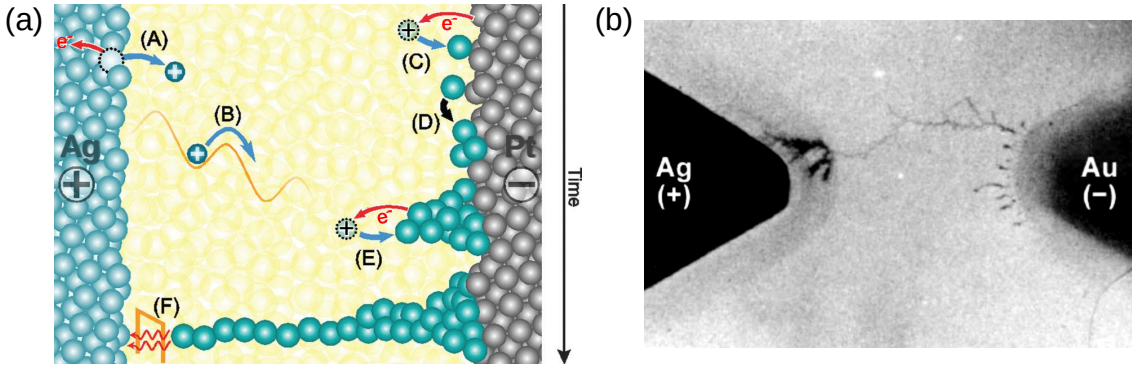

Figure 4.23: Electrochemical Metallization. (a) Illustration of the ECM process during SET operation, comprising: (A) oxidation of the Ag active electrode (charge transfer reaction) and dissolution, (B) migration of Ag cations under the electric field, (C) reduction reaction at the inert electrode/solid film interface, (D) nucleation process prior to (E) filamentary growth driven by further reduction processes, (F) when the filament approaches the active electrode significant electron tunneling current sets and the cell switches to a low resistive state. Source: [260]. (b) Optical microscopy image of a Ag dendrite grown from the (-)Au electrode towards (+)Ag electrode within a As_2S_3 thin film on a glass substrate. Source: [261].

4.4.3 *Verification and Characterization of the Memristive Response of $[Cu_2I_2(TAA)]_n$ Films*

Comparing the results of the preliminar electrical characterization and the features of memristive systems, we highlight the following:

- Most devices with films contacted by **gold or graphite paint electrodes** gave IVs similar to that of a memristor (see figure 4.13(b-d)). As those electrodes do not take an active role in the electrical conduction (which was confirmed by the absence of dendritic filaments in such devices), the films seemed to be **intrinsically memristive**.
- In devices with **silver electrodes**, and only in those devices, there was growth of dentritic paths. This suggested that these dendrites were made of silver. This was supported by the increase of conductivity once they connected both electrodes. All this pointed to the **electrochemical metallization** as the mechanism responsible for this electrical behaviour.[1]

In conclusion, $[Cu_2I_2(TAA)]_n$ films seem to be intrinsically memristive leading to loops even in IVs of non-silver electrodes devices. In silver electrodes devices, the conduction is, adittionally, asisted by the ECM effect which increases the conductivity orders of magnitude once a silver filament connects both electrodes.

As we are interested in the intrinsic properties of the films, we continue studying the electrical properties of **devices made of inert electrodes** (such as gold or graphite paint).

There are some experiments that can be conducted to further check and characterize the memristive nature of the films.

4.4.3.1 *Memristive Kinetics of the Films*

Most of our devices (> 80 %) exhibited an **initial high resistance state (HRS)**, in the positive bias sweep, followed by a decrease in resistance that changes into a lower resistance state (LRS) at higher bias, the device stays in the LRS as the bias is turned to zero. In the negative bias sweep, the device starts in the HRS and turns into a LRS as the bias is further decreased. This is shown in IV of figure 4.24 (in figure 4.13(a-d) as well) in which arrows point the direction of the loops and the HRS and LRS are indicated.

The former response suggests **unipolar RS** (the resistance state is probably changed when approaching 0 V, before changing the voltage polarity). To confirm this unipolar RS, we measured consecutives IV curves in some devices (with gold electrodes) at only one polarity. Figure 4.25 shows three IVs acquired in one of them at negative excitation voltage. As it can be seen, the SET and the RESET operation can be performed in the same polarity, which indicates that the films present **unipolar resistive switching**.

In order to check the **influence of the bias voltage speed**, we acquired IV curves at different voltage rates in some films as figure 4.26 depicts. As it occurs in memristive systems, $[Cu_2I_2(TAA)]_n$ films yield narrower loops in IVs as the sweep rate increases. When it is high enough the IV collapse into the HRS, without loops. This is displayed in figure 4.27.

1 The IVs obtained in silver electrodes devices (figures 4.13(a) and 4.12) differ, however, from the standard memristive IVs. This is due to the fact that both electrodes were made of silver whereas in a ECM cell one of them should be a inert metal. We also had devices with a gold electrode and a silver electrode, but unfortunately the measurements were done applying the wrong (i.e. negative) voltage polarity to the silver electrode at the beggining of the IVs (see figure 4.23). Anyway ECM effect was not the final goal of this research.

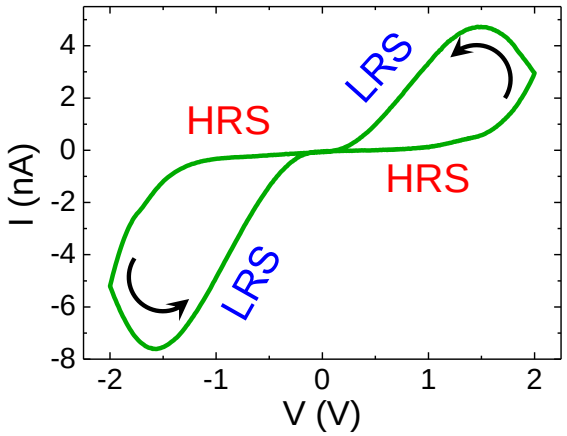

Figure 4.24: IV showing the HRS and the LRS as well as the direction of the loops. It was acquired on a device with gold electrodes. Film's thickness: ~15 nm. Size of the device: W = 58 µm and L = 25 µm.

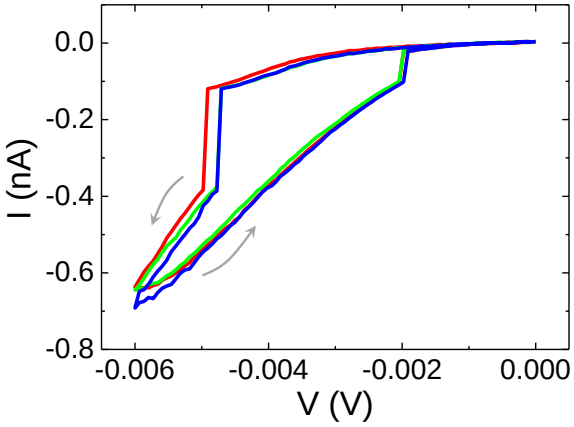

Figure 4.25: IVs at one polarity to check the RS mode. Three IVs acquired consecutively in a 25 nm thick film contacted by gold electrodes revealing unipolar resistive switching. Size of the device: W = 58 µm and L = 25 µm.

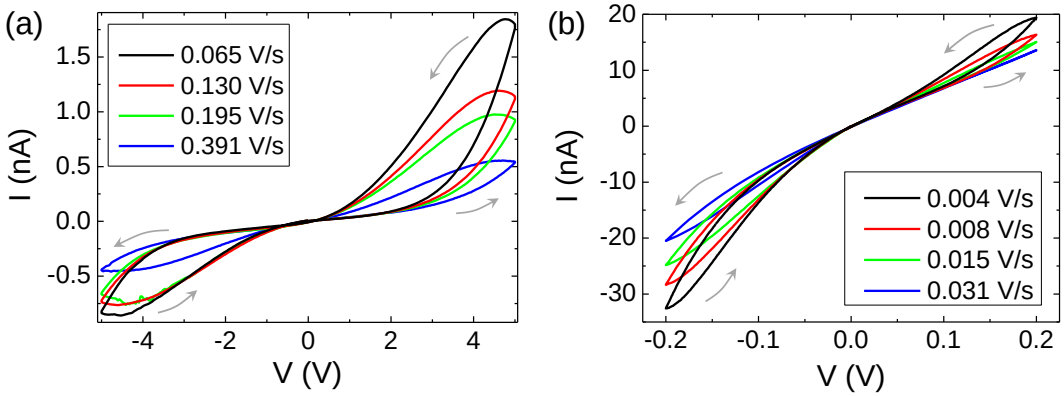

Figure 4.26: Influence of bias voltage speed on IV curves. (a) IVs acquired on the device of figure 4.11(b) at different sweep rates. (b) IVs performed on the device shown in figure 4.11(c) at several voltages speeds.

Interestingly, the **HRS did not change with the frequency** of the sweeps (our maximum sweep rate was 10^4 V/s), but the **LRS did change**, presenting a decreasing resistance with decreasing sweep speed starting at about 0.3 V/s. The **R_{off}/R_{on} ratio ranges from 1.5 up to 30**.

These results for the kinetics of the electrical of the films are the expected for a memristive material, which reinforces our guess about the memristive character of the films.

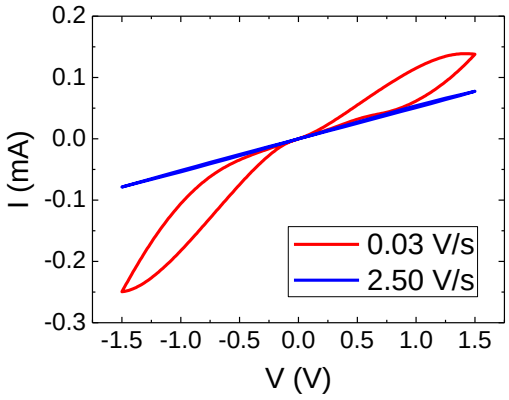

Figure 4.27: Collapse of an IV curve at the HRS when it is measured at high voltage speed. Both IVs were acquired on a device with gold electrodes, lateral dimensions W = 58 μm and L = 25 μm and a film's thickness of ~50 nm.

4.4.3.2 *Type of Mechanism: Area Dependent Studies*

As the optical microscope images have shown, devices with silver electrodes have a filamentary conduction mechanism. For the rest of devices the conducting paths can be filamentary (with filaments not visible under the optical microscope) or interface-type (see figure 4.22). The measurement of the resistance of the devices as the interface area between the film and the electrodes is reduced discloses the nature (filamentary or not) of the RS mechanism in the films. If the resistance remains constant as the area is reduced, the RS is local, caused by one filament. However, if the resistance scales with the inverse of the area, the RS is uniform and the mechanism is interface-type and not filamentary [259, 262].

Consequently, variable area measurements were performed in several devices made of gold electrodes. The performance of each device was measured while reducing the interface area between the film and the electrodes (i.e. ~width of the device × film's thickness). This was achieved by reducing the width of each device, keeping constant the thickness of the film. A micro-sized tip was used to sequentially scratch the polymer in its sides. The process consists of the following steps: first the resistance of the as-prepared device (whose width is W_1) was measured, then the film was scratched to disconnect a lateral stripe of it (having a new width of W_2), afterwards the resistance was measured in this narrower film, and so on. Figure 4.28 shows the procedure followed and the results obtained in a representative device. The thickness of the film was 30 nm, the length of the device was 35 μm and the series of widths was W_1 = 90 μm, W_2 = 70 μm, W_3 = 55 μm, W_4 = 35 μm and W_5 = 12 μm. For each width, an IV characteristic was acquired between ±1 V at 0.067 V/s. The resistance was calculated at -0.5 V. As figure 4.28(b) depicts, the resistance scales with the inverse of the device width (which is proportional to the interface area). This tendency discards the growth of a conducting filament as the underlying electrical mechanism in this polymer.

In **summary**, the films have a conductivity that spans **from 10^{-4} S/cm** (a typical value for an organic conductor) [228] **to 50 S/cm** (comparable to that of best conjugated polymers as polypyrrole) [263] depending on the region measured, with no dependence on the device channel length, from 2 to hundreds of μm, or film thickness, from 4 to 60 nm. For sweeping speeds **below 0.3 V/s**, most of our devices showed **pinched-hysteresis loops in IV** curves at room temperature. The size of the loops increases as the voltage sweep rate is reduced. These hysteresis loops showed two resistance states with **R_{off}/R_{on} ratio up to 30**. These features are typical of memristive systems, where the resistance depends on the history of the current previously flowed through the device. In these films, the

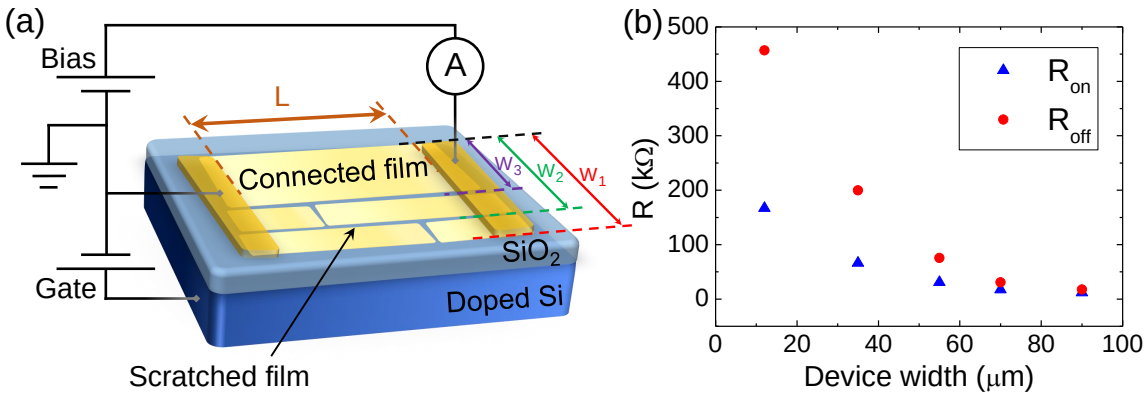

Figure 4.28: Area dependent studies in the electrical performance of $[Cu_2I_2(TAA)]_n$ films. (a) Diagram of a device measured as its width is being reduced. (b) Electrical resistance of a device as a function of its width (which is proportional to interface area, width of the device × film's thickness).

mechanism behind this response is **not filamentary**. We will unravel this mechanism in some detail in next sections.

4.4.4 *Electrical characterization of films*

In order to (i) explain the dispersion in the electrical conductivity of $[Cu_2I_2(TAA)]_n$ films, (ii) the different kinds of IV they provide and (iii) figure out the mechanism that yields the resisitive switching in most of them, we conduct additional experiments.

4.4.4.1 *Influence of Atmosphere*

Further electrical studies revealed that **atmosphere did not have an influence** on the electrical properties: equivalent measurements in ambient conditions (T = 25°C, relative humidity 55%) and high vacuum (T = 25°C, P = 10^{-5} mbar) did not show any difference in conductivity. Indeed, experiments performed with the devices annealed in vacuum allowed us to discard purely surface diffusion of adsorbates. Additionally, XPS on the films after applying ±10 V show the same peaks than those present in the as-prepared film, confirming its chemical stability during the electrical characterization experiments discarding redox processes (figure D.2 in appendix D). This last result discards the three mechanisms based on redox effects (Electrochemical Metallization, Valence Change and Thermochemical Memory effects, see figure 4.21) as the ones behind the RS of the films.

4.4.4.2 *Transversal Electrical Conductivity Measurements*

Out-of-plane conductivity was evaluated by collecting films on gold surfaces and contacting them with Ga_2O_3/EGaIn [264] as top electrode (figure 4.29(a)). The measured values of *ca.* 10^{-8} S/cm confirmed a tunnel conduction mechanism of the films in the out-of-plane direction (figure 4.29(b)). This evinces a strong anisotropic conduction in the films confirming a bidimensional behaviour in terms of electrical conductivity.

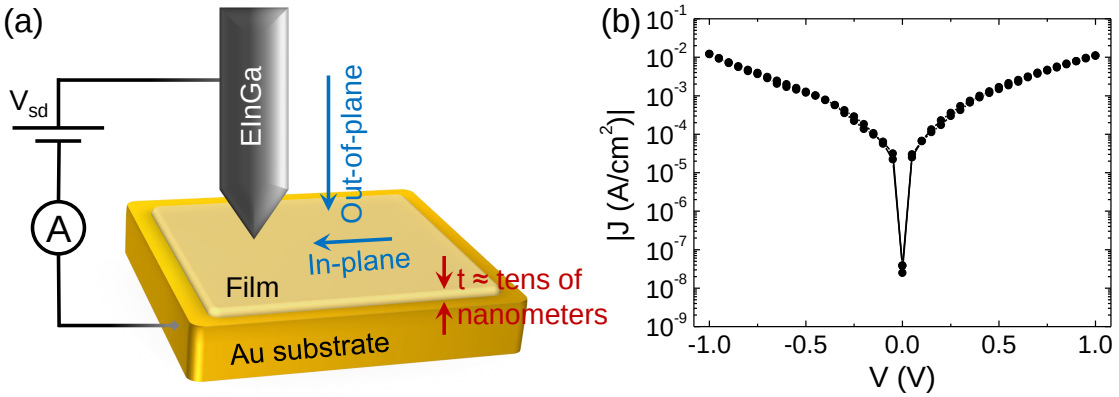

Figure 4.29: Measurement of the transversal conductivity in $[Cu_2I_2(TAA)]_n$ films. (a) Experimental scheme used for the measurement of transversal (out-of-plane) conductivity. (b) Averaged trace (current density versus bias voltage plot) obtained from 456 traces of 25 junctions. The thickness of the films is ~40 nm, and the tip contact ~400 nm^2, which yields a transversal conductivity of *ca.* $4{\cdot}10^{-8}$ S/cm.

4.4.4.3 *Material Displacement under High Current Density*

Interestingly, high conductivity films reached up to **current densities** of $2{\cdot}10^{-4}$ $\mu A/nm^2$ at RT, similar to that of best conducting polymers as polypyrrole [263]. For higher density currents we have observed significant material displacement before failure of devices (see figure 4.30). This threshold current density for material displacement is increased by more than one order of magnitude when temperature is lowered to 80 K.

4.4.4.4 *Influence of an External Field*

Three terminal measurements with a global back gate showed very weak dependence of current upon an external electric field as shown in figure 4.31, which also indicates that the transport is due to positive carriers.

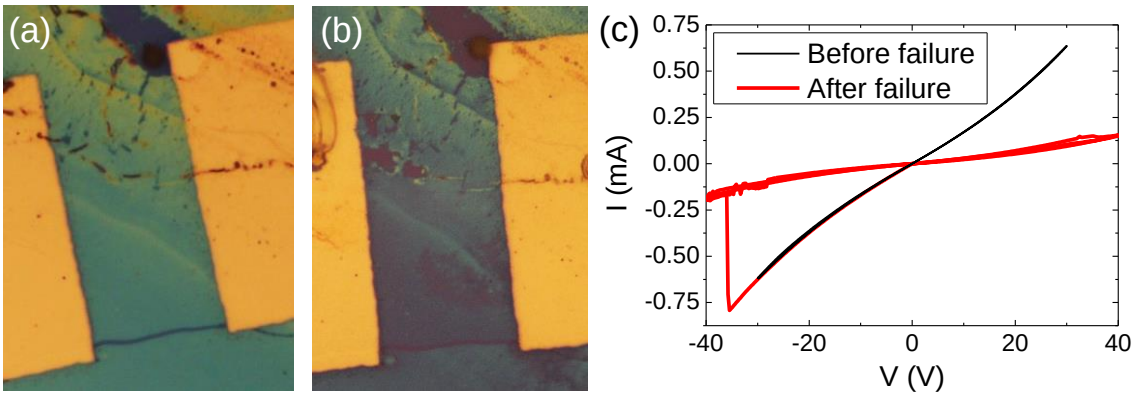

Figure 4.30: Material displacement under high current density. (a) Optical microscope image of a film electrically contacted by gold electrodes before (a) and after (b) the electrical failure of the device. After device failure, we observed that some material in the film was displaced. (c) IV curves acquired at 86 K just before (black line), during (vertical red line) and after (almost flat red line) the electrical failure of the device. The sudden drop of the current shown in the red curve is indicative of electrical failure.

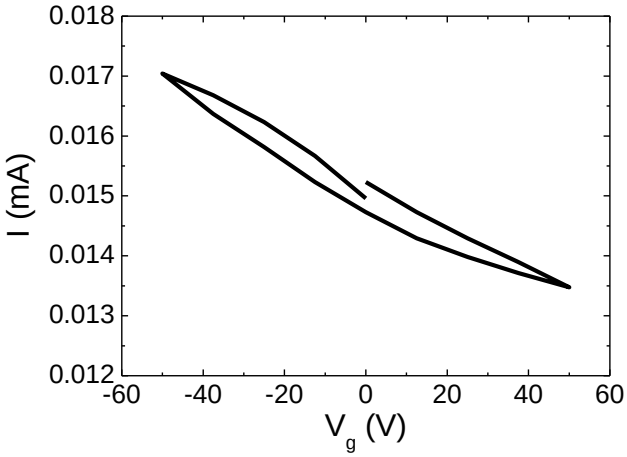

Figure 4.31: Current *vs.* gate voltage at a fixed bias voltage of 3 V. It was acquired at 89 K at HV. Film's thickness: *ca.* 30 nm. Size of the device: W = 58 µm and L = 25 µm.

4.4.4.5 *Influence of Temperature*

Upon cooling from 300 to 85 K the **memristive films** showed a conductivity decrease of **one order of magnitude** (see figure 4.32(b)). Moreover, the IV loops close as temperature is decreased: the high and low resistance states converge at low temperatures but present clear different behaviour at temperatures near RT. The threshold temperature (between both behaviors) is around 180 K, which is depicted in the Arrhenius plot of figure 4.32(c) with a gray dashed line. This graph shows that, while the characteristic activation energy for electrical conduction at low temperatures is **13.0** $\pm$ 0.2 meV, for temperatures above 200 K the HRS and LRS separate into two different slopes with activation energies of **100** $\pm$ 10 meV and **160** $\pm$ 20 meV, respectively. This behaviour suggests the existence of at least **two conduction mechanisms** contributing to the conductivity in different temperature ranges as observed in other polymers [228]. The first one is responsible for the **base** electrical **conductivity** of the films (observed at high bias sweeping speeds or low temperatures) and for the **HRS** observed at slow sweep rates (and T > 180 K). The second one, with higher activation energy, is responsible for the **LRS** at slow sweep rates (and T > 180 K). The combination of both mechanisms would lead to the memristive character of our films.

Furthermore, **AC conductivity** measurements did not show any dependence from 1 to 107 Hz. The low activation energies together with the AC measurements and the insensitivity of electrical transport to air exposure strongly suggest **electronic** rather than ionic (proton) conductivity, as reported in similar polymers [265].

Figure 4.33 summarizes the effect of the voltage sweep rate at low temperature and at RT, in the memristive device of figure 4.32(a). At low temperature the memristive response is quenched even at low voltage speed.

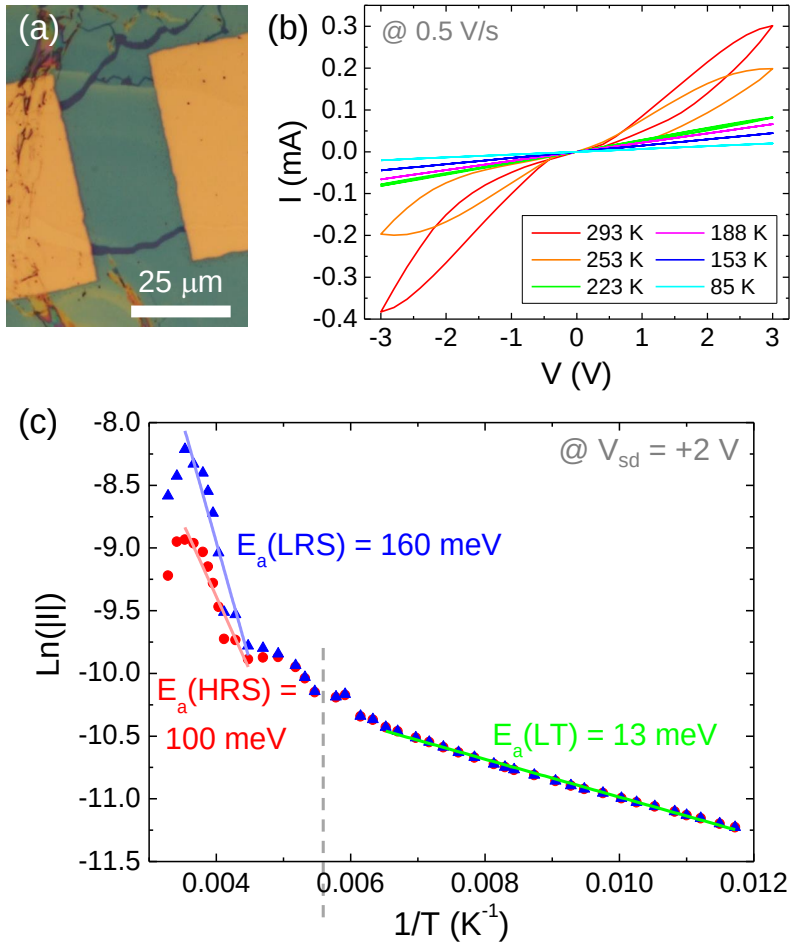

Figure 4.32: Influence of T in the electrical performance of a memristive film. (a) Optical micrograph of the device studied. Lateral sizes: W = 58 µm and L = 25 µm. Film's thickness: *ca.* 30 nm. (b) Selection of IVs acquired at different temperatures, at a voltage rate of 0.5 V/s. (c) Logarithm of the current *vs.* inverse 1/T (Arrhenius plot). The current is measured at a bias voltage of 2 V. The lines are linear fits to the corresponding range of data, from which the activation energies are obtained. The vertical gray dashed line indicates the location of the threshold temperature.

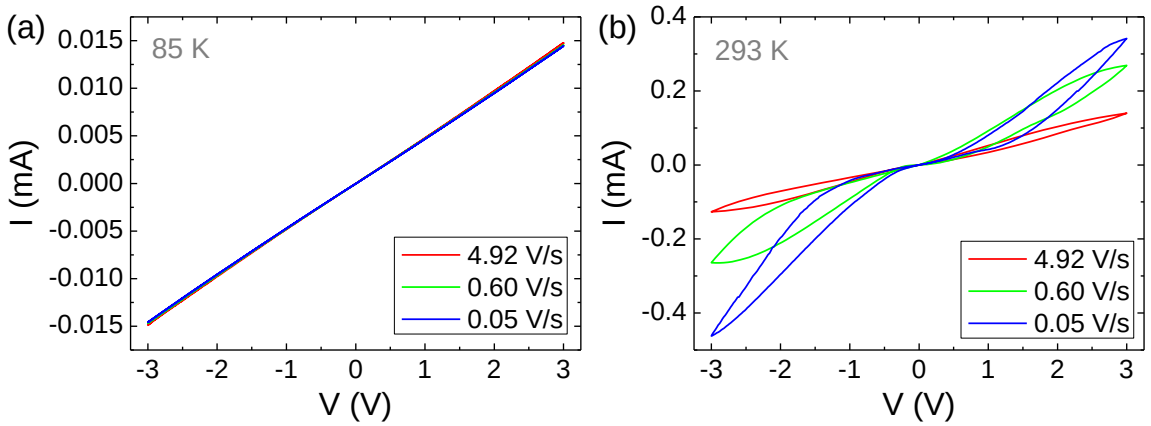

Figure 4.33: Effect of the voltage sweep rate at low and room temperature in a memristive film. IV characteristics measured in the device of 4.32(a) at 85 K (a) and 293 K (b) at three voltage sweep rates.

We repeat the same kind of experiments in a **device that yield linear IVs**. The results are shown in figure 4.34. In this case the excitation voltage is restricted to ±0.3 V to avoid a high density current that can lead to breakdown of this device. It has a thinner film (~15 nm) and a lower distance between electrodes (~3 µm, see figure 4.34(a)) that together with a considerable conductivity (1.4 S/cm) favors higher current densities. For this device, cooling from RT to 95 K reduces the conductivity a **factor of ~0.5**. Unlike the studied memristive device, IVs do not show hysteresis loop nor at RT (see figure 4.34(b). The corresponding Arrhenius plot is shown in figure 4.34(c). It presents two regimes: at low temperatures and at temperatures near room temperatures, with a threshold temperature of around 180 K (vertical gray dashed line in the Arrhenius plot), as in the case of the memristive device of figure 4.32. This suggests two differenciated mechanisms for the conduction, both of them with activation energy bellow $K_B T$: **6.4** ± 0.2 meV for temperatures below 180 K and **16.2** ± 0.6 meV for higher temperatures.

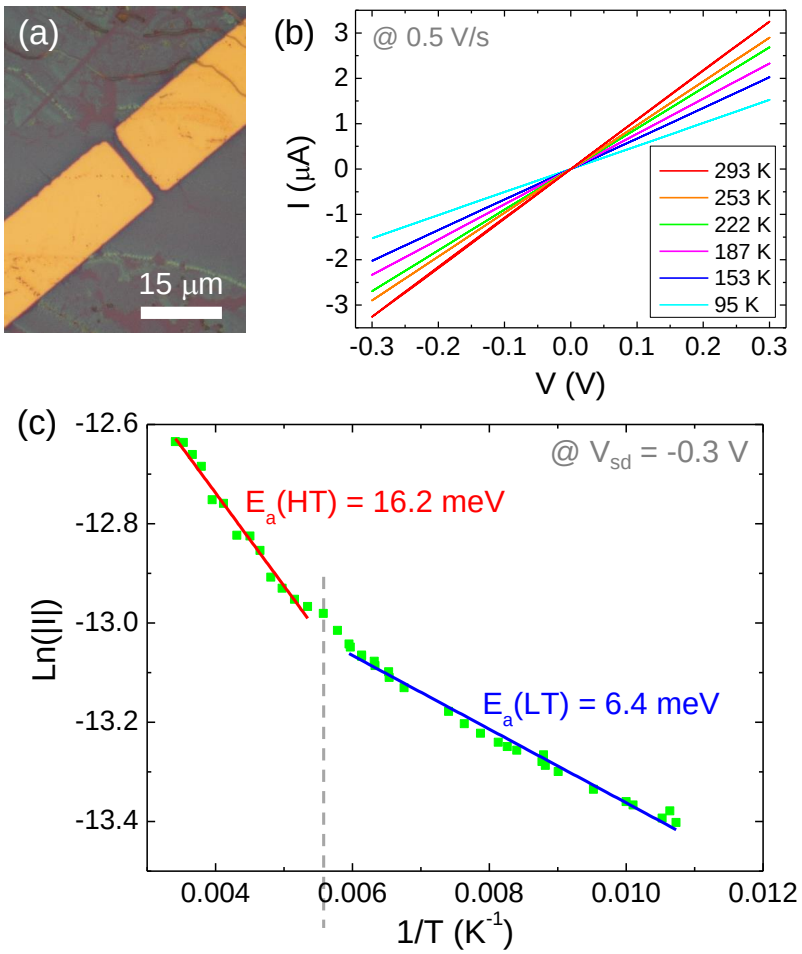

Figure 4.34: Influence of T in the electrical performance of a film with linear IVs. (a) Optical micrograph of the device studied. Lateral sizes: W = 15 µm and L = 3 µm. Film's thickness: *ca.* 15 nm. (b) Selection of IVs acquired at several temperatures, at a voltage rate of 0.5 V/s. (c) Logarithm of the current (measured at -0.3 V) *vs.* 1/T. The lines are linear fits to the corresponding range of data, that provide the activation energies. The vertical gray dashed line is at the threshold temperature (~180 K).

Figure 4.35 depicts IVs acquired at three voltage sweep rates at 95 K and at RT. Extremely narrow loops emerge only at RT at the lower voltage speeds.

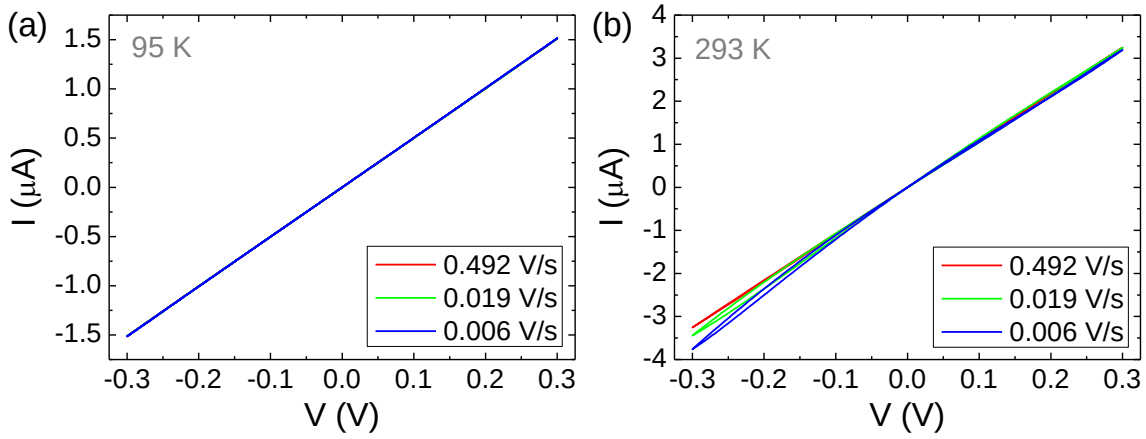

Figure 4.35: Effect of the voltage sweep rate at low and room temperature in a $[Cu_2I_2(TAA)]_n$ film with linear IVs. IV characteristics measured in the device of 4.34(a) at 95 K (a) and 293 K (b) at three voltage sweep rates.

4.4.5 *Conduction Mechanism*

We expect to have two different conduction mechanisms for memristive devices: one responsible for the high resistance state (or base conduction) and other one, with higher activation energy, responsible for the low resistance state.

4.4.5.1 *What we know so far*

Fortunately, we have clear hints from the results of two experiments already described. First, when measuring the resistance of the device as its area is reduced, we obtained that the resistance scales with the inverse of the area (section 4.4.3.2). This **discards a filamentary mechanism**. Second, crystals of this material annealed at 343 K experience a conductivity rise of five orders of magnitude (section 4.4.1.2). This corresponds to a amorphization process that increases the number of grain boundaries, therefore we thought that the conduction was **mediated by grain boundaries**. This result in crystals prompted us to look for signatures of amorphization in our films.

In contrast to usual stack memristive cells (figure 4.20(a)), the planar nature of our devices and their in-plane conductivity (section 4.4.4.2) provide an excellent platform for the *in situ* acquisition of local surface potential maps of the films. We obtained these maps by Kelvin Probe Microscopy (KPM, section 2.1.8). This allowed us to elucidate the conduction and switching mechanisms in the devices.

4.4.5.2 *Surface Potential Maps*

Figure 4.36 depicts representative data of **high conductivity devices** ($\sigma > 1$ S/cm). Figure 4.36(a) and (b) shows the topography and the simultaneously acquired surface potential map of the as-prepared device (before any electrical test). Clear distinct regions with different surface potentials are visible. A similar map acquired after two bias sweeps (figure 4.36(c)) shows a dramatic change in the surface potential distribution. The bottom right area of the film presents now an assembly of patches (with several μm in lateral size) with surface potential differences of few hundred millivolts, in contrast with the featureless top left region. Surface potential images of this device recorded *in-operando*,

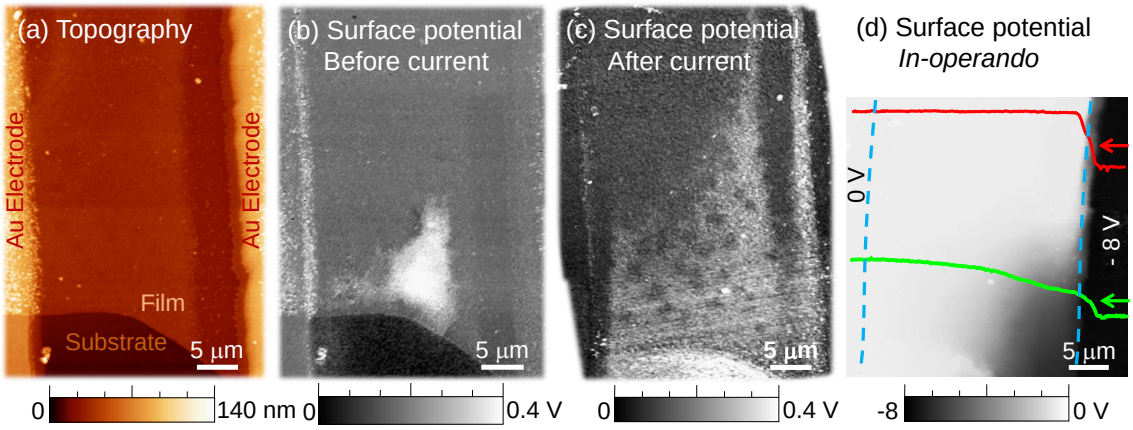

Figure 4.36: Surface potential maps of highly conductive $[Cu_2I_2(TAA)]_n$ films. (a) AFM topographic image of a representative device with no significant topographic features. Film's thickness ~35 nm. (b) Surface potential map acquired by KPM in the same area as panel (a) before applying electrical field between electrodes. (c) Surface potential map acquired in the same area as panel (b) after two bias sweeps. (d) Surface potential map acquired in the same area as the previous panels, while a voltage of -8 V was applied to the right electrode. The red and green lines are the surface potential profiles across the horizontal lines indicated by the arrows in corresponding colors. The blue dashed lines are drawn at the electrode borders.

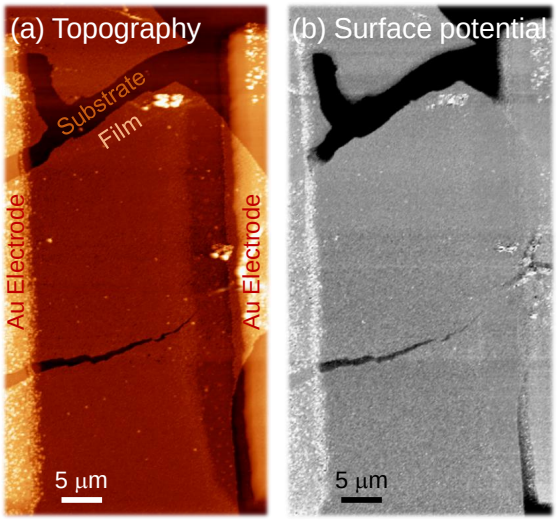

Figure 4.37: Surface potential map of a low conductivity $[Cu_2I_2(TAA)]_n$ film. Representative (a) topography and (b) surface potential map of a low conductivity device where the KPM image appears featureless.

shown in figure 4.36(d), reveal that in the regions with no observable patches in figure 4.36(c), the voltage drop takes place mainly at the contacts with the metal electrodes (red profile in figure 4.36(d)). However, in the regions where we observed patches, the voltage drop occurs all through the film length (green profile in figure 4.36(d)). This ensemble of images allowed establishing a direct **correlation between the areas rich in surface potential patches and high conducting regions**. As expected from these images, devices with **low conductivity** ($\sigma < 0.1$ S/cm) did not show any features in the KPM images (figure 4.37). This, along with observations in crystals, makes it plausible to ascribe the observed **patches/regions in surface potential to different crystallographic structures/orientations** determined by X-ray diffraction (as it has been previously observed in other 2D materials) [266, 267]. It thus follows that the mechanism governing

charge transport in our films is **grain boundary mediated**. In common conductive (ohmic) materials, the presence of grain boundaries usually leads to a decrease in conductivity, however, accumulation of certain charge carriers and emerge of midgap states at these domain walls in insulating materials might render the regions near boundaries much more conductive than the bulk and provide lower resistance paths for charge movement as reported in related coordination polymers crystals [265]. While the structural disorder revealed by X-ray spectroscopy makes it difficult to define the atomic structure at these interphases, the accumulated iodine or sulfur vacancies, as already observed in MoS_2 [267], are good candidates to explain such effect. Independent of the specific cause, grain boundary conduction is certainly a plausible cause to account for the high dispersion of values found for the conductivity of our ultrathin films: a higher (lower) concentration of grain boundaries in an area would lead to a higher (lower) conductivity in it. Hence, the **dispersion of the conductivity would reflect the dispersion in the grain boundary concentration**.

Accordingly, our proposed **HRS or base conduction mechanism relies on the presence of new available electronic states at these grain boundaries**. At the same time the wide band gap or nearly insulating character of the crystal domains would be responsible for its high transparency.

As mentioned above, our devices also show memristive behavior at low-frequency bias sweeps. Surface potential maps of memristive devices with high applied bias (> 3 V) revealed **boundary migration** (see figure 4.38), suggesting that this is the main mechanism involved in memristive behavior. Indeed, the significant change of grain

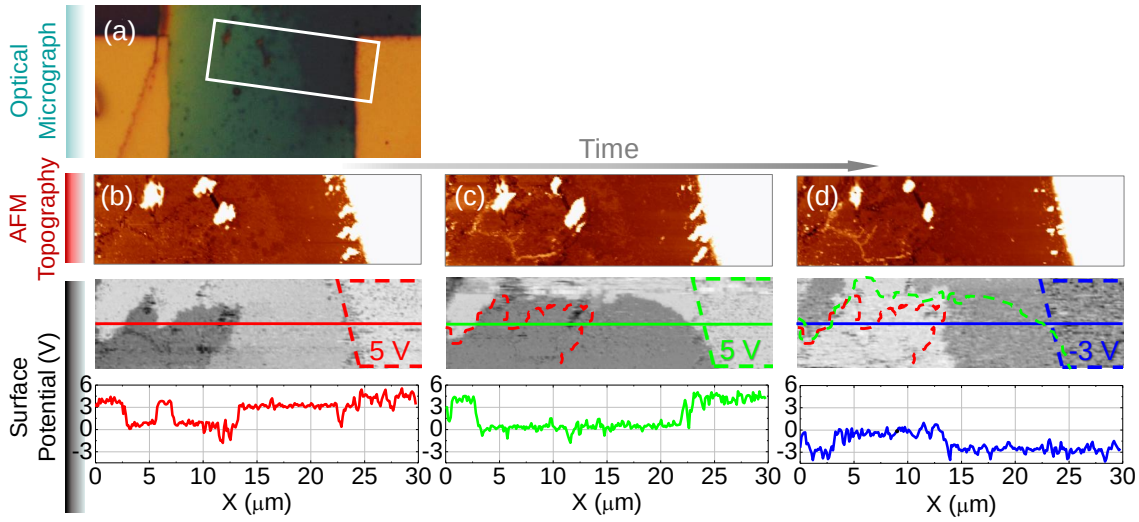

Figure 4.38: Measurement of grain boundary migration. (a) Optical image of the device where subsequent images were acquired. Image size: 59 × 28 μm^2. (b) and (c) AFM topographies and surface potential maps of the region of the device marked in (a) while 5 V were applied to the right electrode (indicated by dotted lines in KPM images). The left electrode is located several microns to the left of each image. It was not scanned to minimize the image acquisition time. The time lapse between (b) and (c) is 3 minutes. (d) Topography and surface potential map of the same region with -3 V applied to the right electrode. The time between (c) and (d) was 3 minutes. Lower panels are the corresponding profiles along the lines in each KPM image. In surface potential maps of (c) and (d) the borders of surface potential regions of the previous images are marked with dashed coloured lines.

boundary distribution after several sweeps in the films shown in figure 4.36 and the easy amorphization at relatively low temperatures (343 K) of the crystals, point towards easy creation and migration of grain boundaries. The highly dynamic character of this process makes its observation very challenging since scanning techniques that allow high spatial resolution always require rastering times in the range of few seconds or even minutes. Yet, we were able to capture the motion of boundaries in some memristive devices by KPM. Figure 4.38(b) and (c) presents two consecutive surface potential images of the same region of a memristive device while applying a bias voltage of 5 V with a time interval of 3 minutes. Expansion and migration of the dark (low surface potential) region is well evidenced when comparing both images. A subsequent applied negative bias of - 3 V (4.38(d)) resulted in the reversed motion of this region, indicating the reversible mobile character of these boundaries. This **grain boundary migration/reconstruction is indeed the most plausible mechanism responsible for the LRS**, with memory of the current flown through the device, which leads to the resistive switching of our devices.

As explained above, the other resistance state (HRS, required for memristive behaviour together with the LRS) is proposed to be related to available electronic states at grain boundaries. Whether the grain boundary migration is caused by the *direct electrostatic force* (as a result of the electric field) or by the *electron wind force* (caused by momentum transfer of the conduction electrons) is difficult to discern from our data. However, the fact that we have observed significant material displacement before failure of devices always at current densities higher than $2{\cdot}10^{-4}$ $\mu A/nm^2$ at room temperature (section 4.4.4.3), points towards an electromigration related mechanism, probably assisted by temperature induced by joule heating. This threshold current density for material displacement is increased by more than one order of magnitude when temperature is lowered to 70 K, and is consistent with the absence of resistive switching at low temperature.

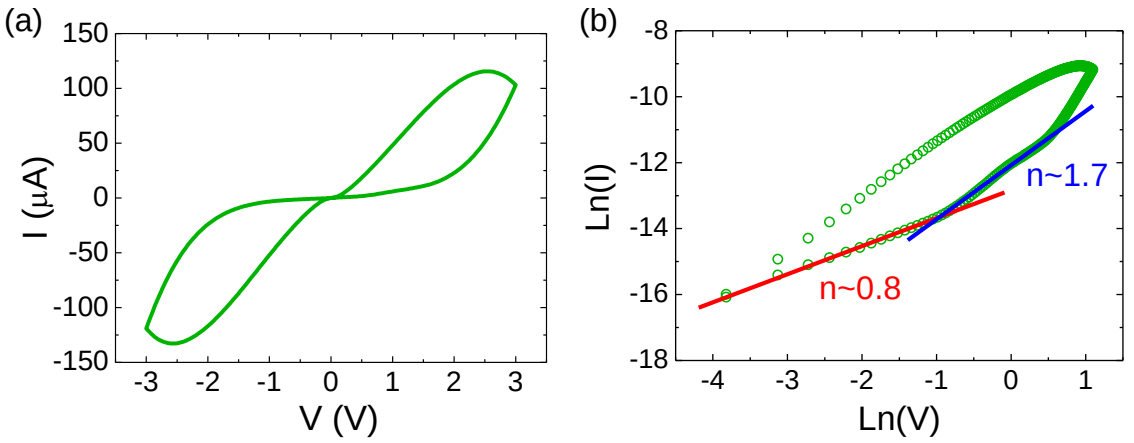

Figure 4.39: IV curve fitting to Space Charge Limited Current (SCLC) model. (a) IV curve of a representative film acquired at 0.062 V/s. (b) The Ln-Ln representation of the positive-bias loop of the IV curve plotted in (a) together with linear fittings showing the slopes (exponent in $I \propto V^n$) of two characteristic regions of typical SCLC [258]: an ohmic part at low voltages and a second region with $I \propto V^2$ where the traps begin to be filled with the injected carriers. In the third region with $n > 2$ all traps are filled up, so the subsequently injected carriers can move in the dielectric film causing the following current increasing.

Further support for the proposed boundary-mediated conduction comes from the observation that the slow initial sweeps in bias of our films are typical of **Space Charge Limited Current (SCLC)** (see figure 4.39). This conduction mechanism is characteristic of dielectric solids with trapped charges due to spatially inhomogeneous resistance [258]: IV curves show a power law dependence $I \propto V^n$, where n increases with bias. In figure 4.39(b) we can distinguish an ohmic part at low voltages, a second region with $I \propto V^2$, where the traps begin to be filled with the injected carriers, and a third region with $n > 2$, where all traps are filled up, so the subsequently injected carriers can move in the dielectric film.

4.4.6 *Comparison of Electrical and RS Performance of $[Cu_2I_2(TAA)]_n$ Films with other Coordination Polymers and Memristive Materials*

The maximum measured electrical conductivities of some CP films and other conductive materials are gathered in table 4.1(2), including the data we obtained for the $[Cu_2I_2(TAA)]_n$ films. As this table reveals, these films present a very high conductivity among CP films.

Material	Max. Conductivity (S/cm)	Source
Cu	$6.5{\cdot}10^5$	[268]
Graphene	$\sim 10^4$ (2)	[10, 75]
$Cu_3(BHT)_2$	~1600	[229]
ITO	~1400	[239]
Polypyrrole	~300	[263]
$[Cu_2I_2(TAA)]_n$	~50	[230]
$TCNQ@Cu_3(BTC)_2$	$7{\cdot}10^{-2}$	[269]
Cu-CAT-1	10^{-4}	[227]
$[Ag(C_5H_4NS)]_n$	$2{\cdot}10^{-5}$	[270]
$[Cu_2Br(IN)_2]_n$	$1.7{\cdot}10^{-5}$	[220]
$[Cu(\mu\text{-}pym_2S_2)(\mu\text{-}Cl)]_n \cdot nMeOH$	$4{\cdot}10^{-7}$	[221]

Table 4.1: Comparison of conductivities at RT for a selection of CP films and other conducting materials.

Table 4.2 shows that the RS performance of the $[Cu_2I_2(TAA)]_n$ films, quantified in terms of R_{off}/R_{on}, is far from that of other memristive materials including some CPs. In addition to R_{off}/R_{on}, other parameters account for the RS performance, such as the endurance (number of cycles a memristive cell can withstand) or the retention time in a resistance state. We did not measure these magnitudes for our films, but some other measurements suggested deficient values for them. Furthermore, the memristive behaviour is obtained only at low voltage sweeps. Therefore, this CP is not suitable for technologic applications. However, other similar polymers can be synthesized inspired by $[Cu_2I_2(TAA)]_n$ towards such applications.

2 As graphene does not have a defined thickness, the 3D conductivity has no sense. We have computed the value shown in the table, $\sim 10^4$ S/cm, from the 2D conductivity given in [10] (~1 mS) and the 2D resistivity from [75] (~500 Ω/□) assuming a thickness of 0.3 nm.

Material	R_{off}/R_{on}	Source
Peripherally substituted subphthalocyanine films	10^6-10^8	[271]
Ag–TCNQ nanowires	10^4	[272]
$SrTiO_3$ films	$>10^3$	[273]
MoS_2 single layers	10^3	[267]
Ag/Rb-CD-MOF single crystal/Ag	150	[274]
Co(III) Conj.Pol.+azo-aromatic backbone films	100	[275]
$[Cu_2I_2(TAA)]_n$ films	30	[230]
PMMA-MAPOM films	~5	[276]

Table 4.2: Comparison of R_{off}/R_{on} ratios for a selection of memristive materials, including some coordination compounds.

4.5 MECHANICAL PROPERTIES OF $[Cu_2I_2(TAA)]_n$ FILMS: ROBUSTNESS

In section 4.3 we already saw that $[Cu_2I_2(TAA)]_n$ films could be suspended on circular holes in SiO_2 substrates. This already indicated mechanical robustness (and maybe a certain degree of hydrophobicity) of the films.

These resulting nanodrums allowed us to measure the mechanical properties of the films by indentation experiments with AFM tips. We followed the same procedure used in chapter 3. Indentation curves were performed with Si AFM tips of ~2.8 N/m spring constant and 20 nm radius. Under these conditions, the radius of the tip is much smaller than the radius of the drumhead, and therefore the force *vs.* indentation F(δ) curve in

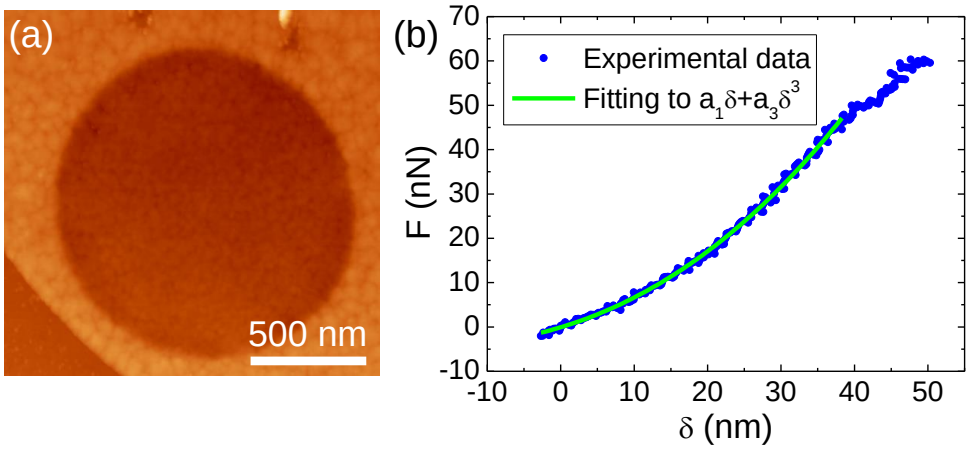

Figure 4.40: Mechanical robustness of $[Cu_2I_2(TAA)]_n$ films. (a) Representative AFM image of a 1.5 μm diameter and 10 nm thick $[Cu_2I_2(TAA)]_n$ drum where indentations were performed. (d) Representative F(δ) curve acquired on drumhead of panel (a) that yields a E_{3D} of ~11 GPa. The bending of the curve to lower forces at high δ suggests certain plasticity of the material (these data were not considered in the fitting).

the elastic region can be well approximated to equation 3.7 introduced in section 3.4.1 of chapter 3. This equation can be simplified to the following expression:

$$F = \pi\sigma_0 \cdot \delta + \left(\frac{q^3 E_{3D} t}{R^2}\right) \cdot \delta^3 \tag{4.5}$$

where the bending regidity term (first term in equation 3.7) was removed assuming that it is negligible compared to pretension term (first term in 4.5). F is the loading force, δ is the indentation at the central point, σ_0 is the pretension accumulated in the sheet during the preparation procedure, $q \approx 1$ is a factor that accounts for the Poisson ratio of the material, R is the drumhead radius, t is the thickness of the measured membrane, and E_{3D} is the elastic modulus of the film. A representative $F(\delta)$, performed on the drumhead shown in figure 4.40(a), is depicted in figure 4.40(b). The fitting of our experimental curves to equation 4.5 yielded values of $\mathbf{E_{3D} = 11 \pm 3\ GPa}$.

In addition to the stiffness, we could also observe the **breaking strength** of the membranes by loading some drumheads up to the failure point that was at 170 nN with a 30 nm radius tip. The breaking strength can be roughly estimated by the following expression presented in chapter 3:

$$\sigma_{max}^{3D} = \sqrt{\frac{F_{fr} E_{3D}}{4\pi R_{tip} t}} (Pa) \tag{4.6}$$

where F_{fr} is the force at which fracture takes place and R_{tip} is the radius of the AFM tip. This leads to an estimation of $\sigma = \mathbf{1.0 \pm 0.3\ GPa}$, showing that these ultrathin films can sustain quite large deformations without breaking. Notice that this simple expression for the breaking strength is for a linear material (the model from where it is derived ignores nonlinear elasticity) and tends to overestimate this figure.

For the sake of comparison, the commonly accepted values for E and σ_{max} in graphene are 1 TPa and 0.13 TPa, respectively [44]. Importantly, even for loads higher than the breaking strength, we have never observed catastrophic failure of our films (characteristic of laminar inorganic crystals), in fact the notch created by the tip does not propagate through the films. This observation suggests the presence of defects in the atomic lattice that stabilize the films against mechanical failure [199]. Besides the concrete values of these mechanical properties, which are lower than those reported in covalent polymers [277], our observations sustain that, contrary to what one might expect, coordination bonds allow producing robust, ultrathin, flexible, and mechanically stable films.

4.5.1 *Comparison of Mechanical Properties of $[Cu_2I_2(TAA)]_n$ Films with other 2D Materials*

Table 4.3 collects the values of Young's modulus of several 2D materials made of different elements, with different structures and chemical bondings. As expected, covalent-bond materials present the highest elastic moduli while the materials based on coordination bonds the lowest. Among 2D coordination polymers, one of the most investigated from the mechanical point of view is the $ZnO_4(BDC)_3$ (known as MOF-5 or Isoreticular MOF-1) [215]. This MOF has an experimental E_{3D} slightly lower (7.9 GPa [278]) than that of $[Cu_2I_2(TAA)]_n$ films (11 GPa). Another MOF more recently studied, $[Cu(\mu\text{-}pym_2S_2)(\mu\text{-}Cl)]_n$, also presents a lower elastic modulus [216]. Hence, the nanosheets of$[Cu_2I_2(TAA)]_n$ are among the stiffest CPs.

Material	E_{3D}(GPa)	Bond	Source
Graphene	1000	Covalent	[44]
MoS_2	330	Covalent	[92]
Polyimine based 2D polymer	267	Covalent	[277]
Black Phosphorus	46	Covalent	[179]
Fluorohectorite 2D clays	20	Ionic	[279]
$[Cu_2I_2(TAA)]_n$ films	11	Coordinate	[230]
$ZnO_4(BDC)_3$ (IRMOF-1)	7.9	Coordinate	[278]
$[Cu(\mu\text{-}pym_2S_2)(\mu\text{-}Cl)]_n$ MOF	5	Coordinate	[216]

Table 4.3: Comparison of Young's modulus of different 2D materials.

4.6 CONCLUSIONS

In summary, we report a bottom-up approach to fabricate $[Cu_2I_2(TAA)]_n$ coordination polymer films, based on cheap building blocks (Copper(I) Iodide and thioacetamide). They have a thickness down to 4 nm, extend across macroscopic regions and are highly transparent. Furthermore, the films withstand free-standing geometry with elastic constants of 11 GPa and 1 GPa for the Young's modulus and breaking strength, respectively. Additionally, these films exhibit in-plane electrical conductivity up to 50 S/cm that is controlled by the concentration of grain boundaries. Interestingly, they present intrinsic memristive response. We have unraveled the working mechanism for this behaviour and showed that it is mediated by the migration of grain boundaries. The easy creation and motion of these boundaries suggest that they could be manipulated (through temperature quenching methods for instance) to create novel devices with tunable electro-mechanical properties.

5

DEVELOPMENT OF PROBE-ASSISTED NANOWIRE CIRCUITRY (PANC)

5.1 MOTIVATION

The motivation of this work goes back 20 years ago in the Nanoforces group with one of its most important research lines: measurement of electrical transport in mesoscopic systems (STM break junctions, carbon nanotubes, DNA and graphene). In fact, I took then my first steps in AFM and conductivity measurements in some of such systems during my first stay in the laboratory. At that time, the electrical contacts on those nanoobjects were successfully performed (by thermal evaporation of metals) but they were larger than desired in some applications. There was a lack of control of the positioning of the electrical contacts, furthermore the AFM (or STM) was always required to fulfill the electrical measurements (having the standard C-AFM configuration).

Eventually, a new research line started to flourish in the laboratory: measurement of mechanical properties of 2D materials (graphene, coordination polymers and black phosphorus). At the same time the group began to carry out electrical measurements, this time in new 2D materials, specifically in few-layer antimonene flakes. That is when Probe-Assisted Nanowire Circuitry (PANC) emerged as a technique to achieve controlled, reliable, clean and versatile electrical nanocontacts that allows the electrical characterization of antimonene. Dr. Pablo Ares had already started the development of PANC in his PhD thesis, however, at that point, the C-AFM was still needed to accomplish the measurements. Here I present further development of this technique: from the obtaining of a stand-alone device (not requiring the C-AFM) to the realization of complex nanocircuits and finally approaching nano- and molecular electronics. PANC constitutes another useful methodological technique conceived and developed in the Nanoforces group, as many other instrumental developments [37, 61, 244, 280].

5.1.1 *Electrical Nanocontacts Problem*

Some challenges of nanoelectric circuitry are the design and assembly of devices incorporating emerging materials and/or architectures and the understanding of their properties. Electrical characterization of nanomaterials frequently implies the fabrication of metal electrodes. The standard option of choice to accomplish this task is Electron Beam Lithography (EBL or e-beam). There are **other techniques** used to electrically contact nanoobjects, namely, the Atomic Force Microscopy (AFM) and the ones used for the fabrication of metallic atomic-size contacts. Among the latter ones, we find the Scanning Tunneling Microscopy (STM), the Mechanical Controlable Break Junctions (MCBJ) and others not so widespread such as molecular trapping, Transmission Electron Microscopy (TEM), electromigration technique and electrochemical methods [34, 281]. Figure 5.1 summarizes the most common techniques used to electrically contact nanoobjects.

EBL [10, 285, 286] is a Scanning Electron Microscopy (SEM) based technology developed in the sixties by M. Hatzakis [287]. EBL comprises the following **steps** (see figure 5.2):

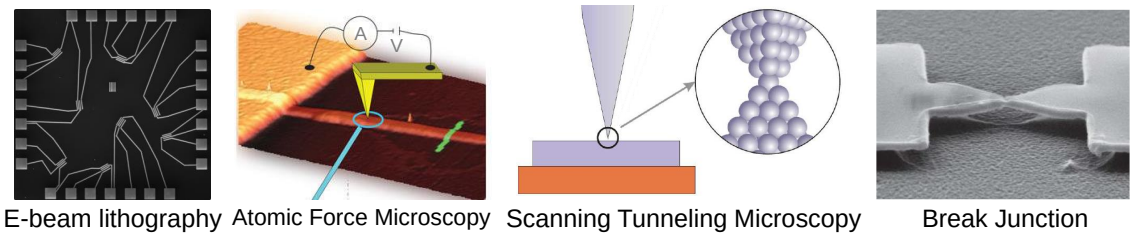

Figure 5.1: Main existing techniques used to electrically contact nanoobjects. Sources: [34, 282, 283].

(i) deposition of a polymer mask, called resist that is usually poly(methyl methacrylate), onto the sample surface, (ii) drawing of the custom circuitry onto the polymer using a computer-controlled focused electron beam that cracks the polymer chains, (iii) removal of the marked regions using an organic solvent, (iv) deposition of a metal layer, (v) final removal of the polymer (lift-off) leaving the custom circuit on the surface. EBL is a well-established technique with thousands of users worldwide. The final resolution of EBL ranges between 30-2 nm (30 nm for standard EBL) that is good enough for multiple applications in nanotechnology [288]. However, it presents some **drawbacks**, as the need of an expensive computer-controlled SEM, the exposition of the samples to vacuum and chemicals that might damage the nanoobjects, and the presence of residues left by the polymer mask. In addition, the circuits made by EBL are not reconfigurable: once they have been fabricated it requires a tremendous effort, if possible at all, to modify or upgrade them.

The **AFM**, developed in the eighties [38], can work in very different environments: liquids, air ambient atmosphere and ultrahigh vacuum at cryogenic temperatures. Apart from imaging with resolution down to the atomic range [289], AFM has also nanolithography modes. In the nineties, Dip-Pen lithography and local oxidation [95, 96, 98] were proposed for the fabrication of nanocircuits. A variation of the AFM is the so-called Conductive AFM (C-AFM, introduced in section 2.1.7) that measures simultaneously the force and the current in a nanoobject already contacted by other electrode. It uses a metal-covered tip that acts as a second mobile electrode. None of these techniques deliver nanocircuits with the low electrical resistances provided by EBL [290]. Furthermore, Dip-Pen lithography and local oxidation are restricted to very few special applications.

In the **STM** [1] the tip can be indented into a metal surface and carefully withdrawn until an atomic size contact or short wire is formed [291]. The advantages of the STM for this purpose are the speed and the HV clean environment, but it also presents some drawbacks: the exact atomic configuration of the atomic-contact cannot be measured directly, the limited stability with respect to the change of external parameters and the short lifetime

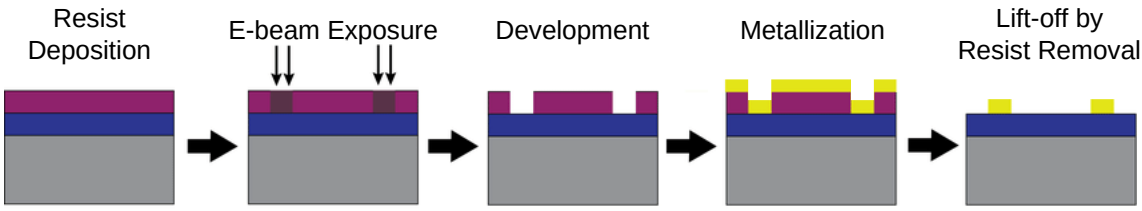

Figure 5.2: E-beam lithography process description. Adapted from: [284].

of the contacts because of the sensitivity to vibrations. The STM can be combined with an AFM, the former registers the current while the latter the force necessary to form or break the contact [292]. Some issues related to stability can be improved working at criogenic temperatures, but this requires very complex and expensive experimental setups.

In a **MCBJ** [293] a suspended metallic bridge is fixed on a flexible substrate, which is mounted in a bending mechanism consisting of a pushing rod and two counter-supports (see figure 5.3). The position of the pushing rod is controlled by a motor or piezo drive. The electrodes on top of the substrate are elongated by increasing the bending of the substrate. In order to break a junction to the tunneling regime, considerable bending of the substrate is required. MCBJ mechanisms can operate in various environments: ambient conditions, vacuum, very low temperatures or liquid solutions. The latter one is of particular interest for the study of single molecule junctions. This technique requires the use of the EBL and metal deposition by evaporation for the nanofabrication of the bridge. The disadvantages of MCBJs are the small speed and the fact that the surrounding area of the contact cannot be easily scanned. The sample preparation does not require clean conditions because the contacts are only formed during the measurement by breaking the bulk of the electrodes.

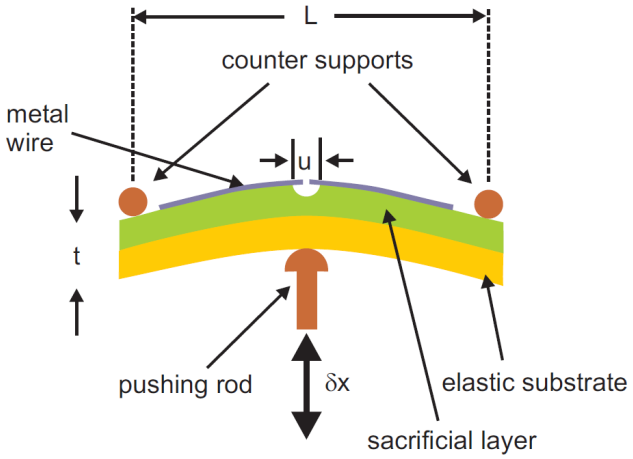

Figure 5.3: Working principle of the MCBJ (not to scale). Extracted from: [34].

Carbon nanotubes based circuitry was developed in 2002 as an attempt to characterize the electrical transport properties of nanoobjects by Thelander and coworkers [294]. They manipulate the carbon nanotubes with SPM to electrically contact nanometer-scaled objects. However, the dependence of the nanotubes electronic gap with the chirality, the variation of their electrical resistance upon mechanical deformation and, more importantly, the high electrical resistance observed in nanotube junctions (inherent to systems with strong covalent bonding as carbon nanotubes) hampered the use of this technique.

5.1.2 *Main Goal of this Chapter*

In 2010 Yang Lu *et al.* demostrated the **cold welding** of metal nanowires, and predicted that it will have potential applications for electrical connectivity at the nanoscale [118]. Our goal is to develop a technique that, by leveraging the nanomanipulation and cold welding of gold nanowires with the AFM tip, allows the fabrication of highly conductive and

complex nanocircuits. We have named this technique **Probe-Assisted Nanowire Circuitry** (**PANC**). As we will see in more detail, this methodology has a **gradual reduction of the dimensions of the electrodes**: macroscopic wires (~ mm), printed circuit board pads (~ mm), microwires (~ μm), microelectrodes (~ μm - hundreds of nm) and finally nanowires (or even nanorods or nanoparticles) (~ nm).

The first results of PANC, obtained by Dr. Pablo Ares, revealed **low electrical contact resistance** between NW-NW and NW-nanoobject, and **high reproducibility and stability** of the so assembled nanocircuits [37]. Following developments of the methodology, made along this thesis, proved the capabilities of this new AFM-based nanoelectrode fabrication technique: the **robustness** of the created circuits to **low temperature** and vacuum, the **reconfigurable character** of the electrodes, and the possibility of fabricating several-electrode **stand-alone devices**, which can be inserted in conventional experimental setups for further electrical characterization. In addition, we were able to conduct an experiment showing the potential of PANC for **molecular electronics**. All these features open a wide range of possible applications of PANC that in the near future can broaden the narrow catalogue of existing techniques for nanofabrication.

The work presented is gathered in a manuscript which is currently under revision in a high impact factor research journal. The title of such work is **"Probe-Assisted Nanowire Circuitry"** and its authors are Pablo Ares*, **Miriam Moreno-Moreno***, Consuelo Moreno, Félix Zamora, Cristina Gómez-Navarro and Julio Gómez-Herrero. Pablo Ares started the research by conducting the first experiments to prove the technique and a more recent one to show its spatial resolution. I fabricated most of devices shown in this paper, obtained using PANC, and performed different experiments on them to demonstrate the capabilites of the technique. Consuelo Moreno synthesized the gold nanowires. Félix Zamora, Cristina Gómez-Navarro and Julio Gómez-Herrero designed the experiments and assist during their development.

5.2 GOLD NANOWIRES

Gold nanowires (Au NWs) are suggested as a perfect choice to connect different elements in electrical nanodevices [295]. This is due to two main reasons: their high conductance and, unlike other metal nanowires like silver or copper, their resistance to corrosion or oxidation. The synthesis of single crystalline silver or copper nanowires dates back in the late nineties [296–298]. However, that was not the case of gold nanowires, on the contrary, their chemical synthesis was limited to nanowires either very thick (> 100 nm) or very short (< 300 nm) [299, 300] until 2008. In that year, Kim *et al.* allowed the synthesis of reproducible Au NWs at room temperature in acidic solutions [301]. These NWs had tunable diameters between 16 and 66 nm, lengths up to 10 μm and well-defined surfaces. Further improvements in nanowire monodispersing and scaling lead nowadays to commercial available gold, and other metals, nanowires [302–304].

In Nanoforces group, at the very early stages of the development of PANC methodology, Dr. Pablo Ares started to use commercial Au NWs from Sigma Aldrich S. A. [302] without success. Afterwards, he adsorbed Au NWs from Nanopartz Inc. [303] on SiO_2 substrates obtaining good quality NWs. They follow a gaussian distribution for the diameter of 49 ± 6 nm. Their lengths range from hundreds of nm to 9 μm. This kind of Au NWs was used in experiments shown in section 5.5. After that, I received the baton of continuing developing PANC. I was able to deposited Au NWs from Nanopartz Inc. on substrates,

however they were shorter and had a lower concentration. The NWs degraded after some months. Countless tests using fresh new NWs from the same company revealed deficient NWs (very few, too short, dirty). Finally, we synthesized our own NWs in collaboration with Prof. Consuelo Moreno, member of the inorganic chemistry department of U.A.M. She provided us not only with Au NWs but also with gold nanoparticles, used for other purposes. For the rest of the experiments presented in the chapter we used the Au NWs made by Prof. Consuelo Moreno. Figures 5.4 and 5.5 show these home-synthesized Au NWs adsobed on SiO_2 and their dimensions statistics, respectively.

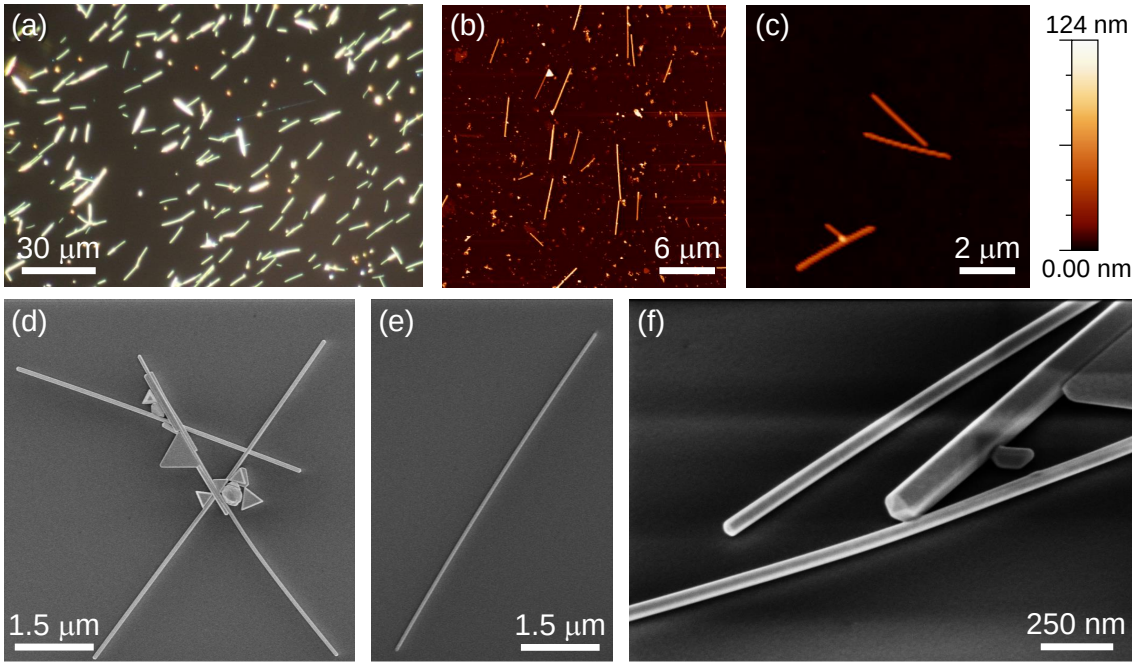

Figure 5.4: Home-synthesized gold nanowires adsorbed on flat SiO_2. (a) Dark field optical microscope image. (b) and (c) AFM topographic images. (d-f) SEM images. In (d) a few parallel NWs are stack together near the center of the image. Panel (e) shows an isolated NW. In (f) the facets and pentagonal cross section of the NW in the center of the image are clearly visible.

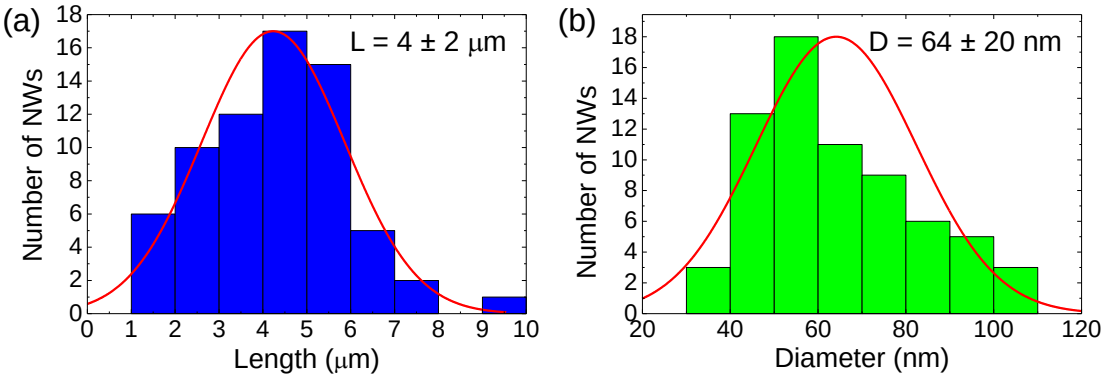

Figure 5.5: Histograms of the length (a) and diameter (b) of home-synthesized gold nanowires. Gaussians fits provides 4 ± 2 μm for the length and 64 ± 20 nm for the diameter (mean ± standar deviation).

5.2.1 *Synthesis of Gold Nanowires*

The home-synthesized Au NWs were prepared following a modification of the literature method by Kim *et al.* [301], based on the well-established three-step protocol for nanorods synthesis published by Jana *et al.* [300]; its synthesis first involves the preparation of aqueous gold seed nanoparticle of 3-5 nm by reduction of chloroauric acid ($HAuCl_4$) solution by sodium borohydride ($NaBH_4$) in the presence of sodium citrate. For the growth of nanowires, the seed particles are added to a growth solution containing a mixture of $HAuCl_2$ (Au^+) which was reduced from Au^{3+} salt by a weak reducing agent as ascorbic acid in the presence of a structure directing agent as CTAB. The growth was allowed to continue for at least 48 h. See appendix E for additional details. During the synthesis there is a number of critical factors, such as the temperature. In fact, some Au NWs dispersions provide fewer or shorter NWs due to slight variations of the temperature. This fact is mainly attibuted to the low solubility and the tendency towards precipitation of CTAB at temperatures below 25°C. Furthermore, the purity of the CTAB also plays an important role in the synthesis, leading a higher NWs yield when using CTAB from certain companies [305].

5.2.2 *Cold welding of Gold Nanowires*

Cold welding is a solid state welding process in which two materials are joined without heat or fusion. It was used centuries ago as reported by a encyclopedist of the 12th century [306]. Bulk cold welding is achieved either by a high applied normal/frictional load or in atomically clean flat ductile surface in ultra-high vacuum environment [118]. In 1991 an article published in Science [307] demostrated experimentally the cold welding between thin gold films under low applied pressure at ambient conditions. In 2010 Lu and co-workers [118] cold welded Au NWs with diameters between 3 and 10 nm by simply contacting them by mechanical manipulation (see figure 5.6). They also showed experimentally the cold welding between silver NWs and between a Au NW and a Ag NW.

It is already an established fact that, at the nanoscale, the diffusion barrier for a single metal atom on a clean metal surface is so low that thermal activation even at RT is enough to trigger atomic diffusion [308]. But the creation of an isolated atom demands higher energy, which is provided by mechanical manipulation of nanoobjects [118]. This allows clean metal surfaces, such as that of gold, to flow like a liquid at RT, which is far below the melting point of pure bulk gold (1064°C). Atomic diffusion and surface relaxation are the two key processes responsible for such fluid-like behaviour of metallic surfaces at the nanoscale. Thus, highly curved surfaces and entities with high surface-to-volume ratios either become filled, fused, or welded to form larger nanostructures with the aim to reduce surface free energy or the chemical potential, which acts as a driving force for the cold welding process [309]. Other mechanisms, which vary depending on the nanoobjects' morphology and chemistry, can assist or enable the cold welding (capillary forces, rotation of nano-objets, and migration of grain boundaries [309]).

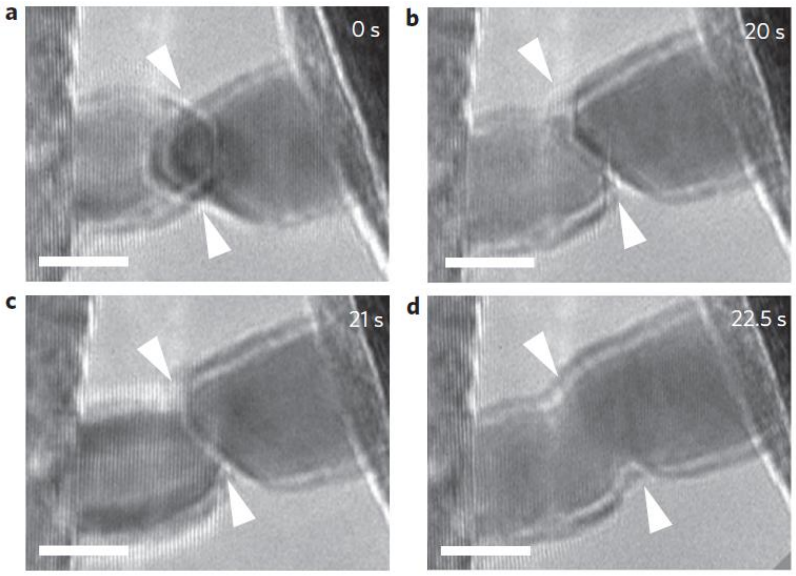

Figure 5.6: Welding process of two gold nanorods. The right one is approached to the left one and the welding is completed after 1.5 s. Triangles indicate the front edges of both nanorods. Process carried out in a high-resolution transmission electron microscope. Scale bars: 5 nm. Source: [118].

5.3 PANC PROCEDURE

This nanocircuit fabrication technique is a complex process that involves numerous steps, many of them common to EBL. Figure 5.7 depicts the steps required for the realization of nanocircuits by means of PANC:

1. Preparation of the nanoobjects on a flat insulating substrate
2. Fabrication of micrometer-sized electrodes
3. Au nanowires adsorption
4. Wire soldering
5. AFM manipulation of the Au NWs to form continuous paths
6. Checking and improving of electrical contacts

The paragraphs below give a brief description of these steps. Further information regarding any of them can be found in appendix F.

Preparation of the nanoobjects on a flat insulating substrate. The samples studied in this work are 2D materials, multiwalled carbon nanotubes (MWCNTs) and finally benzene dithiol (BDT) molecules. 2D materials were prepared by microexfoliation while MWCNTs were adsorbed by drop casting. In the case of BDT we followed another approach in which the orders of the first steps were modified. We will describe it in section 5.9.5. Depending on the nature of the nanoobjects, **this first step could (or should) be conducted after the fabrication of the microelectrodes or even after the NWs adsorption.** For instance, a molecule that can be damaged when exposed to the conditions of steps 2 and 3 should

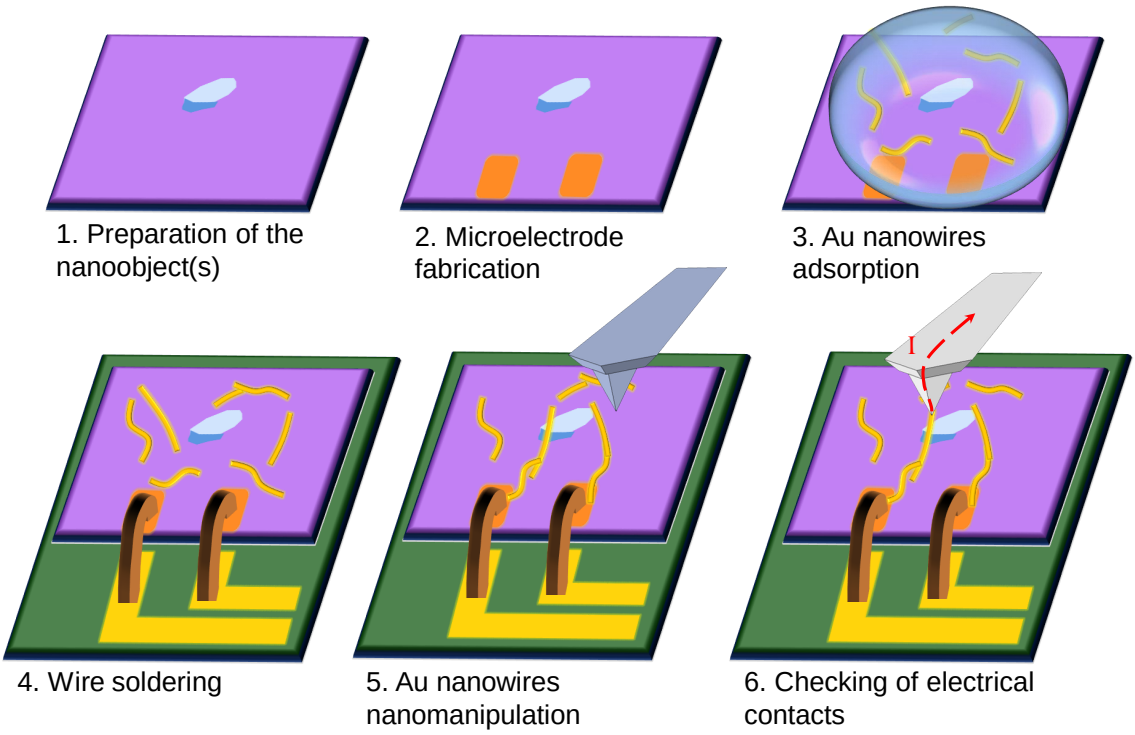

Figure 5.7: Steps of PANC process.

be adsorbed on the substrate after those stages. See section F.1 for additional information regarding this step.

Fabrication of micrometer-sized electrodes. Microelectrodes, together with macroscopic wires, are required to link the PANC nanoelectrodes (made of Au NWs) with the macro-scale measuring devices. **Any conventional microelectrode fabrication procedure** can be employed at this stage: thermal evaporation, sputtering, e-beam evaporation, etc. To achive the desired shapes and location of the microelectrodes stencil masks can be used, or even the complete EBL procedure can be conducted provided that the nanoobject(s) can bear it. In this work, we have always performed thermal evaporation with stencil masks. For more details concerning this process see section F.2.

Au nanowires adsorption. It consist of depositing Au NWs from a water suspension by careful drop casting. Several depositions are usually needed to reach an appropiate concentration of NWs in the sample. More details about this process can be found in section F.3.

Wire soldering. The sample containing the nanoobjects, the Au NWs and the microelectrodes, is usually mounted on a PCB board that has some pads connected to macroscopic wires. These wires will be connected to the transport measuring setups. The microelectrodes in the sample have to be electrically connected with the pads. Wire bonding is the standard method to achieve that connection, not only in research but also in semiconductor device fabrication. It links a microelectrode with a pad of the PCB through a metallic wire welded in each of them with the aid of heat, preassure and ultrasonic energy [310]. Other techniques can be employed. Here, we used an alternative method: a metallic wire glued to microelectrode at one side and to the pad at the other side by means of conductive epoxy. To go deeper into this topic, read section F.4. This step must

be conducted always after the Au NWs adsorption, otherwise the NWs disperion flows through the small gap between the sample surface and the wire(s) due to capillarity.

AFM manipulation of the Au NWs to form continuous paths. To accomplish this task, we first image the sample in amplitude modulation mode (AM-AFM), which ensures low tip-sample forces avoiding unwanted NW motion. Then, we bring the tip into hard contact with the substrate and we move it along a predefined trajectory manipulating the Au NW. Finally, we lift the tip back to AM-AFM mode to image the results of the manipulation. When two NWs are brought into mechanical contact, as a consequence of the high surface area-to-volume ratio, they cold weld spontaneously [118]. See section F.5 for much more detailed information about NWs manipulation.

Verification and improvement of electrical contacts. Once the nanowires are assembled to form a path, its conductivity must be checked. For that purpose we conduct IV curves on top of the Au NWs with a conductive AFM tip (C-AFM configuration) at different path distances from the microelectrode. If there is a junction with a very high resistance or even not electrically connecting two NWs at all, the NWs are manipulated

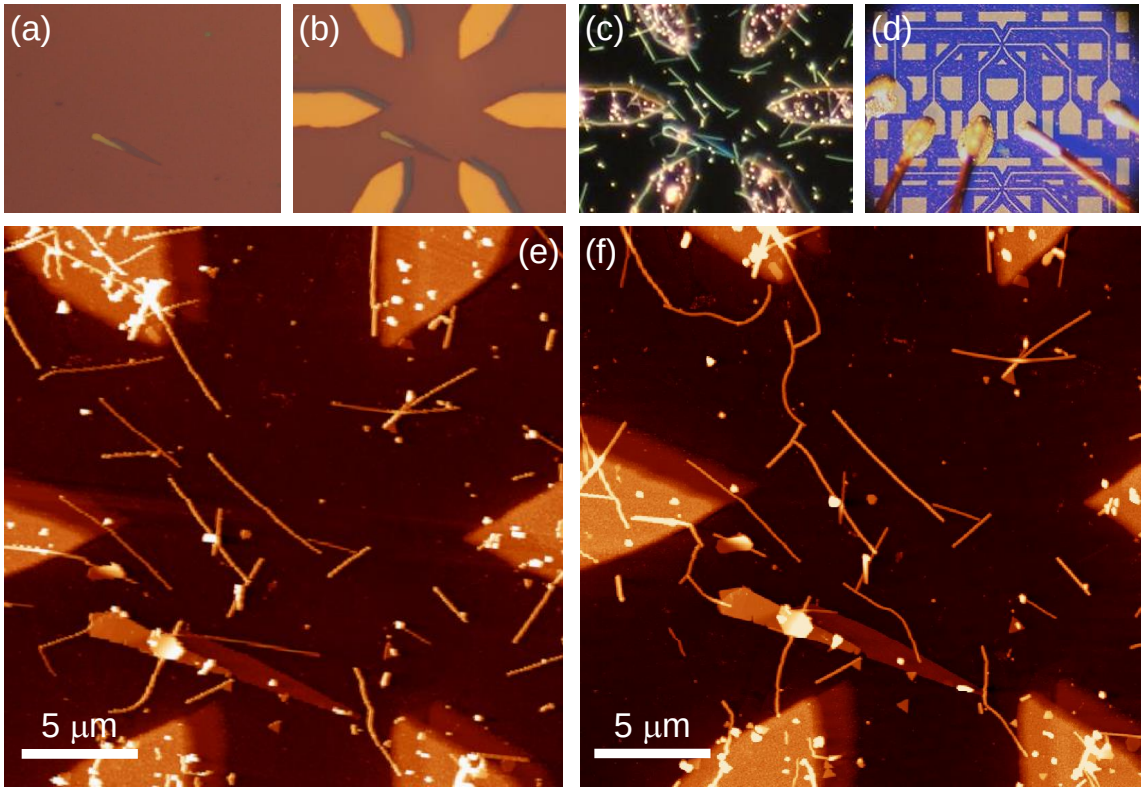

Figure 5.8: Fabrication of a nanocircuit by PANC technique. The resulting nanocircuit is composed of a few-layer graphene flake, four Au NWs paths that connected it to four microelectrodes which are connected to macroscopic wires. (a) Micrograph of an exfoliated flake on SiO_2 substrate. (b) Micrograph of Cr/Au microelectrodes obtained by thermal evaporation on sample of panel (a). (c) Dark fiel optical image of the same sample after the adsorption of Au NWs. (d) Micrograph of the sample once the wire soldering with conductive eapoxy is conducted in five microelectrodes. (e) AFM topography of the gap among the microelectrodes and the flake, before NWs manipulation. (f) Same as (e) after NWs manipulation showing four Au NWs paths connecting the flake with four microelectrodes. Images' sizes: (a-c) 33×44 µm^2, (d) 830×1150 µm^2, (e-f) 25×25 µm^2.

again until a linear IV curve is obtained with a low resistance (from few to ~20 kΩ depending on the conductive tip used). The electrical contact between the nanoobject and the last NW of the path (which should be partially on top of the nanoobject) can be also poor. It can be optimized by indenting with the AFM probe onto the NW, pushing the NW agaisnt the nanoobject. This should preferably be done while a voltage is applied between the ends of the nanoobject. More details about this procedure, the suitable AFM tips, and some examples are described in section F.6.

Figure 5.8 depicts the fabrication of a nanocircuit using PANC methodology. The nanocircuit is composed of a few-layer graphene flake connected to four microelectrodes. Figure 5.9 is a picture of the resulting device composed of the sample with the nanocircuit, wires, PCB board and macroscopic cables).

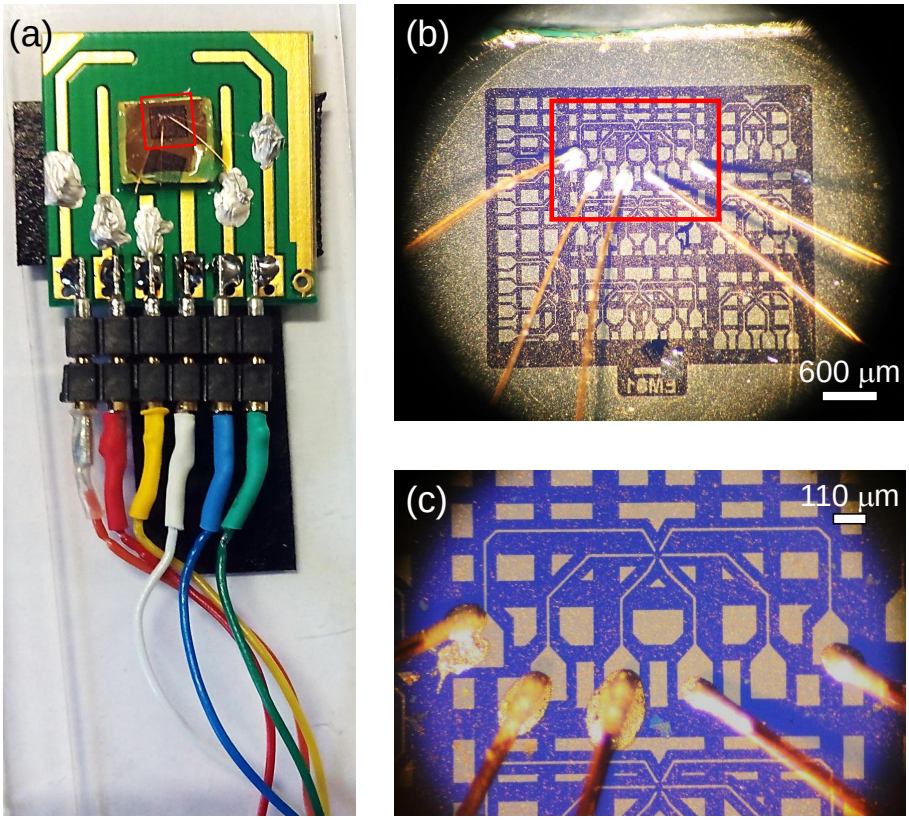

Figure 5.9: Device containing a PANC nanocircuit. The nanocircuit is the one shown in figure 5.8(f). (a) Full device image. (b) Optical micrograph of the area inside the red rectangle in (a). (c) Optical micrograph of the area inside the red rectangle in (b).

5.4 POSSIBLE CIRCUIT TOPOLOGIES

PANC can provide several circuit topologies depending on the number of Au NWs electrodes employed to contact the nanoobject. Some of them are depicted in figure 5.10:

(a) **1 Au NWs electrode + C-AFM**: one NWs path connects one microelectrode with the nanoobject, the second electrode is a mobile conductive AFM tip that closes the circuit.

(b) **2 Au NWs electrodes** (2-wire sensing setup, described in section 2.2.2): two paths are fabricated to make the electrical contact between two microelectrodes and the nanoobject. This setup is usually discarded for nanoobjects with low electrical resistance, as the electrical contact resistance of the circuit elements can be much higher than the intrinsic electrical resistance of the nanoobject.

(c) **3 Au NWs electrodes**, where one of them can be used to apply a **lateral gate voltage**.

(d) **4 Au NWs electrodes** (4-wire sensing setup, section 2.2.2) to measure the electrical resistance of the nanoobject without contact resistance.

(e) ***n* Au NWs electrodes**: from a general point of view, PANC can provide a n-terminal scheme with n Au NWs electrodes.

(f) A **back-gate voltage** can be applied in any configuration if using an appropriate substrate (as for instance standard SiO_2/Si substrates).

In this PhD nanocircuits with topologies (a), (b) and (d) were fabricated. All circuit topologies except (a) are stand-alone devices in the sense that they are fully independent of the AFM used to build them. Consequently, they can be taken to other experimental setups for further characterization.

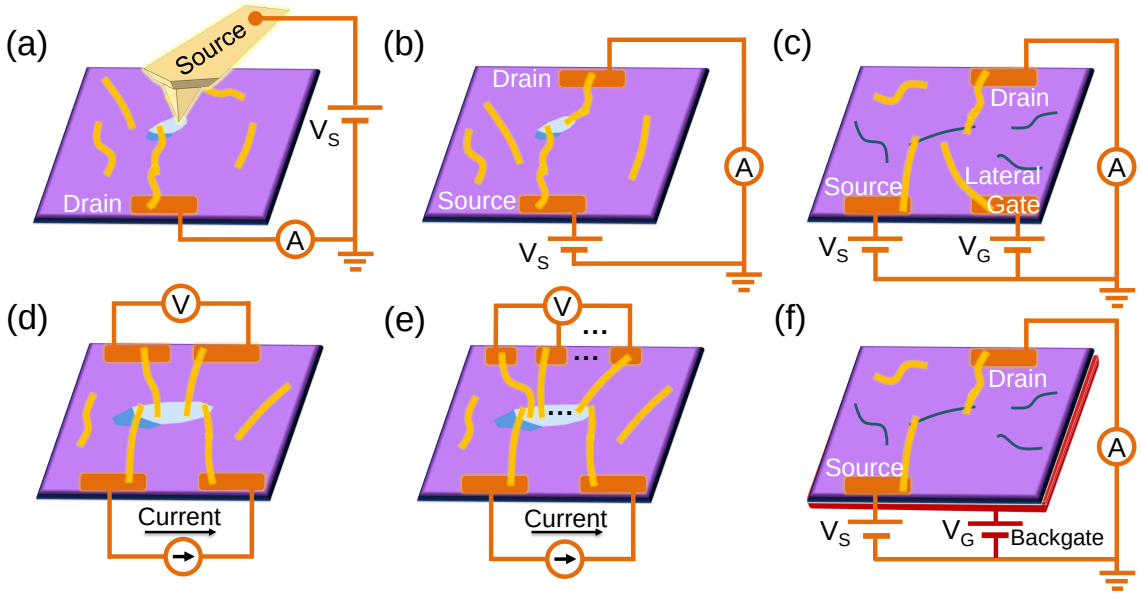

Figure 5.10: Possible PANC nanocircuits' topologies. (a) 1 Au NWs electrode + C-AFM. (b) 2 Au NWs electrodes. (c) 3-terminal design where one of the Au NWs paths is used to apply a lateral gate voltage. (d) 4 Au NWs electrodes implementing the 4-wire sensing setup. (e) A general n-terminal configuration. (f) A 2-terminal design with a back-gate voltage.

5.5 PROOF OF CONCEPT OF PANC: 1 TERMINAL + C-AFM CONFIGURATION

As it was already introduced in the motivation of this chapter, the origin of PANC goes back to the characterization of the electrical transport properties of few layer antimonene

flakes [19]. To this end Diego Aldave, Dr. Pablo Ares, Dr. Eduardo Lee, and professor Julio Gómez-Herrero followed the standard procedures using EBL to fabricate the nanocircuitry. For unknown reasons, probably related with contamination or not enough spatial resolution, they could never measure electrical current through the flake. After some attempts, they envisioned PANC as an alternative technique for the electrical connectivity of those flakes. Then, Dr. Pablo Ares connected a gold microelectrode with several few layer antimonene flakes through a remarkably long (150 μm) Au NWs electrode using PANC. This allowed him to conduct not only the measurement of the electrical response of the flakes, but also the electrical characterization of a long Au NWs path, which is crucial to address the validity of PANC. Another experiment that assesses the suitability of PANC was carried out by Dr. Ares as well: the measurement of the known sheet resisvity of a few-layer graphene flake using PANC.

Althoguh I was not involved in the aforementioned experiments, they should be included in this chapter because they constitute a robust proof of concept of this new methodoly.

5.5.1 *Resistance vs. Length of a long Au NWs electrode*

Figure 5.11(a) shows a dark field optical microscope image where a **150 μm long path formed by 93 Au NWs** (surrounded by a cyan line) connects three different few layer antimonene flakes (inside small squares) to a gold microelectrode. Coexisting with these NWs conforming the path, there are many other NWs not used to build the circuit. The NWs used in this sample were purchased to Nanopartz Inc. [303]. For the sake of clarity, we depict in figure 5.11(b) the corresponding AFM topographic image but now suppressing the NWs that do not participate in the circuit. The circuit topology, in this case, corresponds to the one portrayed in figure 5.10(a). We can plot the resistance of the path as a function of its length by acquiring IV characteristics at different locations along the path (see schematics in figure 5.11(b)). From this plot we can **quantify the electrical resistance of the NWs junctions**. We compare the experimental resistance *vs.* length of the path with its ideal resistance, obtained by calculating the volume of each NW (from diameter and length values from AFM imaging) and considering that the resistivity of a single NW is that of bulk gold (2.2 μΩ·cm) [295]. The difference between the ideal resistance at the end of the path and the measured one is about 800 Ω. Hence, as we have 93 NWs junctions, we end up with a figure of ~ **9 Ω/junction**. Studies on the conductivity of metallic thin films and wires conclude that grain boundary reflections rather than surface scattering are the dominant contributions to the resistivity of NWs [311, 312]. Thus, since Au NWs of the same diameters as the ones here present the resistivity of bulk gold[295], the obtained resistance per junction, excellent for nanocircuitry, can be attributed mainly to the formation of just a single grain boundary in each of the junctions [313].

The 150 μm long path made of Au NWs allowed Dr. Ares to electrically contact and characterize the few-layer antimonene flakes inside the squares. That was the first electrical characterization of an antimonene flake as thin as 4 nm. Just for that reason, that kind of nanoobject does not allowed us to validate PANC technique in the sense that the obtained results cannot be compared to others previously reported and accepted for the same material. Therefore, Dr. Ares measured the resistiviy of a few-layer graphene flake using PANC.

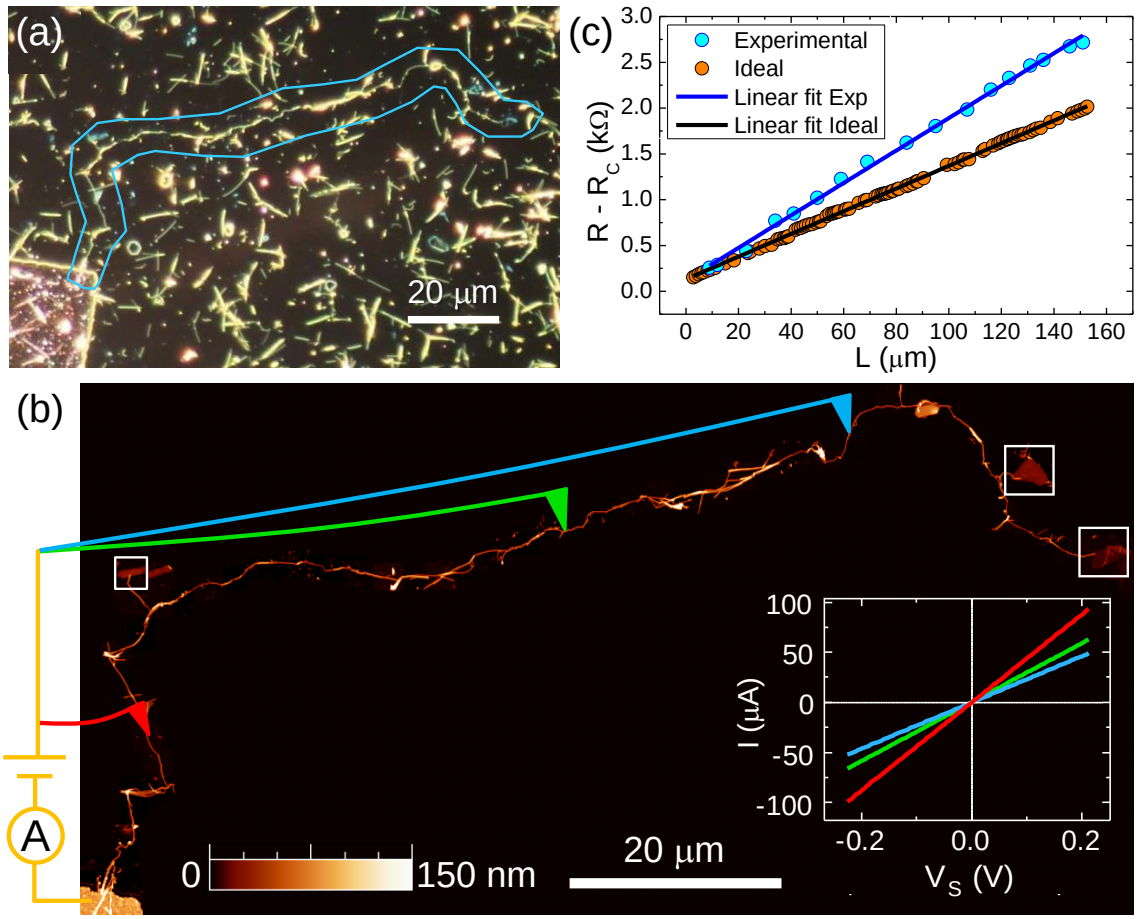

Figure 5.11: Au NWs paths characterization. (a) Dark field optical microscopy image showing a microelectrode (bottom left) and a random distribution of nanowires. The blue line encircles a nanowires path made by AFM nanomanipulation. (b) AFM topographic image showing the nanowire path. The rest of the nanowires were suppressed. The path connects three thin antimonene flakes (enclosed by squares) to a microelectrode (at the bottom left). We used a conductive AFM tip as a second mobile electrode. The inset shows three IVs acquired along the path at the locations indicated by the schematic cantilevers in the main image. (c) Resistance *vs.* length plot (cyan circles) measured along the nanowires path. The orange circles represent the ideal resistance of this path assuming that the resistivity of the NWs is the same as the bulk gold. The difference between both lines yields the NW-NW contact resistance.

For the same reason, in the next sections, the nanoobjects to be study are already widely electrically characterized in the literature. We basically used them as **fiducial samples** to show the reliability and the potential of this technique. Each section demonstrates a specific feaure of PANC, namely, its robustness to temperature and vacuun, the reconfigurability of the nanoelectrodes, the possibility of fabricating complex nanocircuits and finally its potential in molecular contacts.

5.5.2 *Resistance vs. Length of a Graphene Flake*

Dr. Ares validated the 1-terminal + C-AFM PANC configuration using a few layer graphene flake as fiducial sample (with a thickness of ~2.5 nm and a width of ~740

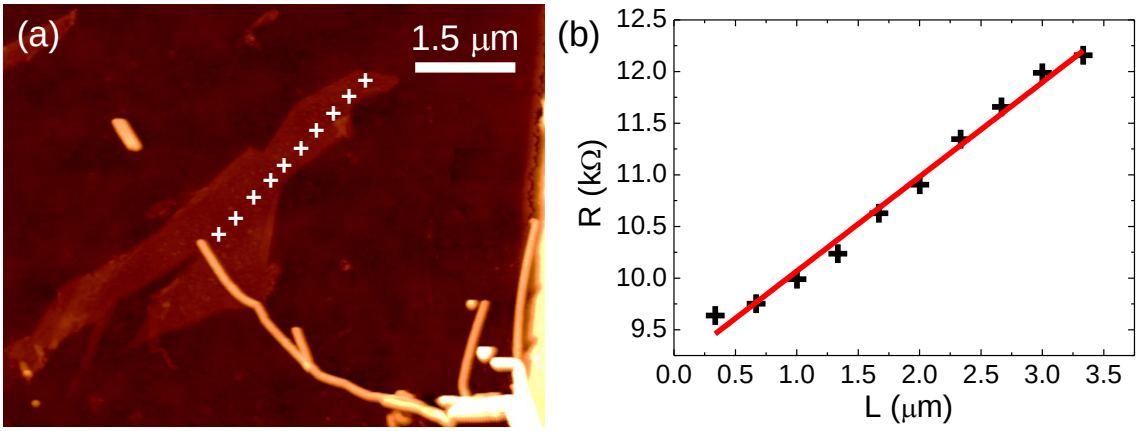

Figure 5.12: Resistance *vs.* length dependence of a few-layer graphene flake using PANC. A single Au NWs path is used in combination with C-AFM. (a) AFM topography of the flake and its connection to a microelectrode through a Au NWs path. (b) Resistance *vs.* length plot acquired along the trajectory marked by the white crosses in (a).

nm). He firstly contacted it to a microelectrode through a short path of NWs (figure 5.12(a)). Then he measured the resistance *vs.* length dependence, R(L), of the flake with a metallized AFM tip following the white crosses drawn in figure 5.12(a). Figure 5.12(b) shows the result of the measurements. From this plot a **contact resistance of ~9 kΩ** is infered (from the intercept) and, from its slope, a 1D resistivity of $\rho_{1D} = \Delta R/\Delta L = 9.2 \pm 0.1$ kΩ is obtained. The linear dependence of R(L) is expected for a material with a constant sheet resistance that can be defined as:

$$\rho_{2D} = \frac{\Delta R}{\Delta L} \cdot W = \rho_{1D} \cdot W \tag{5.1}$$

where ΔR is the contribution to the resistance of a portion of the flake in a length ΔL and W is the width of the flake. Taking into account the width of the few-layer graphene flake, a **sheet resistivity of 670 ± 60 Ω/□** is obtained (the units of ρ_{2D} are Ω but Ω/□ are usually used to express the 2D character of the magnitude). This value is in good agreement with those reported for few-layer graphene: ~450 - 590 Ω/□ [10, 75, 314]. This result, together with the R(L) of the 150 μm long Au NWs path, constitutes a proof of concept of PANC technique and validates its 1-terminal + C-AFM configuration.

5.6 FIRST STAND-ALONE 2-CONTACT DEVICE

The first device fabricated via PANC that was completely independent of the AFM after its fabrication, was a multi-layer graphene nanoribbon connected to two Au NWs electrodes, having a backgate doped silicon electrode below (circuit geometry shown in figure 5.10(f)). Specifically with the sample of this section we demostrate the **robustness of the technique to the temperature and vacuum**.

Figure 5.13(a) presents the AFM topography of the nanocircuit, showing four gold microelectrodes, a multi-layer graphene nanoribbon (6.6 nm thick, 4.5 μm long, 182 nm wide) whose silhouette is marked with a blue line, and two NWs paths connecting the nanoribbon with the bottom left and upper rigth microelectrodes (highlighted in yellow). Panel (b) displays a zoom of the green square of (a).

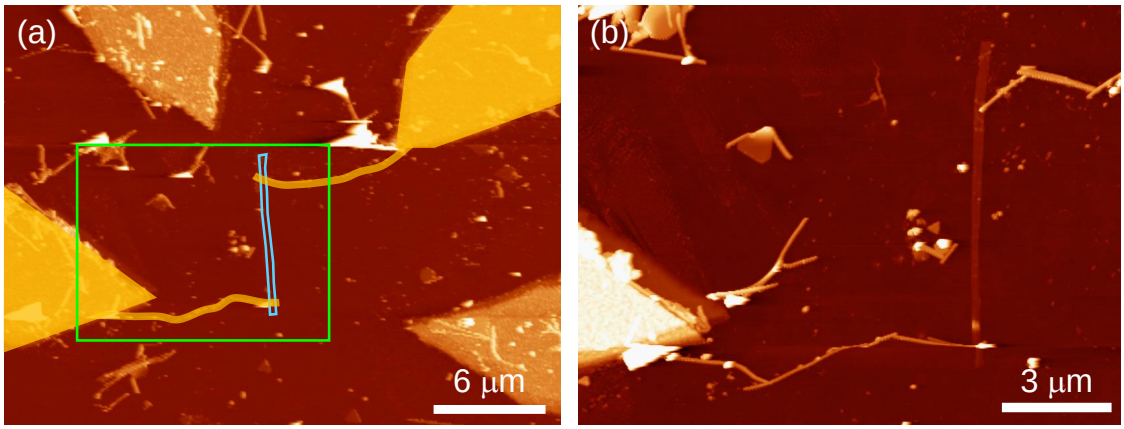

Figure 5.13: Nanocircuit of the first stand-alone device fabricated by means of PANC. (a) AFM topography showing a few layer graphene nanoribbon (blue ribbon) connected to two microelectrodes by two nanowires paths (highlighted in yellow). (b) AFM topography of the area inside the green square in (a).

5.6.1 *Results in Air at Room Temperature*

After creating the electrical contacts with Au NWs within the AFM, we conducted an initial electrical characterization inside the microscope, in ambient atmosphere and at RT. I acquired **IV curves** (with a backgate voltage of 0 V) and **IV$_g$ curves** (I *vs.* a global backgate voltage applied through the 300 nm SiO_2 layer) at a bias voltage of 0.5 V. I measured the drain-source current through the NWs electrodes (the AFM probe did not participate at all in these measurements). The obtained data are plotted in figure 5.14.

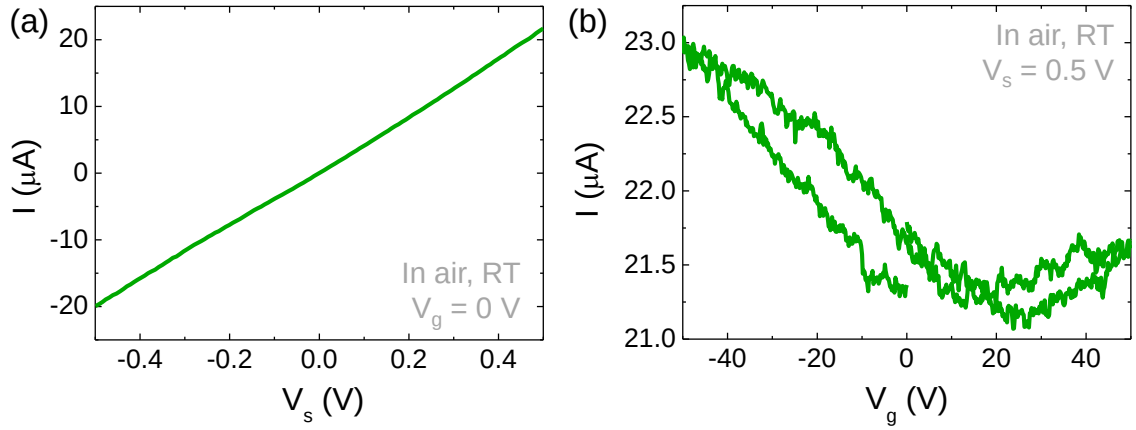

Figure 5.14: Electrical characterization of a few layer graphene nanoribbon in air at RT. (a) Drain-source current as a function of the bias voltage (at a gate voltage of 0 V) for the nanocircuit of figure 5.13. (b) Current *vs.* gate voltage dependence in the same device with a bias voltage of 0.5 V.

The resistance derived from the inverse of the slope of figure 5.14(a) is the **total resistance of the device (R_{tot}) and takes the value of 23 kΩ**. It includes: (i) the resistances of two protection resistors (R^1_{prot} and R^2_{prot}), each connected in series to a microelectrode, (ii) the contact resistance between the ribbon and the NW (R_{NW-rib}) at each end of the ribbon and finally (iii) the resistance of the ribbon itself R_{rib}. The total resistance

value for the two protection resistors is 5.3 kΩ. We do not know the value of contact resistance between the ribbon and the NW but, thanks to experiments performed in section 5.8 we can estimate it, taking a value of ~ 5.7 kΩ. This gives $R_{tot} = R^1_{prot} + R^2_{prot} + 2{\cdot}R_{NW-rib} + R_{rib} \approx 5.3\ k\Omega + 2{\cdot}5.7\ k\Omega + R_{rib} \approx 23\ k\Omega$ (where we have assumed that R_{NW-rib} is similar at both ends of the flake. Therefore $\mathbf{R_{rib} \approx 6.3\ k\Omega}$. Assuming a linear dependence of the resistance with the length of the ribbon, we have $\rho_{1D} = \Delta R / \Delta L = 6.3\ k\Omega / 4.5\ \mu m \sim 1.4\ k\Omega/\mu m$, which is in agreement with reported value of 1.5 kΩ/µm [75] for wide ribbons (W > 200 nm). If we follow the expression for ρ_{2D} of equation 5.1 we would have a sheet resistivity of 255 Ω/□, much lower than those reported for few-layer graphene (~450 - 590 Ω/□ [10, 75, 314]). The reason behind this discrepancy is the different thickness between flakes of those works (~0.3 - 2.5 nm, truly few-layer) and the thickness of the ribbon we measured (~6.6 nm). Values obtained with equation 5.1 can be compared provided that the nanoobject's thickness is similar. Indeed, if we consider this ribbon as a 3D object, and compute its resistivity as:

$$\rho_{3D} = R\frac{t \cdot W}{L} \tag{5.2}$$

we obtained $1.6{\cdot}10^{-6}\Omega{\cdot}m$, which completely agrees with in-plane resistivity of graphite [315] (the in-plane resistivity is the one we are measuring). Although the out-of-plane conductivity of graphite is much lower that the in-plane one [316], it has been shown that the sheet resistivity of multilayer graphene decreases with the number of layers [317], which further explains our 2D resistivity value. This decrease with thickness, could be due to a relevant inter-layer transport at long distances (more than one micron), where defects present in a layer considerably increases the resistance in that layer, and electrons jump to another one.

The effect of absorbed water on the flake leads to an **unintentioned p-doping** of the flakes, reflected in the position of the minimum of IV_g curve at positive voltages [10]. The **hysteresis** in the same plot it is related to slow motion of carriers coming from the sorrounding environment (adsorbates from ambient air and trapped charges in the substrate) [318, 319]. By performing a slow enough backgate voltage sweep, this hysteresis would be considerably reduced.

5.6.2 *Results in HV at Variable Temperature*

After the previous initial characterization in ambient atmosphere, we placed the sample in the vacuum probe station described in section 2.2.4.1, allowing electrical characterization between 96 and 373 K at high vacuum. Figure 5.15 shows the dependence of the electrical current with the drain-source bias voltage and with the backgate voltage. After submiting the sample to high vacuum for several days and to two annealings (up to 373 K), the p-doping disappears and the conductivity slightly increases with respect to the first results in air at RT. The **vannishing of p-doping** is caused by water and other adsorbates desorption while the **slight hystereis** in IV_g curve can be attributed to charge trapping in the substrate.

The **small increase of conductivity with temperature** can be ascribed to different reasons: (i) a narrow electronic gap in the ribbon (around 1 meV according to [314] for 182 nm wide graphene nanoribbons, which is the same width as our ribbon), (ii) a certain

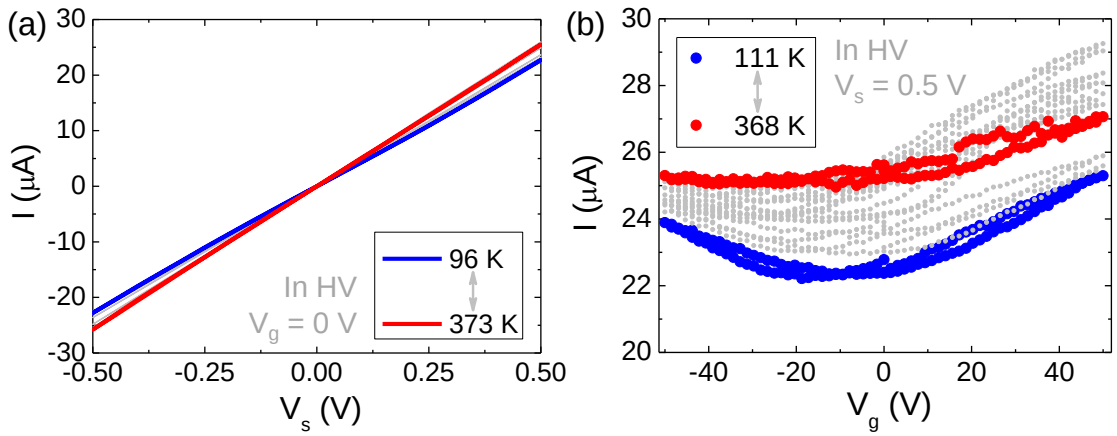

Figure 5.15: Electrical characterization of a few layer graphene nanoribbon in high vacuum at variable temperature. Measurements conducted for the nanoribbon shown in figure 5.13 in a vacuum probe-station in the stand-alone configuration. (a) Drain-source current as a function of the bias voltage at temperatures between 96 and 373 K, for a gate voltage of 0 V. (b) Current *vs.* gate voltage dependence for temperatures between 111 and 368 K and a bias voltage of 0.5 V.

degree or disorder in the atomic structure of the ribbon and finally (iii) a little variation of the contact resistances between nanoribbon and nanowire at each end of the ribbon. We believe this last mechanism is least contributing: the variation of the total resistance of the device at RT in HV during 11 days was less than 4% (20.0-20.7 kΩ). Moreover, the gap openning mentioned in (i) is expected for graphene nanoribbons, whereas this flake is much thicker. Therefore, structural disorder seems the most plausible reason for this conductivity response.

The attainment of these data demonstrates the **PANC-made circuits endurance to temperature and pressure variations**.

5.7 VERSATILITY OF PANC: RECONFIGURABLE ELECTRODES

Thanks to the flexibility of Au NWs manipulation, PANC methodology gives the option to reconfigure the position of the nanoelectrodes in a nanocircuit. To prove this remarkable feature, I made a new device via PANC, containing a nanocircuit with a multiwall carbon nanotube (MWCNT, 6.6 nm thick, 8.7 μm long) connected to two microelectrodes through Au NWs electrodes, as figure 5.16 shows. I will present electrical measurements' results **acquired at different positions of the upper nanoelectrode along the MWCNT**, thus demonstrating the versatility of PANC technique. All measurements conducted in this device were performed in air at room temperature.

5.7.1 *Initial Electrical Characterization*

After assembling both NWs paths, and connecting them to the MWCNT, I performed an initial electrical characterization in air at RT. The initial distance between the nanolectrodes along the MWCNT was 4.7 μm, therefore, that is the length (L) of the tube that takes part in the electrical response of these measurements.

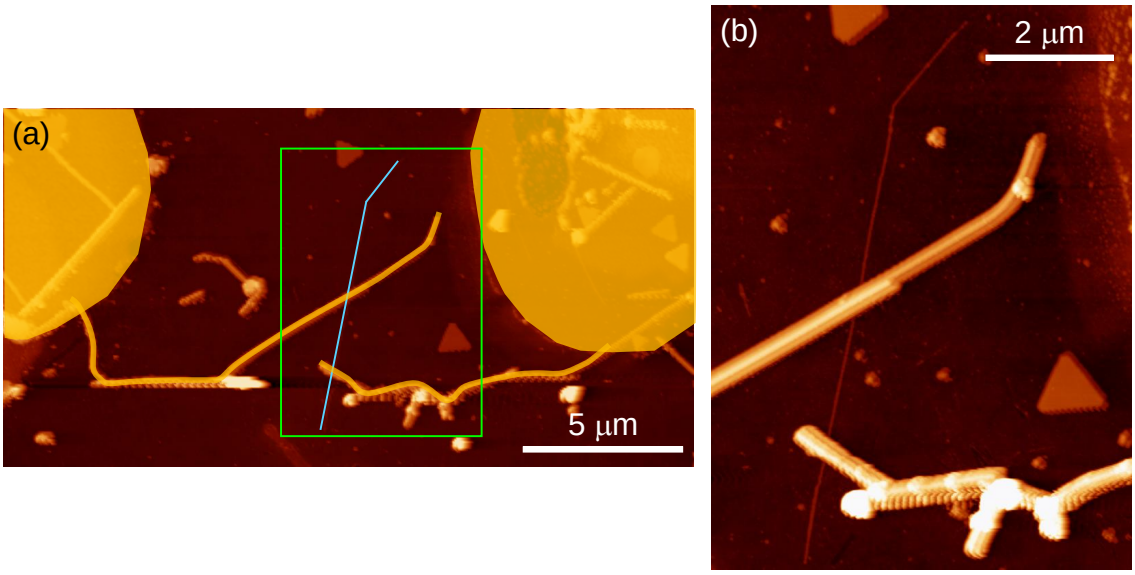

Figure 5.16: Nanocircuit obtained via PANC to show the reconfiguration of nanoelectrodes. (a) AFM topography containing a MWCNT (blue line) connected to two microelectrodes by two nanowires paths (highlighted in yellow). (b) AFM topography of the green rectangle in (a).

Figure 5.17 shows the IV and the IVg curves acquired. Panel (a) presents an almost **linear response of the drain-source current *vs.* bias voltage**, while panel (b) shows a strong hysteresis with backgate voltage.

A MWCNT nanotube mixes metallic and semiconducting layers. The inter-layer coupling and the diameter of the constituent layers (larger than a few nm which means small band gaps) make the distinction between metal and semiconductor not as pronounced as for single-wall nanotubes [320]. Furthermore, the probability of having a metallic single wall carbon tube (or shell in this case) is one third [321]. This MWCNT, which in principle

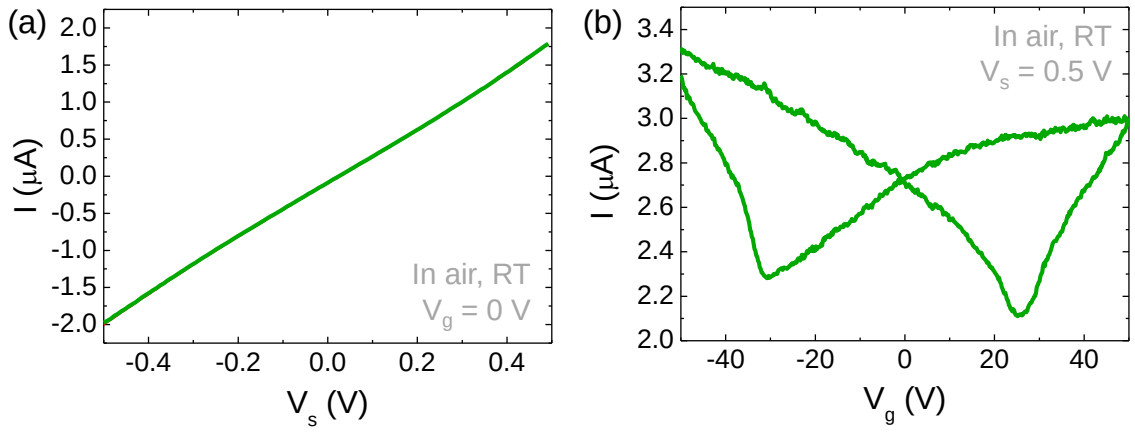

Figure 5.17: Initial electrical characterization of a MWCNT electrically contacted via PANC. Performed in air at RT. (a) Drain-source current as a function of the bias voltage (at a gate voltage of 0 V) for the nanocircuit of figure 5.16. (b) Current *vs.* gate voltage dependence in the same device with a bias voltage of 0.5 V.

has 5 shells[1], surely has at least one metallic. All this explains the **shape of the IV curve**. The value of the current is much lower than that of the few-layer graphene ribbon of the previous section (with approximately the same thickness and length). This is expected due the reduced number of accesible electronic states at the Fermi level for the case of the nanotube compared to the graphene ribbon.

Concerning the **gate hysteresis**, its is quite common in this kind of devices and it has been attributed to charge trapping by water molecules around the nanotubes, including SiO_2 surface-bound water close to the nanotubes [323].

5.7.2 *Resistance vs. Length Measurements*

Afterwards, I reconfigured the position of the upper Au NW bringing it down to the vicinity of the lower Au NWs electrode (see figure 5.18(a)). Each position of the upper NW corresponds to a specific distance between the nanoelectrodes along the MWCNT (L, highlighted in color at the top of each topography in panel (a)). At each position (L = 4.7, 4.4, 3.4, 1.8, 1 μm) I conducted an optimization of the contact of the upper NW with the tube (this process is explained in section F.6 of appendix F). Also, at each position of the upper nanoelectrode I acquired an IV curve (inset of figure 5.18(c)). From that set of IV curves we can plot the resistance of the nanotube *vs.* its length between the nanolectrodes (L). The resulting graph is depicted in figure 5.18(c). In the Y axis we have already subtracted the other contributions to the total resistance of the device, $R_{tot} = R_C + R_{MWCNT} = R^1_{prot} + R^2_{prot} + 2{\cdot}R_{NW-MWCNT} + R_{MWCNT}$, being R^1_{prot} and R^2_{prot} the protection resistors, $R_{NW-MWCNT}$ the contact resistance between NW and MWCNT and R_{MWCNT} the intrinsic resistance of the MWCNT. The value of the sum $R^1_{prot} + R^2_{prot}$ is known. By acquiring IV curves with a metallic AFM probe with the C-AFM configuration on a point of the MWCNT close to each NW-MWCNT junction and comparing their resistances between them and with the one measure all through the device along the NWs electrodes, we were able to estimate $R_{NW-MWCNT}$ at each end of the nanotube. This **NW-MWCNT contact resistance estimation was 21 ± 5 kΩ**.

The previous NW-MWCNT contact resistance value of 21 kΩ is similar to that obtained by Gomez-Navarro *et al.* [324] (whose nanotubes were partially covered by a thermally evaporated Au microelectrode). EBL provides contact resistances in the range of tens of kΩ [83, 325] to more than 10 MΩ [326, 327]. Some authors achieve contact resistances similar to ours if they sumbit the nanotube to an electron beam exposure [326] or they perform a thermal annealing of the sample [327]. **PANC provides low contact resistances** without the need of such subsequent procedures, which can be extremely harmful to the nanoobjects.

Regarding the expected resistance *vs.* length depence for a MWCNT, it is generally admitted that electron transport in a metallic multiwall nanotube at room temperature is diffusive (or with a weak localization) [83] with a resistance per unit lenght (or 1D resistivity) of 10 kΩ/μm. This would lead to a linear R(L) plot with a slope of ~10 kΩ/μm. Our data shows a linerar dependence for L < 3.5 μm (with a 1D resistivity of ~18 kΩ/m), for higher lengths the resistances highly increases. We attribute this behaviour to the

1 According to the expression $n = 1 + \mathrm{integer}[(D/2)/(2 \cdot 0.34)]$ (being n the number of shells, D the tube's diameter in nm, and 0.34 the intershell distance in nm [322]), this tube is supposed to have five shells. However, the incertity in the calibration of the AFM piezo scanner, and the underneath layer of water and other adsorbates, always present, hinders a precise determination of D, and hence n.

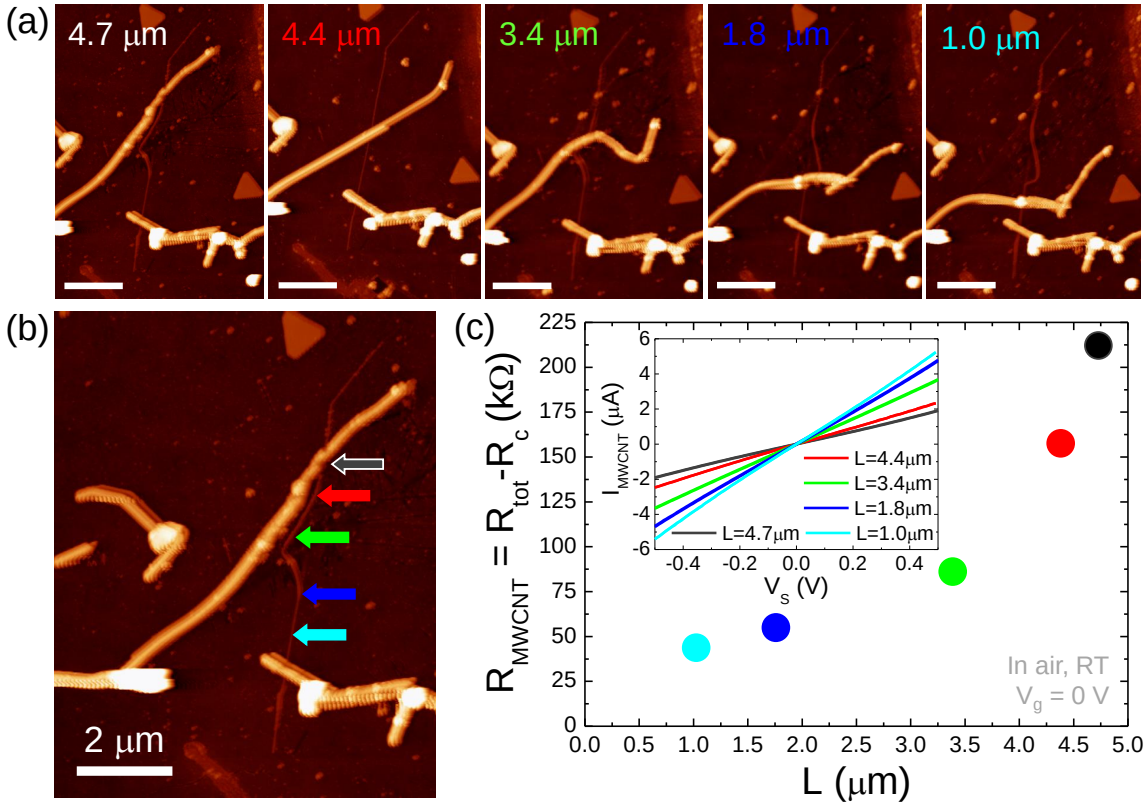

Figure 5.18: Electrical characterization of a MWCNT while one nanoelectrode is being moved along its length. Performed in air at RT. The nanotube was contacted via PANC. (a) Sequence of AFM topographies of a MWCNT connected to two nanowires paths. They show the different locations of the upper nanoelectrode as it is approached to the lower nanoelectrode. The distance between the nanoelectrodes along the MWCNT is written in color in the top of each image. Scale bars: 2 μm. (b) AFM topographic image of the nanocircuit for the maximum separation between nanoelectrodes (first image of (a)). The arrows mark the locations where IV curves were acquired by repositioning the upper nanowire. (c) Plot of the nanotube resistance *vs.* its length between the nanoelectrodes. The insent contains the corresponding IVs acquired at each length. The length-color code is mantained in the whole figure.

presence of a kink near L = 3.5 μm (green arrow and point) that surely introduces defects and deformations in the tube, increasing the electron scattering and hence the resistance [324, 328].

The nanocircuit fabricated and electrically studied in this section proves PANC as a versatile technique that **allows the repositioning of the NWs-based electrodes**. This property can be applied to repair nanocircuits. Aditionally, **it procures low contact resistances** without any extra procedure.

5.8 COMPLEX CIRCUITS OBTAINED WITH PANC: 4-CONTACT CONFIGURATION

We have already seen and experimentally analyzed some of the useful features of PANC methodology, namely its endurance to temperature and vacuum conditions, its flexibility to reconfigure the position of nanoelectrodes and the low contact resistance it provides. Fortunately PANC offer other valuable properties beyond those ones. One of them is

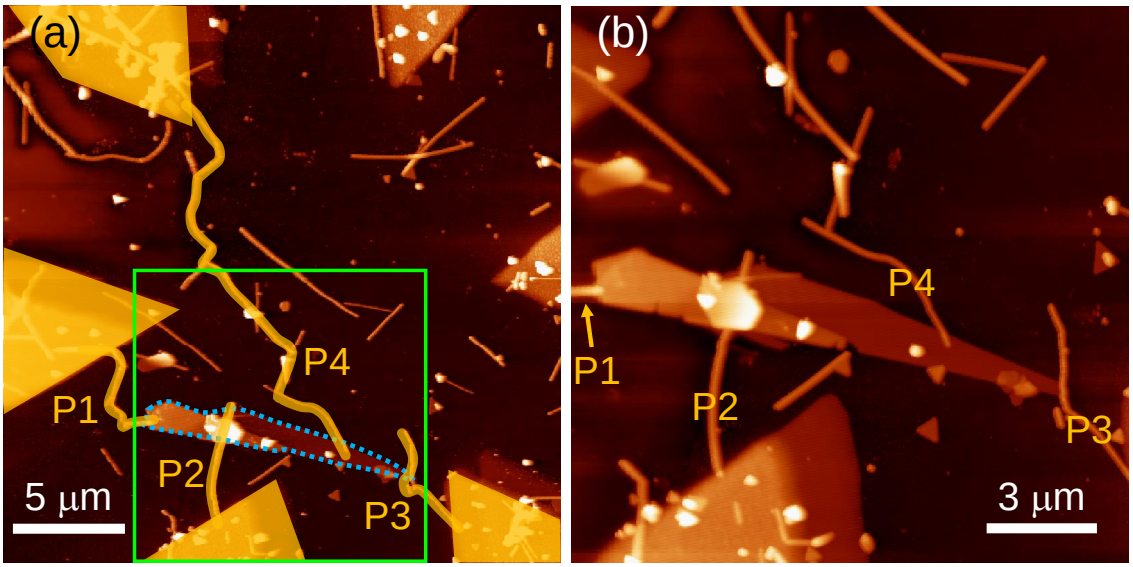

Figure 5.19: Nanocircuit with four nanoelectrodes obtained via PANC. (a) AFM topography showing a multilayer graphene flake (encircled by dashed blue line) connected to four microelectrodes by four nanowires paths (P1, P2, P3 and P4 highlighted in yellow). (b) AFM topography of the area inside the green square in (a).

the possibility of building complex nanocircuits, for instance **nanocircuits with several nanoelectrodes**. In this section we show a **4-contact device** obtained via PANC together with its electrical characterization.

Figure 5.19 shows the AFM topography of a nanocircuit fabricated by means of PANC. It includes a few layer graphene flake electrically contacted to four microelectrodes through four NWs electrodes. Although the fabrication procedure and the type of devices of this setup are similar to the two NWs electrodes scheme, this Kelvin sensing topology enables the experimental measurement of the resistance of a nanoobject **without contact resistances** (see section 2.2.2). This configuration is the one required if the contact resistance is higher than the intrinsic nanoobject resistance.

The path in the bottom left corner (P2) of figure 5.19(a) is a single Au NW electrically connecting the flake to the microelectrode at the bottom of the image. The other Au NWs paths (P1, P3 and P4) connect, in the same way, the flake (at different points) with three different microelectrodes (which are highlighted in yellow as well as the NWs electrodes). The part of the flake between the two inner electrodes has these dimensions: length of 5 μm, width of ~ 1.6 μm and it has two thicknesses of 11 nm in the majority of its area and 21 nm on the left bottom side. Close to it, there is a hexagonal gold island (just above the end of the nanowire of path P2).

5.8.1 *Resistance Measured with 2- and 4-terminal Scheme in Air and RT*

We first measured the dependence of the electrical current with the drain-source voltage at room temperature in a **two-contact configuration** using paths P2 and P4. This response is shown with the red line in figure 5.20, from which a **total resistance of $R^{2c}_{tot} \approx 20$ kΩ** is derived. This value is very similar to the 23 kΩ obtained in section 5.6 for the few layer graphene nanoribbon using the two electrode configuration as well. R^{2c}_{tot} includes the

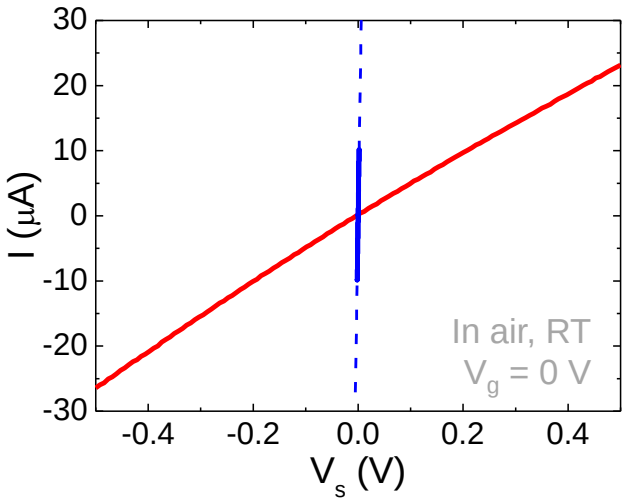

Figure 5.20: Drain-source current *vs.* bias voltage for a multilayer graphene flake obtained by 2-probe (red line) and 4-probe (blue line) measurement. Data acquired in air, at room temperature and zero gate voltage.

resistance of the flake between nanoelectrodes P2 and P4 (R_{flake}) and the total contact resistance in the circuit (R_C).

Afterwards, we acquired the current *vs.* voltage in the **four-contact topology**, which is depicted in the same figure with a steeper blue line. In this case, as the measurement is not affected by the contact resistance, the total resistance acquired has a much lower value: $\mathbf{R}^{4c}_{tot} \approx$ **150** Ω, that corresponds exclusively to the resistance of the part of flake between the inner nanoelectrodes (R_{flake}).

We can **estimate the contact resistance between a nanowire and the flake** once we have the total resistances obtained from both previous methods. We have that $R^{2c}_{tot} = R_{flake} + R_C = R^{4c}_{tot} + R_C$, therefore R^{2c}_{tot} - $R^{4c}_{tot} = R_C$ = 20 - 0.150 kΩ ≈ 20 kΩ. The contact resistance includes the resistance of two protection resistors (one attached to the microelectrode connected to P2 and the other attached to the microelectrode connected to P4) and the nanowire-flake contact resistances: $R_C = R^{P2}_{prot} + R^{P4}_{prot} + R^{P2}_{NW-Fl} + R^{P4}_{NW-Fl}$ ≈ 20 kΩ. We know the resistance of both protection resistors (8.6 kΩ in total). We assume that $R^{P2}_{NW-Fl} \approx R^{P4}_{NW-Fl} \approx R_{NW-Fl}$. Thus we will have: $2 \cdot R_{NW-Fl} \approx$ 20 - 8.6 kΩ, leading to $\mathbf{R}_{NW-Fl} \approx$ **5.7 kΩ**.

5.8.2 *Resistance vs. Length Measured with 3-terminal Scheme and C-AFM*

After the previous experiments, we took advantange of the topology of the circuit and a conductive AFM tip to acquire the **flake electrical resistance *vs.* length plot without contact resistance**. To this end, we acquired IV curves leaving path P4 unconnected and using a conductive AFM tip as a fourth mobile electrode (always placed between P2 and P3). Figure 5.21(a) shows with colored symbols the locations where the conductive tip is in contact with the flake during each experiment. The advantage with respect to the typical conductive AFM measurements (with a two-electrode topology) is the absence of contact resistance. Figure 5.21(b) portrays the result of these measurements, mainting the shape and color of the symbols for each location. As the tip is the mobile electrode between P2 and P3, the length L corresponds to the distance between P2 and the tip. As P2 is attached to a hexagonal gold island, the length is measured from the right edge of that island closer to the tip location.

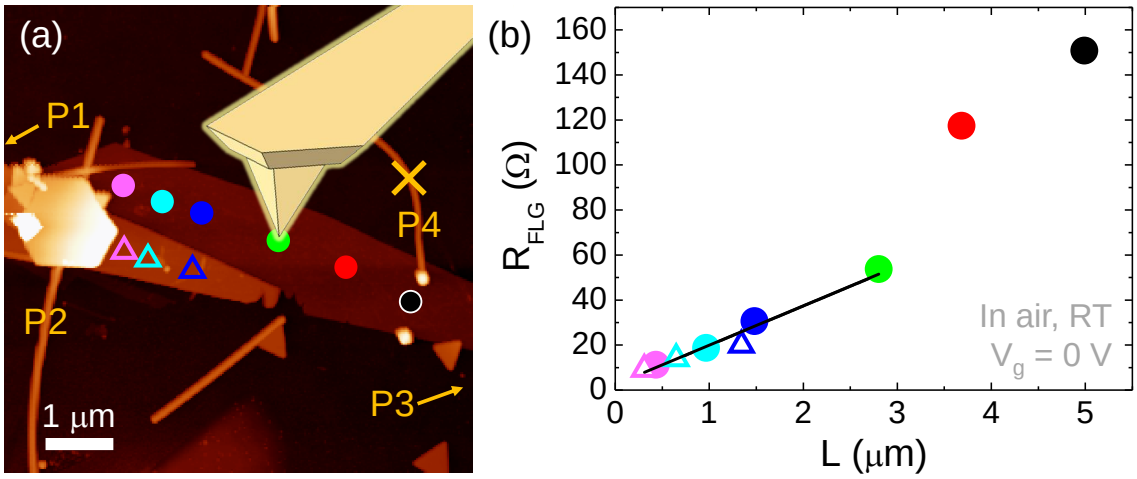

Figure 5.21: Electrical characterization of a multilayer graphene flake using the four electrode configuration being a conductive AFM tip one of the inner electrodes. (a) AFM topography of the flake connected to a conductive AFM tip and three nanowires paths: P1 (outside the image), P2, and P3 (outside the image). P4 was left unconnected during the this set of measurements (its role is played now by the AFM probe). Coloured symbols show the different locations of the tip. (b) Plot of the flake resistance *vs.* its length (= distance between P2 and the tip). The black line depicts the linear fitting of the data with L < 3 μm. The color and shape code of the symbols is the same as in (a).

Although this flake cannot be considered as a ribbon, it has two thicknesses and its length (distance between left electrode and tip) is not well defined, the data below 3 μm show a linear dependence, giving a linear fit with an intercept at almost zero (R_C = 2 ± 2 Ω) and a slope of ρ_{1D} = **17** ± **1** Ω/μ**m**. We cannot compare this figure with others previously reported due to the lack of defined thickness, width and length in this flake.

5.8.3 *Resistance measured with 4-terminal Scheme in HV at Variable Temperature*

Finally, we took the whole device containing the nanocircuit and inserted it in the vacuum probe station described in section 2.2.4.1. We used again electrode P4 to measure the current *vs.* voltage variation in the four-terminal configuration in the stand-alone setup (without the need of the AFM probe), at variable temperature from 100 K to room temperature. Figure 5.22 displays the response obtained. The resistance of the flake slightly varies with temperature being **lower for low temperatures** (R(100 K) ≈ 170 Ω *vs.* R(298 K) ≈ 178 Ω). This behaviour is the one expected for a metal and it is due to the electron-phonon scattering which increases with temperature, leading to higher resistivity at higher temperatures [329].

5.9 PANC AS AN ALTERNATIVE TO MOLECULAR CONTACTS

In this section we first explore the spatial resolution of PANC technique with the aim of electrically contact molecules and second, we introduce a **preliminary experiment** on molecular electronics using PANC technique. This kind of experiment cannot be carried out by means of EBL.

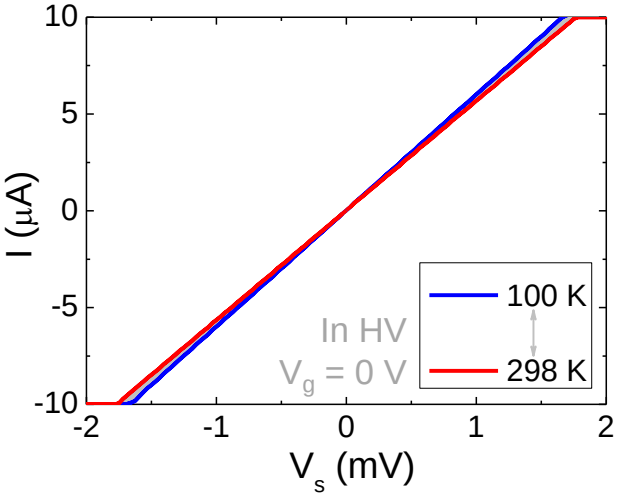

Figure 5.22: Drain-source current *vs.* bias voltage characteristics of a few layer graphene measured in the stand-alone 4-wire sensing setup in high vacuum at variable temperature.

Section 5.1.1 introduced the main existing techniques used to electrically contact nanoobjects: Electron Beam Lithography (EBL), Scanning Probe Microscopy (SPM) and Mechanical Controlable Break Junctions (MCBJ). Molecular electronics is mainly dominated by SPM and MCBJ. The basic idea in both of them is to form atomic size gaps that are "filled" with molecules in a random manner. By inducing mechanical stress, the gap varies as a function of time creating new molecular junctions. The current flowing through the junctions so formed is measured and analyzed by statistical methods (histograms and cluster analysis) that allow quantifying the conductance of the molecules. There are other experimental techniques to electrically contact molecules: electromigration, Transmission Electron Microscope and gold nanoparticle dumbbell (or dimers), among others [34].

In the **electromigration** technique, a metal nanowire is broken in a controlled manner due to the motion of ions in high electrical current densities (electromigration process[2]). Before the wire finally fails and the current drops drastically, atomic size contacts are formed for a rather short time span [330]. The electromigration will nucleate at the thinnest part of the electrode structure (see figure 5.23). This technique has been optimized for the formation of nanometer sized gaps for trapping individual molecules or other nanoobjects [331].

The **gold nanoparticle dimers** technique uses gold nanoparticles (Au NPs) with a typical diameter of 10 nm. The molecules to be contacted are functionalized at both ends with thiol anchoring groups, which have a high affinity to gold. The molecules are attached to the NPs through these thiol bonds such that two NPs are combined to form a dumbbell having the molecules in between. Those dumbbells now have a suitable size for bridging lithographically defined nanogaps and can be deposited onto them straightforwardly [34, 332]. Figure 5.24 shows the dimer contacting scheme.

5.9.1 *PANC Approaches to Contact Molecules*

Electromigration and gold nanoparticle dimers techniques are compatible with PANC methodology (and MCBJ too with the suitable experimental setup). On one hand a Au NW

2 The two most important factors contributing to the motion on ions in electromigration are: the so-called direct force (due to the electric field, and thus points into the direction of the field) and the wind force (caused by momentum transfer of the conduction electrons onto the ions, it has opposite sign). When the total force overcomes the binding force of the ions, they start to diffuse [34].

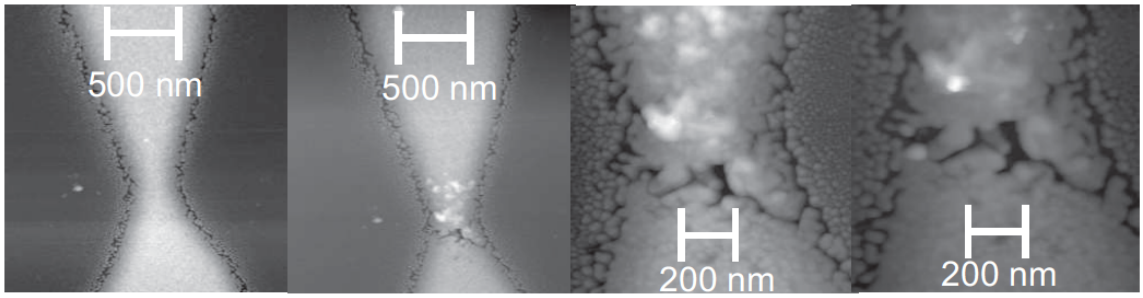

Figure 5.23: Electromigration technique. Series of AFM topographies of an electromigrated contact made of Au on Si in different phases of the electromigration process. Extracted from [34].

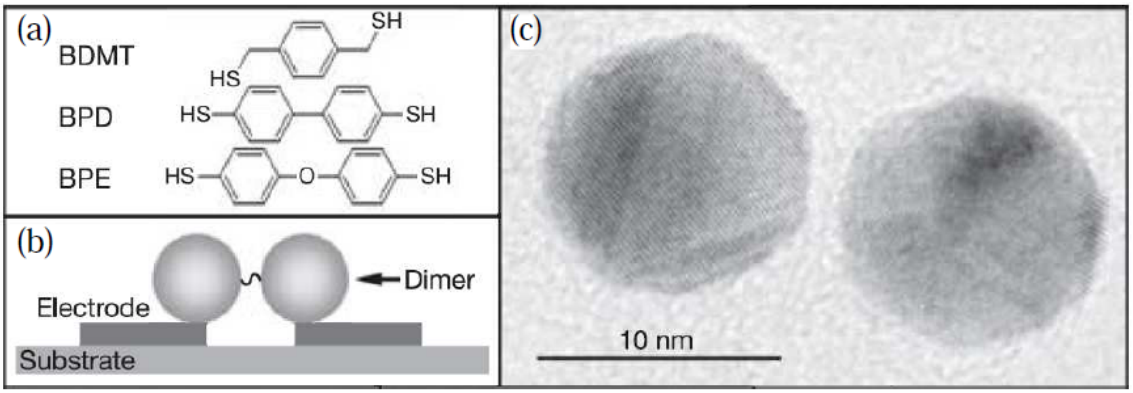

Figure 5.24: (a) Structures of three molecules studied with the dumbbell technique. (b) The dimer contacting scheme. (c) TEM image of a BDMT dimer made of 10 nm colloidal gold particles. The separation between the two particles corresponds approximately to the BDMT length (0.9 nm). Extracted from [34].

(or a concatenation of them) can be subjected to electromigration, on the other hand the NPs conforming the dimers can be connected to Au NWs. A problem arises in the latter case: the diameter of the Au NWs is very high compared to that of Au NPs: 60 nm (Au NWs) » 5-10 nm (Au NPs). Additionally, the size of the contacting electrodes at their end should be as small as possible to reduce the number of contacted molecules. To circumvent this problem, the so-called **nanorods** can be used. A nanorod (NR) is a nanowire with lower diameter and lower aspect ratio [300]. They are commercially available [302, 303]. By the time of these experiments we did not have good quality home-made NRs. On the contrary, Au NPs were already succesfully synthesized by our collaboratot Dr. Consuelo Moreno when we started the experiments of this section. Their diameter ranged from 5 to 30 nm.

In the framework of PANC, **Au NPs and Au NRs combined with Au NWs can be used in many ways to contact nanoobjetcs or molecules** (see figure 5.25): (i) assembling NRs to the NPs of a dimer (panel (b)), (ii) contacting a NP covered by molecules with two NRs (panel (c)), (iii) contacting a dymer through slightly bigger NPs (panel (d)), (iv) a NR welded at each of their ends to a NW path to conduct electromigration (the breakdown would preferably occur at the narrowest part, i. e. the nanorod or a thin junction) (panel (e)), (iv) joinning NRs at the ends of Au NWs paths to directly contact nanobjects (panel

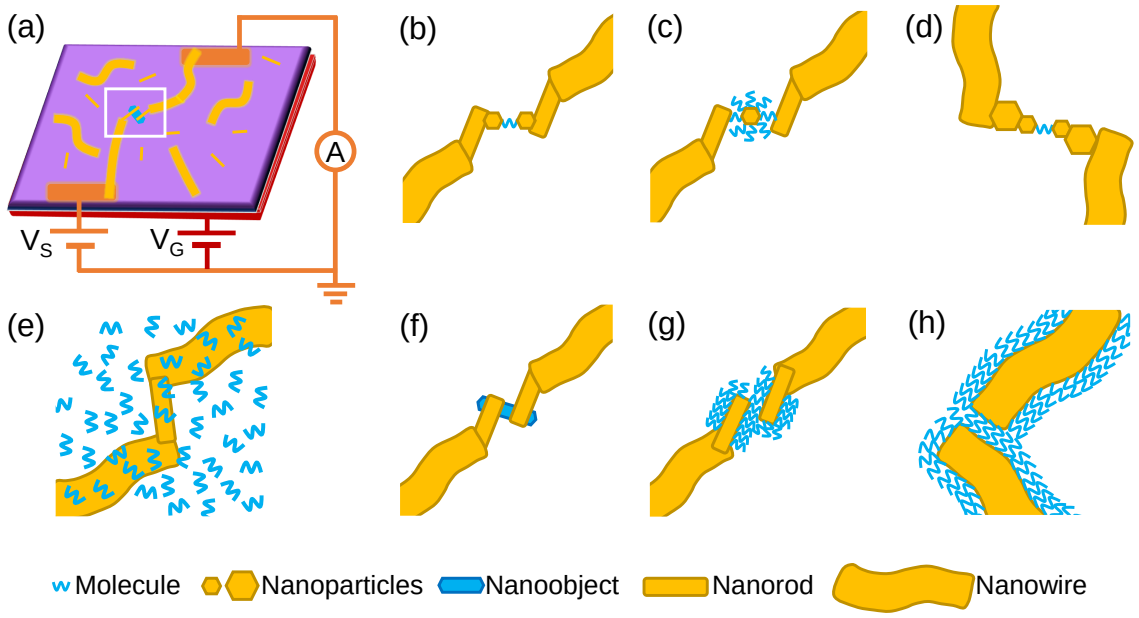

Figure 5.25: PANC approaches to contact nanoobjects or molecules. (a) Structure of a PANC device highlighting the area with the nanoobject or molecules to be contacted. This area is zoomed-in in panels (b-h). (b) A dimer connected to NRs. (c) A NP covered by molecules connected to NRs. (d) Dymer contacted by slightly bigger NPs. (e) A NR between two NWs to conduct electromigration. (f) A nanoobject contacted by NRs. (g) Two close NRs coated by molecules. (h) Two close NWs covered by molecules. Bottom: legend of the elements.

f)) or (v) even molecules that cover the nanorods (panel (g)) and (vi) using exclusively nanowires previously coated by molecules (panel (h)).

Therefore, a key parameter to be considered is the **minimum distance between non-electrically contacted nanowires** (or nanorods). This is treated in the next section.

5.9.2 *Spatial Resolution of PANC*

We measured the minimum distance between two non-electrically contacted nanowires, and contacted gold nanoparticles in order to explore the spatial resolution of PANC.

5.9.2.1 *Minimum Distance between Gold Nanowires*

Figure 5.26 shows a TEM image of two adjacent nanowires. According to this image, the **minimum gap width between NWs is about 1.6 nm**. We attribute this distance to the presence of CTAB surfactant that prevents NWs coalescence.

5.9.2.2 *Contacting Gold Nanoparticles*

This experiment was carried out by Dr. Pablo Ares. He adsorbed 15 nm diameter Au NPs on a conventional SiO_2 substrate where Au NWs were previously desposited. Then he assembled two Au NWs electrodes that connected two Au NPs in parallel. Panels (a) and (b) of figure 5.27 show the final circuit configuration. The diameter of the bottom NP is ~20 nm and that of the top is ~10 nm. This NP was contacted through a third NP of

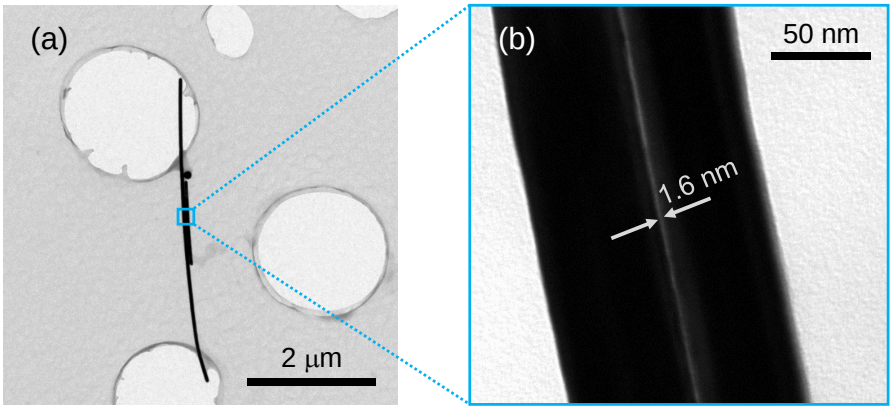

Figure 5.26: TEM images of two adjacent Au NWs. (a) Large area image. (b) Zoom image showing the region enclosed in (a) by a square. A gap of about 1.6 nm can be readily seen.

diameter ~25 nm. The final IV characteristic is shown in figure 5.27(d), whose resistance suggests that the contact resistances between the NW and the NPs are very low. This experiment allows us to conclude that the resolution of PANC at this stage is ~10 nm, well below the EBL standard, that which is about 30 nm.

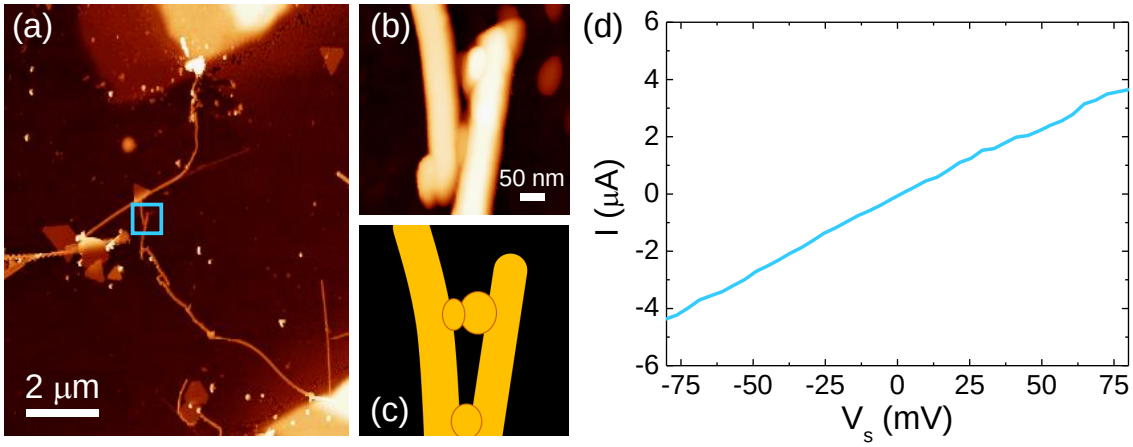

Figure 5.27: Contacting gold nanoparticles via PANC. (a) AFM topographic image of two Au NWs electrodes connecting two gold nanoparticles in parallel. (b) Zoom of the region enclosed by the blue square in (a). (c) Schematics of the final configuration with both the bottom and the top Au NPs in contact with the Au NWs electrodes.(d) Current *vs.* voltage characteristic of the circuit in (a).

5.9.3 *1-4 Benzenedithiol Molecule*

We chose 1-4 benzenedithiol (BDT[3]) as the first molecule to be electrically characterized using PANC. This was motivated by two main reasons: its **affinity to gold** and the fact that its conductance has been **widely studied** for more than twenty years.

3 We omit "1-4" in the molecule's acronym.

5.9.3.1 *Structure and Conductance of BDT*

BDT is one of the simplest thiolated conjugated organic molecules. Its thiol terminal groups (-SH) bond convalently to metal electrodes. Its lower HOMO-LUMO gap (compared to other thiolated molecules such as alkanedithiol chains) and the possibility of functionalizing this molecule make it attractive for molecular electronic applications [333]. BDT has a planar structure, shown in figure 5.28(a). The distance between sulfur atoms is estimated to be 0.65 nm [334, 335].

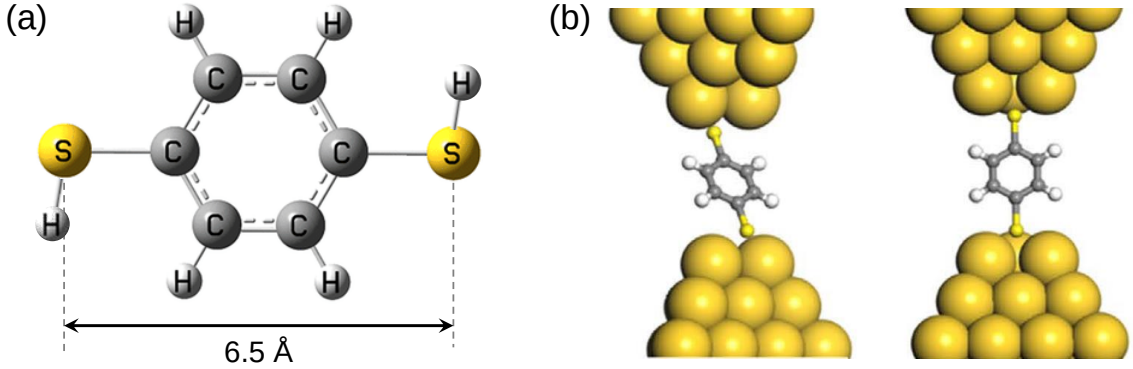

Figure 5.28: Structure of 1-4 benzenedithiol molecule. (a) Atomic structure. (b) Two BDT molecular junctions with different orientations. Adapted from [336] and [337].

The conductance of BDT has been widely investigated experimentally by STM [333] and by MCBJ [334, 338]. Indeed, the experiment of Reed and coworkers in 1997 [338] is often considered as the beginning of the field of single-molecule conduction. It was performed using a MCBJ device at RT, with the junction immersed in a solution of BDT, which has become a workhorse in this field. Theoretical works emerged later. **The conductance of BDT has been a longstanding problem**, with significant variation in experimental values (10^{-4} - $10^{-1} \cdot G_0$ [333, 334, 339, 340]). The different results are usually attributed to the different types of setups, the change of contact geometry and molecular orientation (see figure 5.28(b)) [334, 337].

5.9.3.2 *Methods to Coat Gold with BDT Molecules*

BDT molecules can coat bare clean gold surface simply by inmersing gold in a **solution of BDT molecules in etanol** for an incubation time (~5 hours) and then rinsing with ethanol and drying with nitrogen or argon [334]. Depending on the type of experiment, the drying can be omitted, for example, in liquid environment STM or MCBJ setups. If gold surface is covered by surfactant molecules, the exchange of surfactant by BDT can be carried out in a similar way.

Another method to deposite molecules on metals is the **thermal evaporation** of them in vacuum. Unlike the aforementioned procedures, thermal evaporation is completely dry. **Electrospray ionization** is another option to cover metal surface with molecules in which charged droplets of a solution containing the molecules are created and directed to a metal electrode thanks to a strong electric field [34]. As far as we know, none of these two methods, thermal evaporation and electrospray ionization are commonly used with BDT.

5.9.4 *PANC as an AFM-based Break Junction Technique*

We conducted several attempts to measure the conductance of BDT molecules using some of the configurations shown in figure 5.25. At the time of the experiments, we unfortunately did not obtain good quality nanorods, but we did have suitable Au NWs and Au NPs. Therefore we made used of the following available configurations:

- **NW-(coated NP)-NW**: an Au NP covered by BDT molecules attached to two NWs paths (similar to diagram (c) of figure 5.25 but connecting directly the NWs to the coated NP).
- **(coated NW)-(coated NW)**: two close paths of Au NWs previously covered by BDT molecules. They can be arranged as shown in figure 5.25(h), or they may be crossing (one on top of the other).

In both cases the coating of gold with BDT molecules was conducted by the substitution of CTAB surfactant with BDT molecules in liquid phase.

To open and close BDT-Au junctions, we started by manipulating the involved NWs with the AFM tip so that the NWs and the NP in mentioned systems approach, until current peaks can be detected. We performed the movement of the AFM tip and monitored the current of the circuit simultaneously. Several current peaks were measured when approaching as well as withdrawing the NWs. We were able to measure some increasing peaks while pushing one NW agaisnt the other, ending with a Au-Au cold welding. Remarkably, we could also break that welding and recorded some current peaks while separating the NWs, until there was no current. In this regard, **PANC can be seen as an AFM-based break junction technique**. Unfortunately the data thus obtained were not reproducible enough. This approach can be further improved, for instance, by performing automated movements of the tip while simultaneously recording the circuit current and the position of the tip/NWs. This would allow the acquisition of big amount of data from which relevant information can be extracted through a statistical analysis (like in MCBJ experiments). We finally followed a different (and more successful) strategy described below.

5.9.5 *Measurement of 1-4 Benzenedithiol Conductance via PANC*

5.9.5.1 *Initial Au NWs Manipulation and NW-NW Gap Characterization*

Our experiment started with two gold nanowires, each connected to a different gold microelectrode. Then we used the AFM tip to **approach the nanowires as much as possible but avoiding cold welding** (figure 5.29(a)). To check the gap width between both NWs we used a sharp tip (from Nanosensors Inc. [341]). To estimate tip radius we use a fiducial sample containing many MWCNTs. A MWCNT was imaged with that tip yielding a height of h ~15 nm and width W ~38 nm (see the corresponding profile in figure 5.29(c)). From these two magnitudes, we obtained a tip radius of ~10 nm calculated as $R_{tip} = W^2/8h$ (following reference [342]). Finally, as the inset of figure 5.29(a) shows, **the gap width** between NWs was within the tip resolution (**< 10 nm**).

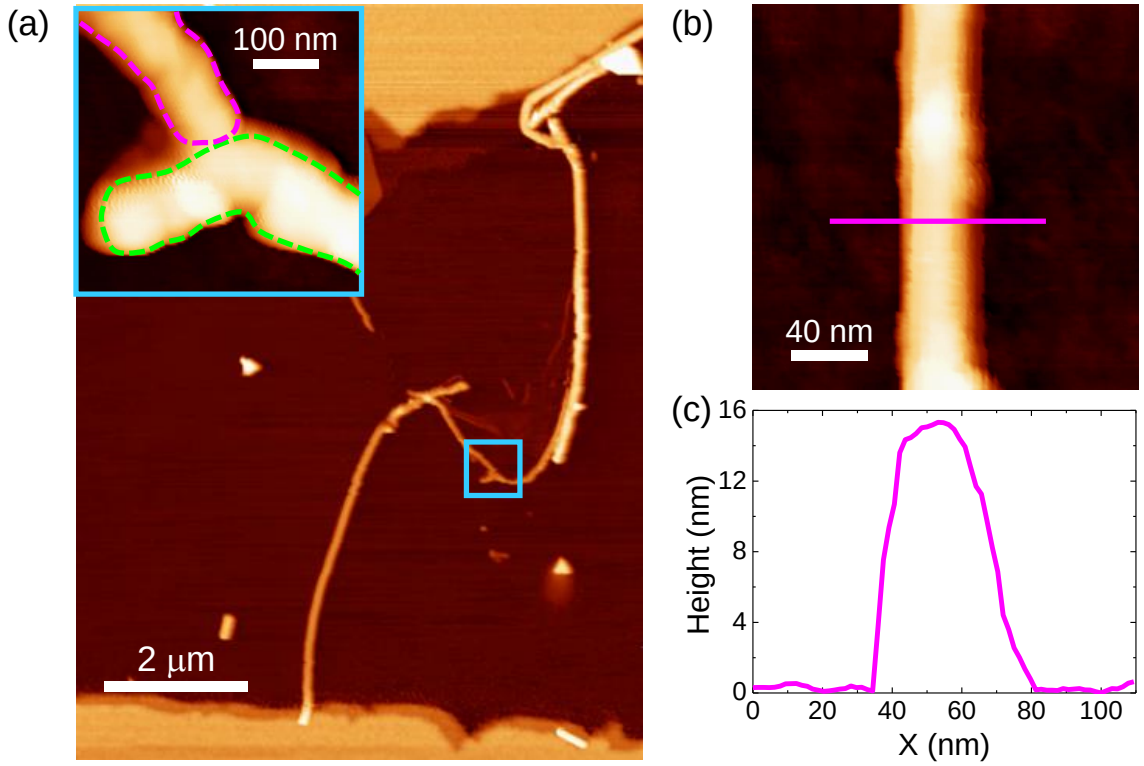

Figure 5.29: Topography of two close BDT-coated Au NWs and tip radius calibration. (a) AFM topographic image of two Au NWs electrodes covered by BDT brought into close proximity. The inset shows the region enclosed by the blue square. The dotted lines show the edges of the NWs. The absence of contact between them was verified by the absence of current. (b-c) Tip radius calibration of the tip used to acquire the inset in (a): (b) AFM topographic image of a MWCNT used to obtain the tip radius, (c) Height profile along the pink line in (b).

5.9.5.2 *BDT Deposition*

Once the nanowires were so prepared, we inserted the sample in a vacuum chamber (base pressure 10^{-6} mbar). We first induced an oxygen plasma to remove the CTAB surfactant. Then **we sublimated BDT powder** and kept a BDT partial pressure of $5{\cdot}10^{-4}$ mbar for 30 seconds in the chamber. Previously, we had checked by ellipsometry that this very same procedure applied to a gold thin film produced a **molecular layer of ~0.8 nm**, compatible with the size of a BDT molecule (see appendix G for more details regarding BDT deposition and ellipsometry data).

5.9.5.3 *IVs at Different Bias Voltage Ranges*

Upon BDT deposition, we imaged the sample again observing no variations in the nanowires position. We confirmed the absence of cold welding by measuring current *vs.* voltage characteristics showing no measurable current for bias voltages between 0 and 4.5 V. We performed IVs at higher bias voltages until we observed the **onset of current for a bias voltage of ~5 V** (see figure 5.30(a)). Then, we acquired **IVs at lower bias voltages**, roughly obtaining the same conductance in all of them figure 5.30(b)). For

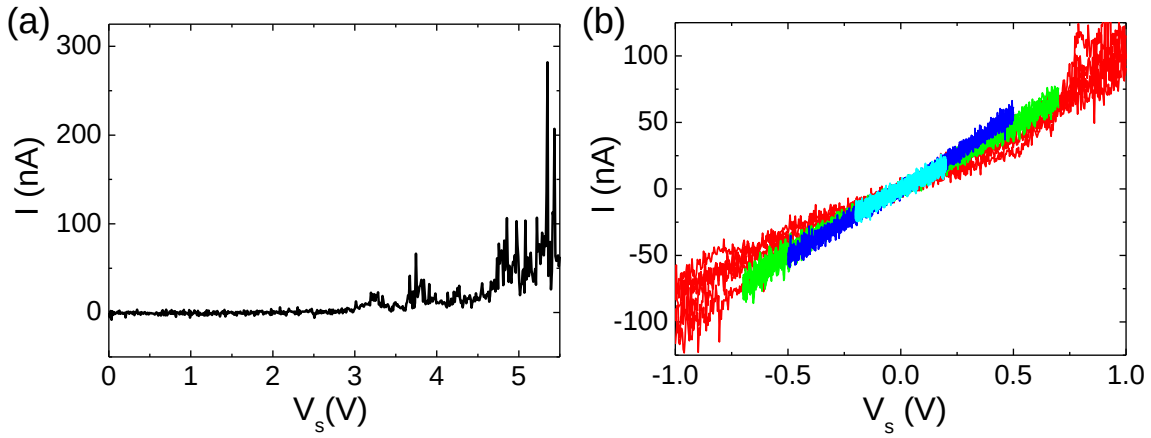

Figure 5.30: Onset of the current and subsequent IVs acquired in the NW-BDT-NW junction of figure 5.29(a). (a) Asymmetric IV where the onset of the current is observed when reaching a bias voltage of ~5 V. (b) Current *vs.* voltage characteristics carried out increasing the bias voltage range.

bias voltages higher than 0.8 V, peaks in the current appeared, a common feature in molecular electronics transport measurements [343].

We carried out additional **IVs with increasing bias voltage range** observing a final drop to almost zero resistance that we interpret as a cold welding event. Figure 5.31 shows a collection of representative IVs acquired with increasing bias voltage.

Finally, we **reset the experiment** by mechanically breaking the contact through AFM NWs manipulation and started over.

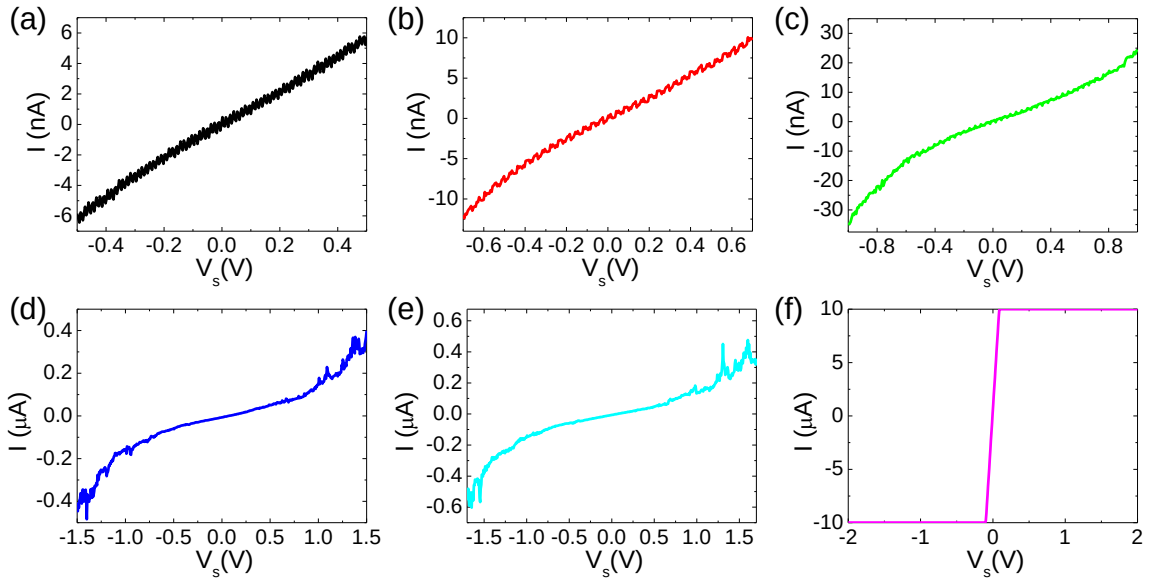

Figure 5.31: IVs acquired with increasing bias voltage range of BDT molecules contacted by PANC. (a) ± 0.5 V. (b) ± 0.7 V. (c) ± 1.0 V. (d) ± 1.5 V. (e) ± 1.7 V. (f) ± 2.0 V where the cold welding finally takes place.

5.9.5.4 *Measured Conductance*

We checked the stability of the contacts so formed for more than one hour, yielding a quite stable conductance of about **0.06·G_0** (see figure 5.32), being G_0 the conductance quantum ($G_0 = 7.75{\cdot}10^{-5}$ S = (13.3 kΩ)$^{-1}$).

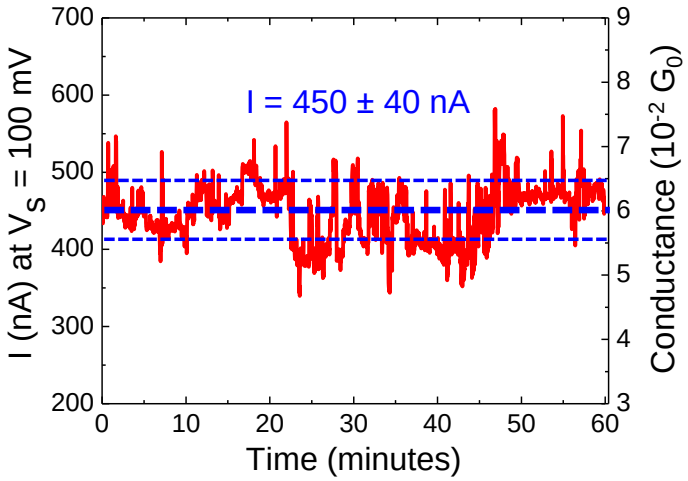

Figure 5.32: Current/conductance variation through the NW-BDT-NW contact during one hour. A bias voltage of 100 mV was applied. The mean current ± standard deviation values are shown graphically and numerically.

The conductance of BDT molecules depends critically on the experimental setup and the molecular orientation. Different groups reported values ranging from ~$10^{-4}{\cdot}G_0$ to ~ $0.5{\cdot}G_0$ [333, 334, 338, 340, 344], in good agreement with our experimental results. Furthermore, many experimental works indicate a common BDT conductance peak in the MCBJ histograms at ~$0.01{\cdot}G_0$ [333, 334, 339, 340, 345] of the same order as the conductance we obtained (see table 5.1).

Source	Conductance (G_0)
Xiao *et al.* 2004 [333]	**0.011**
Tsutsui *et al.* 2006 [339]	**0.01** • 0.1
Haiss *et al.* 2008 [344]	10^{-4}
Kim *et al.* 2011 [334]	$5{\cdot}10^{-4}$ • **0.01** • 0.5
Yamauchi *et al.* 2012 [340]	0.001 • **0.04**
Bruot 2012 *et al.* [345]	**0.01**
This work	**0.06**

Table 5.1: Comparison of measured conductances of BDT from several experiments. Values of the order or $0.01{\cdot}G_0$ are highlighted in bold font.

5.9.5.5 *Spectral Analysis of Traces*

The spectral analysis of conductance temporal traces gives information about the existence of electrical junctions involving few molecules [343]. A representative **conductance trace** measured once a NW-BDT-NW junction is achieved, is displayed in figure 5.33(a). This

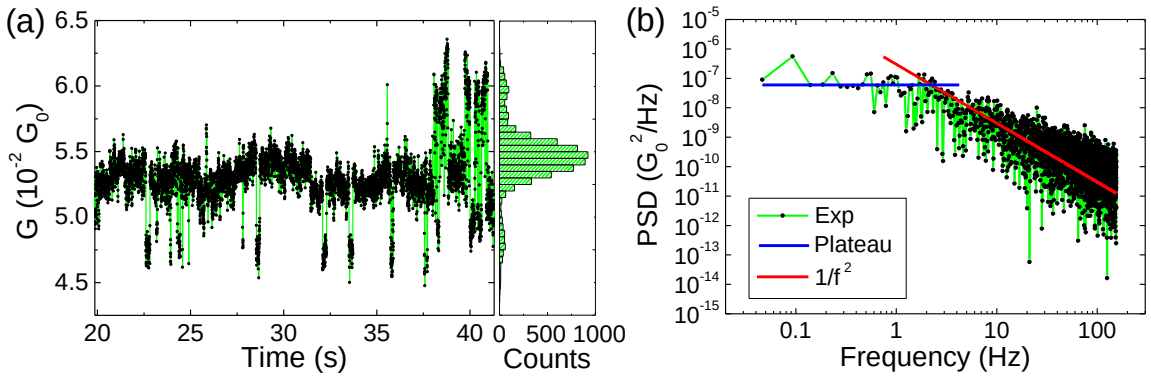

Figure 5.33: Temporal and spectral analysis of a conductance trace of a NW-BDT-NW junction. (a) Conductance temporal trace (data plotted with black points connected by a green line). The right panel is the corresponding histogram, showing a wide high peak between two lower peaks, which correspond to the central most probable value of the conductance and the two other levels, respectively. (b) Power Spectral Density (PSD) of the trace shown in (a) together with the corresponding fitting to a plateau and $1/f^2$, characteristic of RTS spectra.

trace has two parts. The first one, from 20 s to around 37 s, reveals that the conductance is switching between two values. The second part (for time > 37 s) also displays two levels for the conductance; in this case, the lower one matches the upper level of the first part of the plot. The right panel in 5.33(a) shows the corresponding conductance histogram. The three values of the conductance are evidenced by the three visible peaks. The higher number of counts of the central peak suggests enhanced stability around that conductance value for that time interval.

The obtained **switching behavior between two values** (with a superimposed background noise in our data) is characteristic of the so-called **Random Telegraph Signal (RTS)** or bi-stable noise [346]. This telegraphic noise occurs once a molecular junction is formed [343], and it is attributed to spontaneous binding and unbinding of molecules to the electrodes (BDT molecules (un)binding to NWs, in this experiment). Therefore, the **diference between consecutive conductance levels** ($\sim 6 \cdot 10^{-3} \cdot G_0$) in mentioned histogram could be ascribed to the **binding/unbinding of one (or few) BDT molecules**.

The **power spectral density (PSD) of the trace** is depicted in 5.33(b) disclosing the expected **shape for a RTS**: a plateau for low frequencies followed by a $1/f^2$ decay for high frequencies [343, 346]. This plot further supports the existence of molecular junctions in our measurements.

5.9.5.6 *Stability of the Contacts*

In the experiment described above, we cannot completely discard some complex combination of tunneling and molecule transport, or some contamination such as CTAB rests. The experiment **can be improved** in many different ways, as for instance inserting the AFM in a vacuum chamber with a controlled atmosphere of the molecule that we want to study. Nevertheless, what we would like to remark is the **stability of the PANC configuration *vs.* STM or break junctions**. These two techniques are three-dimensional setups where thermal and mechanical stability are of the utmost importance. Consequently, when working at room temperature, it is very difficult to stabilize the junctions for long times. In STM experiments, the current is stable in the open loop configuration for less than 1 minute

[291]. For break junctions, the best experiments report time stability of the order of 1 minute [343]. The standard procedure to increase stability consists in working at cryogenic temperatures, but then the experimental setups become much more complicated. On the contrary, PANC presents a **two dimensional configuration** that inherently stabilizes the system and the stability time goes up to more than hour (see figure 5.32).

5.9.6 *PANC Under Review*

The nanocircuitry technique we present along this chapter is not free of certain **drawbacks**. Most of them are present during the nanocircuit fabrication, being some of them detailed in appendix F. PANC technique comprises many stages until the nanocircuit is finished, which is **time-consuming**. Furthermore, a mistake in some steps can ruin the previous work. Other PANC disadvantages are: (i) it requires **microelectrodes**, (ii) there is risk of microelectrode (and even NWs protuding from them) **blowing** when conducting the wire soldering due to electrostatic-discharge[4], (iii) the **debris** left some times by the manipulating tip on the sample can hinder the manipulation and degrade the nanoobjects, (iv) depending on the chemical nature of the nanoobjects and its purity, the **improvement of the NW-nanoobject electrical contact** may be needed and (v) PANC works **better in vacuum** environment or inert atmosphere. During the fabrication of the first two-terminal device containing a few-layer nanoribbon (section 5.6) we observed that, as the time passed, it was more difficult to perform the nanoobjetct-NW electrical contact. We thought that this fact was due to gradual contamination of the sample in air. Therefore, next devices were assembled and characterized in a argon+air atmosphere. Moreover, we firstly tried to make the NW-nanoobject connections (to avoid contamination of the nanoobject), and then the manipulation and assembling of the NWs conforming each nanoelectrode.

We have already seen most of PANC's **advantages**: (i) it is cost-effective, (ii) it does not require chemicals (except a water or alcohol solution of Au NWs), (iii) it provides many possible configurations and (iv) reconfigurable electrodes, (v) it allows achieve low contact resistances, (vi) its spacial resolution is about few nanometers (or even less) and (vii) due to its 2D geometry it presents an enhaced stability for molecular junctions compared to STM or MCBJs. Table 5.2 summarizes the PANC's pros and cons.

Pros	*Cons*
Cost effective	Time-consuming
Clean	Need of microelectrodes
Many circuit topologies	Risk of electrode blowing
Electrode reconfiguration	Some debris when manipulating
Low contact resistances	Sometimes need to improve contact
Resolution ~nm	Better in HV or inert atmosphere
Enhanced stability	

Table 5.2: PANC's pros and cons.

4 All devices shown in this chapter needed resistors to protect them from electrostatic-discharge. Infact, all of them had a few kΩ protection resistors in series. This is a common procedure in nanocircuits.

A suitable way to asses the benefits and drawbacks of PANC is to **compare** it with the so-far dominant technique in the fabrication of nanocircuits, *i.e.* **EBL**. Table 5.3 compares both techniques considering **five key aspects**: cost, consumption of time, use of chemicals, resolution and circuit reconfiguration. Analyzing each of them for both methodologies, we have that: (i) EBL is more expensive, (ii) both are quite time-consuming, (iii) EBL needs several chemicals while PANC is much more innocous, (iv) resolution of EBL ranges between 30-2 nm whereas PANC can reach ~10 nm as it has been shown in section 5.9.2.2 (and even less: see sections 5.9.2.1 and 5.9.5), and (v) EBL does not allow reconfigurable electrodes while PANC does.

EBL	Key Aspect	PANC
✗	Cost	✓
✗	Time	✗
✗	Use of chemicals	✓
~	Resolution	✓
✗	Reconfiguration of electrodes	✓

Table 5.3: Comparison of EBL and PANC considering five aspects.

5.10 CONCLUSIONS AND FUTURE PROSPECTS

So far, the use of highly conductive nanostructures, as those fabricated by PANC, was a long-standing goal of circuit miniaturization [118, 347, 348]. In this chapter, we have demonstrated that PANC is a cost-effective, versatile and robust technique that provides nanocircuitry for stand-alone devices. Unlike EBL, PANC also allows circuit reconfiguration in a straightforward and quick manner. Besides, PANC requirements and preparation are simple and clean as it uses drop casting of a water or alcohol (ethanol, isopropanol, methanol, etc.) suspension of nanowires. Hence, PANC is compatible with delicate materials.

It is not difficult to envision combined nanocircuitry of EBL and PANC for the electrical characterization of materials that do not support the chemical agents required for EBL, as emerging organics, organometallics and even biomolecules, among others. While EBL is a mature and well-developed technique, PANC has just been born and the results presented in this chapter give a highly limited picture of its possibilities. As PANC is still in its very infancy, it can be improved in many ways. For example, a desirable improvement would be the automation of the manipulation of nanowires [117]. This would short the time needed to assemble a nanocircuit.

In the next future Nanoforces group aims to introduce a broader catalogue of possibilities that shall include the use of longer nanowires, thinner nanorods and smaller nanoparticles made of different materials: silver, nickel, cobalt, platinum, etc. Likewise, the group plans to further extend PANC within the molecular electronics realm, a field where, up to now, the current experimental methods have limited applicability. In this context, PANC also allows, for instance, fabricating high resolution lateral gate nanoelectrodes and performing *in-operando* electrical measurements, which are not trivial but very useful for typical molecular electronics measurements (e.g. STM break junctions). Moreover,

PANC could be used to fabricate nanocircuitry in ultrahigh vacuum by using spray or electrospray methods. That way extremely clean circuits would be obtained, minimizing the contact resistance that dominates today's nanoelectronics.

6 CONCLUSIONS

In this thesis, we have conducted a mechanical and electrical characterization of two 2D materials. We have performed both characterizations mainly making use of atomic force microscopy as well as probe station technology. Furthermore, we have developed a new technique to create electrical contacts in nanoobjects and to construct nanocircuits. This has allowed us to fulfilled the three **objectives** presented in section 1.2:

O1 **Synthesize new 2D materials in a cost-effective manner.** In chapter 4 a new material ($[Cu_2I_2(TAA)]_n$ coordination polymer) has been obtained and processed to form ultrathin films. It is shown that its building blocks as well as its synthesis and processability are cost-effective.

O2 **Measure physical properties of new or already existing 2D materials.** In chapter 3 we conducted a mechanical characterization of few-layer black phosphorus nanosheets and we assessed the effect of the exposure to air ambient atmosphere on their mechanical properties. Chapter 4 presents a complete characterization of ultrathin films of the aforementioned coordination polymer. Specifically we measured its electrical, mechanical and optical properties with particular emphasis in its electrical response.

O3 **Develop new techniques to characterize 2D materials**. We have managed to develop a new methodology that provides nanocircuits and good electrical contacts with nanometric resolution. In chapter 5 (and appendices E, F and G) a thorough description of such technique is given. Moreover, some devices obtained via this technique are presented demonstrating the advantages of the technique.

The measurements conducted in **few-layer black phosphorus nanosheets**, with thickness ranging from 4 to 30 nm, allow us to draw the following conclusions:

- They exhibit an elastic modulus of 46 ± 10 GPa and a breaking strength of 2.4 ± 1 GPa in high vacuum conditions.
- When exposed to ambient atmosphere, they showed significant changes in their topography as a consequence of water absorption. This phenomenon is thickness dependent.
- For the thicker flakes (> 7 nm), the elastic modulus barely decreases with exposure time, reaching a value of ~30 GPa after 200 hours. Their breaking strength, after the same exposure, is reduced to ~1.6 GPa. This implies a reduction factor of ~0.66 for both magnitudes with respect to pristine black phosphorus. On the contrary, the thinnest nanosheets showed a highly decreasing elastic modulus, and spontaneously broke after less than 25 hours of exposure. These results are compatible with previous works in which the variation in the mechanical properties is ascribed to the oxidation of black phosphorus in air, and suggest a ~70% oxygen content in our flakes after 200 hours of exposure.

From the work presented in chapter 4 on the **metal-organic compound** $[\mathbf{Cu_2I_2(TAA)}]_n$ we can conclude that:

- Ultrathin films of this coordination polymer are easily obtained from cheap building blocks (copper(I) iodide and thioacetamide) at the water-air interface by the Langmuir-Schäfer technique.
- The films thickness can be as low as 4 nm, they extend across macroscopic regions and are highly smooth and transparent.
- The mechanical characterization of the films reveals that they can be free-standing, giving a Young's modulus of ~11 GPa and a breaking strength of ~1 GPa. That elastic modulus, low compared with those of metals, is among the highest ones for 2D materials based on coordinate bonds.
- The films exhibit in-plane electrical conductivity up to 50 S/cm that is controlled by the concentration of grain boundaries. This value is significantly high compared to those of other metal-organic polymers.
- Intrinsic memristive response was found for these films. The working mechanism for this behaviour is mediated by the migration of grain boundaries. We believe they could be manipulated to create novel devices with tunable electro-mechanical properties.

We have developed the **Probe-Assisted Nanowire Circuitry (PANC)** technique, which is based on the use of gold nanowires and its subsequent manipulation by an AFM probe to create nanoelectrodes. They are formed by the spontaneous cold welding of gold nanowires upon mechanical contact. The PANC's development and further test leads to the following conclusions:

- PANC enables:
  1. the creation of electrical contacts in the nanometer (or even smaller) scale with low contact resistances
  2. the fabrication of many circuit topologies and, therefore, complex nanocircuits
  3. the reconfiguration and repair of the so-obtained nanoelectrodes
  4. to some extent, the creation of molecular contacts with high stability
- This technique is:
  1. clean (compatible with delicate materials as it hardly requires chemicals)
  2. cost-effective (with simple requirements and preparation)
  3. versatile (flexible, it does not require vacuum, compatible with e-beam lithography)
  4. robust (against temperature and preassure variations, against vibrations and changes of external parameters)
- Among disadvantages of PANC we can mention that: it is time-consuming, it needs microelectrodes, it presents a small risk of electrode blowing if there is a electrostatic-discharge, some debris can be left when manipulating the nanowires,

some electrical contacts must be optimized with mechanical preassure, and it has a better performance when working in vacuum or inert atmosphere.

- We envision PANC as method to create high resolution lateral gate electrodes and to perform *in-operando* electrical measurements.

After the completion of this thesis we identify various **future research lines**. Regarding the mechanical properties of **black phosphorus nanosheets**, we envision these possible research works:

- Measurements in high vacuum and ambient conditions with different drumheads geometries to obtain the elastic modulus in the zigzag and armchair in-plain directions separately.
- Register the time evolution of the breaking force of the flakes in air.
- Accurately asses the influence of the nanosheets' thickness on the variation of the elastic modulus and breaking force when they are exposed to air. The results could be used to design humidity sensors.
- Assess the influence of mechanical strain in the optical and electrical properties of this 2D material in its pristine and oxidized form. These results could have impact in diverse devices' fabrication.

Concerning the $[\mathbf{Cu_2I_2(TAA)}]_n$ **films**, their mechanical and electrical characterization fosters the fullfilment of these tasks:

- Asses the effect of mechanical strain, temperature quenching and others methods on the modification of grain boundaries of the films to tune their conductivity and memristivity. This would allow the fabrication of novel devices with tunable electro-mechanical properties.
- Characterize the electrical response of the films using a gold electrode and a silver electrode, system in which the conduction is due to an electrochemical mechanism.
- Rationally synthesize similar coordination polymers in the search for optimum properties for technological applications.

Finally, the results accomplished using **PANC** encourage us to:

- Use longer nanowires, thinner nanorods and smaller nanoparticles made of different materials: silver, nickel, cobalt, platinum, etc.
- Fabricate and test high resolution lateral gate nanoelectrodes by means of PANC.
- Perform *in-operando* electrical measurements in nanocircuits obtained via PANC, for instance map a magnitude via AFM as a current flows through the nanoobject contacted, or a source-drain or gate voltage is applied. A fascinating experiment would be the use of a silver nanowires nanoelectrode and a gold nanowires path to contact a small $[Cu_2I_2(TAA)]_n$ film, and then visualize, via AFM, the grow of silver dendrites within the film while a source-drain bias voltage is applied.

- Use electrospray ionization technique to deposite molecules on gold nanoelectrodes obtained by PANC.
- Perform the whole (or part) of the PANC fabrication process in vacuum (or controlled environment) conditions.
- Automate the manipulation of nanowires to short the time needed to assemble each nanocircuit.

CONCLUSIONES

En esta tesis, hemos realizado una caracterización mecánica y eléctrica de dos materiales bidimensionales. Ambas se han llevado a cabo, principalmente, mediante el uso de microscopía de fuerza atómica y estaciones de puntas. Además, hemos desarrollado una nueva técnica para crear contactos eléctricos en nanoobjetos y para construir nanocircuitos. Esto nos ha permitido cumplir los tres **objetivos** presentados en la sección 1.2:

O1 **Sintetizar nuevos materiales 2D de manera rentable.** En el capítulo 4 se ha obtenido y procesado un nuevo material (el polímero de coordinación $[Cu_2I_2(TAA)]_n$), obteniendo películas ultrafinas del mismo. Se ha mostrado que sus bloques de construcción, así como su síntesis y procesado, son rentables.

O2 **Medir las propiedades físicas de materiales 2D nuevos o ya existentes.** En el capítulo 3 llevamos a cabo una caracterización mecánica de láminas de fósforo negro de pocas capas y evaluamos el efecto de la exposición condiciones ambiente en sus propiedades mecánicas. El capítulo 4 presenta una caracterización completa de películas ultrafinas del polímero mencionado anteriormente. En concreto, medimos sus propiedades eléctricas, mecánicas y ópticas con especial énfasis en su respuesta eléctrica.

O3 **Desarrollar nuevas técnicas para caracterizar materiales 2D**. Hemos logrado desarrollar una nueva metodología que proporciona nanocircuitos y buenos contactos eléctricos con resolución nanométrica. En el capítulo 5 (y los apéndices E, F y G) se da una descripción detallada de dicha técnica. Además, se presentan algunos dispositivos obtenidos con ella mostrando las ventajas de la técnica.

Las medidas realizadas en **láminas de fósforo negro de pocas capas**, con un grosor de 4 a 30 nm, nos permiten extraer las siguientes conclusiones:

- Exhiben un módulo de elasticidad de 46 ± 10 GPa y una tensión de rotura de 2.4 ± 1 GPa en condiciones de alto vacío.
- Al exponerlas a condiciones ambiente, muestran cambios significativos en su topografía como consecuencia de la absorción de agua. Este fenómeno depende del espesor de la lámina.
- Para las láminas más gruesas (> 7 nm), el módulo elástico apenas disminuye con el tiempo de exposición, alcanzando un valor de ~30 GPa después de 200 horas. Su tensión de rotura, tras la misma exposición, se reduce a ~1.6 GPa. Esto implica un factor de reducción de ~0.66 para ambas magnitudes con respecto al fósforo negro prístino. Por el contrario, las láminas más finas mostraron una reducción mucho más acusada del módulo elástico y se rompieron espontáneamente después de menos de 25 horas de exposición. Estos resultados son compatibles con trabajos anteriores, en los que la variación en las propiedades mecánicas se atribuye a la oxidación del fósforo negro en el aire, y sugieren un contenido de oxígeno de ~70% en nuestras nanoláminas después de 200 horas de exposición.

Del trabajo presentado en el capítulo 4 sobre el **compuesto metal-orgánico** $[\mathbf{Cu_2I_2(TAA)}]_n$ podemos concluir que:

- Películas ultrafinas de este polímero de coordinación se obtienen fácilmente a partir de bloques de construcción baratos (yoduro de cobre(I) y tioacetamida) en la interfaz agua-aire mediante la técnica Langmuir-Schäfer.
- El grosor de las películas llega a ser tan bajo como 4 nm, se extienden por regiones macroscópicas y son muy planos y transparentes.
- La caracterización mecánica de las películas revela que pueden ser suspendidas, dando un módulo de Young de ~11 GPa y una tensión de rotura de ~1 GPa. Ese módulo de elasticidad, comparativamente bajo con el de mucho metales, es de los más altos para materiales 2D basados en enlaces de coordinación.
- Las películas exhiben una conductividad eléctrica en el plano de hasta 50 S/cm que está controlada por la concentración de fronteras de grano. Este valor es notablemente más alto que los de otros polímeros metal-orgánicos.
- Se encontró respuesta memristiva intrínseca en estas películas. El mecanismo responsable de este comportamiento está mediado por la migración de las frontera de grano. Creemos que éstas podrían manipularse para crear nuevos dispositivos con propiedades electro-mecánicas modulables.

Hemos desarrollado la técnica **Probe-Assisted Nanowire Circuitry (PANC)**, que se basa en el uso de nanocables de oro y su posterior manipulación por una sonda de AFM para crear nanoelectrodos. Éstos se obtienen gracias a la soldadura en frío que se da espontáneamente entre los nanocables cuando contactan mecánicamente. Del desarrollo de la técnica y su evaluación posterior extraemos las siguientes conclusiones:

- PANC permite:
  1. la creación de contactos eléctricos en la escala nanométrica (o incluso más pequeña) con bajas resistencias de contacto
  2. la fabricación de circuitos con muchas topologías y, por lo tanto, de nanocircuitos complejos
  3. la reconfiguración y reparación de los nanoelectrodos obtenidos con ella
  4. hasta cierto punto, la creación de contactos moleculares con alta estabilidad
- Esta técnica es:
  1. limpia (compatible con materiales delicados, ya que apenas requiere productos químicos)
  2. rentable (con requisitos sencillos y preparación simple)
  3. versátil (flexible, no requiere vacío, compatible con litografía por haz de electrones)
  4. robusta (contra variaciones de temperatura y presión, contra vibraciones y cambios de parámetros externos)

- Entre las desventajas de PANC podemos mencionar que: requiere mucho tiempo, necesita microelectrodos, presenta un pequeño riesgo de voladura de electrodos si hay descargas electrostáticas, puede dejar algunos residuos al manipular los nanocables, algunos contactos eléctricos deben optimizarse aplicando presión, y presenta mejor rendimiento cuando se trabaja en vacío o en atmósfera inerte.
- Visualizamos PANC como un método adecuado para crear nanoelectrodos laterales de alta resolución espacial (donde aplicar un voltaje *gate*) y para realizar mediciones eléctricas *in-operando*.

Tras completar esta tesis, identificamos varias **líneas de investigación futuras**. Con respecto a las propiedades mecánicas de **nanoláminas de fósforo negro**, concebimos estos posibles trabajos de investigación:

- Mediciones en alto vacío y condiciones ambientales en los nanotambores con diferentes geometrías, para obtener el módulo de elasticidad en las dos direcciones dentro de plano, *zigzag* y *armchair*, por separado.
- Registrar la evolución temporal de la tensión de rotura de las láminas al exponerse al aire.
- Evaluar con precisión la influencia del grosor de las nanoláminas en la variación de su módulo elástico y la tensión de rotura cuando están expuestas al aire. Los resultados podrían utilizarse para diseñar sensores de humedad.
- Evaluar la influencia de la tensión mecánica en las propiedades ópticas y eléctricas de este material 2D en su forma prístina y oxidada. Estos resultados podrían tener impacto en la fabricación de dispositivos variados.

Con respecto a los **films de** $[\mathbf{Cu_2I_2(TAA)}]_n$, su caracterización mecánica y eléctrica promueve la realización de estas tareas:

- Evaluar el efecto de la tensión mecánica, enfriado rápido y otros métodos en la modificación de las fronteras de grano de las películas para modular su conductividad y memristencia. Esto permitiría la fabricación de nuevos dispositivos con propiedades electro-mecánicas modulables.
- Caracterizar la respuesta eléctrica de las películas utilizando un electrodo de oro y un electrodo de plata, sistema en el que la conducción se da por un mecanismo electroquímico.
- Sintetizar racionalmente polímeros de coordinación similares en la búsqueda de propiedades óptimas para aplicaciones tecnológicas.

Finalmente, los resultados logrados usando la técnica **PANC** nos animan a:

- Usar nanocables más largos, nanobastones más delgados y nanopartículas más pequeñas de diferentes materiales: plata, níquel, cobalto, platino, etc.
- Fabricar por medio de PANC, y probar, nanoelectrodos laterales de voltaje *gate* de alta resolución.

- Realizar medidas eléctricas *in-operando* en nanocircuitos obtenidos a través de PANC, por ejemplo, mapear una magnitud por AFM a medida que una corriente fluye a través del nanoobjeto contactado o se aplica un voltaje entre electrodos. Un experimento fascinante sería el uso de un nanoelectrodo de nanocables de plata y otro de nanocables de oro para contactar una pequeña película de $[Cu_2I_2(TAA)]_n$, y después visualizar con AFM el crecimiento de dendritas de plata en la película mientras se aplica una tensión de polarización.
- Utilizar la técnica de ionización por electrospray para depositar moléculas sobre nanoelectrodos de oro obtenidos por PANC.
- Realizar todo (o parte) del proceso de fabricación de PANC en condiciones de vacío (o atmósfera controlada).
- Automatizar la manipulación de nanocables para reducir el tiempo necesario para ensamblar cada nanocircuito.

APPENDICES

A

AFM DYNAMIC MODES

A.1 AMPLITUDE MODULATION AFM (AM-AFM)

If we consider the cantilever as a point-mass spring, **in the absence of tip-sample interaction but under the influence of damping**, the motion of the tip can be regarded as a driven (or forced) damped harmonic oscillation [349]. Accordingly, it is described by the equation:

$$F = -kz - \frac{m\omega_0}{Q}\frac{dz}{dt} + F_0 cos(\omega t) \tag{A.1}$$

where F is the total force on the tip, the first term on the right is the linear restoring force, the second one the viscous damping force and the third one the external driven force (which is exerted by a dither small piezo attached to the the cantilever). z is the vertical position of the tip at each moment, k is the spring constant of the cantilever, m is the mass of the tip, ω_0 is the angular resonance frequency of the free cantilever ($\omega_0 = \sqrt{k/m}$), Q is the quality factor of the cantilever, F_0 and ω are the amplitude and frequency of the driving force.

We can rewrite A.1 as:

$$m\frac{d^2z}{dt^2} + \frac{m\omega_0}{Q}\frac{dz}{dt} + kz = F_0 cos(\omega t) \tag{A.2}$$

whose solution has the following form:

$$z(t) = A_1 e^{\frac{-\omega_0 t}{2Q}} cos(\omega_1 t - \phi_1(\omega_)) + A(\omega) cos(\omega t - \phi(\omega_)) \tag{A.3}$$

that includes a transient and a steady term respectively. For $t >> 2Q/\omega_0$ the steady term contains all the information. The amplitude and the phase shift with respect to the driving force are:

$$A(\omega) = \frac{\frac{F_0}{m}}{\sqrt{(\omega_0^2 - \omega^2)^2 + \left(\frac{\omega_0\omega}{Q}\right)^2}} \tag{A.4}$$

$$\phi(\omega) = \arctan\left(\frac{\frac{\omega_0\omega}{Q}}{\omega_0^2 - \omega^2}\right) \tag{A.5}$$

From these expressions two important facts are derived:

- From A.3 and A.5: there is a phase difference between the driving force and the resultant motion of the tip: a real delay between the action of the driving force and the response of the system takes place. This delay ranges from $\phi = 0$ at $\omega = 0$ to $\phi = \pi$ at $\omega \to \infty$, having a value of $\phi = \pi/2$ at $\omega = \omega_0$.
- From A.4: if $\omega = \omega_0$, then the amplitude takes the value:

$$A(\omega = \omega_0) = A_0 = \frac{QF_0}{m\omega_0^2} = \frac{QF_0}{k} \tag{A.6}$$

there is a maximum of the $A(\omega)$ at $\omega = \omega_R$, being ω_R:

$$\omega_R = \omega_0 \sqrt{1 - \frac{1}{2Q^2}} \tag{A.7}$$

Therefore, damping causes a change in the resonance frequency of the cantilever: from its natural free resonance frequency (ω_0) to ω_R. This change modifies the phase shift (ω takes the value of ω_R, instead of ω_0, in A.5). Hence, phase imaging in the AM-AFM mode is a way to map the tip-sample inelastic interactions [62], such as adhesion, viscoelasticity, Young's modulus, etc. [63, 64].

If we now **discard the damping but introduce a tip-sample force** (F_{ts}), assuming a parabolic tip-sample interaction potential, the total force, F, applied to the tip includes the elastic response kz and F_{ts}. For small displacements with respect from the equilibrium position (z_0), the tip-sample interaction can be treated as a perturbation [57]:

$$F = F_0 + \left(\frac{dF}{dz}\right)_{z_0} (z - z_0) \tag{A.8}$$

In these conditions an effective spring constant can be defined as:

$$k_{eff} = -\frac{dF}{dz} = \left(k - \frac{dF_{ts}}{dz}\right)_{z_0} \tag{A.9}$$

hence, the new effective resonance frequency is given by $\sqrt{k_{eff}/m}$:

$$\omega_{o,eff} = \sqrt{\frac{k_{eff}}{m}} = \sqrt{\frac{\left(k - \frac{dF_{ts}}{dz}\right)_{z_0}}{m}} \tag{A.10}$$

and if the force gradient is smaller than k, which usually happens, then:

$$\omega_{o,eff} \approx \omega_0 \left(1 - \frac{1}{2k}\frac{dF_{ts}}{dz}\right) = \omega_0 - \Delta\omega_0 \tag{A.11}$$

This expression for $\omega_{0,eff}$ reflects that the resonance frequency of a weakly perturbed harmonic oscillator is modified by the gradient of the interaction force. According to equation A.4, a change in the resonance frequency implies a whole shift of the resonance curve, $A(\omega)$ (where ω_0 is replaced by $\omega_{0,eff}$) (and a shift in the phase curve, $\phi(\omega)$, too).

Attractive interacting forces decrease the resonance frequency of the cantilever while the repulsive ones increase it. From equation A.10 one notices that no uniform force ($dF_{ts}/dz=0$) causes the mentioned frequency shift, it only changes de equilibrium point (the tip-sample distance) [65].

For small force gradient, the amplitude change is given by [65]:

$$\Delta A = \frac{2A_0 Q}{3\sqrt{3}k}\frac{dF_{ts}}{dz} \tag{A.12}$$

which is proportional to the quality factor and very sensitive to the variations of the tip-sample distance. This allows the use of the amplitude as the feedback magnitude to image the samples in the AM-AFM mode. In summary: a change in the tip-sample distance yields a variation in the force gradient, this implies a shift of the resonance frequency which changes the amplitude.

A.2 AMPLITUDE MODULATION + PHASE LOCK LOOP AFM (AM+PLL-AFM)

This is a variation of the standard AM-AFM mode, in which there is an extra parallel feedback loop to maintain the cantilever phase constant. This extra loop is called Phase Lock Loop (PLL) [68]. As stated above, when $\omega = \omega_0$, the phase shift takes the value $\phi = \pi/2$, ergo, by keeping ϕ equal to $\pi/2$, the cantilever will oscillate at its resonance frequency ω_0.

The output of the PLL is the shift of the driving frequency (the change of the frequency of the signal applied to the dither piezo). The main difference between using AM-AFM and AM+PLL-AFM is that in the case of AM-AFM the amplitude drop is originated by a mix of conservative and dissipation interactions. On the contrary, in AM+PLL-AFM the amplitude drop is caused exclusively by dissipaction forces (the cantilevers is allways at resonance). When using PLL, the driving frequency shift only includes information from conservative interactions [350] and the phase signal is only the error signal of the feedback loop, it does not contain physical information. Another advantage of the use of PLL is that, as the cantilever is always oscillating at its resonance frequency, it is very sensitive to amplitude changes caused by topography variation.

A.3 DRIVE AMPLITUDE MODULATION AFM (DAM-AFM)

In the case of DAM-AFM dynamic mode, the magnitude that is kept constant to acquire the topography of the sample is the amplitude of the driving force, which is related to dissipation.

Although AM-AFM is the most widespread dynamic mode, it is not possible to extend its use to high vacuum. In such case, the Q factor is highly increased (~1-2 orders of magnitude with respect to air environment), extremely reducing the bandwidth of the system. Q controls the response of the system against parameter variations. A variation is, for example, moving to a new point of the sample. After that, the $A(t)$ of the system contains, apart from the steady-state term (a new resonance curve) two transient terms that decay with time constant $\tau/2$ and $\tau = 2Q/\omega_0$. Hence it is necessary to wait until those transients dissapear. That wait time is characterized by τ, which is too long when Q is as high as in high vacuum (HV) environment. This makes the slope detection method

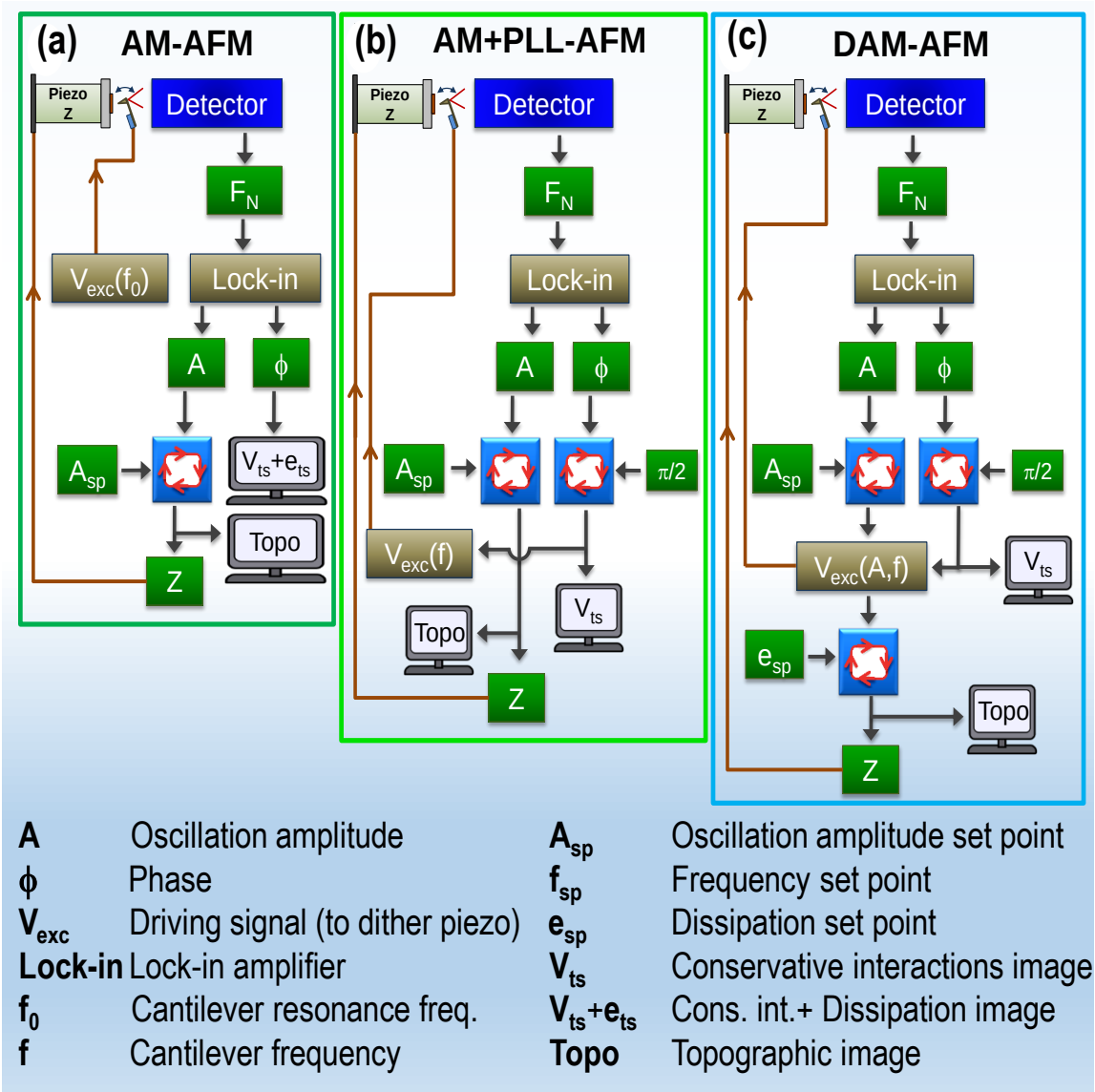

Figure A.1: Feedback diagrams for different dynamic AFM modes. (a) AM-AFM, (b) AM+PLL-AFM and (c) DAM-AFM. Adapted from [37] and [59].

used in AM-AFM not suitable for vacuum applications [57]. This problem is overcome by FM-AFM and by DAM-AFM.

DAM-AFM mode employs three feedback loops: two nested loops to acquire the topography and a parallel PLL that provides a map of conservative interactions [59]. The first of the two nested loops adjusts the driving signal amplitude to mantain the cantilever oscillation amplitude constant. The PLL adjusts the phase of the driving force to keep the phase of the cantilever equal to $\pi/2$ (tracks the resonance frequency). The second nested loop adjusts the z position of the scanner piezo to mantain constant the dissipation of the cantilever, giving the topography of the sample.

Figure A.1 shows the operation diagrams for the three described dynamic AFM modes.

B

STANDARD ELECTRICAL MEASUREMENTS USING A PROBE STATION

The 2-wire sensing topology together with a backgate voltage has a **Field Effect Transistor (FET) configuration**, thus, the voltage applied between the 2 wires (or probes) is usually called V_{ds} (drain-source), V_s (source) or simply V, while the backgate voltage is V_g (gate).

Some of the most **common electrical measurements** that are performed on a device using a probe station (or another setup) are the acquisition of (see figure B.1):

- The already introduced *IV characteristics* (I *vs.* V_{ds}, see section 2.1.7) for a given V_g (figure B.1(a)). In the 2-wire configuration the voltage between both electrodes is changed while the generated current is registered, providing the IV. In the 4-wire setup, for each point of the IV curve, the current in the outer loop is modified until the expected value for the voltage in inner loop is achieved. This is performed through a feedback loop.

- I *vs.* V_g for a set V_{ds} in a 2-wire setup (figure B.1(b)). For the 4-wire scheme, the equivalent measurement would be the acquisition of the drop voltage *vs.* the V_g for a given a current. From these curves the *doping* of the material measured can be derived.

- *IV curves as the temperature is varied* (figure B.1(c)). From these plots the resistance and the conductance *vs.* the temperature is yielded, therefore an *Arrhenius plot* can be also obtained (from which the corresponding *activation energy*, or energies, can be computed) [351, 352]. If a collection of IVs for a range of temperature is acquired *for several gate voltages*, then the activation energy *vs.* the gate voltage can be derived [351, 352].

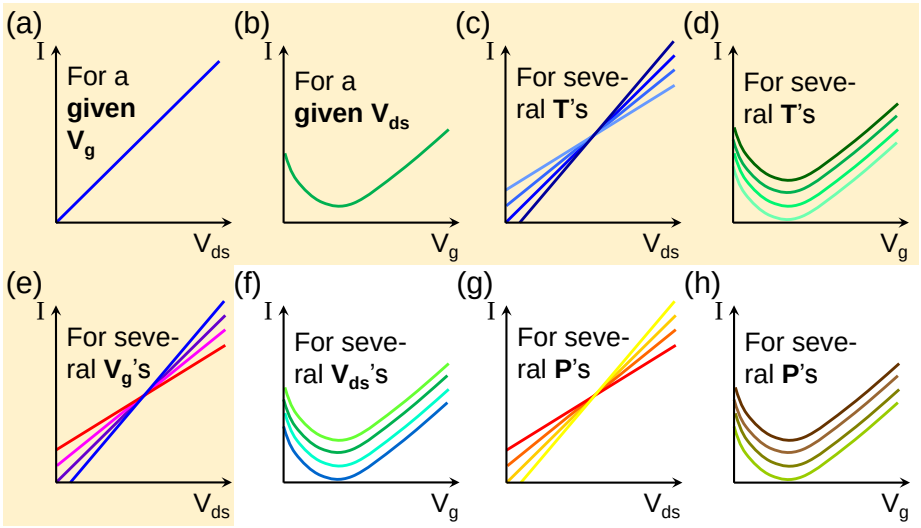

Figure B.1: Some electrical measurements that can be performed on a device using FET notation. The shaded ones are the most common ones.

- I *vs.* V_g *for different temperatures* (figure B.1(d)).
- *IV curves for a collection of* V_g*'s* (figure B.1(e)).
- I *vs.* V_g *for several* V_{ds}*'s* (figure B.1(f)).
- *IVs for a range of preassure* of a controlled atmosphere (figure B.1(g)).
- I *vs.* V_g *for a range of preassure* of a controlled atmosphere (figure B.1(h)).
- *Photocurrent*: generated by the exposure to radiant power. A possible measurement is its variation as a function of time with a modulated light excitation. Many combinations can be performed: photocurrent *vs.* wavelenght of light, or *vs.* power of light, etc. These measurements are usually done with the 2-wire sensing topology [353].
- And many more.

An important measurement, not mentioned above, is the acquisition of **leakage current** through the backgate electrode to check that it is always below a suitable value.

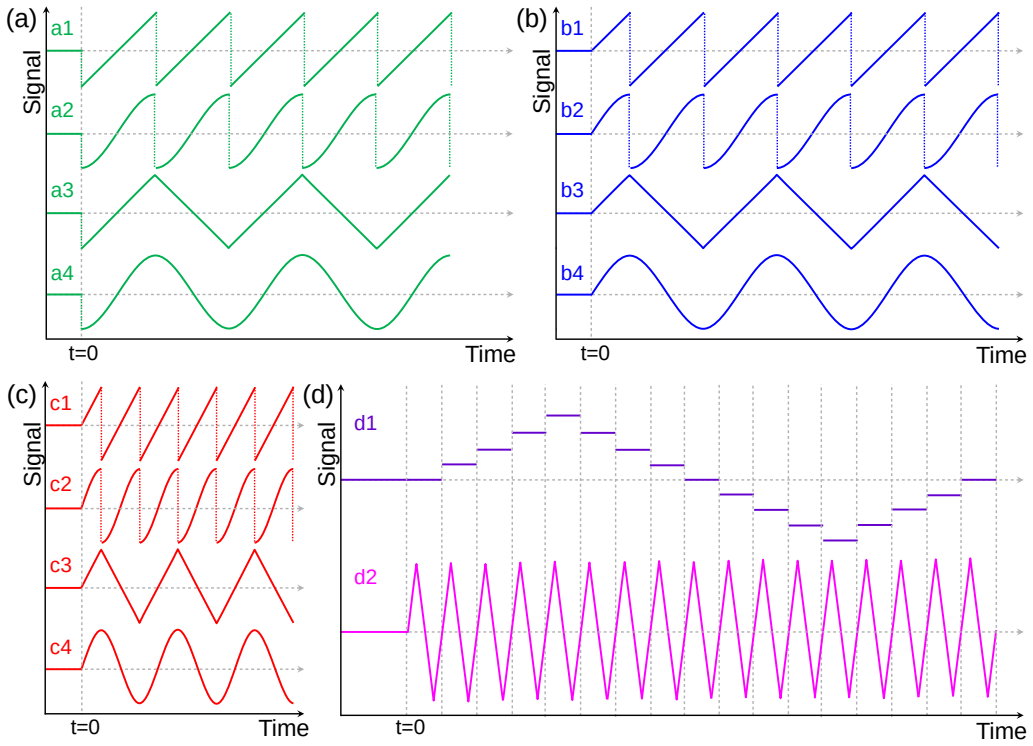

Figure B.2: Features of the excitation signals used in electrical measurements. (a) Signals that jumps from zero to a low value at t=0: a1: sawtooth waveform with increasing linear ramps, a2: sawtooth waveform with increaing sinusoidals, a3: triangle waveform, a4: sinusoidal waveform. a1 and a2 present discontinuities whereas a2 and a3 are smooth except at t=0, this is avoided in (b). (b) Same signals as (a) smoothly decreasing from zero at t=0. (c) Same waveforms as (b) but with double frequency. (d) Two nested signals needed to performs some electrical measurements as for instance IVs for several V_g's (figure B.1(e)), V_g would be d1 waveform and V_{ds} d2. Both change in a triangle fashion with time; for a certain value of V_g a complete cycle of V_{ds} is applied.

A significant issue is the **variation of the independent variables**. The excitation voltage can have a linear, sinusoidal, or other **waveforms**. They can have abrupt changes or they can change smoothly. This is depicted in figure B.2 (a) and (b). Another key parameter in some experiments is the waveforms' **speed** or frequency (figure B.2(c)). As I will present in chapter 4, the speed of the excitation voltage (in V/s) can cause different responses of the samples studied. Sample temperature is another magnitude usually changed during experiments. Its control is more complicated due to the thermal inertia of the parts to be heated or cooled.

In some electrical measurements, for example in the acquisition of IV curves for different values of backgate voltage, there will be two excitation magnitudes. In these cases we will have **nested excitation waveforms** as the ones shown in figure B.2(d).

C

AFM CANTILEVERS TO CONDUCT NANOINDENTATIONS ON FEW-LAYER BLACK PHOSPHORUS DRUMHEADS

C.1 CHOICE OF SUITABLE COMMERCIAL AFM CANTILEVERS

The cantilevers must meet several requirements:

- They should be made of a **hard material**.
- Their tip should have a **smooth and well defined contact geometry**, that does not change while performing nanoindentations nor drilling the nanodrums. Rough tip surfaces will increase the pressure locally, puncturing and breaking the membranes.
- They must have a **suitable spring constant** that allow reaching breaking forces without saturating the photodetector (too soft cantilevers) and without giving a very low change in the deflection (too hard cantilevers). A cantilever spring constant close to the spring constant of the drumhead would be the best option. The spring constant of the BP membrane is around 1 N/m for low indentations but it highly increases with the indentation, thus, cantilevers with spring constant much higher than 1 N/m are the best option.
- They must have an **appropiate tip radius**: (i) not too low not to apply an excessive preassure on the drumhead leading to its fracture at low and non-reproducible forces, (ii) not too low not to splinter the tip giving a new and unkown radius, and (iii) not too high to consider the tip as a punctual load (R_{tip}<0.15·$R_{drumhead}$), which is assumed in the equation of F(δ) (equation 3.7) [195].

After taking into account the previous requirements, and the experience of Dr. Guillermo López-Polín using different kind of cantilevers to indent graphene drumheads [183], we used HSC60 commercial cantilevers from Team Nanotec-NanoScience Instruments [198]. Their tips have **hemispherical geometry** and low wear coating of **tungsten carbide** with nominal final tip radius of **60 nm**. The cantilever spring constants were calibrated by Sader method (see next section) and yielded values in the range of **25-35 N/m**.

These cantilevers fulfill all mentioned requirements. Specifically, concerning the punctual load assumption, the smallest diameter of the indented drumheads is 476 nm, that gives a $R_{tip}/R_{drumhead}$ ratio of 0.13, validating the assumption in our experiments. Figure C.1 is a SEM image of the kind of AFM tip used in our measurements.

C.2 SPRING CONSTANT CALIBRATION

An important issue not mentioned yet is the **precision of the value of the spring constant of the cantilever** used to conduct the nanoindentations. It is crucial for determining the applied force. The nominal value has a very high error, therefore all the cantilevers used along this PhD were calibrated by means of *the Sader method* [355]. This method relates the spring constant of a rectangular cantilever with its width, length, resonance frequency, its

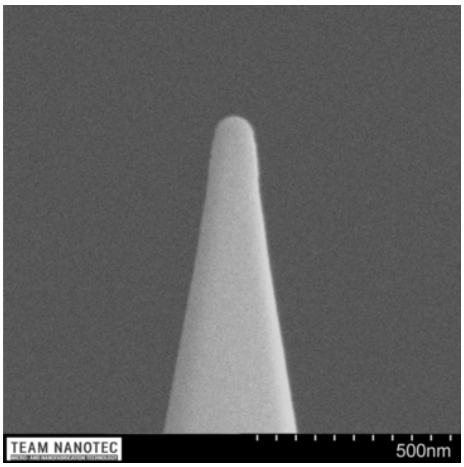

Figure C.1: SEM image of a tungsten carbide tip with 60 nm radius (HSC60). Scale bar: 500 nm. Source: [354].

quality factor and a function that depends on the viscosity of the environment. Therefore, by acquiring a resonance curve at air (with a known viscosity) and knowing the width (35 μm nominal) and length (125 μm nominal) of the cantilever, we can calibrate its spring constant. The nominal values of the width and length are quite precise, on the contrary, the thickness (not needed in this method), highly varies among the cantilevers even from the same batch.

D

SPECTRA AND THERMAL STABILITY OF $[Cu_2I_2(TAA)]_n$

D.1 XPS SPECTRA

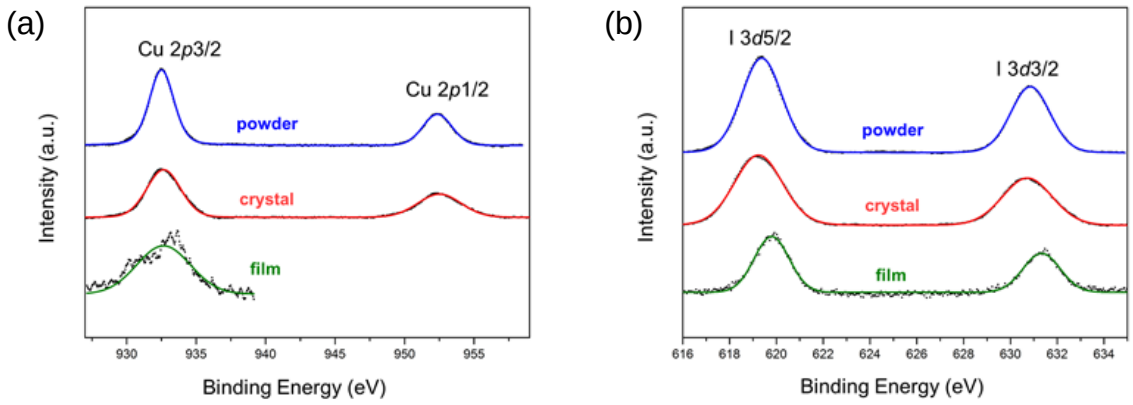

Figure D.1: XPS copper (a) and iodine (b) spectra of $[Cu_2I_2(TAA)]_n$ powder, crystal and film.

Sample	Binding energy (eV)				
	Cu $2p_{3/2}$	I $3d_{5/2}$	S 2p	N 1s	C 1s
$[Cu_2I_2(TAA)]_n$ powder	932.5	619.4	162.8	399.9	284.8 (65 %) 286.2 (35 %)
$[Cu_2I_2(TAA)]_n$ crystal	932.6	619.3	162.9	399.9	284.8 (67 %) 286.3 (33 %)
$[Cu_2I_2(TAA)]_n$ film	932.5	619.4	162.9	399.3	284.8 (65 %) 286.3 (35 %)

Table D.1: Binding energy values for different $[Cu_2I_2(TAA)]_n$ samples determined from XPS measurements.

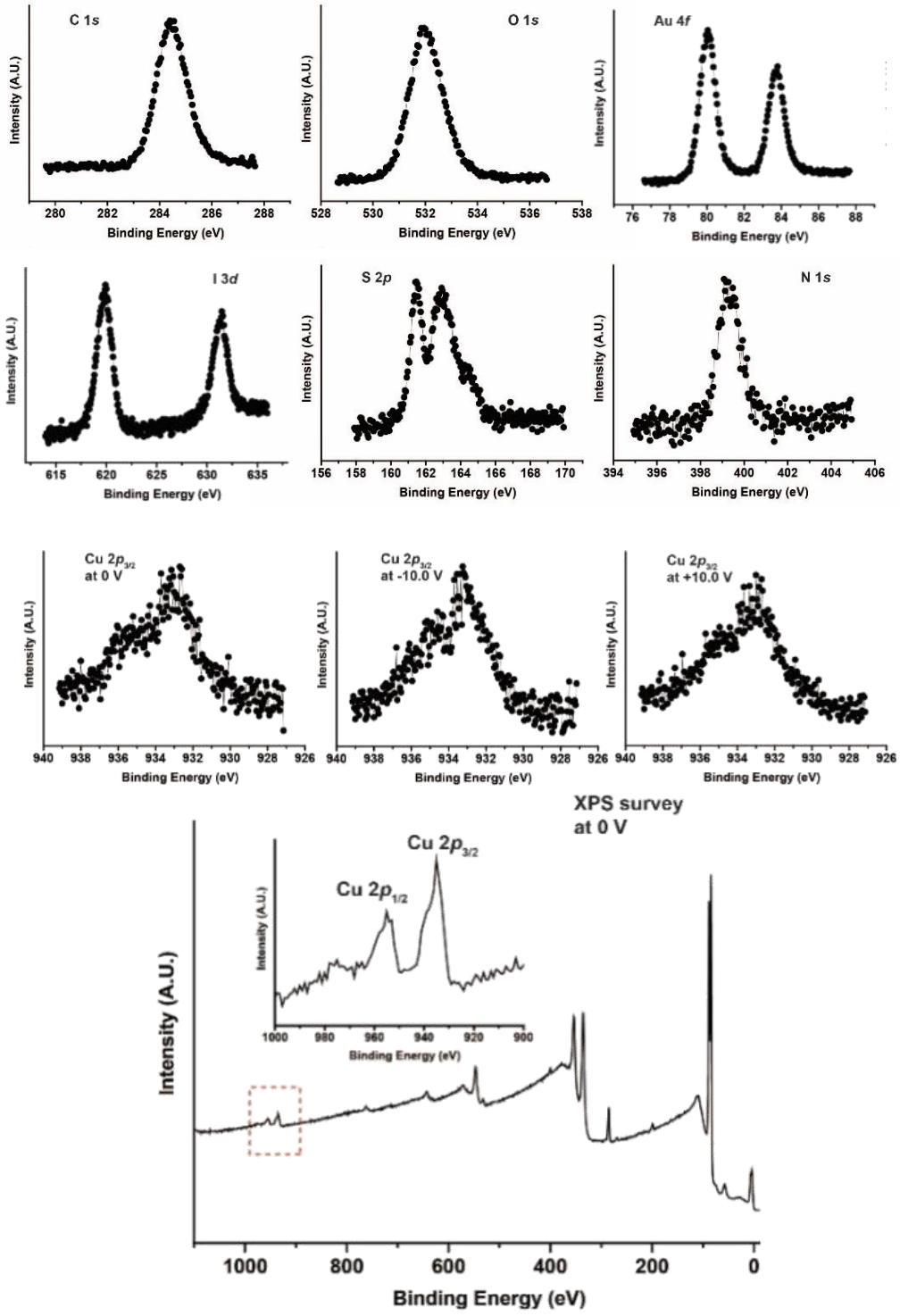

Figure D.2: High resolution XPS spectra of $[Cu_2I_2(TAA)]_n$ films after applying 10 V characterized by synchrotron XPS. XPS of copper was registered at 0 and $\pm$10 V.

D.2 FTIR SPECTRA

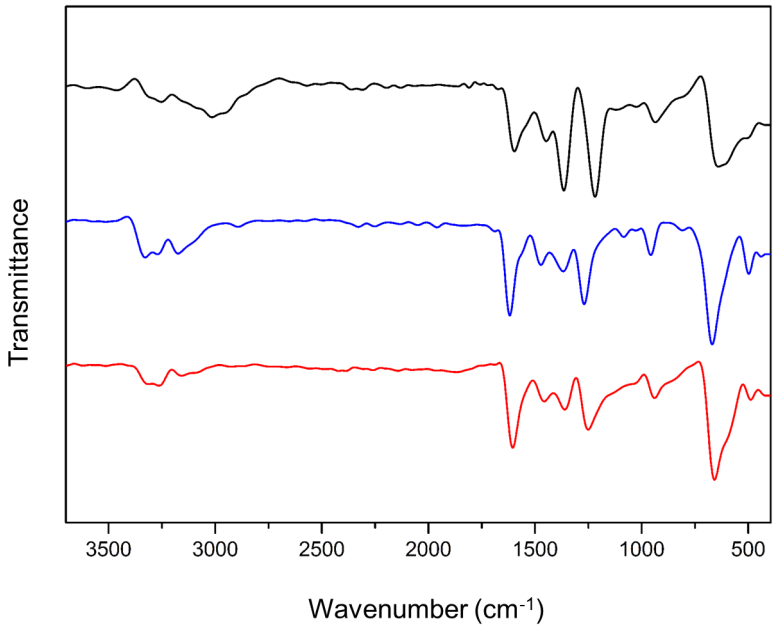

Figure D.3: FTIR spectra of $[Cu_2I_2(TAA)]_n$ crystals (black), powder (blue) and film (red). The spectra agree with an analogous structure for the $[Cu_2I_2(TAA)]_n$ crystals, powder and film.

D.3 THERMAL ANALYSIS

For the thermal analysis of $[Cu_2I_2(TAA)]_n$ powder, we first obtained the thermal gravimetric analysis (TGA) curve and its first derivative. A weight loss of ~15 % was observed from 150 to 350°C, reaching a plateau for higher temperatures (figure D.4(a)). The mass loss determined by TGA correlates with the loss of TAA molecules giving rise to a CuI residue (theoretical mass loss = 16 %). This transformation was confirmed by X-ray powder diffraction (XRPD) analysis of the product after heating $[Cu_2I_2(TAA)]_n$ powder at 200°C for 1 h under inert atmosphere as shown in figure D.4(b). Accordingly, we carried out a differential scanning calorimetry (DSC) experiment in this temperature range (from 25 to 350°C) in order to determine the phase transition (T = 170°C).

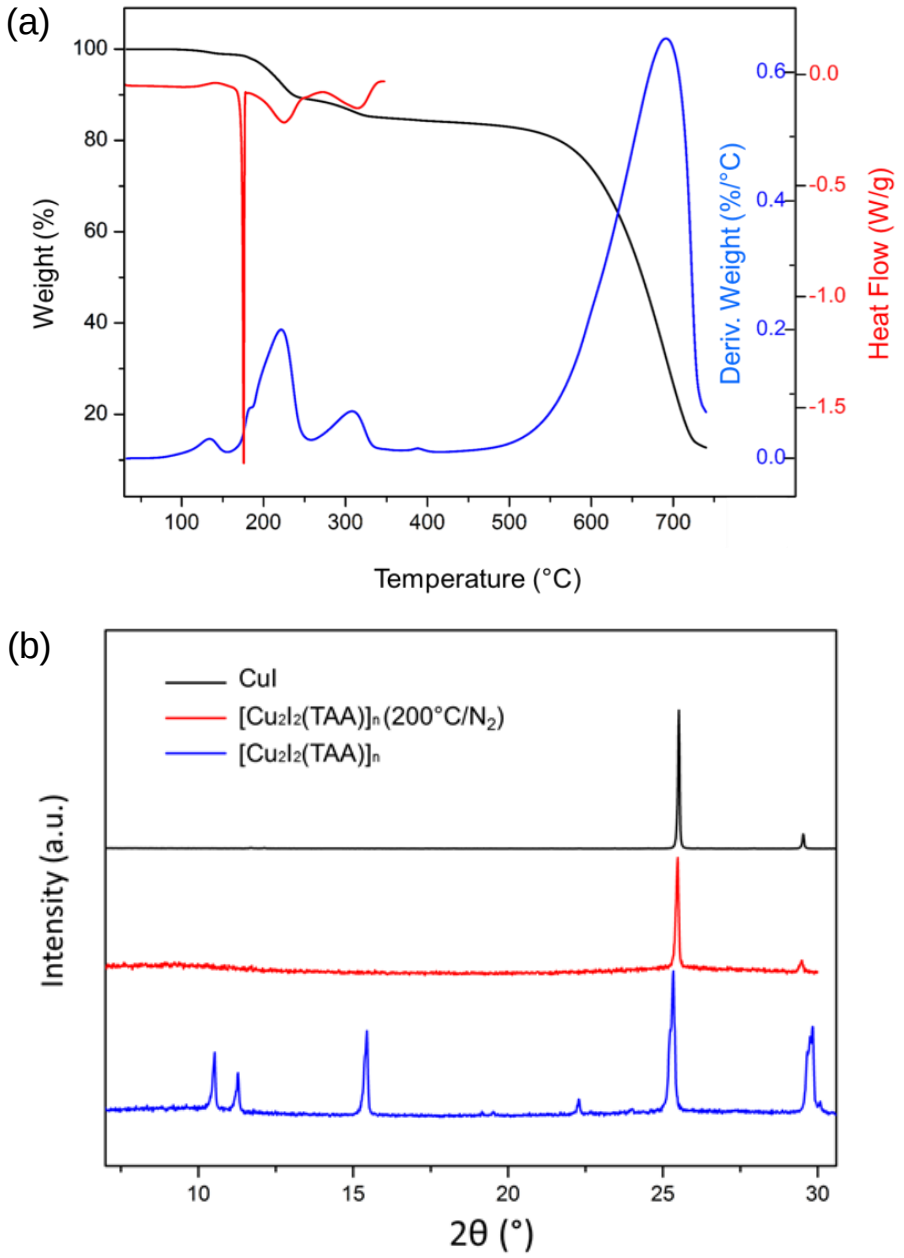

Figure D.4: Thermal analysis of $[Cu_2I_2(TAA)]_n$ powder. (a) TGA (black), derivative TGA (blue) and DSC (red). (b) XRPD before (blue) and after (red) heating at 200°C for 1 h under N_2 atmosphere compared to CuI (black).

E

SYNTHESIS OF GOLD NANOWIRES

E.1 CHEMICALS

Gold(III) chloride hydrate (99.999%) was purchased from Aldrich, Hexadecyltrimethylammonium bromide (CTAB, 99%) from Sigma, sodium borohydride, trisodium citrate 2-hidrate (99%) and L(+)-ascorbic acid (90%) were purchased from Panreac. All synthetic reagents were used as received. Milli-Q water was used in all synthesis. All the glassware must be washed with aqua regia and rinsed thoroughly with Milli-Q water.

E.2 PREPARATION OF SEED GOLD NANOPARTICLES

The colloidal solution was prepared according to standard literature procedure [300]. To a 10 mL aqueous solution containing $HAuCl_4$ (0.25 mM) and trisodium citrate (0.25 mM), prepared in a 30 mL glass vial, was added 0.3 mL of ice cold 0.1 M $NaBH_4$ solution under stirring. The solution turned orange immediately after addition. These nanoparticles can be used as seeds after 5 h preparation and can be stored at 4°C.

E.3 PREPARATION OF GOLD NANOWIRES

A three step seeding method was used for nanowire preparation. 30 mL of the growth solution was prepared by adding 15 mL of chloroauric acid solution (0.5 mM) to 15 mL of CTAB (0.2 M). Two 20 mL glass vials (labeled A and B) and a 50 mL PP tube labeled C were prepared. Vials A and B containing 2.25 mL of growth solution were mixed with 12.5 µL of 0.1 M ascorbic acid solution. Tube C, containing 23 mL of growth solution, was mixed with 130 µL of 0.1 M ascorbic acid solution and 100 µL of nitric acid. Next, 200 µL of 4 nm seed solution was mixed with sample A and stirred, the color of A turned

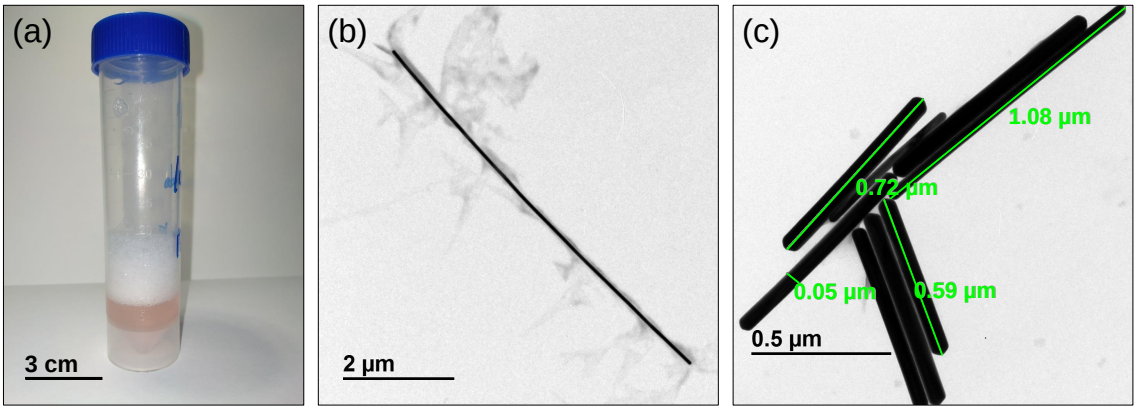

Figure E.1: Home-synthesized gold nanowires. (a) Falcon tube containing a dispersion of nanowires synthesized by the method explained. The bubbles are produced by the surfactant and stiring. (b-c) TEM images of some so-obtained nanowires.

pink. After 5 s, 200 μL of A was added to sample B followed by thorough mixing during 5 s. The color of B turned light pink. After 5 s, 200 μL of B was added to C and stirring during 10 s. The nanowires were allowed to grow during 48 h without stirring at 28.5°C, this temperature is essential in order to avoid CTAB precipitation problems.

Figure E.1 shows a falcon tube with a dispersion of gold nanowires obtained by method described and two TEM images of some of them.

F

STEPS OF PANC METHODOLOGY

F.1 PREPARATION OF THE NANOOBJECT(S) ON A FLAT INSULATING SUBSTRATE

This stage must include the choice of a proper **insulating flat substrate** (with a conductive underlying layer if back-gate voltages are needed), the **cleaning** of the substrate, the **placing of the nanoobjects** on it (by means of exfoliation, adsorption, evaporation, etc.), and the checking of the cleanlinness of the resulting sample. The substrate surface should be flat and smooth enough to be measured in AFM. Furthermore, sometimes it should be smoother than that, specifically when the nanoobject to be studied has a height similar to standard substrates' roughness. The cleanlinnes is another important aspect to be fulfill, if there is to much dirt, the eventual manipulation of NWs will become unfeasible.

F.2 FABRICATION OF MICROMETER-SIZED ELECTRODES

Thermal evaporation. We deposited 10-15 nm of Cr followed by a thicker layer of gold (~100 nm) on the substrates (300 nm oxide silicon grown thermally on a highly-doped Si (111)) by thermal evaporation.

Evaporation masks. We used ad hoc stencil masks made of nickel for thermal evaporation. We designed them with the layout depicted in figure F.1. Each mask contains 8 motifs that were designed to allow the fabrication of four and six microelectrode setups with gaps ranging between 50 and 5 μm. We ordered Gilder Grids Ltd. the fabrication of these masks [356].

Figure F.2 shows, in panel (a), three substrates with some masks on them, in panel (b), a resulting motif with 6 microelectrodes after the thermal evaporation and (c) is a zoom of the square in (b).

We considered two different types of samples: (i) **Inhomogeneous**, the nanoobjects of interest are located by inspection, usually with an optical microscope. In this case the sample substrate is glued to a strong Cobalt-Samarium magnet and the gap of one mask motif is located on top of the object with a micromanipulator. As the mask is made of nickel, it remains firmly attached to the substrate thanks to the magnetic force of the magnet. Then, the magnet with the sample and the attached mask are inserted on a thermal evaporator. (ii) **Homogeneous** sample. The nanoobjects cover the sample uniformly. In this case, there is no need to locate the mask in any particular region of the substrate.

In order to avoid unwanted shadows during evaporation, the sample must lay down on the surface as flat as possible. The magnet helps to keep it in strong contact with the surface.

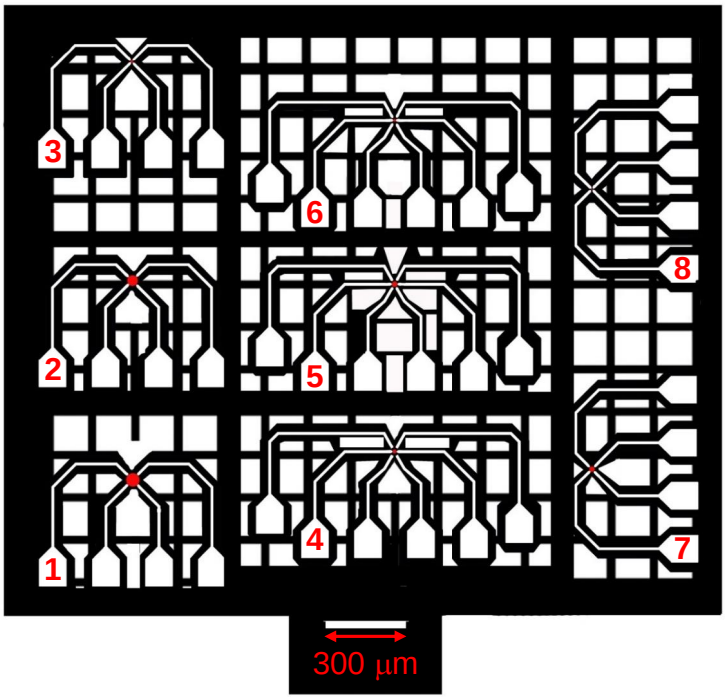

Figure F.1: Stencil masks' layout. Nickel mask design with the following gap sizes in each motif in µm: 1) 50, 2) 40, 3) 20, 4) 15, 5) 10, 6) 6, 7) 10 and 8) 5.

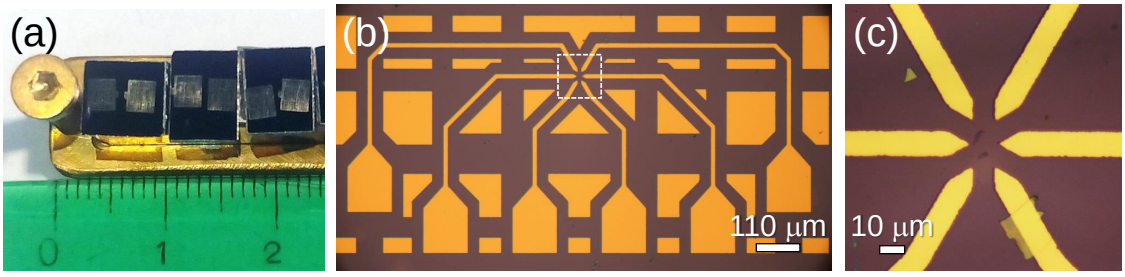

Figure F.2: Metallization using stencil masks. (a) 3 SiO_2 substrates with 2 masks on each of them, the substrates are glued to a cobalt-samarium magnet. (b) Micropragh of a motif with 6 microelectrodes after the thermal evaporation of chromium and gold. (c) Micrograph of the square in (b).

F.3 GOLD NANOWIRES ADSORPTION

We first placed the dispersion containing the Au NWs on a vortex mixer for 15 seconds, then we heated and sonicated a 200 µl aliquot in an ultrasound bath (30°C, 37 kHz, 380 W) for 2-5 minutes to resuspend aggregated NWs. Afterwards, we cast a 10 µl drop on the substrate and left it for ~10 minutes at a temperature of almost 30°C. After that time, we washed the substrate with deionized water at this same temperature and dried it with a N_2 gas flow. We performed both washing and drying processes very smoothly to avoid dragging of the NWs. We carried out all the steps at ~30°C to avoid aggregation of CTAB, which tends to form crystals. We then inspected the substrate containing the NWs with an optical microscope (Zeiss Axiovert microscope with x5, x10, x20, x50 and x100 magnifications) in dark field mode to check the density and spatial distribution of NWs. We repeated the drop-casting step (using the same aliquot) until a concentration of around 1 NW per 5 μm^2 was achieved. This usually requires several (five or more) repetitions. Just before each drop casting step, the aliquot was agitated with the vortex mixer to prevent the NWs from depositing at the bottom of the vial.

Figure F.3 gathers different images of Au NWs. Subfigure (a) displays a substrate with the nanoobject to be studied (a few-layer graphene flake), a Cr/Au metallization using the stencil mask introduced in F.2 (its shape is visible) and a drop of the Au NWs dispersion on it. Panel (b) of the same figure is a dark field optical microscope image of a small area of sample in (a) that contains the nanoobject, the microelectrodes around it, and the Au NWs already adsorbed. We performed eight drop castings to obtained that landscape of nanowires. Panel (c) is a brigth field optical microscope image of the area inside the white rectangle in (b). In this image the few-layer graphene flake is clearly visible, but that is not the case of the Au NWs, which are more visible in dark field mode.

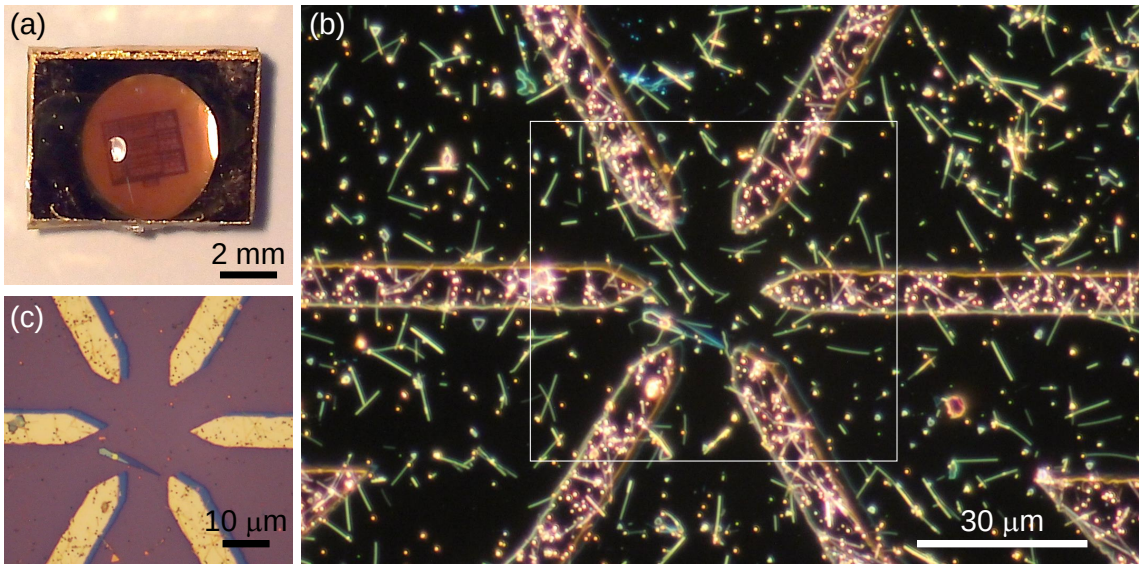

Figure F.3: Adsorption of gold nanowires. (a) Sample with a drop of Au NWs on it. (b) Dark field micrograph containing a few-layer graphene flake, the microelectrodes around it, and Au NWs adsorbed all over after eight depositions. (c) Brigth field micrograph of the area inside the white rectangle in (b) showing the few-layer graphene flake near the electrodes at the bottom left.

F.4 WIRE SOLDERING

After many attempts of connecting the microelectrodes to the PCB pads using a commercial wire bonder [357], our success rate was very low: most of the times part of the microelectrodes lifted off when soldering due to poor adhesion of the metal to the substrate. We attributed this lack of adhesion to the presence of glue tape debris wich are common after micromechanical exfoliation with tape. Therefore **we finally used silver conductive epoxy** [358] at one end of a 40 μm diameter thick copper wire to glue it to the microelectrode and silver conductive paint [359] to glue the other end of the wire to the PCB pad, achieving the electrical connection between them. The use of conducting epoxy is a quite extended procedure for electrical connections in micromechanically exfoliated samples. Figure F.4 shows two samples: (a) corresponds to one of the very few soldered with a commercial wire bonder and (b) to another where wire welding was conducted with conductive epoxy on the microelectrodes.

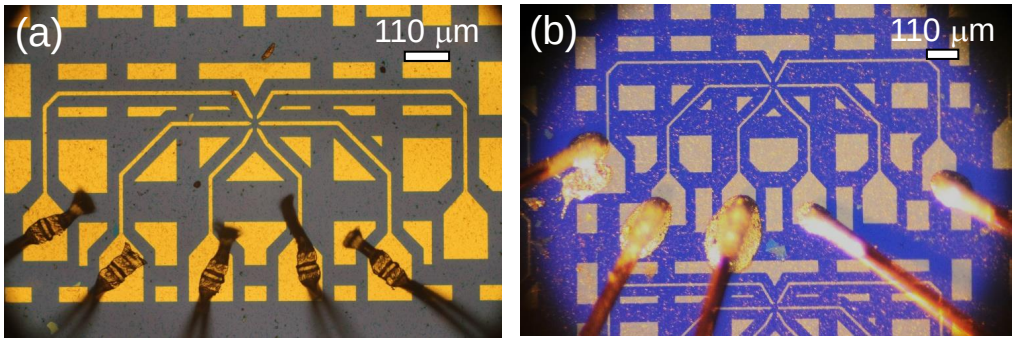

Figure F.4: Wire welds obtained by means of a commercial wire bonder (a) and through conductive epoxy (b).

With the aid of an optical microscope, a syringe needle and a XYZ micromanipulator, we are able to place the end of the copper wire (previously wetted in the conductive epoxy) on the desired microelectrode. It achieves an operational cure at 80°C for 10 minutes. Then we move the needle to the PCB pad and attached it with silver paint. Figure F.5 summarizes the epoxy-based wire soldering method we used.

An important issue when soldering with epoxy is to **avoid microelectrode blowing** caused by electrostatic discharge. This phenomenon can happen if any of the elements that will be electrically connected (microelectrode - thin copper wire - macroscopic wire coming from a PCB pad) are not at the same electrostatic potential. To avoid it, one should connect all macroscopic wires to ground, as well as the thin copper wire, before making the connection. It is recommended to have a protection resistor (of a few kΩ) in series with each macroscopic wire.

F.5 AFM MANIPULATION OF GOLD NANOWIRES TO FORM CONTINUOUS PATHS

We moved the NWs by means of the AFM of figure 2.4(e-f) (section 2.1.1) using the **lithography** option of WSxM [54, 55]. We performed the motion of the NWs to assembly the paths by moving the AFM tip in contact mode along predefined trajectories [116]. We used PPP-FM cantilevers from Nanosensors [360], with nominal resonance frequency of 75 kHz and normal spring constant of 2.8 Nm^{-1}.

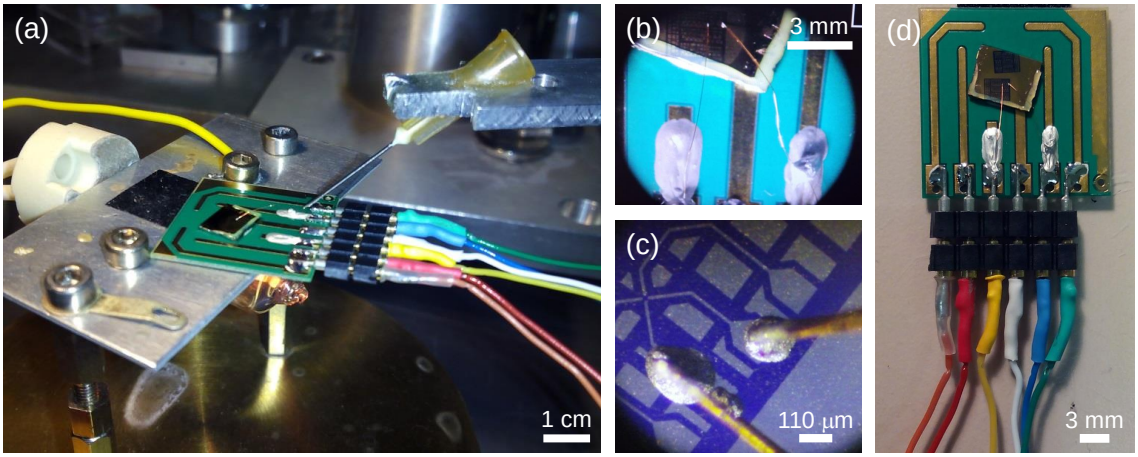

Figure F.5: Wire soldering using conductive epoxy. (a) Setup used to solder the end of a thin copper wire to a microelectrode of the sample and the other end to a PCB pad. (b) Image of a sample with two microelectrodes connected to two pads, using silver epoxy at the microelectrodes and silver paint at the pads. (c) Micrograph of two epoxy weldings at two microelectrodes. (d) Image of the resulting device.

Figure F.6 depicts the **steps comprising the Au NWs manipulation** with an AFM probe. After imaging the sample in amplitude modulation mode (AM-AFM), we bring the tip down to the substrate surface applying a normal load in the range of 60 to 300 nN (F.6(a)) and we move it along a predefined trajectory (F.6(b)), thus manipulating the Au NW of our choice (F.6(c)). After this, we lift the tip back to AM-AFM mode and we image the results of the manipulation (F.6(d)).

Several trajectories can be performed in a single nanomanipulation step to translate/rotate the NWs. Figure F.7 shows **an example of these nanomanipulations** and the corresponding script in the control software [54], where a remarkably simple procedure is employed. Panel (a) shows the lithography interface and scripts used to perform the manipulation of two NWs by means of 5 movements of the tip in contact with the substrate (in this case the tip is lowered 100 nm leading to a normal force of 125-150 nN). Subfigure (b) is an AFM topography of the NWs before the manipulation. The trajectories that the tip will follow in contact with the substrate (at 1.5 µm/s) to manipulate the Au NWs are depicted with blue lines. Numbers beside each line indicate the order of the manipulations. The yellow arrow shows the direction of the trajectories. Panel (c) corresponds to an AFM topography of the same area as in (b) after the manipulation and the trajectories of the tip. The NWs appear in a new position defined by the ends of the movements of the tip in contact. Plot depicted in (d) is the evolution of the normal (blue line) and lateral (red line) forces during the manipulation. The normal force was obtained in nN following the method explained in section 2.1.9 with the (normal) spring constant of the cantilever. The lateral force was computed in mN in a similar way using the lateral spring constant of the cantilever ($k_{lat} = 2 \cdot k_{nor} \cdot (L/h_{tip})^2$, k_{lat} is the lateral spring constant, k_{nor} the normal spring constant, L is the length of the cantilever and a the height of the tip [361]).

The value of the **normal force needed** to move a NW depends on a number of factors, being the most important one the interaction of the wire with the substrate. Moving a NW for the first time usually needs a higher normal force than that required for subsequent movements. The orientation of the NW with respect to the direction of movement also

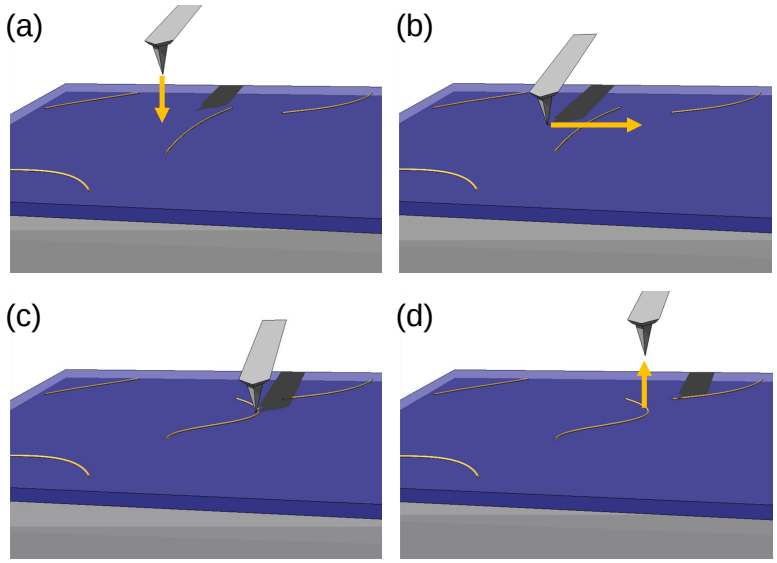

Figure F.6: Gold nanowires manipulation schematics. (a) After imaging Au NWs in AM-AFM mode, we bring the tip into contact. (b) We move the tip along a predefined trajectory to manipulate the Au NW. (c) The selected Au NW is moved. (d) We bring the tip back to AM-AFM mode and a new image is taken.

plays an important role: many NWs can be moved with lower forces in certain directions. The NWs which are adjacent to gold islands (which usually have triangular or hexagonal shapes) are hardly movable. Regardless previous factors, a few NWs are kind of "anchored" to the substrate and cannot be moved or they require much higher loads.

There are other issues found when performing the nanomanipulations. One is the tendendy of the tip to **leave debris particles** from time to time, after having performed some manipulations. This is solved by replacing the tip and then moving the debris away with the new tip, as any other nanomanipulation. Another problem is the fact that **some nanowires break** during the manipulation, generally the longest ones, however the broken parts can be also easily moved and welded. Finally, we have seen that the NWs some times appear stuck along in groups of two (or more), as the NWs shown in figure F.9(a). In those cases we can manipulate both NWs as if they were one (by doing that they some times separate), or we can willfullly separate them.

To obtain an **optimum electrical contact** between two NWs, one of them is pushed against the other and they will cold weld just by mechanical contact [118]. In the work by Lu *et al.* [118], they cold weld Au NWs with diameters between 3 and 10 nm. They used diferent relative orientations between the NWs: (i) "head-to-head" (parallel NWs "touching" each other at the end), (ii) "side-to-side" (parallel NWs laterally "touching" each other) and (iii) "head-to-side" (perpendicular NWs, the end of one of them "touchs" one side of the other). In that work any configuration was succesful, but in our case, we manipulate much higher diameters (44 - 84 nm) and the "head-to-side" geometry was the one providing better electrical joining. Furthermore, it is the one most easily accesible from a manipulation point of view. Anyhow, we obtained some good electrical junctions with the other two configurations.

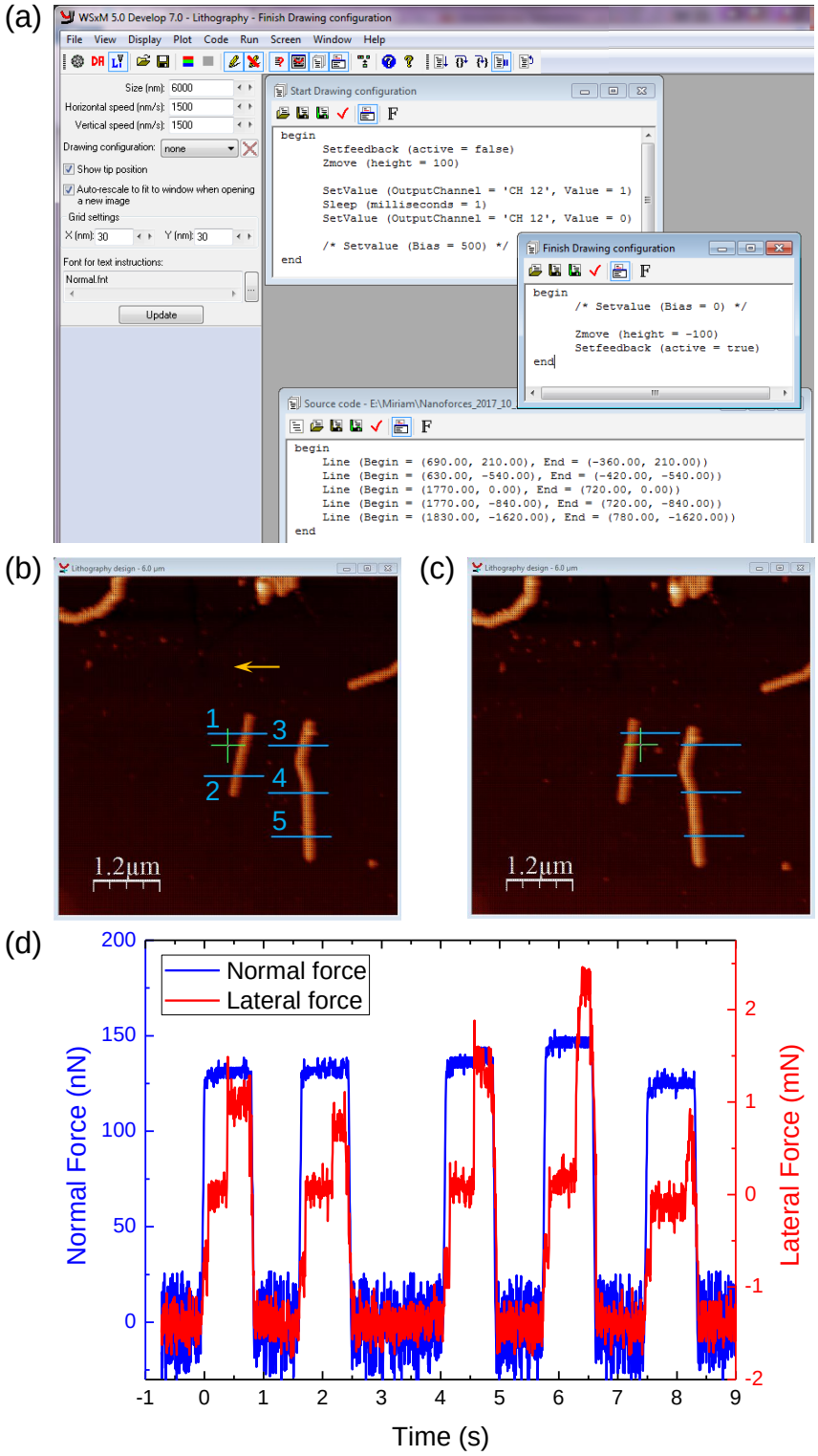

Figure F.7: Example of Au NWs manipulation. (a) WSxM Lithography interface. AFM topographies of NWs before (b) and after (c) their manipulation. (d) Evolution of the normal and lateral forces during the process.

F.6 VERIFICATION AND IMPROVEMENT OF ELECTRICAL CONTACTS

We checked the **electrical continuity and resistance of the NWs paths** using conductive diamond coated tips (Budget Sensors All-In-On-DD [362] with nominal spring constants of 6.5 N/m and 18 N/m). We performed IV curves on top of the Au NWs at different path distances from the microelectrode. If there is a junction with a very high resistance or even not electrically connecting two NWs at all, the same diamond tip is used to further push the Au NWs until a linear IV curve is obtained with a low resistance (of about ~20 kΩ, this figure is only a few kΩ if a metallized tip is used). Figure F.8 depicts in panel (a) an example of the process followed to check the conductivity of the Au NWs based electrode. Panel (b) of the same figure plots the type of IV curve expected for any point along the Au NWs paths (the slope slightly varies depending on the distance from the microelectrode at which the curve is acquired).

For the acquisition of data of figure 5.11, 5.12 and 5.21 we used CrPt coated tips (Budget Sensors ElectriMulti75-G [363] with a nominal spring constant of 3 N/m) to improve the electrical contact between the nanoobject and the tip. Metal coated tips can be also employed to check the resistance of the NWs nanoelectrodes, but we have observed that (i) they present a high adhesion with the NWs which can result in unwanted NW extraction and (ii) they were more prone to leave debris than the other kind of tips.

Sometimes the **electrical contact between a NW and a nanoobject** is not good enough. It can be due to the presence of dirt or a poor mechanical contact. It also depends on the chemical composition of the nanoobjetc. In such cases the welding is achieved by aplying force with the AFM probe onto the NW - nanoobject intersection. Thus, the NW (which is on top of t he nanoobject) is pushed against the nanoobject. This is done preferably while

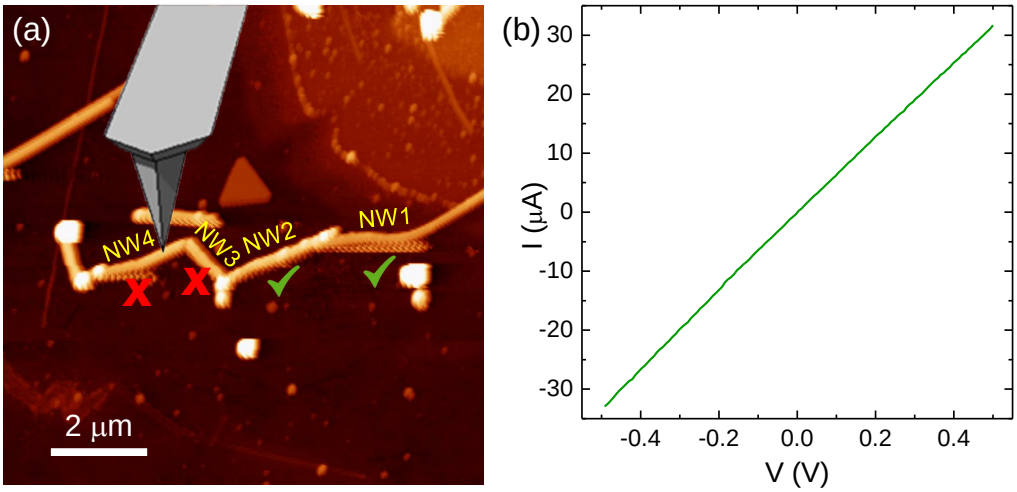

Figure F.8: Checking of the electrical continuity of a path of Au NWs. (a) AFM topography showing a microelectrode (top right) and a path of Au NWs (NW1 + NW2 + NW3 + NW4) protuding from it. The panel portrays the testing procedure followed: an IV conducted on NW4 gave no current, the same happened in NW3. On NW1 a linear and low resistance IV was obtained. Another IV on NW2 gives the same result, so the deficient junction is the one between NW2 and NW3, there we should push one NW to the other until a linear IV similar to the one shown in (b) is obtained (acquired using a conductive diamond tip). (b) IV curve acquired on NW4 of (a) after fixing all broken junctions.

a voltage is applied between the ends of the nanoobject (in that case it has to be already electrically contacted by two Au NWs paths).

Figure F.9 shows an example of improvement of the electrical contact between a multiwall carbon nanotube (MWCNT) and a gold nanowire by indenting with the AFM tip at their intersection. Subfigure F.9 (c) depicts current that flows through the MWCNT *vs.* indentation (IZ curve) having a voltage of -25 mV between the NW shown and another NWs electrode (outside the image) that contacts the MWCNT at other point. The indentation is being increased, leading to and increase of the current (more negative due to negative bias voltage) when the AFM probe is not in contact with the NW (Z < 50 nm). This means that the NW is being welded to the MWCNT. Panel (d) plots several IV curves across the NWs-electrode - MWCNT - NWs-electrode, each of them is acquired just after the IZ curve of the same color in (c).

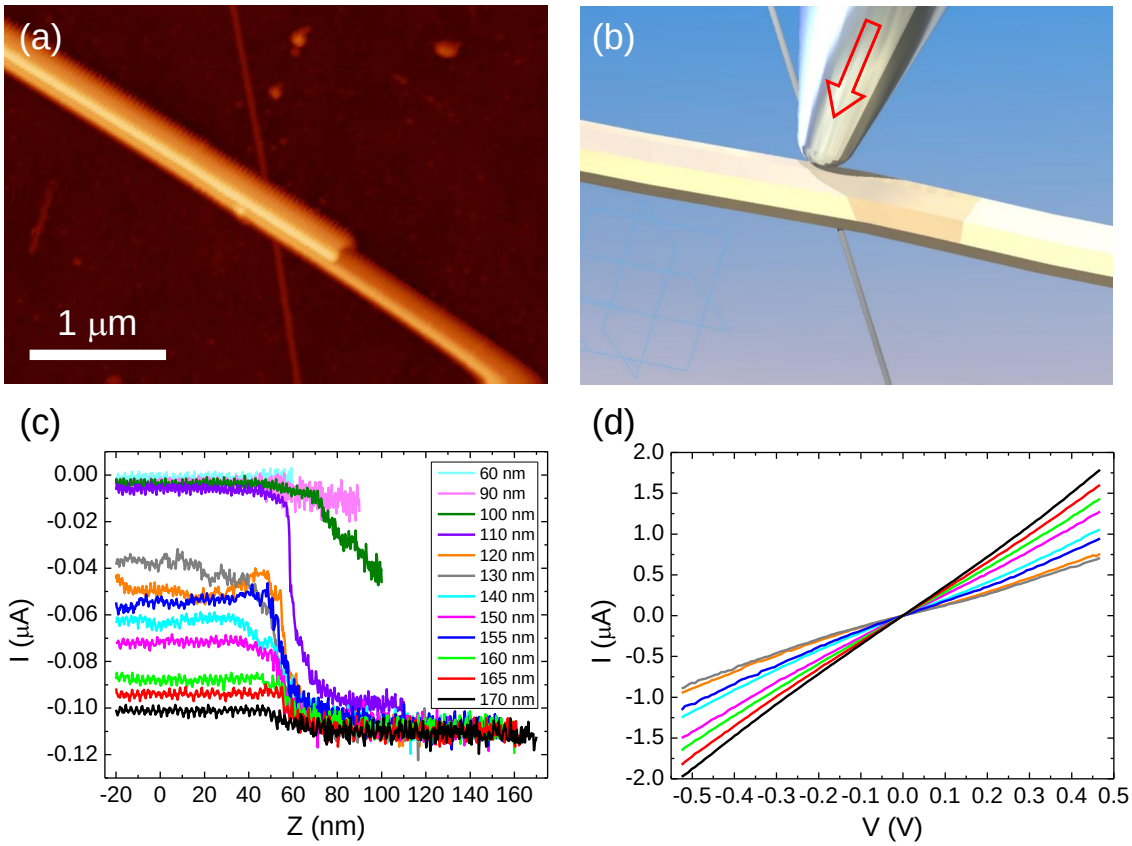

Figure F.9: Improvement of the electrical contact between a carbon nanotube and a gold nanowire. (a) AFM topography of a Au NW crossing over a MWCNT (there are actually two Au NWs stuck along). (b) Rendered image of the nanoobjects in (a) and a AFM probe pushing the intersection of both tubes. (c) IZ curves acquired having a constant bias of -25 mV between the Au NW of (a) and another Au NWs electrode contacting the MWCNT at 4.7 µm from the NW shown in (a). The current while the tip is not in contact is increased with higher indentations. The maximum load applied at the end of each IZ curve varies from 66 to 730 nN. (d) Set of IVs curves, each of them acquired after the IZ depicted in (c) with the same color.

G

BENZENEDITHIOL DEPOSITION BY SUBLIMATION

G.1 SUBLIMATION ON FLAT GOLD

To test this deposition technique within our vacuum chamber and afterwards measure the thickness of the BDT layer thus obtained, we performed the sublimation on a flat substrate covered by thermally evaporated gold. To this end we placed that substrate in the vacuum chamber with a base preassure of 10^{-6} mbar. Then we induced glow discharge in the vacuum chamber by having a preasure of oxygen of $\sim 5 \cdot 10^{-2}$ mbar and applying ~840 V between two large electrodes inside the chamber (the sample was located between them). The oxygen plasma was inmediately visible and left it for two minutes. This process cleaned the gold surface, removing any organic contaminat such as CTAB. This is crucial in the case of CTAB-coated Au NWs. After that, we waited a few minutes until preassure has a value of $\sim 10^{-4}$ mbar.

Then we conducted the BDT sublimation. A glass bulb containing BDT powder at ~90°C was connected to the chamber trough a valve. We opened it until the preassure rised to a pressure of $5 \cdot 10^{-4}$ mbar and then we waited 30 s at that pressure. Finally, once the preassure reached $\sim 10^{-5}$ mbar we introduced nitrogen gas in the chamber and finally we opened it. The sample temperature during the whole process was always below 35°C.

G.2 ELLIPSOMETRY DATA TO OBTAIN THE THICKNESS OF THE BDT LAYER

The sample was then taken to an ellipsometry setup to measure the thickness of the BDT layer. Considering 1.59 as the refractive index of BDT [364] and fitting to a model the acquired data of the complex reflectance ratio for different wavelengths (190 - 890 nm) (see figure G.1), after two fitting iterations a **thickness of 0.8 $\pm$ 0.1 nm** was obtained for the BDT layer. That value is compatible with the size of a BDT molecule.

The described deposition procedure was followed on the sample of section 5.9.5 to obtain a monolayer of BDT.

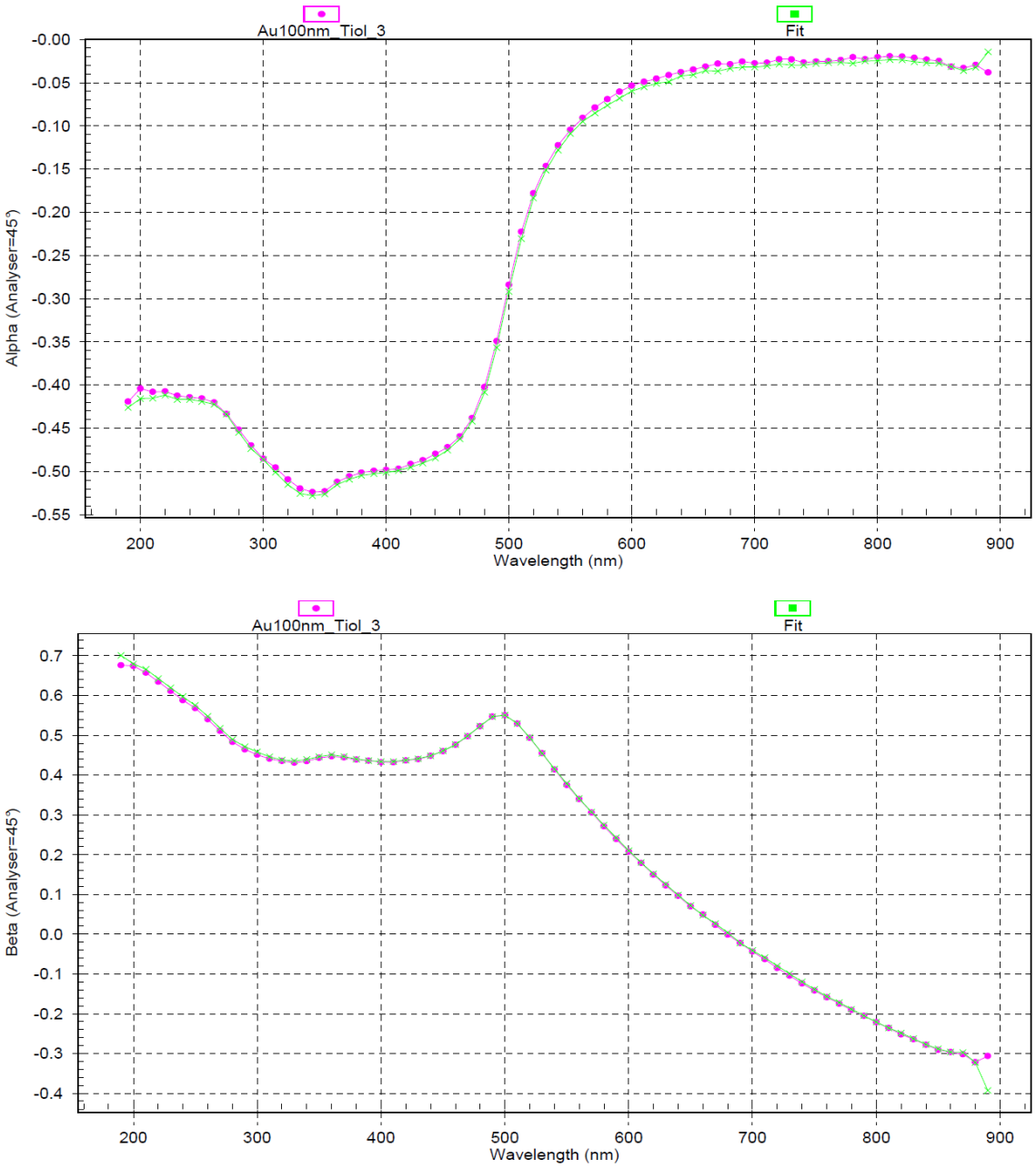

Figure G.1: Ellipsometry data of the BDT layer deposited on gold. Data of complex reflectance ratio (pink) fitted to model (green). Top: Alpha = tan(amplitude component). Bottom: Beta = cos(phase difference).

BIBLIOGRAPHY

[1] G. Binnig, H. Rohrer, Ch. Gerber, and E. Weibel. "Surface Studies by Scanning Tunneling Microscopy." In: *Phys. Rev. Lett.* 49 (1 1982), pp. 57–61.

[2] G. Binnig and H. Rohrer. "Scanning Tunneling Microscopy." English (US). In: *Helvetica Physica Acta* 55 (Dec. 1982), pp. 726–735.

[3] G. Binnig and H. Rohrer. "Scanning Tunneling Microscopy." In: *Surface Science* 126.1 (1983), pp. 236 –244. ISSN: 0039-6028.

[4] Charles P Poole. *Introduction to nanotechnology*. eng. Hoboken: John Wiley and Sons, 2003. ISBN: 0471079359.

[5] Stuart M Lindsay. *Introduction to Nanoscience*. eng. Oxford: Oxford University Press, 2010. ISBN: 9780199544219.

[6] D. Rodríguez-San-Miguel. "Processing of Imine-based Covalent Organic Frameworks." PhD thesis. Universidad Autónoma de Madrid, 2018.

[7] E. Berganza. "A study of complex magnetic configurations using Magnetic Force Microscopy." PhD thesis. Universidad Autónoma de Madrid, 2018.

[8] Harold W Kroto, James R Heath, Sean C O'Brien, Robert F Curl, and Richard E Smalley. "C60: Buckminsterfullerene." In: *Nature* 318.6042 (1985), p. 162.

[9] Sumio Iijima. "Helical microtubules of graphitic carbon." In: *nature* 354.6348 (1991), p. 56.

[10] K. S. Novoselov, A. K. Geim, S. V. Morozov, D. Jiang, Y. Zhang, S. V. Dubonos, I. V. Grigorieva, and A. A. Firsov. "Electric Field Effect in Atomically Thin Carbon Films." In: *Science* 306.5696 (2004), pp. 666–669. ISSN: 0036-8075.

[11] Pere Miró, Martha Audiffred, and Thomas Heine. "An atlas of two-dimensional materials." In: *Chem. Soc. Rev.* 43 (18 2014), pp. 6537–6554.

[12] Ganesh R. Bhimanapati et al. "Recent Advances in Two-Dimensional Materials beyond Graphene." In: *ACS Nano* 9.12 (2015). PMID: 26544756, pp. 11509–11539.

[13] Mircea Dragoman. *2D Nanoelectronics Physics and Devices of Atomically Thin Materials*. eng. NanoScience and Technology. 2017. ISBN: 3-319-48435-4.

[14] Hua Zhang. "Ultrathin Two-Dimensional Nanomaterials." In: *ACS Nano* 9.10 (2015). PMID: 26407037, pp. 9451–9469.

[15] Rubén Mas-Ballesté, Cristina Gómez-Navarro, Julio Gómez-Herrero, and Félix Zamora. "2D materials: to graphene and beyond." In: *Nanoscale* 3 (1 2011), pp. 20–30.

[16] Patrick Vogt, Paola De Padova, Claudio Quaresima, Jose Avila, Emmanouil Frantzeskakis, Maria Carmen Asensio, Andrea Resta, Bénédicte Ealet, and Guy Le Lay. "Silicene: Compelling Experimental Evidence for Graphene-like Two-Dimensional Silicon." In: *Phys. Rev. Lett.* 108 (15 2012), p. 155501.

[17] M E Dávila, L Xian, S Cahangirov, A Rubio, and G Le Lay. "Germanene: a novel two-dimensional germanium allotrope akin to graphene and silicene." In: *New Journal of Physics* 16.9 (2014), p. 095002.

[18] Han Liu, Adam T. Neal, Zhen Zhu, Zhe Luo, Xianfan Xu, David Tománek, and Peide D. Ye. "Phosphorene: An Unexplored 2D Semiconductor with a High Hole Mobility." In: *ACS Nano* 8.4 (2014), pp. 4033–4041.

[19] Pablo Ares, Fernando Aguilar-Galindo, David Rodríguez-San-Miguel, Diego A. Aldave, Sergio Díaz-Tendero, Manuel Alcamí, Fernando Martín, Julio Gómez-Herrero, and Félix Zamora. "Mechanical Isolation of Highly Stable Antimonene under Ambient Conditions." In: *Advanced Materials* 28.30 (2016), pp. 6332–6336.

[20] Carlos Gibaja, David Rodriguez-San-Miguel, Pablo Ares, Julio Gómez-Herrero, Maria Varela, Roland Gillen, Janina Maultzsch, Frank Hauke, Andreas Hirsch, Gonzalo Abellán, and Félix Zamora. "Few-Layer Antimonene by Liquid-Phase Exfoliation." In: *Angewandte Chemie International Edition* 55.46 (2016), pp. 14345–14349.

[21] Kenji Watanabe, Takashi Taniguchi, and Hisao Kanda. "Direct-bandgap properties and evidence for ultraviolet lasing of hexagonal boron nitride single crystal." In: *Nature Materials* 3 (2004), pp. 404–409.

[22] S. S. Lin. "Light-Emitting Two-Dimensional Ultrathin Silicon Carbide." In: *The Journal of Physical Chemistry C* 116.6 (2012), pp. 3951–3955.

[23] Manish Chhowalla, Hyeon Suk Shin, Goki Eda, Lain-Jong Li, Kian Ping Loh, and Hua Zhang. "The chemistry of two-dimensional layered transition metal dichalcogenide nanosheets." In: *Nature chemistry* 5.4 (2013), p. 263.

[24] Qing Hua Wang, Kourosh Kalantar-Zadeh, Andras Kis, Jonathan N Coleman, and Michael S Strano. "Electronics and optoelectronics of two-dimensional transition metal dichalcogenides." In: *Nature nanotechnology* 7.11 (2012), p. 699.

[25] Priya Johari and Vivek B Shenoy. "Tuning the electronic properties of semiconducting transition metal dichalcogenides by applying mechanical strains." In: *ACS nano* 6.6 (2012), pp. 5449–5456.

[26] Yubing Zhou, Yufeng Nie, Yujing Liu, Kai Yan, Jinhua Hong, Chuanhong Jin, Yu Zhou, Jianbo Yin, Zhongfan Liu, and Hailin Peng. "Epitaxy and Photoresponse of Two-Dimensional GaSe Crystals on Flexible Transparent Mica Sheets." In: *ACS Nano* 8.2 (2014). PMID: 24392815, pp. 1485–1490.

[27] Jannika Lauth, Friederieke E. S. Gorris, Mahdi Samadi Khoshkhoo, Thomas Chassé, Wiebke Friedrich, Vera Lebedeva, Andreas Meyer, Christian Klinke, Andreas Kornowski, Marcus Scheele, and Horst Weller. "Solution-Processed Two-Dimensional Ultrathin InSe Nanosheets." In: *Chemistry of Materials* 28.6 (2016), pp. 1728–1736.

[28] Wikipedia. *MXenes*. 2018. URL: https://en.m.wikipedia.org/wiki/MXenes.

[29] Jin-Cheng Lei, Xu Zhang, and Zhen Zhou. "Recent advances in MXene: Preparation, properties, and applications." In: *Frontiers of Physics* 10.3 (2015), pp. 276–286.

[30] Minoru Osada and Takayoshi Sasaki. "Exfoliated oxide nanosheets: new solution to nanoelectronics." In: *J. Mater. Chem.* 19 (17 2009), pp. 2503–2511.

[31] Qiang Wang and Dermot O'Hare. "Recent Advances in the Synthesis and Application of Layered Double Hydroxide (LDH) Nanosheets." In: *Chemical Reviews* 112.7 (2012), pp. 4124–4155.

[32] John W. Colson and William R. Dichtel. "Rationally synthesized two-dimensional polymers." English (US). In: *Nature Chemistry* 5.6 (June 2013), pp. 453–465. ISSN: 1755-4330.

[33] Santanu Das, Moonkyung Kim, Jo-won Lee, and Wonbong Choi. "Synthesis, properties, and applications of 2-D materials: a comprehensive review." In: *Critical Reviews in Solid State and Materials Sciences* 39.4 (2014), pp. 231–252.

[34] J.C. Cuevas and E. Scheer. *Molecular Electronics: An Introduction to Theory and Experiment*. EBSCO ebook academic collection. World Scientific Publishing Company Pte Limited, 2010. ISBN: 9789814282598.

[35] Gordon E. Moore. "Cramming more components onto integrated circuits." In: *Electronics* 38.8 (1965).

[36] J. Gomez-Herrero and R. Reifenberger. "Scanning Probe Microscopy." In: *Encyclopedia of Condensed Matter Physics*. Ed. by Franco Bassani, Gerald L. Liedl, and Peter Wyder. Oxford: Elsevier, 2005, pp. 172 –182. ISBN: 978-0-12-369401-0.

[37] P. Ares. "Advanced Atomic Force Microscopy for Low-Dimensional Systems." PhD thesis. Universidad Autónoma de Madrid, 2017.

[38] G. Binnig, C. F. Quate, and Ch. Gerber. "Atomic Force Microscope." In: *Phys. Rev. Lett.* 56 (9 1986), pp. 930–933.

[39] T Junno, K Deppert, L Montelius, and L Samuelson. "Controlled manipulation of nanoparticles with an atomic force microscope." In: *Applied Physics Letters* 66.26 (1995), pp. 3627–3629.

[40] Ricardo Garcia, Armin W Knoll, and Elisa Riedo. "Advanced scanning probe lithography." In: *Nature nanotechnology* 9.8 (2014), p. 577.

[41] Matthias Rief, Filipp Oesterhelt, Berthold Heymann, and Hermann E Gaub. "Single molecule force spectroscopy on polysaccharides by atomic force microscopy." In: *Science* 275.5304 (1997), pp. 1295–1297.

[42] J. Colchero, A. Gil, and A. M. Baró. "Resolution enhancement and improved data interpretation in electrostatic force microscopy." In: *Phys. Rev. B* 64 (24 2001), p. 245403.

[43] M Nonnenmacher, MP o'Boyle, and H Kumar Wickramasinghe. "Kelvin probe force microscopy." In: *Applied physics letters* 58.25 (1991), pp. 2921–2923.

[44] Changgu Lee, Xiaoding Wei, Jeffrey W. Kysar, and James Hone. "Measurement of the Elastic Properties and Intrinsic Strength of Monolayer Graphene." In: *Science* 321.5887 (2008), pp. 385–388.

[45] D Rugar, HJ Mamin, P Guethner, SE Lambert, JE Stern, I McFadyen, and T Yogi. "Magnetic force microscopy: General principles and application to longitudinal recording media." In: *Journal of Applied Physics* 68.3 (1990), pp. 1169–1183.

[46] Sergei V Kalinin and Dawn A Bonnell. "Imaging mechanism of piezoresponse force microscopy of ferroelectric surfaces." In: *Physical Review B* 65.12 (2002), p. 125408.

[47] C. Mathew Mate, Gary M. McClelland, Ragnar Erlandsson, and Shirley Chiang. "Atomic-scale friction of a tungsten tip on a graphite surface." In: *Phys. Rev. Lett.* 59 (17 1987), pp. 1942–1945.

[48] F. Moreno Herrero. "Aplicaciones de la microscopía de fuerzas al estudio de sistemas de moléculas biológicas individuales." PhD thesis. Universidad Autónoma de Madrid, 2003.

[49] C. Gómez Navarro. "Medidas de transporte electrónico en cables moleculares nanotubos de carbono y ADN." PhD thesis. Universidad Autónoma de Madrid, 2005.

[50] C. Carrasco Pulido. "Caracterización estructural y mecánica de nanosistemas biológicos mediante microscopía de fuerzas atómicas." PhD thesis. Universidad Autónoma de Madrid, 2008.

[51] D. Martínez Martín. "Nuevas técnicas basadas en microscopía de fuerza atómica: del vacío a los líquidos." PhD thesis. Universidad Autónoma de Madrid, 2011.

[52] M. Hernando Pérez. "Caracterización de las propiedades mecánicas de bacteriófagos mediante microscopía de fuerzas atómicas." PhD thesis. Universidad Autónoma de Madrid, 20141.

[53] A. Ortega Esteban. "Caracterización de las propiedades mecánicas de bacteriófagos mediante microscopía de fuerzas atómicas." PhD thesis. Universidad Autónoma de Madrid, 2015.

[54] I Horcas, Rs Fernández, JM Gomez-Rodriguez, JWSX Colchero, JWSXM Gómez-Herrero, and AM Baro. "WSXM: a software for scanning probe microscopy and a tool for nanotechnology." In: *Review of scientific instruments* 78.1 (2007), p. 013705.

[55] Alejandro Gimeno, Pablo Ares, Ignacio Horcas, Adriana Gil, José M Gómez-Rodríguez, Jaime Colchero, and Julio Gómez-Herrero. "'Flatten plus': a recent implementation in WSxM for biological research." In: *Bioinformatics* 31.17 (2015), pp. 2918–2920.

[56] School of medicine University of Virginia. *Atomic Force Microscope (AFM)*. 2018. URL: https://pharm.virginia.edu/facilities/atomic-force-microscope-afm/.

[57] Ricardo García and Rubén Pérez. "Dynamic atomic force microscopy methods." In: *Surface science reports* 47.6-8 (2002), pp. 197–301.

[58] TR Albrecht, Pr Grütter, D Horne, and D Rugar. "Frequency modulation detection using high-Q cantilevers for enhanced force microscope sensitivity." In: *Journal of Applied Physics* 69.2 (1991), pp. 668–673.

[59] Miriam Jaafar, David Martínez-Martín, Mariano Cuenca, John Melcher, Arvind Raman, and Julio Gómez-Herrero. "Drive-amplitude-modulation atomic force microscopy: From vacuum to liquids." In: *Beilstein journal of nanotechnology* 3 (2012), p. 336.

[60] Franz J Giessibl. "Advances in atomic force microscopy." In: *Reviews of modern physics* 75.3 (2003), p. 949.

[61] PJ De Pablo, J Colchero, J Gomez-Herrero, and AM Baro. "Jumping mode scanning force microscopy." In: *Applied Physics Letters* 73.22 (1998), pp. 3300–3302.

[62] Javier Tamayo and Ricardo García. "Relationship between phase shift and energy dissipation in tapping-mode scanning force microscopy." In: *Applied Physics Letters* 73.20 (1998), pp. 2926–2928.

[63] SN Magonov, V Elings, and M-H Whangbo. "Phase imaging and stiffness in tapping-mode atomic force microscopy." In: *Surface science* 375.2-3 (1997), pp. L385–L391.

[64] I Schmitz, M Schreiner, G Friedbacher, and M Grasserbauer. "Phase imaging as an extension to tapping mode AFM for the identification of material properties on humidity-sensitive surfaces." In: *Applied surface science* 115.2 (1997), pp. 190–198.

[65] Yongho Seo and Wonho Jhe. "Atomic force microscopy and spectroscopy." In: *Reports on Progress in Physics* 71.1 (2007), p. 016101.

[66] M Luna, J Colchero, J Gómez-Herrero, and AM Baró. "Study of tip–sample interaction in scanning force microscopy." In: *Applied surface science* 157.4 (2000), pp. 285–289.

[67] A. Gil Gil. "Study of the tip-sample interaction at the scanning force microscopy and its aplication to the visualization of adsorption processes on surfaces." PhD thesis. Universidad Autónoma de Madrid, 2001.

[68] U Dürig, O Züger, and A Stalder. "Interaction force detection in scanning probe microscopy: Methods and applications." In: *Journal of Applied Physics* 72.5 (1992), pp. 1778–1798.

[69] Michel Gauthier, Rubén Pérez, Toyoko Arai, Masahiko Tomitori, and Masaru Tsukada. "Interplay between nonlinearity, scan speed, damping, and electronics in frequency modulation atomic-force microscopy." In: *Physical review letters* 89.14 (2002), p. 146104.

[70] GB Kaggwa, JI Kilpatrick, JE Sader, and SP Jarvis. "Artifact-free dynamic atomic force microscopy reveals monotonic dissipation for a simple confined liquid." In: *Applied Physics Letters* 93.1 (2008), p. 011909.

[71] Jeffrey M Mativetsky, Yueh-Lin Loo, and Paolo Samorì. "Elucidating the nanoscale origins of organic electronic function by conductive atomic force microscopy." In: *Journal of Materials Chemistry C* 2.17 (2014), pp. 3118–3128.

[72] C Shafai, DJ Thomson, M Simard-Normandin, G Mattiussi, and PJ Scanlon. "Delineation of semiconductor doping by scanning resistance microscopy." In: *Applied physics letters* 64.3 (1994), pp. 342–344.

[73] Hongjie Dai, Eric W Wong, and Charles M Lieber. "Probing electrical transport in nanomaterials: conductivity of individual carbon nanotubes." In: *Science* 272.5261 (1996), pp. 523–526.

[74] C Gomez-Navarro, PJ de Pablo, J Colchero, Y Fan, M Burghard, J Gomez-Herrero, and AM Baro. "Probing electrical transport in nanowires: current maps of individual V2O5 nanofibres with scanning force microscopy." In: *Nanotechnology* 14.2 (2003), p. 134.

[75] Miriam Moreno-Moreno, Andrés Castellanos-Gomez, Gabino Rubio-Bollinger, Julio Gomez-Herrero, and Nicolás Agraït. "Ultralong natural graphene nanoribbons and their electrical conductivity." In: *Small* 5.8 (2009), pp. 924–927.

[76] Per Sundqvist, Francisco J Garcia-Vidal, Fernando Flores, Miriam Moreno-Moreno, Cristina Gómez-Navarro, Joseph Scott Bunch, and Julio Gómez-Herrero. "Voltage and length-dependent phase diagram of the electronic transport in carbon nanotubes." In: *Nano letters* 7.9 (2007), pp. 2568–2573.

[77] Yves Martin, David W Abraham, and H Kumar Wickramasinghe. "High-resolution capacitance measurement and potentiometry by force microscopy." In: *Applied Physics Letters* 52.13 (1988), pp. 1103–1105.

[78] Huang Wen Hao, AM Baro, and JJ Saenz. "Electrostatic and contact forces in force microscopy." In: *Journal of Vacuum Science & Technology B: Microelectronics and Nanometer Structures Processing, Measurement, and Phenomena* 9.2 (1991), pp. 1323–1328.

[79] S Belaidi, P Girard, and G Leveque. "Electrostatic forces acting on the tip in atomic force microscopy: Modelization and comparison with analytic expressions." In: *Journal of applied physics* 81.3 (1997), pp. 1023–1030.

[80] HO Jacobs, Pascal Leuchtmann, OJ Homan, and A Stemmer. "Resolution and contrast in Kelvin probe force microscopy." In: *Journal of Applied Physics* 84.3 (1998), pp. 1168–1173.

[81] S Gómez-Moñivas, LS Froufe, Rémi Carminati, Jean-Jacques Greffet, and Juan-José Sáenz. "Tip-shape effects on electrostatic force microscopy resolution." In: *Nanotechnology* 12.4 (2001), p. 496.

[82] Sacha Gómez Moñivas. "Análisis de la Interacción electrostática en microscopía de fuerzas." PhD thesis. Universidad Autónoma de Madrid, 2003.

[83] A Bachtold, MS Fuhrer, S Plyasunov, M Forero, Erik H Anderson, A Zettl, and Paul L McEuen. "Scanned probe microscopy of electronic transport in carbon nanotubes." In: *Physical review letters* 84.26 (2000), p. 6082.

[84] Hiroshi Yokoyama and Takahito Inoue. "Scanning Maxwell stress microscope for nanometre-scale surface electrostatic imaging of thin films." In: *Thin Solid Films* 242.1-2 (1994), pp. 33–39.

[85] Wilhelm Melitz, Jian Shen, Andrew C Kummel, and Sangyeob Lee. "Kelvin probe force microscopy and its application." In: *Surface science reports* 66.1 (2011), pp. 1–27.

[86] Th Glatzel, S Sadewasser, and M Ch Lux-Steiner. "Amplitude or frequency modulation-detection in Kelvin probe force microscopy." In: *Applied surface science* 210.1-2 (2003), pp. 84–89.

[87] Brunero Cappella and Giovanni Dietler. "Force-distance curves by atomic force microscopy." In: *Surface science reports* 34.1-3 (1999), pp. 1–104.

[88] Matthias Rief, Mathias Gautel, Filipp Oesterhelt, Julio M Fernandez, and Hermann E Gaub. "Reversible unfolding of individual titin immunoglobulin domains by AFM." In: *science* 276.5315 (1997), pp. 1109–1112.

[89] Anja Vinckier and Giorgio Semenza. "Measuring elasticity of biological materials by atomic force microscopy." In: *FEBS letters* 430.1-2 (1998), pp. 12–16.

[90] WH Roos, R Bruinsma, and GJL Wuite. "Physical virology." In: *Nature physics* 6.10 (2010), p. 733.

[91] Mercedes Hernando-Pérez, Roberto Miranda, María Aznar, José L Carrascosa, Iwan AT Schaap, David Reguera, and Pedro J de Pablo. "Direct measurement of phage phi29 stiffness provides evidence of internal pressure." In: *Small* 8.15 (2012), pp. 2366–2370.

[92] Andres Castellanos-Gomez, Menno Poot, Gary A Steele, Herre SJ van der Zant, Nicolás Agraït, and Gabino Rubio-Bollinger. "Elastic properties of freely suspended MoS2 nanosheets." In: *Advanced Materials* 24.6 (2012), pp. 772–775.

[93] Ampere A Tseng, Andrea Notargiacomo, and TP Chen. "Nanofabrication by scanning probe microscope lithography: A review." In: *Journal of Vacuum Science & Technology B: Microelectronics and Nanometer Structures Processing, Measurement, and Phenomena* 23.3 (2005), pp. 877–894.

[94] John A Dagata, J Schneir, Howard H Harary, CJ Evans, Michael T Postek, and J Bennett. "Modification of hydrogen-passivated silicon by a scanning tunneling microscope operating in air." In: *Applied Physics Letters* 56.20 (1990), pp. 2001–2003.

[95] HC Day and DR Allee. "Selective area oxidation of silicon with a scanning force microscope." In: *Applied Physics Letters* 62.21 (1993), pp. 2691–2693.

[96] Ricardo García, Montserrat Calleja, and Francesc Pérez-Murano. "Local oxidation of silicon surfaces by dynamic force microscopy: Nanofabrication and water bridge formation." In: *Applied Physics Letters* 72.18 (1998), pp. 2295–2297.

[97] TA Jung, A Moser, HJ Hug, D Brodbeck, R Hofer, HR Hidber, and UD Schwarz. "The atomic force microscope used as a powerful tool for machining surfaces." In: *Ultramicroscopy* 42 (1992), pp. 1446–1451.

[98] Richard D Piner, Jin Zhu, Feng Xu, Seunghun Hong, and Chad A Mirkin. "" Dip-pen" nanolithography." In: *science* 283.5402 (1999), pp. 661–663.

[99] HJ Mamin and D Rugar. "Thermomechanical writing with an atomic force microscope tip." In: *Applied Physics Letters* 61.8 (1992), pp. 1003–1005.

[100] William P King, Bikramjit Bhatia, Jonathan R Felts, Hoe Joon Kim, Beomjin Kwon, Byeonghee Lee, Suhas Somnath, and Matthew Rosenberger. "Heated atomic force microscope cantilevers and their applications." In: *Annual Review of Heat Transfer* 16.16 (2013).

[101] T Onoue, Martin Herman Siekman, Leon Abelmann, and JC Lodder. "Probe recording on CoNi/Pt multilayered thin films by using an MFM tip." In: *Journal of magnetism and magnetic materials* 272 (2004), pp. 2317–2318.

[102] César Moreno, Carmen Munuera, Sergio Valencia, Florian Kronast, Xavier Obradors, and Carmen Ocal. "Reversible resistive switching and multilevel recording in Lao. 7Sro. 3MnO3 thin films for low cost nonvolatile memories." In: *Nano letters* 10.10 (2010), pp. 3828–3835.

[103] Song Xu and Gang-yu Liu. "Nanometer-scale fabrication by simultaneous nanoshaving and molecular self-assembly." In: *Langmuir* 13.2 (1997), pp. 127–129.

[104] RS Becker, JA Golovchenko, and BS Swartzentruber. "Atomic-scale surface modifications using a tunnelling microscope." In: *Nature* 325.6103 (1987), p. 419.

[105] JS Foster, JE Frommer, and PC Arnett. "Molecular manipulation using a tunnelling microscope." In: *Nature* 331.6154 (1988), p. 324.

[106] Joseph A Stroscio and DM Eigler. "Atomic and molecular manipulation with the scanning tunneling microscope." In: *Science* 254.5036 (1991), pp. 1319–1326.

[107] Donald M Eigler and Erhard K Schweizer. "Positioning single atoms with a scanning tunnelling microscope." In: *Nature* 344.6266 (1990), p. 524.

[108] TR Ramachandran, C Baur, A Bugacov, A Madhukar, BE Koel, A Requicha, and C Gazen. "Direct and controlled manipulation of nanometer-sized particles using the non-contact atomic force microscope." In: *Nanotechnology* 9.3 (1998), p. 237.

[109] DM Schaefer, R Reifenberger, A Patil, and RP Andres. "Fabrication of two-dimensional arrays of nanometer-size clusters with the atomic force microscope." In: *Applied Physics Letters* 66.8 (1995), pp. 1012–1014.

[110] Michael R Falvo, GJ Clary, RM Taylor Ii, V Chi, FP Brooks Jr, S Washburn, and R Superfine. "Bending and buckling of carbon nanotubes under large strain." In: *Nature* 389.6651 (1997), p. 582.

[111] Tobias Hertel, Richard Martel, and Phaedon Avouris. "Manipulation of individual carbon nanotubes and their interaction with surfaces." In: *The Journal of Physical Chemistry B* 102.6 (1998), pp. 910–915.

[112] Shuchen Hsieh, Sheffer Meltzer, CR Chris Wang, Aristides AG Requicha, Mark E Thompson, and Bruce E Koel. "Imaging and manipulation of gold nanorods with an atomic force microscope." In: *The Journal of Physical Chemistry B* 106.2 (2002), pp. 231–234.

[113] Noriaki Oyabu, Oscar Custance, Insook Yi, Yasuhiro Sugawara, and Seizo Morita. "Mechanical vertical manipulation of selected single atoms by soft nanoindentation using near contact atomic force microscopy." In: *Physical Review Letters* 90.17 (2003), p. 176102.

[114] Yoshiaki Sugimoto, Masayuki Abe, Shinji Hirayama, Noriaki Oyabu, Óscar Custance, and Seizo Morita. "Atom inlays performed at room temperature using atomic force microscopy." In: *Nature materials* 4.2 (2005), p. 156.

[115] Yoshiaki Sugimoto, Pablo Pou, Oscar Custance, Pavel Jelinek, Masayuki Abe, Ruben Perez, and Seizo Morita. "Complex patterning by vertical interchange atom manipulation using atomic force microscopy." In: *Science* 322.5900 (2008), pp. 413–417.

[116] Hong-Zhi Liu, Sen Wu, Jun-Ming Zhang, Hui-Tian Bai, Fan Jin, Hai Pang, and Xiao-Dong Hu. "Strategies for the AFM-based manipulation of silver nanowires on a flat surface." In: *Nanotechnology* 28.36 (2017), p. 365301.

[117] Sen Wu, Huitian Bai, and Fan Jin. "Automated manipulation of flexible nanowires with an atomic force microscope." In: *Manipulation, Manufacturing and Measurement on the Nanoscale (3M-NANO), 2017 IEEE International Conference on*. IEEE. 2017, pp. 229–235.

[118] Yang Lu, Jian Yu Huang, Chao Wang, Shouheng Sun, and Jun Lou. "Cold welding of ultrathin gold nanowires." In: *Nature nanotechnology* 5.3 (2010), p. 218.

[119] Doug Merrill. *Probe station basics*. 2017. URL: http://blog.semiprobe.com/probe-station-basics.

[120] Wikipedia. *Mechanical probe station*. 2018. URL: https://en.wikipedia.org/wiki/Mechanical_probe_station.

[121] Janis Research Company. *Micro–manipulated Cryogenic & Vacuum Probe Systems for Chips, Wafers and Device Testing from 3.5 K to 675 K*. 2018. URL: https://www.janis.com/Products/productsoverview/MicromanipulatedProbeStations.aspx.

[122] ATV-systems. *ATV exhibits at the PCIM 2017 in Nuremberg*. 2017. URL: https://www.atv-systems.de/en/news_archive/atv_exhibition_stand_at_the_pcim_2017.html.

[123] J Laskar and J Kolodzey. "Cryogenic vacuum high frequency probe station." In: *Journal of Vacuum Science & Technology B: Microelectronics Processing and Phenomena* 8.5 (1990), pp. 1161–1165.

[124] MPI Corporation. *TS2500–RF The First Fully Automatic Probe System Dedicated for RF Production Test*. 2016. URL: http://www.mpi-corporation.com/ast/engineering-probe-systems/mpi-fully-automated-systems/ts2500-rf-probe-system/.

[125] Leopoldo B Valdes. "Resistivity measurements on germanium for transistors." In: *Proceedings of the IRE* 42.2 (1954), pp. 420–427.

[126] Yadunath Singh. "Electrical resistivity measurements: a review." In: *International journal of modern physics: Conference series*. Vol. 22. World Scientific. 2013, pp. 745–756.

[127] electrical4u. *Measurement of Resistance*. 2018. URL: https://www.electrical4u.com/measurement-of-resistance/.

[128] S Narasiwodeyar, M Dwyer, M Liu, WK Park, and LH Greene. "Two-step fabrication technique of gold tips for use in point-contact spectroscopy." In: *Review of Scientific Instruments* 86.3 (2015), p. 033903.

[129] M.C Baykul. "Preparation of sharp gold tips for {STM} by using electrochemical etching method." In: *Materials Science and Engineering: B* 74.1–3 (2000), pp. 229 –233. ISSN: 0921-5107.

[130] Max Eisele, Michael Krüger, Markus Schenk, Alexander Ziegler, and Peter Hommelhoff. "Note: Production of sharp gold tips with high surface quality." In: *Review of Scientific Instruments* 82.2 (2011), p. 026101.

[131] Andres Castellanos-Gomez, Michele Buscema, Rianda Molenaar, Vibhor Singh, Laurens Janssen, Herre SJ Van Der Zant, and Gary A Steele. "Deterministic transfer of two-dimensional materials by all-dry viscoelastic stamping." In: *2D Materials* 1.1 (2014), p. 011002.

[132] Wikipedia. *Phosphorus*. 2018. URL: https://en.wikipedia.org/wiki/Phosphorus#Characteristics.

[133] Xi Ling, Han Wang, Shengxi Huang, Fengnian Xia, and Mildred S. Dresselhaus. "The renaissance of black phosphorus." In: *Proceedings of the National Academy of Sciences* 112.15 (2015), pp. 4523–4530.

[134] PW Bridgman. "Two New Modifications of Phosphorus." In: *Journal of the American Chemical Society* 36.7 (1914), pp. 1344–1363.

[135] A Morita. "Semiconducting black phosphorus." In: *Applied Physics A* 39.4 (1986), pp. 227–242.

[136] AS Rodin, A Carvalho, and AH Castro Neto. "Strain-induced gap modification in black phosphorus." In: *Physical review letters* 112.17 (2014), p. 176801.

[137] DW Boukhvalov, AN Rudenko, DA Prishchenko, VG Mazurenko, and MI Katsnelson. "Chemical modifications and stability of phosphorene with impurities: a first principles study." In: *Physical Chemistry Chemical Physics* 17.23 (2015), pp. 15209–15217.

[138] Allan Brown and Stig Rundqvist. "Refinement of the crystal structure of black phosphorus." In: *Acta Crystallographica* 19.4 (1965), pp. 684–685.

[139] Meysam Akhtar, George Anderson, Rong Zhao, Adel Alruqi, Joanna E Mroczkowska, Gamini Sumanasekera, and Jacek B Jasinski. "Recent advances in synthesis, properties, and applications of phosphorene." In: *npj 2D Materials and Applications* 1.1 (2017), p. 5.

[140] Andres Castellanos-Gomez et al. "Isolation and characterization of few-layer black phosphorus." In: *2D Materials* 1.2 (2014), p. 025001.

[141] Jack R Brent, Nicky Savjani, Edward A Lewis, Sarah J Haigh, David J Lewis, and Paul O'Brien. "Production of few-layer phosphorene by liquid exfoliation of black phosphorus." In: *Chemical Communications* 50.87 (2014), pp. 13338–13341.

[142] Joshua B Smith, Daniel Hagaman, and Hai-Feng Ji. "Growth of 2D black phosphorus film from chemical vapor deposition." In: *Nanotechnology* 27.21 (2016), p. 215602.

[143] Fengnian Xia, Han Wang, and Yichen Jia. "Rediscovering black phosphorus as an anisotropic layered material for optoelectronics and electronics." In: *Nature communications* 5 (2014), p. 4458.

[144] Pablo Solís-Fernández, Juan Ignacio Paredes, S Villar-Rodil, Amelia Martínez-Alonso, and Juan Manuel D Tascón. "Determining the thickness of chemically modified graphenes by scanning probe microscopy." In: *Carbon* 48.9 (2010), pp. 2657–2660.

[145] Manchester Nanomaterials. *Black phosphorus (phosphorene)*. 2013. URL: https://mos2crystals.com/product/black-phosphorus-phosphorene/.

[146] Andres Castellanos-Gomez. "Black phosphorus: narrow gap, wide applications." In: *The journal of physical chemistry letters* 6.21 (2015), pp. 4280–4291.

[147] Munkhbayar Batmunkh, Munkhjargal Bat-Erdene, and Joseph G Shapter. "Phosphorene and Phosphorene-Based Materials–Prospects for Future Applications." In: *Advanced Materials* 28.39 (2016), pp. 8586–8617.

[148] Ruixiang Fei, Alireza Faghaninia, Ryan Soklaski, Jia-An Yan, Cynthia Lo, and Li Yang. "Enhanced Thermoelectric Efficiency via Orthogonal Electrical and Thermal Conductances in Phosphorene." In: *Nano Letters* 14.11 (2014), pp. 6393–6399.

[149] Alexander N Rudenko and Mikhail I Katsnelson. "Quasiparticle band structure and tight-binding model for single-and bilayer black phosphorus." In: *Physical Review B* 89.20 (2014), p. 201408.

[150] Hongyan Guo, Ning Lu, Jun Dai, Xiaojun Wu, and Xiao Cheng Zeng. "Phosphorene nanoribbons, phosphorus nanotubes, and van der Waals multilayers." In: *The Journal of Physical Chemistry C* 118.25 (2014), pp. 14051–14059.

[151] Joshua D. Wood, Spencer A. Wells, Deep Jariwala, Kan-Sheng Chen, EunKyung Cho, Vinod K. Sangwan, Xiaolong Liu, Lincoln J. Lauhon, Tobin J. Marks, and Mark C. Hersam. "Effective Passivation of Exfoliated Black Phosphorus Transistors against Ambient Degradation." In: *Nano Letters* 14.12 (2014), pp. 6964–6970.

[152] Vy Tran, Ryan Soklaski, Yufeng Liang, and Li Yang. "Layer-controlled band gap and anisotropic excitons in few-layer black phosphorus." In: *Physical Review B* 89.23 (2014), p. 235319.

[153] Bilu Liu, Marianne Köpf, Ahmad N Abbas, Xiaomu Wang, Qiushi Guo, Yichen Jia, Fengnian Xia, Richard Weihrich, Frederik Bachhuber, Florian Pielnhofer, et al. "Black arsenic–phosphorus: layered anisotropic infrared semiconductors with highly tunable compositions and properties." In: *Advanced Materials* 27.30 (2015), pp. 4423–4429.

[154] S. Appalakondaiah, G. Vaitheeswaran, S. Lebègue, N. E. Christensen, and A. Svane. "Effect of van der Waals interactions on the structural and elastic properties of black phosphorus." In: *Phys. Rev. B* 86 (3 2012), p. 035105.

[155] Qun Wei and Xihong Peng. "Superior mechanical flexibility of phosphorene and few-layer black phosphorus." In: *Applied Physics Letters* 104.25, 251915 (2014). DOI: http://dx.doi.org/10.1063/1.4885215. URL: http://scitation.aip.org/content/aip/journal/apl/104/25/10.1063/1.4885215.

[156] Jin-Wu Jiang and Harold S Park. "Mechanical properties of single-layer black phosphorus." In: *Journal of Physics D: Applied Physics* 47.38 (2014), p. 385304.

[157] Jin-Wu Jiang and Harold S Park. "Negative poisson's ratio in single-layer black phosphorus." In: *Nature communications* 5 (2014), p. 4727.

[158] Feng Hao and Xi Chen. "Mechanical properties of phosphorene nanoribbons and oxides." In: *Journal of Applied Physics* 118.23 (2015), p. 234304.

[159] Zenghui Wang and Philip X-L Feng. "Design of black phosphorus 2D nanomechanical resonators by exploiting the intrinsic mechanical anisotropy." In: *2D Materials* 2.2 (2015), p. 021001.

[160] Zhaoyao Yang, Junhua Zhao, and Ning Wei. "Temperature-dependent mechanical properties of monolayer black phosphorus by molecular dynamics simulations." In: *Applied Physics Letters* 107.2 (2015), p. 023107.

[161] Mohammad Elahi, Kaveh Khaliji, Seyed Mohammad Tabatabaei, Mahdi Pourfath, and Reza Asgari. "Modulation of electronic and mechanical properties of phosphorene through strain." In: *Physical Review B* 91.11 (2015), p. 115412.

[162] Jin Tao, Wanfu Shen, Sen Wu, Lu Liu, Zhihong Feng, Chao Wang, Chunguang Hu, Pei Yao, Hao Zhang, Wei Pang, et al. "Mechanical and electrical anisotropy of few-layer black phosphorus." In: *ACS nano* 9.11 (2015), pp. 11362–11370.

[163] Jia-Ying Wang, Yang Li, Zhao-Yao Zhan, Tie Li, Liang Zhen, and Cheng-Yan Xu. "Elastic properties of suspended black phosphorus nanosheets." In: *Applied Physics Letters* 108.1 (2016), p. 013104.

[164] Hao Chen, Peng Huang, Dan Guo, and Guoxin Xie. "Anisotropic mechanical properties of black phosphorus nanoribbons." In: *The Journal of Physical Chemistry C* 120.51 (2016), pp. 29491–29497.

[165] Yang Liu, Yuhong Liu, and Jianbin Luo. "Atomic Scale Simulation on the Fracture Mechanism of Black Phosphorus Monolayer under Indentation." In: *Nanomaterials* 8.9 (2018), p. 682.

[166] Rafael Roldán, Andres Castellanos-Gomez, Emmanuele Cappelluti, and Francisco Guinea. "Strain engineering in semiconducting two-dimensional crystals." In: *Journal of Physics: Condensed Matter* 27.31 (2015), p. 313201.

[167] Shikai Deng, Anirudha V. Sumant, and Vikas Berry. "Strain engineering in two-dimensional nanomaterials beyond graphene." In: *Nano Today* 22 (2018), pp. 14 –35. ISSN: 1748-0132.

[168] Deniz ÇakIr, Hasan Sahin, and François M. Peeters. "Tuning of the electronic and optical properties of single-layer black phosphorus by strain." In: *Phys. Rev. B* 90 (20 2014), p. 205421.

[169] Ruixiang Fei and Li Yang. "Strain-Engineering the Anisotropic Electrical Conductance of Few-Layer Black Phosphorus." In: *Nano Letters* 14.5 (2014), pp. 2884–2889.

[170] Joshua O Island, Gary A Steele, Herre S J van der Zant, and Andres Castellanos-Gomez. "Environmental instability of few-layer black phosphorus." In: *2D Materials* 2.1 (2015), p. 011002.

[171] Yanlan Du, Chuying Ouyang, Siqi Shi, and Minsheng Lei. "Ab initio studies on atomic and electronic structures of black phosphorus." In: *Journal of Applied Physics* 107.9 (2010), p. 093718.

[172] Alexandre Favron, Etienne Gaufrès, Frédéric Fossard, Anne-Laurence Phaneuf-L'Heureux, Nathalie YW Tang, Pierre L Lévesque, Annick Loiseau, Richard Leonelli, Sébastien Francoeur, and Richard Martel. "Photooxidation and quantum confinement effects in exfoliated black phosphorus." In: *Nature materials* 14.8 (2015), p. 826.

[173] Steven P Koenig, Rostislav A Doganov, Hennrik Schmidt, AH Castro Neto, and Barbaros Oezyilmaz. "Electric field effect in ultrathin black phosphorus." In: *Applied Physics Letters* 104.10 (2014), p. 103106.

[174] Ahmet Avsar, Ivan J Vera-Marun, Jun You Tan, Kenji Watanabe, Takashi Taniguchi, Antonio H Castro Neto, and Barbaros Ozyilmaz. "Air-stable transport in graphene-contacted, fully encapsulated ultrathin black phosphorus-based field-effect transistors." In: *Acs Nano* 9.4 (2015), pp. 4138–4145.

[175] Manisha B Erande, Mahendra S Pawar, and Dattatray J Late. "Humidity sensing and photodetection behavior of electrochemically exfoliated atomically thin-layered black phosphorus nanosheets." In: *ACS applied materials & interfaces* 8.18 (2016), pp. 11548–11556.

[176] Dattatray J Late. "Liquid exfoliation of black phosphorus nanosheets and its application as humidity sensor." In: *Microporous and Mesoporous Materials* 225 (2016), pp. 494–503.

[177] Zenghui Wang, Arnob Islam, Rui Yang, Xuqian Zheng, and Philip X-L Feng. "Environmental, thermal, and electrical susceptibility of black phosphorus field effect transistors." In: *Journal of Vacuum Science & Technology B, Nanotechnology and Microelectronics: Materials, Processing, Measurement, and Phenomena* 33.5 (2015), p. 052202.

[178] M Donarelli, L Ottaviano, L Giancaterini, G Fioravanti, F Perrozzi, and C Cantalini. "Exfoliated black phosphorus gas sensing properties at room temperature." In: *2D Materials* 3.2 (2016), p. 025002.

[179] Miriam Moreno-Moreno, Guillermo Lopez-Polin, Andres Castellanos-Gomez, Cristina Gomez-Navarro, and Julio Gomez-Herrero. "Environmental effects in mechanical properties of few-layer black phosphorus." In: *2D Materials* 3.3 (2016), p. 031007.

[180] Andres Castellanos-Gomez, Ronald van Leeuwen, Michele Buscema, Herre S. J. van der Zant, Gary A. Steele, and Warner J. Venstra. "Single-Layer MoS2 Mechanical Resonators." In: *Advanced Materials* 25.46 (2013), pp. 6719–6723. ISSN: 1521-4095.

[181] KS Novoselov, D Jiang, F Schedin, TJ Booth, VV Khotkevich, SV Morozov, and AK Geim. "Two-dimensional atomic crystals." In: *Proceedings of the National Academy of Sciences* 102.30 (2005), pp. 10451–10453.

[182] P Blake, EW Hill, AH Castro Neto, KS Novoselov, D Jiang, R Yang, TJ Booth, and AK Geim. "Making graphene visible." In: *Applied Physics Letters* 91.6 (2007), p. 063124.

[183] G. López-Polín Peña. "Propiedades mecánicas de membranas de grafeno: consecuencias de la inducción controlada de defefctos." PhD thesis. Universidad Autónoma de Madrid, 2016.

[184] Ziyi Cui, Guoxin Xie, Feng He, Weiqi Wang, Dan Guo, and Wei Wang. "Atomic-Scale Friction of Black Phosphorus: Effect of Thickness and Anisotropic Behavior." In: *Advanced Materials Interfaces* 4.23 (2017), p. 1700998.

[185] Barry J. Goodno James M. Gere. *Mechanics of Materials*. eng. Stamford: CENGAGE Learning Custom Publishing, 2009. ISBN: 9781111577735.

[186] DT Online. *Strength of Materials*. 2017. URL: http://wiki.dtonline.org/index.php/Strength_of_Materials.

[187] Sundar Dannana. *Stress Strain Curve*. 2017. URL: https://extrudesign.com/stress-strain-curve/.

[188] Inc MechaniCalc. *Mechanical Properties of Materials*. 2014-2018. URL: https://mechanicalc.com/reference/mechanical-properties-of-materials.

[189] NM Bhatia and W Nachbar. "Finite indentation of elastic-perfectly plastic membranes by a spherical indenter." In: *Aiaa Journal* 6.6 (1968), pp. 1050–1057.

[190] Engineering ToolBox. *Young's Modulus - Tensile and Yield Strength for common Materials*. 2003. URL: https://www.engineeringtoolbox.com/young-modulus-d_417.html.

[191] Zhen-Dong Sha, Qing-Xiang Pei, Zhiwei Ding, Jin-Wu Jiang, and Yong-Wei Zhang. "Mechanical properties and fracture behavior of single-layer phosphorene at finite temperatures." In: *Journal of Physics D: Applied Physics* 48.39 (2015), p. 395303.

[192] Lili Li and Jie Yang. "On mechanical behaviors of few-layer black phosphorus." In: *Scientific reports* 8.1 (2018), p. 3227.

[193] Wikipedia. *Flexural rigidity*. 2018. URL: https://en.wikipedia.org/wiki/Flexural_rigidity.

[194] Stephen P Timoshenko and Sergius Woinowsky-Krieger. *Theory of plates and shells*. McGraw-hill, 1959.

[195] Matthew R. Begley and Thomas J. Mackin. "Spherical indentation of freestanding circular thin films in the membrane regime." In: *Journal of the Mechanics and Physics of Solids* 52.9 (2004), pp. 2005 –2023. ISSN: 0022-5096.

[196] Andres Castellanos-Gomez, Vibhor Singh, Herre S. J. van der Zant, and Gary A. Steele. "Mechanics of freely-suspended ultrathin layered materials." In: *Annalen der Physik* 527.1-2 (2015), pp. 27–44. ISSN: 1521-3889.

[197] Guillermo López-Polín, Cristina Gómez-Navarro, Vincenzo Parente, Francisco Guinea, Mikhail I Katsnelson, Francesc Perez-Murano, and Julio Gómez-Herrero. "Increasing the elastic modulus of graphene by controlled defect creation." In: *Nature Physics* 11.1 (2015), p. 26.

[198] Team Nanotec GmbH. *Hemisperical Cone Shaped Tip PDF*. 2018. URL: https://www.team-nanotec.de/UserFiles1/Includes/shop/printpdf.cfm?id=325.

[199] Guillermo Lopez-Polin, Julio Gomez-Herrero, and Cristina Gomez-Navarro. "Confining crack propagation in defective graphene." In: *Nano letters* 15.3 (2015), pp. 2050–2054.

[200] Simone Bertolazzi, Jacopo Brivio, and Andras Kis. "Stretching and Breaking of Ultrathin MoS2." In: *ACS Nano* 5.12 (2011), pp. 9703–9709.

[201] Deniz Armani, Chang Liu, and Narayan Aluru. "Re-configurable fluid circuits by PDMS elastomer micromachining." In: *Micro Electro Mechanical Systems, 1999. MEMS'99. Twelfth IEEE International Conference on*. IEEE. 1999, pp. 222–227.

[202] Wikipedia. *Pasivación*. 2019. URL: https://es.wikipedia.org/wiki/Pasivaci%C3%B3n.

[203] Stuart R Batten, Suzanne M Neville, and David R Turner. *Coordination polymers: design, analysis and application*. eng. Cambridge, UK: RSC PUblishing, 2009. ISBN: 9780854048373.

[204] J. Troyano Prieto. "Cu(I) y Ag (I) con ligandos organoazufrados: una excelente combinación para la preparación de materiales con interesantes propiedades electrónicas." PhD thesis. Universidad Autónoma de Madrid, 2015.

[205] Yonggang Zhao, Kunhao Li, and Jing Li. "Solvothermal synthesis of multifunctional coordination polymers." In: *Zeitschrift für Naturforschung B* 65.8 (2010), pp. 976–998.

[206] J C Bailar and Jolly W. L. *Preparative Inorganic Reactions*. eng. New York: Interscience, 1964, pp. 1–25. ISBN: 867410376.

[207] Mitsuru Kondo, Tomomichi Yoshitomi, Hiroyuki Matsuzaka, Susumu Kitagawa, and Kenji Seki. "Three-Dimensional Framework with Channeling Cavities for Small Molecules:{[M2 (4, 4'-bpy) 3 (NO_3) 4]· xH_2O} n (M=Co, Ni, Zn)." In: *Angewandte Chemie International Edition in English* 36.16 (1997), pp. 1725–1727.

[208] Hailian Li, Mohamed Eddaoudi, Michael O'Keeffe, and Omar M Yaghi. "Design and synthesis of an exceptionally stable and highly porous metal-organic framework." In: *nature* 402.6759 (1999), p. 276.

[209] Christoph Janiak. "Engineering coordination polymers towards applications." In: *Dalton Transactions* 14 (2003), pp. 2781–2804.

[210] Susumu Kitagawa, Ryo Kitaura, and Shin-ichiro Noro. "Functional porous coordination polymers." In: *Angewandte Chemie International Edition* 43.18 (2004), pp. 2334–2375.

[211] Lorena Welte, Arrigo Calzolari, Rosa Di Felice, Felix Zamora, and Julio Gómez-Herrero. "Highly conductive self-assembled nanoribbons of coordination polymers." In: *Nature nanotechnology* 5.2 (2010), p. 110.

[212] Cristina Hermosa, Jose Vicente Alvarez, Mohammad-Reza Azani, Carlos J Gómez-García, Michelle Fritz, Jose M Soler, Julio Gómez-Herrero, Cristina Gómez-Navarro, and Félix Zamora. "Intrinsic electrical conductivity of nanostructured metal-organic polymer chains." In: *Nature communications* 4 (2013), p. 1709.

[213] Ivo Stassen, Nicholas Burtch, Alec Talin, Paolo Falcaro, Mark Allendorf, and Rob Ameloot. "An updated roadmap for the integration of metal–organic frameworks with electronic devices and chemical sensors." In: *Chemical Society Reviews* 46.11 (2017), pp. 3185–3241.

[214] Muhammad Usman, Shruti Mendiratta, and Kuang-Lieh Lu. "Semiconductor Metal–Organic Frameworks: Future Low-Bandgap Materials." In: *Advanced Materials* 29.6 (2017), p. 1605071.

[215] Jin Chong Tan and Anthony K Cheetham. "Mechanical properties of hybrid inorganic–organic framework materials: establishing fundamental structure–property relationships." In: *Chemical Society Reviews* 40.2 (2011), pp. 1059–1080.

[216] Cristina Hermosa, Benjamin R Horrocks, José I Martínez, Fabiola Liscio, Julio Gómez-Herrero, and Félix Zamora. "Mechanical and optical properties of ultralarge flakes of a metal–organic framework with molecular thickness." In: *Chemical science* 6.4 (2015), pp. 2553–2558.

[217] Arnau Carne, Carlos Carbonell, Inhar Imaz, and Daniel Maspoch. "Nanoscale metal–organic materials." In: *Chemical Society Reviews* 40.1 (2011), pp. 291–305.

[218] D Rodriguez-San-Miguel, P Amo-Ochoa, and Felix Zamora. "MasterChem: cooking 2D-polymers." In: *Chemical Communications* 52.22 (2016), pp. 4113–4127.

[219] Alexandre Abhervé, Samuel Manas-Valero, Miguel Clemente-León, and Eugenio Coronado. "Graphene related magnetic materials: micromechanical exfoliation of 2D layered magnets based on bimetallic anilate complexes with inserted [Fe III (acac 2-trien)]+ and [Fe III (sal 2-trien)]+ molecules." In: *Chemical science* 6.8 (2015), pp. 4665–4673.

[220] Pilar Amo-Ochoa, Lorena Welte, Rodrigo González-Prieto, Pablo J Sanz Miguel, Carlos J Gómez-García, Eva Mateo-Martí, Salome Delgado, Julio Gómez-Herrero, and Félix Zamora. "Single layers of a multifunctional laminar Cu (I, II) coordination polymer." In: *Chemical Communications* 46.19 (2010), pp. 3262–3264.

[221] Almudena Gallego, Cristina Hermosa, Oscar Castillo, Isadora Berlanga, Carlos J Gómez-García, Eva Mateo-Martí, José I Martínez, Fernando Flores, Cristina Gómez-Navarro, Julio Gómez-Herrero, et al. "Solvent-Induced Delamination of a Multifunctional Two Dimensional Coordination Polymer." In: *Advanced Materials* 25.15 (2013), pp. 2141–2146.

[222] Thomas Bauer, Zhikun Zheng, Alois Renn, Raoul Enning, Andreas Stemmer, Junji Sakamoto, and A Dieter Schlüter. "Synthesis of free-standing, monolayered organometallic sheets at the air/water interface." In: *Angewandte Chemie International Edition* 50.34 (2011), pp. 7879–7884.

[223] Tetsuya Kambe, Ryota Sakamoto, Ken Hoshiko, Kenji Takada, Mariko Miyachi, Ji-Heun Ryu, Sono Sasaki, Jungeun Kim, Kazuo Nakazato, Masaki Takata, et al. "π-Conjugated nickel bis (dithiolene) complex nanosheet." In: *Journal of the American Chemical Society* 135.7 (2013), pp. 2462–2465.

[224] Tania Rodenas, Ignacio Luz, Gonzalo Prieto, Beatriz Seoane, Hozanna Miro, Avelino Corma, Freek Kapteijn, Francesc X Llabrés i Xamena, and Jorge Gascon. "Metal–organic framework nanosheets in polymer composite materials for gas separation." In: *Nature materials* 14.1 (2015), p. 48.

[225] Víctor Rubio-Giménez, Sergio Tatay, Florence Volatron, Francisco J Martínez-Casado, Carlos Martí-Gastaldo, and Eugenio Coronado. "High-Quality Metal–Organic Framework Ultrathin Films for Electronically Active Interfaces." In: *Journal of the American Chemical Society* 138.8 (2016), pp. 2576–2584.

[226] Ryota Sakamoto, Ken Hoshiko, Qian Liu, Toshiki Yagi, Tatsuhiro Nagayama, Shinpei Kusaka, Mizuho Tsuchiya, Yasutaka Kitagawa, Wai-Yeung Wong, and Hiroshi Nishihara. "A photofunctional bottom-up bis (dipyrrinato) zinc (II) complex nanosheet." In: *Nature communications* 6 (2015), p. 6713.

[227] Víctor Rubio-Giménez, Marta Galbiati, Javier Castells-Gil, Neyvis Almora-Barrios, José Navarro-Sánchez, Garin Escorcia-Ariza, Michele Mattera, Thomas Arnold, Jonathan Rawle, Sergio Tatay, et al. "Bottom-Up Fabrication of Semiconductive Metal–Organic Framework Ultrathin Films." In: *Advanced Materials* 30.10 (2018), p. 1704291.

[228] Gonzalo Givaja, Pilar Amo-Ochoa, Carlos J Gómez-García, and Felix Zamora. "Electrical conductive coordination polymers." In: *Chemical Society Reviews* 41.1 (2012), pp. 115–147.

[229] Xing Huang, Peng Sheng, Zeyi Tu, Fengjiao Zhang, Junhua Wang, Hua Geng, Ye Zou, Chong-an Di, Yuanping Yi, Yimeng Sun, et al. "A two-dimensional π–d conjugated coordination polymer with extremely high electrical conductivity and ambipolar transport behaviour." In: *Nature communications* 6 (2015), p. 7408.

[230] Miriam Moreno-Moreno, Javier Troyano, Pablo Ares, Óscar Castillo, Christian A Nijhuis, Li Yuan, Pilar Amo-Ochoa, Salomé Delgado, Julio Gómez-Herrero, Félix Zamora, and Cristina Gómez-Navarro. "One-Pot Preparation of Mechanically Robust, Transparent, Highly Conductive, and Memristive Metal–Organic Ultrathin Film." In: *ACS nano* 12.10 (2018), pp. 10171–10177.

[231] J Troyano, J Perles, P Amo-Ochoa, JI Martinez, F Zamora, and S Delgado. "Reversible recrystallization process of copper and silver thioacetamide–halide coordination polymers and their basic building blocks." In: *CrystEngComm* 16.35 (2014), pp. 8224–8231.

[232] Frank H Allen. "The Cambridge Structural Database: a quarter of a million crystal structures and rising." In: *Acta Crystallographica Section B: Structural Science* 58.3 (2002), pp. 380–388.

[233] LW Strock. "The crystal structure of high temperature iodine silver alpha-AgI." In: *Zeit. Physik. Chem. B* 25 (1934), pp. 441–459.

[234] LW Strock. "Supplement and announcement on: The crystal structure of high temperature iodine silver alpha-AgI." In: *Zeit. Physik. Chem. B* 31 (1936), pp. 132–136.

[235] B Reuter and K Hardel. "Silbersulfidbromid und silbersulfidjodid." In: *Angewandte Chemie* 72.4 (1960), pp. 138–139.

[236] B Reuter and K Hardel. "Silbersulfidbromid und silbersulfidjodid." In: *Naturwissenschaften* 48 (1961), pp. 161–163.

[237] JN Bradley and Po D Greene. "Potassium iodide+ silver iodide phase diagram. High ionic conductivity of KAg 4 I 5." In: *Transactions of the Faraday Society* 62 (1966), pp. 2069–2075.

[238] JN Bradley and PD Greene. "Solids with high ionic conductivity in group 1 halide systems." In: *Transactions of the Faraday Society* 63 (1967), pp. 424–430.

[239] Zhangxian Chen, Wanchao Li, Ran Li, Yunfeng Zhang, Guoqin Xu, and Hansong Cheng. "Fabrication of Highly Transparent and Conductive Indium–Tin Oxide Thin Films with a High Figure of Merit via Solution Processing." In: *Langmuir* 29.45 (2013), pp. 13836–13842.

[240] Wikipedia. *Óxido de indio y estaño*. 2017. URL: https://es.wikipedia.org/wiki/%C3%93xido_de_indio_y_esta%C3%B1o.

[241] Michael Vosgueritchian, Darren J Lipomi, and Zhenan Bao. "Highly conductive and transparent PEDOT: PSS films with a fluorosurfactant for stretchable and flexible transparent electrodes." In: *Advanced functional materials* 22.2 (2012), pp. 421–428.

[242] Wu Tang, Yipeng Chao, Xiaolong Weng, Longjiang Deng, and Kewei Xu. "Optical Property and the Relationship between Resistivity and Surface Roughness of Indium Tin Oxide Thin Films." In: *Physics Procedia* 32 (2012). The 18th International Vacuum Congress (IVC-18), pp. 680 –686. ISSN: 1875-3892.

[243] Yu-Min Chen, Shih-Ming He, Chi-Hsien Huang, Cheng-Chun Huang, Wen-Pin Shih, Chun-Lin Chu, Jing Kong, Ju Li, and Ching-Yuan Su. "Ultra-large suspended graphene as a highly elastic membrane for capacitive pressure sensors." In: *Nanoscale* 8.6 (2016), pp. 3555–3564.

[244] P Ares, G López-Polín, C Hermosa, F Zamora, J Gómez-Herrero, and C Gómez-Navarro. "Exfoliated graphite flakes as soft-electrodes for precisely contacting nanoobjects." In: *2D Materials* 2.3 (2015), p. 035008.

[245] Peter Grünberg Institut, R. Waser, and M. Wuttig. *Memristive Phenomena - from Fundamental Physics to Neuromorphic Computing - Lecture Notes*. Schriften des Forschungszentrums Jülich / Reihe Schlüsseltechnologien: Schriften des Forschungszentrums Jülich. Forschungszentrum Jülich GmbH, 2016. ISBN: 9783958060913.

[246] Leon Chua. "Memristor-the missing circuit element." In: *IEEE Transactions on circuit theory* 18.5 (1971), pp. 507–519.

[247] Wikipedia. *Memristor*. 2018. URL: https://en.wikipedia.org/wiki/Memristor.

[248] Sascha Vongehr and Xiangkang Meng. "The missing memristor has not been found." In: *Scientific reports* 5 (2015), p. 11657.

[249] Leon O Chua and Sung Mo Kang. "Memristive devices and systems." In: *Proceedings of the IEEE* 64.2 (1976), pp. 209–223.

[250] Dmitri B Strukov, Gregory S Snider, Duncan R Stewart, and R Stanley Williams. "The missing memristor found." In: *nature* 453.7191 (2008), pp. 80–83.

[251] Web of Science. *records for TEMA: (memristive system) OR TEMA: (memristor) OR TEMA: (resistive switching)*. 2018. URL: https://wcs.webofknowledge.com/RA/analyze.do?product=UA&SID=C3R8Y4XFoefPwtcFTRG&field=PY_PublicationYear_PublicationYear_en&yearSort=true.

[252] F. Pan, S. Gao, C. Chen, C. Song, and F. Zeng. "Recent progress in resistive random access memories: Materials, switching mechanisms, and performance." In: *Materials Science and Engineering: R: Reports* 83 (2014), pp. 1 –59.

[253] J Joshua Yang, Dmitri B Strukov, and Duncan R Stewart. "Memristive devices for computing." In: *Nature nanotechnology* 8.1 (2013), p. 13.

[254] Yoshitaka Aoki, Carsten Wiemann, Vitaliy Feyer, Hong-Seok Kim, Claus Michael Schneider, Han Ill-Yoo, and Manfred Martin. "Bulk mixed ion electron conduction in amorphous gallium oxide causes memristive behaviour." In: *Nature communications* 5 (2014), p. 3473.

[255] Christian Walczyk, Damian Walczyk, Thomas Schroeder, Thomas Bertaud, Małgorzata Sowinska, Mindaugas Lukosius, Mirko Fraschke, Dirk Wolansky, Bernd Tillack, Enrique Miranda, et al. "Impact of Temperature on the Resistive Switching Behavior of Embedded HfO2-Based RRAM Devices." In: *IEEE transactions on electron devices* 58.9 (2011), pp. 3124–3131.

[256] Rainer Waser and Masakazu Aono. "Nanoionics-based resistive switching memories." In: *Nature materials* 6.11 (2007), p. 833.

[257] Rainer Waser, Regina Dittmann, Georgi Staikov, and Kristof Szot. "Redox-based resistive switching memories–nanoionic mechanisms, prospects, and challenges." In: *Advanced materials* 21.25-26 (2009), pp. 2632–2663.

[258] Fu-Chien Chiu. "A review on conduction mechanisms in dielectric films." In: *Advances in Materials Science and Engineering* 2014 (2014).

[259] Akihito Sawa. "Resistive switching in transition metal oxides." In: *Materials Today* 11.6 (2008), pp. 28 –36. ISSN: 1369-7021.

[260] Stephan Menzel, Stefan Tappertzhofen, Rainer Waser, and Ilia Valov. "Switching kinetics of electrochemical metallization memory cells." In: *Physical Chemistry Chemical Physics* 15.18 (2013), pp. 6945–6952.

[261] Yooichi Hirose and Haruo Hirose. "Polarity-dependent memory switching and behavior of Ag dendrite in Ag-photodoped amorphous As2S3 films." In: *Journal of Applied Physics* 47.6 (1976), pp. 2767–2772.

[262] Hyunjun Sim, Hyejung Choi, Dongsoo Lee, Man Chang, Dooho Choi, Yunik Son, Eun-Hong Lee, Wonjoo Kim, Yoondong Park, In-Kyeong Yoo, and Hyunsang Hwang. "Excellent resistance switching characteristics of Pt/SrTiO/sub 3/ schottky junction for multi-bit nonvolatile memory application." In: *IEEE InternationalElectron Devices Meeting, 2005. IEDM Technical Digest.* (2005), pp. 758–761.

[263] Tat'yana Vladimirovna Vernitskaya and Oleg Nikolaevich Efimov. "Polypyrrole: a conducting polymer; its synthesis, properties and applications." In: *Russian chemical reviews* 66.5 (1997), pp. 443–457.

[264] Ryan C Chiechi, Emily A Weiss, Michael D Dickey, and George M Whitesides. "Eutectic gallium–indium (EGaIn): a moldable liquid metal for electrical characterization of self-assembled monolayers." In: *Angewandte Chemie International Edition* 47.1 (2008), pp. 142–144.

[265] Wenqian Chen, Satoshi Horike, Daiki Umeyama, Naoki Ogiwara, Tomoya Itakura, Cédric Tassel, Yoshihiro Goto, Hiroshi Kageyama, and Susumu Kitagawa. "Glass formation of a coordination polymer crystal for enhanced proton conductivity and material flexibility." In: *Angewandte Chemie International Edition* 55.17 (2016), pp. 5195–5200.

[266] Pinshane Y Huang, Carlos S Ruiz-Vargas, Arend M van der Zande, William S Whitney, Mark P Levendorf, Joshua W Kevek, Shivank Garg, Jonathan S Alden, Caleb J Hustedt, Ye Zhu, et al. "Grains and grain boundaries in single-layer graphene atomic patchwork quilts." In: *Nature* 469.7330 (2011), p. 389.

[267] Vinod K Sangwan, Deep Jariwala, In Soo Kim, Kan-Sheng Chen, Tobin J Marks, Lincoln J Lauhon, and Mark C Hersam. "Gate-tunable memristive phenomena mediated by grain boundaries in single-layer MoS2." In: *Nature nanotechnology* 10.5 (2015), pp. 403–406.

[268] Gerhard Wegner. "Polymers with Metal-Like Conductivity—A Review of their Synthesis, Structure and Properties." In: *Angewandte Chemie International Edition in English* 20.4 (1981), pp. 361–381.

[269] A Alec Talin, Andrea Centrone, Alexandra C Ford, Michael E Foster, Vitalie Stavila, Paul Haney, R Adam Kinney, Veronika Szalai, Farid El Gabaly, Heayoung P Yoon, et al. "Tunable electrical conductivity in metal-organic framework thin-film devices." In: *Science* 343.6166 (2014), pp. 66–69.

[270] Weiping Su, Maochun Hong, Jiabao Weng, Rong Cao, and Shaofang Lu. "A Semiconducting Lamella Polymer [{Ag (C5H4NS)} n] with a Graphite-Like Array of Silver (I) Ions and Its Analogue with a Layered Structure." In: *Angewandte Chemie International Edition* 39.16 (2000), pp. 2911–2914.

[271] Hing Chan, Hok-Lai Wong, Maggie Ng, Chun-Ting Poon, and Vivian Wing-Wah Yam. "Switching of Resistive Memory Behavior from Binary to Ternary Logic via Alteration of Substituent Positioning on the Subphthalocyanine Core." In: *Journal of the American Chemical Society* 139.21 (2017), pp. 7256–7263.

[272] Fangxu Yang, Qiang Zhao, Chunhui Xu, Ye Zou, Huanli Dong, Yonggang Zheng, and Wenping Hu. "Unveiling the Switching Riddle of Silver Tetracyanoquinodimethane Towards Novel Planar Single-Crystalline Electrochemical Metallization Memories." In: *Advanced Materials* 28.33 (2016), pp. 7094–7100.

[273] K Szot, R Dittmann, W Speier, and R Waser. "Nanoscale resistive switching in SrTiO3 thin films." In: *physica status solidi (RRL)–Rapid Research Letters* 1.2 (2007), R86–R88.

[274] Seok Min Yoon, Scott C Warren, and Bartosz A Grzybowski. "Storage of electrical information in metal–organic-framework memristors." In: *Angewandte Chemie International Edition* 53.17 (2014), pp. 4437–4441.

[275] Anasuya Bandyopadhyay, Satyajit Sahu, and Masayoshi Higuchi. "Tuning of nonvolatile bipolar memristive switching in Co (III) polymer with an extended azo aromatic ligand." In: *Journal of the American Chemical Society* 133.5 (2011), pp. 1168–1171.

[276] Benlin Hu, Chengyuan Wang, Jiangxin Wang, Junkuo Gao, Kai Wang, Jiansheng Wu, Guodong Zhang, Wangqiao Cheng, Bhavanasi Venkateswarlu, Mingfeng Wang, et al. "Inorganic–organic hybrid polymer with multiple redox for high-density data storage." In: *Chemical Science* 5.9 (2014), pp. 3404–3408.

[277] Hafeesudeen Sahabudeen, Haoyuan Qi, Bernhard Alexander Glatz, Diana Tranca, Renhao Dong, Yang Hou, Tao Zhang, Christian Kuttner, Tibor Lehnert, Gotthard Seifert, et al. "Wafer-sized multifunctional polyimine-based two-dimensional conjugated polymers with high mechanical stiffness." In: *Nature communications* 7 (2016), p. 13461.

[278] DF Bahr, JA Reid, WM Mook, CA Bauer, R Stumpf, AJ Skulan, NR Moody, BA Simmons, MM Shindel, and MD Allendorf. "Mechanical properties of cubic zinc carboxylate IRMOF-1 metal-organic framework crystals." In: *Physical Review B* 76.18 (2007), p. 184106.

[279] Daniel A Kunz, Eva Max, Richard Weinkamer, Thomas Lunkenbein, Josef Breu, and Andreas Fery. "Deformation measurements on thin clay tactoids." In: *Small* 5.16 (2009), pp. 1816–1820.

[280] A Ortega-Esteban, I Horcas, M Hernando-Pérez, P Ares, AJ Perez-Berna, C San Martín, JL Carrascosa, PJ De Pablo, and J Gómez-Herrero. "Minimizing tip–sample forces in jumping mode atomic force microscopy in liquid." In: *Ultramicroscopy* 114 (2012), pp. 56–61.

[281] Danny Porath, Alexey Bezryadin, Simon De Vries, and Cees Dekker. "Direct measurement of electrical transport through DNA molecules." In: *Nature* 403.6770 (2000), p. 635.

[282] URL: http://www.picotech.co.il/?page_id=328.

[283] Rubén Mas-Ballesté, Julio Gómez-Herrero, and Félix Zamora. "One-dimensional coordination polymers on surfaces: towards single molecule devices." In: *Chem. Soc. Rev.* 39 (11 2010), pp. 4220–4233.

[284] Kiran Kumar Vudya Sethu. "Spin orbit torques in magnetic materials." PhD thesis. Katholieke Universiteit Leuven, June 2017.

[285] Prosenjit Rai-Choudhury. *Handbook of microlithography, micromachining, and microfabrication: microlithography*. Vol. 1. Iet, 1997.

[286] Sander J Tans, Alwin RM Verschueren, and Cees Dekker. "Room-temperature transistor based on a single carbon nanotube." In: *Nature* 393.6680 (1998), p. 49.

[287] Michael Hatzakis. "Electron resists for microcircuit and mask production." In: *Journal of the electrochemical society* 116.7 (1969), pp. 1033–1037.

[288] Vitor R Manfrinato, Lihua Zhang, Dong Su, Huigao Duan, Richard G Hobbs, Eric A Stach, and Karl K Berggren. "Resolution limits of electron-beam lithography toward the atomic scale." In: *Nano letters* 13.4 (2013), pp. 1555–1558.

[289] Leo Gross, Fabian Mohn, Nikolaj Moll, Peter Liljeroth, and Gerhard Meyer. "The Chemical Structure of a Molecule Resolved by Atomic Force Microscopy." In: *Science* 325.5944 (2009), pp. 1110–1114. ISSN: 0036-8075.

[290] M. Calleja, M. Tello, J. Anguita, F. García, and R. García. "Fabrication of gold nanowires on insulating substrates by field-induced mass transport." In: *Applied Physics Letters* 79.15 (2001), pp. 2471–2473.

[291] JI Pascual, J Mendez, J Gómez-Herrero, AM Baró, N Garcia, and Vu Thien Binh. "Quantum contact in gold nanostructures by scanning tunneling microscopy." In: *Physical review letters* 71.12 (1993), p. 1852.

[292] G Rubio, N Agrait, and S Vieira. "Atomic-sized metallic contacts: mechanical properties and electronic transport." In: *Physical review letters* 76.13 (1996), p. 2302.

[293] CJ Muller, JM Van Ruitenbeek, and LJ De Jongh. "Experimental observation of the transition from weak link to tunnel junction." In: *Physica C: Superconductivity* 191.3-4 (1992), pp. 485–504.

[294] Claes Thelander and Lars Samuelson. "AFM manipulation of carbon nanotubes: realization of ultra-fine nano-electrodes." In: *Nanotechnology* 13.1 (2002), p. 108.

[295] Kevin Critchley, Bishnu P Khanal, Marcin Ł Górzny, Leonid Vigderman, Stephen D Evans, Eugene R Zubarev, and Nicholas A Kotov. "Near-Bulk Conductivity of Gold Nanowires as Nanoscale Interconnects and the Role of Atomically Smooth Interface." In: *Advanced Materials* 22.21 (2010), pp. 2338–2342.

[296] Nikhil R Jana, Latha Gearheart, and Catherine J Murphy. "Wet chemical synthesis of silver nanorods and nanowires of controllable aspect ratioElectronic supplementary information (ESI) available: UV–VIS spectra of silver nanorods. See http://www. rsc. org/suppdata/cc/b1/b100521i." In: *Chemical Communications* 7 (2001), pp. 617–618.

[297] Yugang Sun, Byron Gates, Brian Mayers, and Younan Xia. "Crystalline silver nanowires by soft solution processing." In: *Nano letters* 2.2 (2002), pp. 165–168.

[298] Yu Chang, Mei Ling Lye, and Hua Chun Zeng. "Large-scale synthesis of high-quality ultralong copper nanowires." In: *Langmuir* 21.9 (2005), pp. 3746–3748.

[299] Xiaogang Liu, Nianqiang Wu, Benjamin H Wunsch, Robert J Barsotti Jr, and Francesco Stellacci. "Shape-Controlled Growth of Micrometer-Sized Gold Crystals by a Slow Reduction Method." In: *Small* 2.8-9 (2006), pp. 1046–1050.

[300] Nikhil R Jana, Latha Gearheart, and Catherine J Murphy. "Wet chemical synthesis of high aspect ratio cylindrical gold nanorods." In: *The Journal of Physical Chemistry B* 105.19 (2001), pp. 4065–4067.

[301] Franklin Kim, Kwonnam Sohn, Jinsong Wu, and Jiaxing Huang. "Chemical Synthesis of Gold Nanowires in Acidic Solutions." In: *Journal of the American Chemical Society* 130.44 (2008), pp. 14442–14443.

[302] URL: https://www.sigmaaldrich.com/.

[303] URL: https://www.nanopartz.com/.

[304] URL: https://www.acsmaterial.com/.

[305] Danielle K Smith and Brian A Korgel. "The importance of the CTAB surfactant on the colloidal seed-mediated synthesis of gold nanorods." In: *Langmuir* 24.3 (2008), pp. 644–649.

[306] ZS Pereira and EZ Da Silva. "Cold welding of gold and silver nanowires: a molecular dynamics study." In: *The Journal of Physical Chemistry C* 115.46 (2011), pp. 22870–22876.

[307] Gregory S Ferguson, Manoj K Chaudhury, George B Sigal, and George M Whitesides. "Contact adhesion of thin gold films on elastomeric supports: cold welding under ambient conditions." In: *Science* 253.5021 (1991), pp. 776–778.

[308] David E Sanders and Andrew E DePristo. "Predicted diffusion rates on fcc (001) metal surfaces for adsorbate/-substrate combinations of Ni, Cu, Rh, Pd, Ag, Pt, Au." In: *Surface science* 260.1-3 (1992), pp. 116–128.

[309] Durgesh V Wagle and Gary A Baker. "Cold welding: a phenomenon for spontaneous self-healing and shape genesis at the nanoscale." In: *Materials Horizons* 2.2 (2015), pp. 157–167.

[310] G. Harman. *Wire Bonding in Microelectronics*. McGraw-Hill Education, 2009. ISBN: 9780071642651. URL: https://books.google.es/books?id=rAmJbSQ7BmEC.

[311] Wen Wu, SH Brongersma, Marleen Van Hove, and Karen Maex. "Influence of surface and grain-boundary scattering on the resistivity of copper in reduced dimensions." In: *Applied physics letters* 84.15 (2004), pp. 2838–2840.

[312] W Steinhögl, G Steinlesberger, M Perrin, G Scheinbacher, G Schindler, M Traving, and M Engelhardt. "Tungsten interconnects in the nano-scale regime." In: *Microelectronic engineering* 82.3-4 (2005), pp. 266–272.

[313] Alexander Bietsch and Bruno Michel. "Size and grain-boundary effects of a gold nanowire measured by conducting atomic force microscopy." In: *Applied physics letters* 80.18 (2002), pp. 3346–3348.

[314] Melinda Y Han, Barbaros Özyilmaz, Yuanbo Zhang, and Philip Kim. "Energy band-gap engineering of graphene nanoribbons." In: *Physical review letters* 98.20 (2007), p. 206805.

[315] Hugh O. Pierson. *Handbook of Carbon, Graphite, Diamonds and Fullerenes*. William Andrew Publishing, Noyes, 1994. ISBN: 9780815513391.

[316] Rudolph Roland Haering and PR Wallace. "The electric and magnetic properties of graphite." In: *Journal of Physics and Chemistry of Solids* 3.3-4 (1957), pp. 253–274.

[317] Kosuke Nagashio, Tomonori Nishimura, Koji Kita, and Akira Toriumi. "Mobility variations in mono-and multi-layer graphene films." In: *Applied physics express* 2.2 (2009), p. 025003.

[318] Myrsini Lafkioti, Benjamin Krauss, Timm Lohmann, Ute Zschieschang, Hagen Klauk, Klaus v Klitzing, and Jurgen H Smet. "Graphene on a hydrophobic substrate: doping reduction and hysteresis suppression under ambient conditions." In: *Nano letters* 10.4 (2010), pp. 1149–1153.

[319] Sergey L Rumyantsev, Guanxiong Liu, Michael S Shur, and Alexander A Balandin. "Observation of the memory steps in graphene at elevated temperatures." In: *Applied Physics Letters* 98.22 (2011), p. 222107.

[320] P. Lambin and V.N. Popov. "Carbon Nanotubes: Electronic Structure and Physical Properties." In: *Reference Module in Materials Science and Materials Engineering*. Elsevier, 2016. ISBN: 978-0-12-803581-8.

[321] Teri Wang Odom, JIN-LIN HUANG, and Charles M Lieber. "Single-Walled Carbon Nanotubes." In: *Annals of the New York Academy of Sciences* 960.1 (2002), pp. 203–215.

[322] Zoheir Kordrostami, Mohammad Hossein Sheikhi, and Reza Mohammadzadegan. "Modeling electronic properties of multiwall carbon nanotubes." In: *Fullerenes, Nanotubes, and Carbon Nonstructures* 16.1 (2008), pp. 66–77.

[323] Woong Kim, Ali Javey, Ophir Vermesh, Qian Wang, Yiming Li, and Hongjie Dai. "Hysteresis caused by water molecules in carbon nanotube field-effect transistors." In: *Nano Letters* 3.2 (2003), pp. 193–198.

[324] C Gómez-Navarro, PJ De Pablo, J Gómez-Herrero, B Biel, FJ Garcia-Vidal, A Rubio, and F Flores. "Tuning the conductance of single-walled carbon nanotubes by ion irradiation in the Anderson localization regime." In: *Nature materials* 4.7 (2005), p. 534.

[325] Woong Kim, Ali Javey, Ryan Tu, Jien Cao, Qian Wang, and Hongjie Dai. "Electrical contacts to carbon nanotubes down to 1 nm in diameter." In: *Applied Physics Letters* 87.17 (2005), p. 173101.

[326] A Bachtold, M Henny, C Terrier, C Strunk, C Schönenberger, J-P Salvetat, J-M Bonard, and L Forro. "Contacting carbon nanotubes selectively with low-ohmic contacts for four-probe electric measurements." In: *Applied Physics Letters* 73.2 (1998), pp. 274–276.

[327] Jeong-O Lee, C Park, Ju-Jin Kim, Jinhee Kim, Jong Wan Park, and Kyung-Hwa Yoo. "Formation of low-resistance ohmic contacts between carbon nanotube and metal electrodes by a rapid thermal annealing method." In: *Journal of Physics D: Applied Physics* 33.16 (), pp. 1953–1956.

[328] Marc Bockrath, Wenjie Liang, Dolores Bozovic, Jason H Hafner, Charles M Lieber, M Tinkham, and Hongkun Park. "Resonant electron scattering by defects in single-walled carbon nanotubes." In: *Science* 291.5502 (2001), pp. 283–285.

[329] N.W. Ashcroft and N.D. Mermin. *Solid State Physics*. Cengage Learning, 1976. ISBN: 9788131500521.

[330] R Hoffmann, D Weissenberger, J Hawecker, and D Stöffler. "Conductance of gold nanojunctions thinned by electromigration." In: *Applied Physics Letters* 93.4 (2008), p. 043118.

[331] Zheng Ming Wu, Michael Steinacher, Roman Huber, Michel Calame, Sense Jan van der Molen, and C Schönenberger. "Feedback controlled electromigration in four-terminal nanojunctions." In: *Applied Physics Letters* 91.5 (2007), p. 053118.

[332] Tali Dadosh, Yoav Gordin, Roman Krahne, Ilya Khivrich, Diana Mahalu, Veronica Frydman, Joseph Sperling, Amir Yacoby, and Israel Bar-Joseph. "Measurement of the conductance of single conjugated molecules." In: *Nature* 436.7051 (2005), p. 677.

[333] Xiao, Xu, and Nongjian J. Tao. "Measurement of Single Molecule Conductance: Benzenedithiol and Benzenedimethanethiol." In: *Nano Letters* 4.2 (2004), pp. 267–271.

[334] Youngsang Kim, Torsten Pietsch, Artur Erbe, Wolfgang Belzig, and Elke Scheer. "Benzenedithiol: A Broad-Range Single-Channel Molecular Conductor." In: *Nano Letters* 11.9 (2011), pp. 3734–3738.

[335] Alois Mispelon, Junfeng Yan, Amir H Milani, Mu Chen, Wenkai Wang, Paul OBrien, and Brian R Saunders. "Effects of added thiol ligand structure on aggregation of non-aqueous ZnO dispersions and morphology of spin-coated films." In: *RSC Advances* 5.24 (2015), pp. 18565–18577.

[336] Zong-liang Li, Fu Xiaoxiao, Guang-Ping Zhang, and Chuan-kui Wang. "Effect of Gate Electric Field on Single Organic Molecular Devices." In: *Chinese Journal of Chemical Physics* 26 (Apr. 2013), pp. 185–.

[337] Yuki Komoto, Shintaro Fujii, Hisao Nakamura, Tomofumi Tada, Tomoaki Nishino, and Manabu Kiguchi. "Resolving metal-molecule interfaces at single-molecule junctions." In: *Scientific reports* 6 (2016), p. 26606.

[338] Mark A Reed, C Zhou, CJ Muller, TP Burgin, and JM Tour. "Conductance of a molecular junction." In: *Science* 278.5336 (1997), pp. 252–254.

[339] Makusu Tsutsui, Yumi Teramae, Shu Kurokawa, and Akira Sakai. "High-conductance states of single benzenedithiol molecules." In: *Applied physics letters* 89.16 (2006), p. 163111.

[340] Kazumasa Yamauchi, Shu Kurokawa, and Akira Sakai. "Admittance of Au/1, 4-benzenedithiol/Au single-molecule junctions." In: *Applied Physics Letters* 101.25 (2012), p. 253510.

[341] URL: https://www.nanosensors.com/SuperSharpSilicon-Non-Contact-Tapping-Mode-High-Resonance-Frequency-afm-tip-SSS-NCH.

[342] Peter Markiewicz and M Cynthia Goh. "Atomic force microscopy probe tip visualization and improvement of images using a simple deconvolution procedure." In: *Langmuir* 10.1 (1994), pp. 5–7.

[343] Jan Brunner, Maria Teresa González, Christian Schönenberger, and Michel Calame. "Random telegraph signals in molecular junctions." In: *Journal of Physics: Condensed Matter* 26.47 (2014), p. 474202.

[344] Wolfgang Haiss, Changsheng Wang, Rukkiat Jitchati, Iain Grace, Santiago Martín, Andrei S Batsanov, Simon J Higgins, Martin R Bryce, Colin J Lambert, Palle S Jensen, et al. "Variable contact gap single-molecule conductance determination for a series of conjugated molecular bridges." In: *Journal of Physics: Condensed Matter* 20.37 (2008), p. 374119.

[345] Christopher Bruot, Joshua Hihath, and Nongjian Tao. "Mechanically controlled molecular orbital alignment in single molecule junctions." In: *Nature nanotechnology* 7.1 (2012), p. 35.

[346] Y Yuzhelevski, M Yuzhelevski, and G Jung. "Random telegraph noise analysis in time domain." In: *Review of Scientific Instruments* 71.4 (2000), pp. 1681–1688.

[347] Avigail Stern, Gennady Eidelshtein, Roman Zhuravel, Gideon I Livshits, Dvir Rotem, Alexander Kotlyar, and Danny Porath. "Highly Conductive Thin Uniform Gold-Coated DNA Nanowires." In: *Advanced Materials* (2018), p. 1800433.

[348] Jonathan Pate, Felix Zamora, Scott MD Watson, Nicholas G Wright, Benjamin R Horrocks, and Andrew Houlton. "Solution-based DNA-templating of sub-10 nm conductive copper nanowires." In: *Journal of Materials Chemistry C* 2.43 (2014), pp. 9265–9273.

[349] Jerry B Marion. *Dinámica clásica de las partículas y sistemas*. Reverté, 1992.

[350] Elisa Palacios-Lidón and Jaime Colchero. "Quantitative analysis of tip–sample interaction in non-contact scanning force spectroscopy." In: *Nanotechnology* 17.21 (2006), p. 5491.

[351] Paul V Pesavento, Reid J Chesterfield, Christopher R Newman, and C Daniel Frisbie. "Gated four-probe measurements on pentacene thin-film transistors: Contact resistance as a function of gate voltage and temperature." In: *Journal of Applied Physics* 96.12 (2004), pp. 7312–7324.

[352] Anthony Ayari, Enrique Cobas, Ololade Ogundadegbe, and Michael S Fuhrer. "Realization and electrical characterization of ultrathin crystals of layered transition-metal dichalcogenides." In: *Journal of applied physics* 101.1 (2007), p. 014507.

[353] Michele Buscema, Dirk J Groenendijk, Sofya I Blanter, Gary A Steele, Herre SJ Van Der Zant, and Andres Castellanos-Gomez. "Fast and broadband photoresponse of few-layer black phosphorus field-effect transistors." In: *Nano letters* 14.6 (2014), pp. 3347–3352.

[354] Team Nanotec GmbH. *Hemisperical Cone Shaped Tip*. 2018. URL: https://www.team-nanotec.de/index.cfm?contentid=10&shopAction=showProductDetails&id=325.

[355] John E Sader, James WM Chon, and Paul Mulvaney. "Calibration of rectangular atomic force microscope cantilevers." In: *Review of Scientific Instruments* 70.10 (1999), pp. 3967–3969.

[356] URL: www.gildergrids.co.uk.

[357] URL: https://www.tpt-wirebonder.com/en/start.html.

[358] URL: https://www.chemtronics.com/circuitworks-conductive-epoxy-2.

[359] URL: https://export.rsdelivers.com/es/product/rs-pro/rs-186-3593/rs-pro-silver-conductive-paint-paint-5-g-bottle/1863593?cl=1&lang=es.

[360] URL: https://www.nanosensors.com/PointProbe-Plus-Force-Modulation-Mode-afm-tip-PPP-FM.

[361] J. V. Colchero Paetz. "Reibungskrafmikroscopie." PhD thesis. Universität Konstanz, Germany, 1993.

[362] URL: https://www.budgetsensors.com/multipurpose-afm-probe-conductive-diamond-all-in-one-dd.

[363] URL: https://www.budgetsensors.com/force-modulation-afm-probe-platinum-electrimulti75.

[364] Li Lin, Zhonghui Liu, Xiyao Li, Hongchen Gu, and Jian Ye. "Quantifying the reflective index of nanometer-thick thiolated molecular layers on nanoparticles." In: *Nanoscale* 9 (6 2017), pp. 2213–2218.

LIST OF PUBLICATIONS

Publications during PhD

- **Probe-Assisted Nanowire Circuitry**
  Pablo Ares*, *M. Moreno-Moreno**, C. Moreno, F. Zamora, C. Gómez-Navarro and J. Gómez-Herrero. *These authors contributed equally. *Submitted*.

- **One-Pot Preparation of Mechanically Robust, Transparent, Highly Conductive, and Memristive Metal-Organic Ultrathin Film**
  M. Moreno-Moreno, J. Troyano, P. Ares, O. Castillo, C. A. Nijhuis, L. Yuan, P. Amo-Ochoa, S. Delgado, J. Gómez-Herrero, F. Zamora, and C. Gómez-Navarro. In: ACS nano 12.10 (2018), pp. 10171-10177. *Best paper of the year 2018 by RSEF-GEFES.*

- **Environmental effects in mechanical properties of few-layer black phosphorus**
  M. Moreno-Moreno, G. López-Polín, A. Castellanos-Gómez, C. Gómez-Navarro, and J. Gómez-Herrero. In: 2D Materials 3.3 (2016), p. 031007.

Other publications (before PhD)

- **Feature exploration for biometric recognition using MMW body images**
  E. Gonzalez-Sosa, R. Vera-Rodriguez, J. Fierrez, *M. Moreno-Moreno*, and J. Ortega-Garcia. In: EURASIP Journal on Image and Video Processing 2015.1 (2015), p. 30.

- **Dependence of the single walled carbon nanotube length with growth temperature and catalyst density by chemical vapor deposition**
  V. López, L. Welte, M. A. Fernández, *M. Moreno-Moreno*, J. Gómez-Herrero, P. J. de Pablo, and F. Zamora. In: Journal of nanoscience and nanotechnology 9.5 (2009), pp. 2830–2835.

- **Ultralong natural graphene nanoribbons and their electrical conductivity**
  M. Moreno-Moreno, A. Castellanos-Gomez, G. Rubio-Bollinger, J. Gomez-Herrero, and N. Agraït. In: Small 5.8 (2009), pp. 924–927.

- **Voltage and length-dependent phase diagram of the electronic transport in carbon nanotubes**
  P. Sundqvist, F. J. Garcia-Vidal, F. Flores, *M. Moreno-Moreno*, C. Gómez-Navarro, J. Scott Bunch, and J. Gómez-Herrero. In: Nano letters 7.9 (2007), pp. 2568–2573.

- **Parametric resonance based scanning probe microscopy**
  M. Moreno-Moreno, A. Raman, J. Gomez-Herrero, and R. Reifenberger. In: Applied physics letters 88.19 (2006), p. 193108.

- **Resonant Raman scattering in strained and relaxed InGaN/GaN multi-quantum wells**
  S. Lazić, *M. Moreno-Moreno*, J. M. Calleja, A. Trampert, K. H. Ploog, F. B. Naranjo, S. Fernandez, and E. Calleja. In: Applied Physics Letters 86.6 (2005), p. 061905.

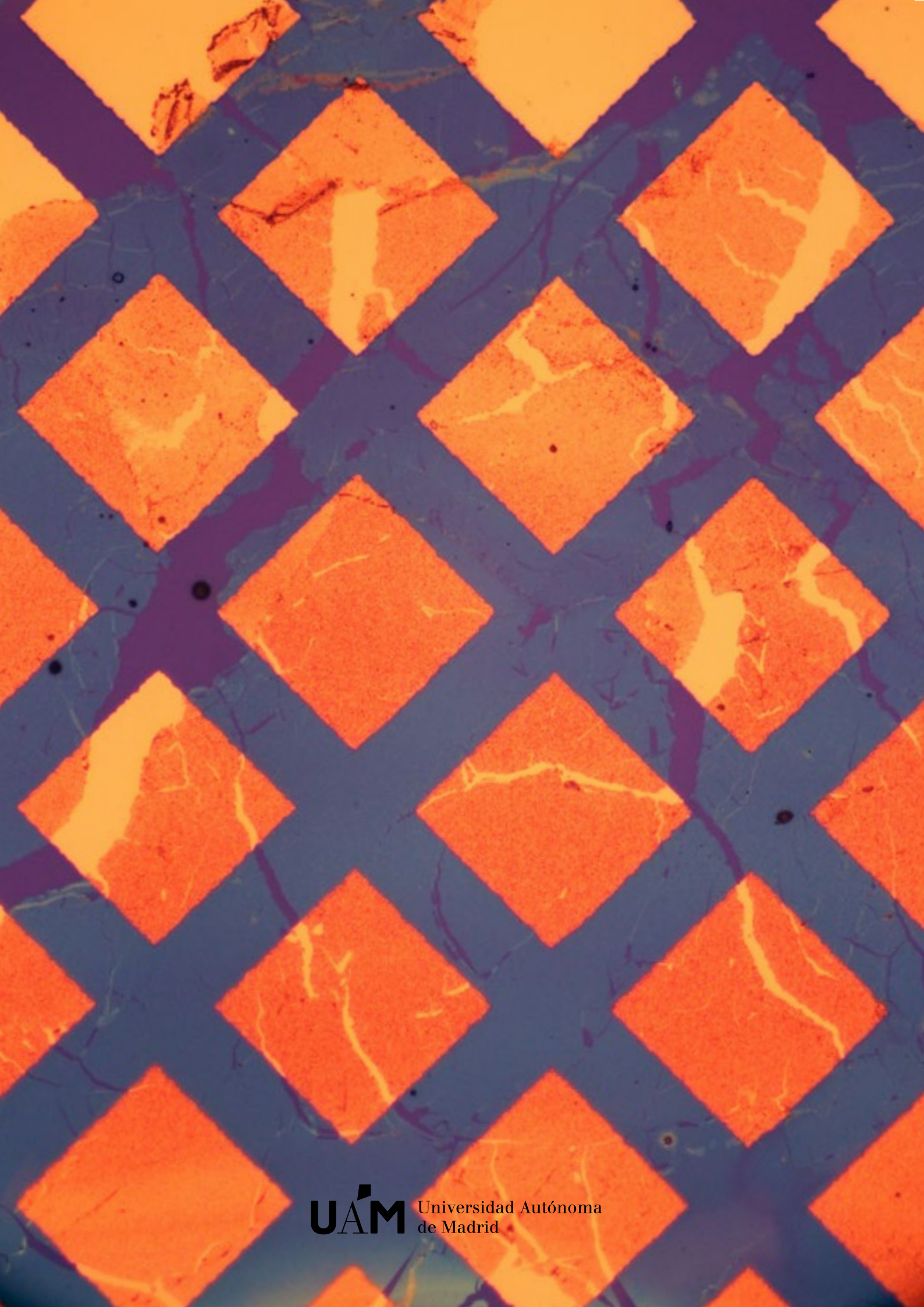

UAM Universidad Autónoma de Madrid